

Heavy Ion Collimation at the Large Hadron Collider Simulations and Measurements

Inaugural-Dissertation
zur Erlangung des Doktorgrades
der Naturwissenschaften im Fachbereich Physik
der Mathematisch-Naturwissenschaftlichen Fakultät
der Westfälischen Wilhelms-Universität Münster

vorgelegt von
Pascal Dominik Hermes
aus
Saarlouis

-2016-

Dekan: Prof. Dr. Markus Donath
Erster Gutachter: Prof. Dr. Johannes P. Wessels
Zweiter Gutachter: Prof. Dr. Max Mustermann

Tag der Disputation: 31.11.2016
Tag der Promotion: 31.11.2016

Contents

1	Introduction	3
2	Particle Accelerator Physics	5
2.1	Particle Dynamics in Electromagnetic Fields	5
2.1.1	Reference frame	5
2.1.2	Magnetic Bending of Particles with different Charges and Masses	7
2.2	Linear Transverse Dynamics	10
2.2.1	The Accelerator Beam Line	10
2.2.2	Equation of Motion	12
2.3	Longitudinal Particle Dynamics	17
3	The Large Hadron Collider	19
3.1	The CERN Accelerator Complex	19
3.2	LHC Layout	21
3.2.1	Global Layout	21
3.2.2	Insertion Region Layout and Optics	21
3.2.3	LHC Cycle	24
3.3	Luminosity	25
3.4	LHC Performance in Operation	27
3.4.1	Proton Beams	27
3.4.2	Heavy-Ion Beams	28
3.5	The LHC Magnets	29
3.5.1	Main Dipoles	29
3.5.2	Quadrupoles	30
3.5.3	Quench Limit	30
3.6	The LHC Collimation System	33

3.6.1	Particle Losses in the LHC	34
3.6.2	Collimation Concept	34
3.6.3	Collimator Types	37
3.6.4	Collimator Settings and Alignment	38
3.6.5	Collimation Cleaning Inefficiency	41
3.6.6	Particle-Matter Interaction and Collision Effects	42
3.6.7	Measurement of Losses in LHC Operation	49
4	Simulation Tools	51
4.1	MAD-X	51
4.2	FLUKA	51
4.3	SixTrack	52
4.3.1	Tracking in SixTrack	52
4.3.2	Collimation SixTrack	53
4.4	SixTrack-FLUKA Coupling	56
4.5	ICOSIM	57
5	Collimation of Heavy-Ion Beams	59
5.1	Heavy-Ion Qualification Loss Maps	59
5.2	Simulation with ICOSIM	61
5.3	Conclusions	62
6	SixTrack with Ion-Equivalent Rigidities	63
6.1	Efficiency of Staged Collimation for Heavy-Ions	63
6.2	The STIER Simulation Tool	66
6.2.1	Optics Calculation	67
6.2.2	Fragmentation Simulation	68
6.2.3	Heavy-Ion Tracking in SixTrack	71
6.3	Simulation Results	72
6.3.1	Full Heavy-Ion Loss Map Simulations	72
6.3.2	Dependence on the starting Collimator Jaw	76
6.3.3	Loss locations of individual isotopes	78
6.3.4	Dependence on the Impact Parameter	80
6.3.5	Loss Classification of Residual Heavy-Ion Fragments	81

6.4	Chromatic Tracking in ICOSIM and SixTrack	82
6.5	Summary and Conclusions	83
7	Heavy-Ion SixTrack	85
7.1	Requirements and Implementation Strategy	85
7.2	Magnetic Tracking of Multiple Isotopes	86
7.2.1	Hamiltonian Formalism of Particle Motion	86
7.2.2	The Accelerator Hamiltonian for Multi-Isotopic Ion Beams	88
7.3	Tracking Maps for Beam-Line Elements	93
7.3.1	Drift Space	93
7.3.2	Dipole	95
7.3.3	Thin Transverse Kicker Magnet	99
7.3.4	Quadrupole	100
7.3.5	Thin Multipole	102
7.3.6	Accelerating RF Cavity	103
7.4	Multi-Isotope Tracking in hiSixTrack	104
7.4.1	Multi-Isotope Tracking	104
7.4.2	Definition of the Heavy-Ion Species	105
7.4.3	Benchmarking of Ion Tracking in hiSixTrack	105
7.5	The hiSixTrack-FLUKA Coupling	110
7.5.1	Heavy Ion Exchange between hiSixTrack and FLUKA	110
7.5.2	Benchmarking of the Fragmentation Simulation	112
7.5.3	Collimator Losses	113
7.5.4	Simulation Output	114
7.6	Loss Map Simulation with the hiSixTrack-FLUKA coupling	114
7.6.1	Initial Distribution	114
7.6.2	Loss Map Benchmarking	116
7.6.3	Contribution of Secondary Fragmentation	118
8	Simulations and Measurements	121
8.1	Preparation of the Heavy-Ion Operation in 2015	121
8.1.1	Validation of Collimator Settings	122
8.1.2	Orbit Bumps in the IR7 DS	125
8.2	Suppression of Losses at the IR2 TCT	129

8.2.1	Situation and Analysis	130
8.2.2	Mitigation Strategies and their Application in the LHC	132
8.2.3	Conclusions	134
8.3	Heavy-Ion Collimation Quench Test	134
8.3.1	Preparation & Experimental Schedule	135
8.3.2	Realization	137
8.3.3	Data Analysis	139
8.3.4	Summary and Outlook	144
9	Future LHC Configurations	145
9.1	Heavy-Ion Operation in 2016	145
9.2	HL-LHC Upgrade with TCLD Collimators	145
9.2.1	LIU and High Luminosity LHC	145
9.2.2	Consistency Check with STIER	147
9.2.3	Simulation with hiSixTrack	149
9.3	Operation with other Heavy-Ion Species	153
10	Outlook	157
10.0.1	157
10.1	Heavy-Ion Loss Maps with Aperture and Orbit Uncertainties	157
11	Summary and Conclusions	159
A		161
A.1	Tracking Map Symplecticity	161
A.1.1	Thick Dipole	161
A.1.2	Thin Dipole	162
A.1.3	Thick Quadrupole	162
A.1.4	Thin Quadrupole	163
A.2	IR2 Loss Mitigation Experiment - Loss Maps	164
A.3	STIER Loss Maps	166
A.3.1	Settings validation for the 2015 heavy-ion run	166
A.4	Accelerator Hamiltonian in a Curved Coordinate System	167
A.5	Implementation of hiSixTrack	169
A.5.1	Variables in hiSixTrack	169

A.5.2 Initialization of hiSixTrack	171
A.5.3 Initial Particle Distribution	172
A.5.4 Implemented Heavy-Ion Tracking Maps	173
A.6 Implementation of the hiSixTrack-FLUKA Coupling	175
A.6.1 Code Structure	175
A.6.2 Changes in FLUKA Input and Subroutines	175
A.6.3 Changes in hiSixTrack	178

Abstract

The LHC collimation system is an essential part of the machine to provide protection against beam halo at high particle intensities at the accelerator.

Für Julia

1. Introduction

- LHC breaking many superlatives, e.g. stored beam energy
- Contrary to the stored beam energy very sensitive hardware, operated closely to quench limit (1K is sufficient to bring to the normal conducting state)
- Collimation system must protect sensitive devices by inducing controlled losses in dedicated devices.
- Heavy ion collisions for the generation of QGP

2. Particle Accelerator Physics

Introduction

The history of particle accelerators goes back to the 1930s when the first accelerators were designed to provide the particle energies required to study atomic nuclei. Nowadays, a vast variety of accelerator types is available for many different applications, reaching from low-energy machines for particle therapy in cancer treatment (for example Heidelberger Ionenstrahl-Therapiezentrum, HIT [HIT]) over synchrotron light sources at intermediate energies (for example SOLEIL [SOL]) to high-energy synchrotron colliders for fundamental research, such as the Large Hadron Collider (LHC), presented in Chap. 3.

Particles in the magnetic lattice of high energy synchrotrons like the LHC perform quasi-harmonic transverse oscillations around a reference trajectory. Furthermore, the accelerating devices lead to longitudinal oscillations. Evidently, these types of particle motion are important for the description of the collimation system and the simulation of particle motion for residual particles created in it. In this chapter, the theoretical background to quantify the transverse and longitudinal motion is briefly introduced. Since the new simulation tool to be developed aims for the tracking of multiple different isotopes, the magnetic bending is quantified for different isotopes at the beginning of the chapter. The following section quantifies the transverse oscillations of beam particles in a lattice of bending and focusing magnets. The last section describes the longitudinal particle motion.

2.1 Particle Dynamics in Electromagnetic Fields

2.1.1 Reference frame

Particle beams in circular accelerators are bent by means of magnetic dipole fields. With the design of the machine, a closed reference trajectory is defined which leads typically through the center of the beam pipes and magnets. This trajectory corresponds to the orbit of a particle at design momentum without transverse offsets, which is referred to as the ideal particle. With

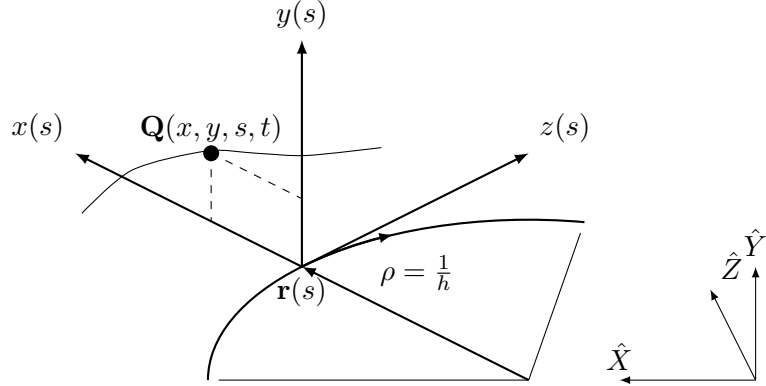


Figure 2.1: Accelerator coordinate system (x, y, z) moving with $\mathbf{r}(s)$. The radius of the bent trajectory is $\rho = \frac{1}{h_x}$. Figure taken from [DMFH15].

respect to the curvilinear laboratory frame $(\hat{X}, \hat{Y}, \hat{Z})$, the position of the reference particle at the time t is defined by the vector $\mathbf{r}(s)$, where $s(t)$ is a parameter describing the distance travelled from a defined reference point in the accelerator (see Fig. 2.1). The cartesian accelerator coordinate system $(\hat{x}, \hat{y}, \hat{z})$, spanned by the unitary vectors $(\mathbf{e}_x, \mathbf{e}_y, \mathbf{e}_z)$, moves with the reference particle and thus with $\mathbf{r}(s)$, as shown in Fig. 2.1. The particle position in the laboratory frame is then fully characterized by the vector

$$\mathbf{Q}(x, y, z, s) = \mathbf{r}(s) + x \mathbf{e}_x + y \mathbf{e}_y + z \mathbf{e}_z. \quad (2.1)$$

Inside the dipole magnets, the trajectory of the vector $\mathbf{r}(s)$ is bent by a radius

$$\rho = \frac{1}{h_x}. \quad (2.2)$$

Electromagnetic fields are generally defined by the gradient of the electric scalar potential V and the magnetic vector potential \mathbf{A} . In the curvliniar reference system (x, y, s, t) , spanned by the unitary vectors $(\mathbf{e}_x, \mathbf{e}_y, \mathbf{e}_s)$, the electromagnetic fields \mathbf{E} and \mathbf{B} can then be derived from the scalar potential $V(x, y, s, t)$ and the vector potential $\mathbf{B}(x, y, s, t)$ as follows [Wol14]

$$\mathbf{E} = -\nabla V - \frac{\partial \mathbf{A}}{\partial t}, \quad (2.3)$$

$$\mathbf{B} = \nabla \times \mathbf{A} = \left(\partial_y A_s - \frac{\partial_s A_y}{1 + h_x x} \right) \mathbf{e}_x + \left(\frac{\partial_s A_x}{1 + h_x x} - \frac{\partial_x A_s}{1 + h_x x} - \partial_x A_s \right) \mathbf{e}_y + (\partial_x A_y - \partial_y A_x) \mathbf{e}_z. \quad (2.4)$$

2.1.2 Magnetic Bending of Particles with different Charges and Masses

This section gives a brief overview on the motion of charged particles in the confining and guiding electromagnetic fields of a particle accelerator. The transverse betatron motion in the accelerator magnets is introduced as the solution of the equations of motion. Important definitions to quantify the rigidity offset of heavy-ions with respect to a reference particle are given in this section.

General Case

The accelerator lattice is designed to provide bending and focusing fields for a reference particle of a defined particle species. Consider a heavy-ion accelerator for the reference species

$${}^{A_0}X_0^{(Z_0-n_{e,0})+} \quad m_0 = m \left({}^{A_0}X_0^{(Z_0-n_{e,0})+} \right), \quad (2.5)$$

where X_0 is the element name, A_0 is the number of nuclei, $Z_0 = q_0/e$ is the nuclear charge multiplicity, m_0 is the rest mass of the reference ion and $n_{e,0}$ is the number of electrons attached to the ion.

Different physical processes can change the ion species or momentum, one of them being the interaction of the ion with the material of a collimator (see Chap. 3.6). The particle properties of an arbitrary ion are generically given as follows:

$${}^A X^{(Z-n_e)+} \quad m = m \left({}^A X^{(Z-n_e)+} \right). \quad (2.6)$$

Here and in the following, quantities subscripted with zero refer to the reference particle, while unsubscripted quantities correspond to the tracked particle.

Charged particles moving in electromagnetic fields are subject to the Lorentz force [Gri13]

$$\mathbf{F} = q (\mathbf{E} + \mathbf{v} \times \mathbf{B}), \quad (2.7)$$

where q is the particle charge, \mathbf{E} is the electric field vector, \mathbf{v} is the particle speed vector, and \mathbf{B} is the magnetic field vector. In absence of an electric field the Lorentz force becomes purely transverse and the interplay between the centripetal force and the Lorentz force bends the particle trajectory by a certain radius ρ defined by [Wie99]

$$B \rho = \frac{P}{q}. \quad (2.8)$$

P is the particle momentum and $B \rho$ is referred to as the magnetic rigidity. The relativistic

particle momentum and energy can be expressed as

$$P = m \beta \gamma c, \quad E = m \gamma c^2, \quad (2.9)$$

where $\beta = \frac{v}{c}$ is the particle speed normalized by the speed of light c and the Lorentz factor by $\gamma = \frac{1}{\sqrt{1-\beta^2}}$. Following Eq. (2.8), the design rigidity can be expressed in terms of the momentum per rest mass $p_0 = P_0/m_0 = \beta \gamma c$ of the reference species:

$$B \rho_0 = \frac{P_0}{q_0} = \frac{m_0 p_0}{Z_0 e}. \quad (2.10)$$

The rigidity of an arbitrary ion with a momentum per rest mass $p_i = p_0 + \Delta p$ can be expressed in the generic way

$$B \rho = \frac{m (p_0 + \Delta p)}{Z e}. \quad (2.11)$$

Using Eq. (2.10) and elementary transformations, the contributions from velocity offset and the mass to charge ratio with respect to that of the reference isotope can be separated into two different factors. The heavy-ion rigidity can then be expressed in terms of the rigidity of the ideal particle

$$B \rho = \frac{m}{m_0} \frac{q_0}{q} B \rho_0 \left(1 + \frac{p - p_0}{p_0} \right) = B \rho_0 \frac{(1 + \delta)}{\chi}. \quad (2.12)$$

The bending radius of a real ion is scaled with respect to the reference bending radius by a factor of $\frac{(1+\delta)}{\chi}$. The two quantities χ and δ are independent from each other and are the source of dispersion in a magnet. The relative momentum per mass offset δ can be expressed in terms of the full ion momenta as

$$\delta = \frac{P \frac{m_0}{m} - P_0}{P_0} = \frac{p - p_0}{p_0} = \frac{\beta \gamma - \beta_0 \gamma_0}{\beta_0 \gamma_0}. \quad (2.13)$$

In the latter expression the dependence of the ion masses is fully eliminated so it is a pure function of the particle velocity. The relative mass to charge offset χ scales with the mass to charge ratio relative to the reference species, defined as

$$\chi = \frac{q}{q_0} \frac{m_0}{m}. \quad (2.14)$$

An alternative way to derive the dependency described in Eq. (2.12) is by considering the ratio

of the rigidities defined in Eq. (2.10) and Eq. (2.8):

$$\frac{B\rho}{B\rho_0} = \frac{P}{P_0} \frac{q_0}{q} = \frac{q_0}{q} \frac{m}{m_0} \frac{\beta\gamma}{\beta_0\gamma_0} = \frac{(1 + \delta)}{\chi}. \quad (2.15)$$

Note that the rigidity of an ion with $\chi \neq 1$ and arbitrary δ is identical to the rigidity of an ion of the reference species ($\chi = 1$) with the effective momentum offset

$$\delta_{\text{eff}} = \frac{(1 + \delta)}{\chi} - 1. \quad (2.16)$$

Hence, the motion in a magnetic field of an arbitrary ion with momentum offset δ and mass/charge offset χ is identical to that of a particle of the reference species with the momentum offset δ_{eff} .

Mono-Isotopic Case

The mono-isotopic case is the standard case which is discussed in literature (see [Pro94, Wie99, Lee12]). The mono-isotopic equations are obtained by the following substitutions:

$$m \rightarrow m_0, \quad q \rightarrow q_0, \quad \chi \rightarrow 1. \quad (2.17)$$

In this case, Eq. (2.13) yields the standard expression used in literature:

$$\delta = \frac{P - P_0}{P_0} = \frac{\beta\gamma - \beta_0\gamma_0}{\beta_0\gamma_0}. \quad (2.18)$$

Note that the latter expression remains unchanged, so δ is always a pure function of the particle velocity. This finding can be drawn back to the velocity dependence of the Lorentz force. Furthermore, it is also a relative momentum offset in the mono-isotopic case and a relative momentum per mass offset if multiple ion types are present.

2.2 Linear Transverse Dynamics

2.2.1 The Accelerator Beam Line

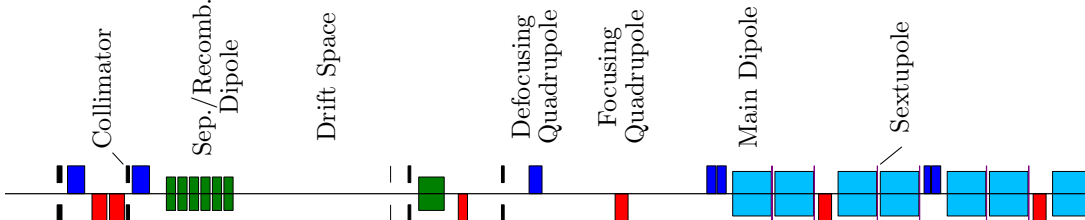


Figure 2.2: Example for a short section of an accelerator beam line. The individual symbols represent different beam line elements which are described on top.

The particle beams in a high energy synchrotron are guided and focussed by means of dedicated magnetic fields of different multipole orders. The magnets are assembled to a beam line to guide the beam on the foreseen trajectory and to confine its transverse dimensions. An example of a short section in the region IR1 of the beam line of the CERN Large Hadron Collider (see Chap. 3) is shown in Fig. 2.2. In this subsection, a brief overview of the functionality of the different beam line elements is given, to conclude on their influence on the particle motion in the next subsection.

Dipole Magnets

Dipole magnets provide uniform transverse magnetic fields to bend the beam orbit to a defined radius $\rho = \frac{1}{h_x}$. The main dipoles (light blue rectangles in Fig. 2.2) provide the bending force to keep the beams on a circular trajectory.

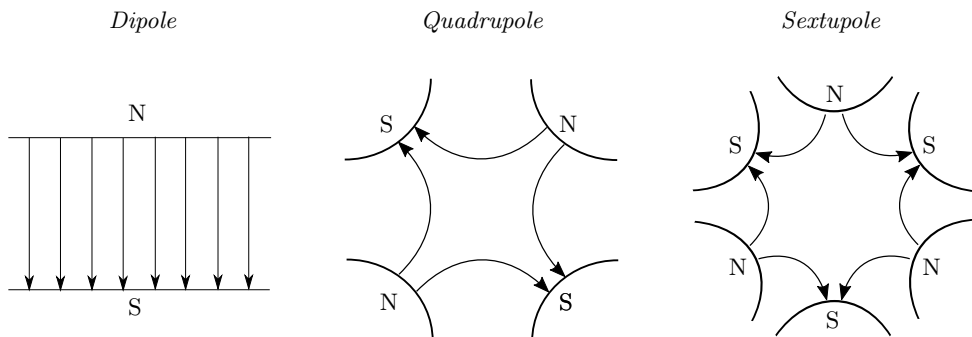


Figure 2.3: Schematic illustration of the magnetic field lines in different magnet types.

If the beam orbit differs from the ideal orbit, the orbit is corrected with kicker dipole magnets. Compared to the main dipoles, the reference trajectory in the kicker magnets is not bent, thus $h_x = 0$. Also the crossing angle and the separation bumps are created by kicker magnets.

Close to the experiments, where the beams collide, the two counter-rotating beams have to be guided from separated beam pipes into a common beam pipe. The recombination and separation dipoles serve this purpose. In the beam line plot they are shown as green rectangles.

Quadrupole Magnets

Quadrupole magnets (see Fig. 2.3) are used to provide focussing in order to confine the transverse dimensions of the particle beams. The magnetic field in a quadrupole is not of equal strength at every position but increases linearly with the distance from the transverse quadrupole center:

$$B_y = g x, \quad B_x = -g y. \quad (2.19)$$

The magnetic field gradient g , measured in T/m, defines the strength of the quadrupole. The quantity g is often expressed normalized by the momentum, referred to as the focusing strength k with the unit m⁻²:

$$k = \frac{q_0}{P_0} g. \quad (2.20)$$

If a particle is not moving through the center of the quadrupole it is subject to a transverse force which is focusing (directed towards the ideal trajectory) in one transverse direction and defocusing in the other. Therefore the effective confinement of the beam dimensions in both transverse directions requires multiple quadrupole magnets which are arranged in a specific manner. Given that the ideal particle is not subject to a magnetic field, the reference trajectory in a quadrupole is straight and $h_x = 0$.

Sextupole Magnets

The Lorentz force depends on the magnetic rigidity of the particle traversing the magnetic field. Thus, the focal length of a quadrupole magnet depends on the particle momentum, so the guidance of the optical lattice becomes momentum dependent. In circular accelerators this momentum dependence, together with an inevitable spread in momentum between beam particles, can lead to instabilities and resonances. They are compensated by means of sextupole magnets, with a cross-section as shown on the right hand side of Fig. 2.3. Sextupoles in the LHC are installed right downstream of the main dipoles and shown in the beam line plot as rose rectangles.

2.2.2 Equation of Motion

General Solution

The transverse motion can be described in leading order by expanding the magnetic dipole and quadrupole fields and considering the equation of motion in the approximation of small x, y and δ [Lee12]. Higher orders are ignored in this approach. The resulting equation of motion for the case of $\chi = 1$ in horizontal direction¹ is given by:

$$x'' - (k(s) - h_x^2(s)) x = \delta h_x(s), \quad (2.21)$$

where $x' = \frac{dx}{ds}$. The general solution of the homogeneous part of this equation is described by

$$\begin{pmatrix} x \\ x' \end{pmatrix} = \begin{pmatrix} C_x(s) & S_x(s) \\ C'_x(s) & S'_x(s) \end{pmatrix} \begin{pmatrix} x_0 \\ x'_0 \end{pmatrix}, \quad (2.22)$$

where, using the substitution $K(s) = -k(s) + h_x^2(s)$, the quantities $S_x(s), C_x(s)$ are defined as

$$S_x(s) = \frac{1}{\sqrt{K}} \sin(\sqrt{K}s) \quad \text{and} \quad C_x(s) = \cos(\sqrt{K}s) \quad \text{for } K > 0, \quad (2.23)$$

$$S_x(s) = \frac{1}{\sqrt{-K}} \sinh(\sqrt{-K}s) \quad \text{and} \quad C_x(s) = \cosh(\sqrt{-K}s) \quad \text{for } K < 0. \quad (2.24)$$

The particle trajectories in any linear beam line element are thus either harmonic oscillations or exponential functions depending on the sign of K . A widely used application of the general solution in Eq. (2.22) is the derivation of transfer maps for the individual beam line elements, defined by the length L and their strength K . The particle coordinates x, x' at the end of the beam line element are then related to the coordinates x_0, x'_0 at its beginning by means of the matrix multiplication

$$\begin{pmatrix} x \\ x' \end{pmatrix} = \begin{pmatrix} C_x(L) & S_x(L) \\ C'_x(L) & S'_x(L) \end{pmatrix} \begin{pmatrix} x_0 \\ x'_0 \end{pmatrix} = \mathcal{M} \begin{pmatrix} x_0 \\ x'_0 \end{pmatrix}. \quad (2.25)$$

The transfer matrix \mathcal{M} is specific for every beam line element. The transformation of the particle coordinates by a sequence of beam line elements can be described by a combined matrix obtained by a matrix multiplication of all involved transfer matrices. Using Eq. (2.25), the transfer matrices \mathcal{M}_D of a drift space ($K = 0$), $\mathcal{M}_{Q,f}$ of a focusing quadrupole ($K > 0$) and

¹This chapter refers to the horizontal direction as x . The derivation for y is equivalent with the difference that in vertical direction $h_x = 0$. Furthermore it should be kept in mind that the quadrupole is always focusing in one and defocusing in the other plane.

$\mathcal{M}_{Q,d}$ of a defocusing quadrupole ($K < 0$) yield

$$\mathcal{M}_D = \begin{pmatrix} 1 & L \\ 0 & 1 \end{pmatrix}, \quad \mathcal{M}_{Q,f} = \begin{pmatrix} \cos(\sqrt{K}L) & \frac{1}{\sqrt{K}} \sin(\sqrt{K}L) \\ -\sqrt{K} \sin(\sqrt{K}L) & \cos(\sqrt{K}L) \end{pmatrix}, \quad (2.26)$$

$$\mathcal{M}_{Q,d} = \begin{pmatrix} \cosh(\sqrt{|K|}L) & \frac{1}{\sqrt{|K|}} \sinh(\sqrt{|K|}L) \\ \sqrt{|K|} \sinh(\sqrt{|K|}L) & \cosh(\sqrt{|K|}L) \end{pmatrix}. \quad (2.27)$$

Thin Lens Approximation

The analytical treatment of the transfer matrices can be significantly simplified if the magnet length L is small compared to $1/KL$. The magnetic bending can then be treated as a point-like transverse kick which is given to the particle at the center of the magnet, while at the rest of the element length the particle trajectory remains undisturbed, so behaves like a drift space (see Fig. 2.4). Mathematically, this thin lens approximation [RS95] corresponds to the limit

$$L \rightarrow 0 \quad \text{with} \quad KL = \text{const.} \quad (2.28)$$

The transfer matrix for a quadrupole magnet simplifies in the thin lens approximation to:

$$\mathcal{M}_{Q,f/d} = \begin{pmatrix} 1 & L \\ KL & 1 \end{pmatrix}, \quad (2.29)$$

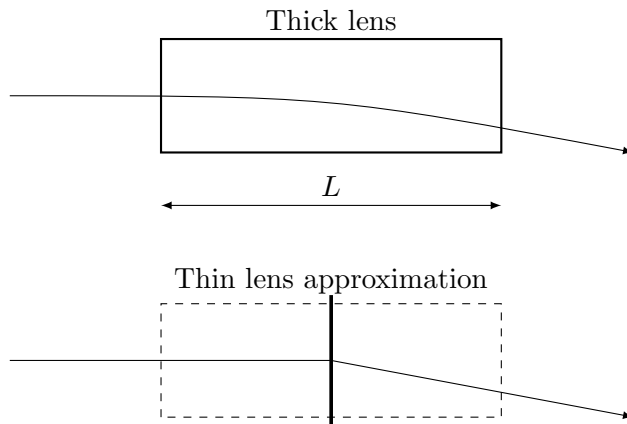


Figure 2.4: Schmematic illustration of the thin lens approximation. The transverse bending of a magnet of length L is approximated by a point-like kick the particle receives only at the center of the magnet. Left and right of the magnet center the particle momentum remaines unchanged.

which is equivalent to the transfer matrix of a thin optical lens with focal length $f = \frac{1}{KL}$.

Periodic Solution and Betatron Motion

An alternative to the solution of the homogeneous part of the equation of motion, given before in matrix form, is given by:

$$x(s) = \sqrt{\tilde{\epsilon}_x} \sqrt{\beta_x(s)} \cos(\psi_x(s) + \phi), \quad (2.30)$$

where $\tilde{\epsilon}$ and ϕ are mathematically the integration constants and represent the initial conditions of the particle. The function $\beta_x(s)$ is the betatron function related to the maximum amplitude the particle trajectory can take at the position s .

In circular accelerators the quantity $K(s)$ is a periodic quantity with period length C :

$$K(s) = K(s + C). \quad (2.31)$$

The equation of motion (2.21) with periodic $K(s)$ is the Hill differential equation [Wie99]. The solution of Hill's equation is identical to Eq. (2.30), but the periodicity implies that also $\beta_x(s)$ is periodic in s with period C :

$$\beta_x(s) = \beta_x(s + C). \quad (2.32)$$

The betatron function is purely defined by the magnetic lattice in the accelerator. The particles perform transverse quasi-harmonic oscillations, with the coordinate x , around the ideal trajectory. The local amplitude of these so-called betatron oscillations is defined by $\tilde{\epsilon}_x$, the betatron function $\beta_x(s)$ and the betatron phase $\psi_x(s)$, defined as

$$\psi_x(s) = \int_0^s \frac{ds}{\beta_x(s)}. \quad (2.33)$$

The total number of horizontal betatron oscillations over one turn is the machine tune

$$Q_x = \frac{1}{2\pi} \int_0^C \frac{ds}{\beta_x(s)}. \quad (2.34)$$

From Eq. (2.30) it can be deduced that $\tilde{\epsilon}_x$ is a constant of motion, mathematically the Courant-Snyder invariant, for the individual particle:

$$\tilde{\epsilon}_x = \gamma_x(s) x'(s) + 2 \alpha_x(s) x(s) x'(s) + \beta_x(s) x'^2(s). \quad (2.35)$$

The quantities $\beta_x(s)$, $\alpha_x(s)$ and $\gamma_x(s)$ are the Twiss parameters [Wie99]. They are defined by

the magnetic lattice in the machine which transforms the beam equivalently to a lattice lenses in classical optics. The Twiss parameters are therefore referred to as the optical functions, and the configuration of the magnetic lattice as the beam optics.

The derivative of the betatron function $\beta_x(s)$ defines the two remaining Twiss parameters as:

$$\alpha_x(s) = -\frac{1}{2}\beta'_x(s) \quad \gamma_x(s) = \frac{1 + \alpha_x(s)^2}{\beta_x(s)}. \quad (2.36)$$

The evolution of an initial set $(\alpha_{x,0}, \beta_{x,0}, \gamma_{x,0})$ of Twiss parameters in the accelerator depends on the lattice elements and is, equivalent to the transformation of the particle coordinates in Eq. (2.25), described by their transfer matrices as follows:

$$\beta_x(s) = C_x^2 \beta_{x,0} - 2 S_x^2 C_x^2 \alpha_{x,0} + S_x^2 \gamma_{x,0}. \quad (2.37)$$

The expression in Eq. (2.35) is the parametric representation of an ellipse in x, x' enclosing a phase space volume of $\pi\tilde{\epsilon}_x$. Shape and orientation of the phase space ellipse are changing as a function of the the Twiss parameters, but the volume in phase space enclosed by the ellipse remains unchanged. Following Eq. (2.30), the largest possible amplitude in x and x' the particle can reach yields:

$$x_{\max} = \sqrt{\tilde{\epsilon}\beta_x(s)} \quad \text{and} \quad x'_{\max} = -\alpha_x(s) \sqrt{\frac{\tilde{\epsilon}}{\beta_x(s)}} \quad (2.38)$$

The phase space volume $\tilde{\epsilon}$ is thus related to the peak amplitude of the betatron oscillation for a given β -function. If many particles compose the beam, the r.m.s. value of the individual $\tilde{\epsilon}$ is

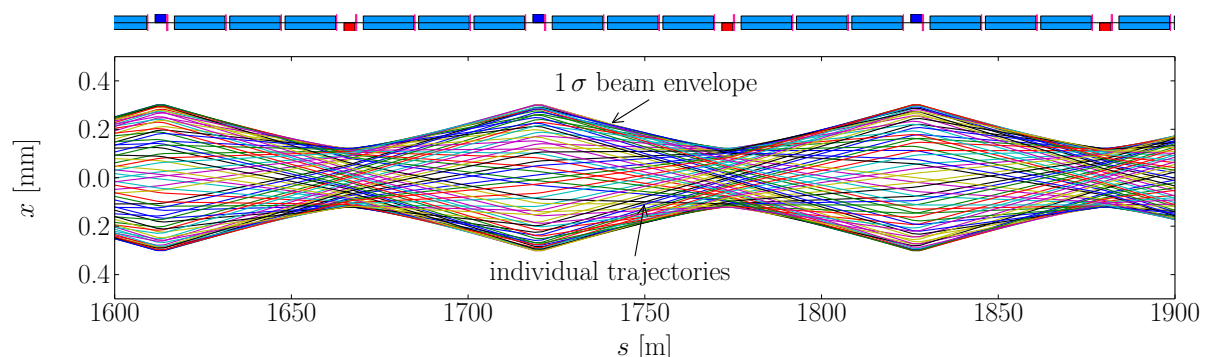


Figure 2.5: Individual particle trajectories in a periodic quadrupole lattice.

referred to as the emittance, which is directly related to the r.m.s. beam size $\sigma_x(s)$:

$$\sigma_x(s) = \sqrt{\epsilon_x \beta_x} \quad \text{with} \quad \epsilon_x = \langle \tilde{\epsilon}_x \rangle_{\text{rms}}. \quad (2.39)$$

The quantity x_{\max} defines an r.m.s. beam envelope containing the individual particle tracks. In Fig. 2.5, the betatron motion of particles with different initial conditions within ϵ_x is shown in a periodic lattice of quadrupoles and bending dipoles. It is clearly visible how the individual particle tracks are confined by σ_x . The emittance is a measure for the beam quality and should be as small as possible. If the particle beam is accelerated, only the longitudinal momentum is increased. One can therefore show that the ratio of transverse momentum to longitudinal momentum decreases $\frac{1}{\beta\gamma}$, which is referred to as adiabatic damping [Wie99]. Consequently, the normalized emittance is defined as

$$\epsilon_N = \epsilon \beta \gamma, \quad (2.40)$$

and remains constant for all particle energies, assuming that, besides the acceleration, only conservative forces act on the beam. The emittance is measured in $\mu\text{m rad}$.

Solution of the inhomogeneous Equation of Motion

The solution of the inhomogeneous equation of motion Eq. (2.21) is given as

$$x(s) = x_h(s) + x_i(s), \quad (2.41)$$

where $x_h(s)$ is the solution of the homogeneous equation shown in Eq. (2.22) and x_i is one particular solution of the inhomogeneous equation, for example

$$x_i(s) = \bar{D}_x(s) \delta. \quad (2.42)$$

The dispersion function $\bar{D}_x(s)$ is a periodic function in s with period length C , depending on the magnetic elements in the entire ring. It is defined as

$$\bar{D}_x(s) = -\frac{\beta_x(s)}{2 \sin(\pi Q_x)} \int_{s_0}^{s_0+C} h_x(\tilde{s}) \sqrt{\beta(\tilde{s})} \cos \left[2\pi \left(\psi(\tilde{s}) - \psi(s_0) - \frac{Q_x}{s} \right) \right] d\tilde{s}. \quad (2.43)$$

In order to be coherent with the definition in the simulation tools used, in the following the dispersion function will be expressed in terms of $D_x(s)$, defined as

$$D_x(s) = -\bar{D}_x(s). \quad (2.44)$$

As shown in Eq. (2.41), the dispersion function relates the momentum offset of the particle to an additional transverse amplitude. The quantity $D_x(s)\delta$ gives the closed orbit around which all off-momentum particles perform betatron oscillations.

Note that this mathematical description represents a linear approximation and higher order dispersive effects are not taken into account. For particles with large momentum offsets, a more accurate description is given by a fully symplectic transformation which can be derived from the accelerator Hamiltonian (see Chap. 7.2.1).

2.3 Longitudinal Particle Dynamics

The beams in the LHC are accelerated and longitudinally confined by means of radiofrequency cavities (RF cavities) [Wie99]. They are operated with RF waves and provide a longitudinal electric field $V(t)$ of a defined angular frequency ω

$$V(t) = V_0 \sin(\omega t), \quad (2.45)$$

where V_0 is the peak amplitude of the electric field. The temporal periodicity of the accelerating field implies that only particles within a certain range of arrival times are within the acceptance of the cavity and others receive inappropriate kicks leading to strong momentum deviations and subsequent particle loss in magnets due to dispersion. Therefore, the longitudinal slots defined by the acceptance of the RF cavities are quantized. Every possible slot where particles can perform stable oscillations is called a bucket. In principle, every bucket can be filled with a bunch of multiple particles, with some limitations given by other beam instruments, such as the extraction kicker magnet. The distance between subsequent buckets defines the minimum bunch spacing that can be achieved.

This chapter gives an overview of the longitudinal particle dynamics associated to this effect and aims to quantify the longitudinal acceptance imposed by the RF cavities.

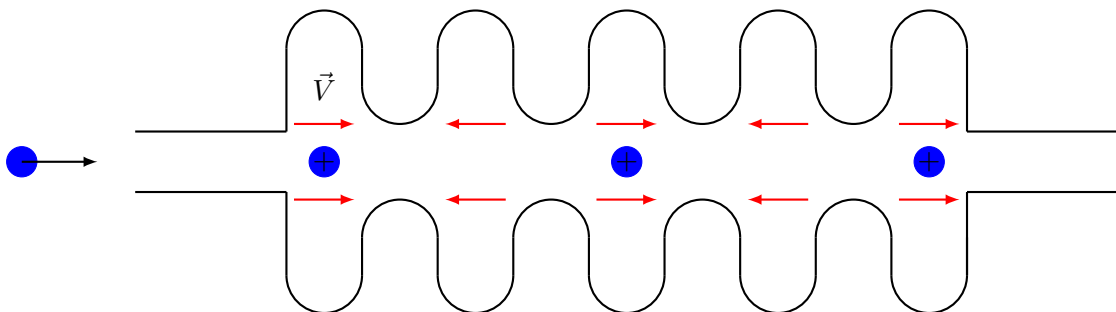


Figure 2.6: Schematic illustration of an accelerating cavity.

Using the revolution time T_S of the synchronous particle, the frequency of the RF cavity can be expressed as

$$\omega = h \frac{2\pi}{T_S}, \quad (2.46)$$

where ω is chosen such that h is an integer, the harmonic number. The latter condition assures that the synchronous particle is in phase with the RF voltage, such that the energetic kick it receives remains constant. A real particle is not in phase with the RF cavity, but arrives with a certain phase offset

3. The Large Hadron Collider

The Large Hadron Collider (LHC) is the world's largest particle accelerator, designed to store and accelerate proton and $^{208}\text{Pb}^{82+}$ beams at unprecedented energies of $7 Z \text{ TeV}$. The LHC is a synchrotron of 26.7 km length, installed in the underground tunnel of the former Large Electron Positron Collider (LEP) at the CERN¹ research center in proximity to Geneva, Switzerland. With the Relativistic Heavy-Ion Collider (RHIC) at the Brookhaven National Laboratory in Long Island (USA), it is one of the two heavy-ion colliders ever built and operated[FJ14]. In the first operational period (LHC run 1), the LHC reached energies up to $4 Z \text{ TeV}$ and collected an integrated luminosity of 29.2 fb^{-1} [Lam13] with proton beams and xx.x fb^{-1} with $^{208}\text{Pb}^{82+}$ beams. With the collected data, the discovery of the long sought Higgs Boson could be announced in July 2012 [Col12a, Col12b]. After a phase of machine and detector upgrades from 2013 to 2015, the LHC re-started and accelerated proton beams to the unprecedented energy of 6.5 TeV and $^{208}\text{Pb}^{82+}$ beams to $6.37 Z \text{ TeV}$.

In this chapter the LHC is presented with the sub-systems relevant for the development of the heavy-ion collimation simulations presented later-on. Particular emphasis is given to the LHC collimation system and the physics processes relevant for heavy-ion collimation.

3.1 The CERN Accelerator Complex

The LHC is a high energy synchrotron operated at the end of a complex chain of injectors which pre-accelerate and prepare the beam for its requirements. The ensemble of accelerators which is presently in operation at CERN, referred to as the CERN accelerator complex, is schematically illustrated in Fig. 3.1.

The LHC injector chain originates from two different ion sources, respectively delivering proton or heavy-ion beams. The generation of proton beam starts at a hydrogen ion source feeding the linear accelerator LINAC2, in which the proton beam is accelerated to a momentum of 50 MeV^2

¹Centre Européen pour la Recherche Nucléaire

²For clarity, in this chapter the momentum is given in natural units. All given momenta shall correspond to the correct unit of eV/c . Furthermore, the energies for the non fully stripped ions are given in terms of

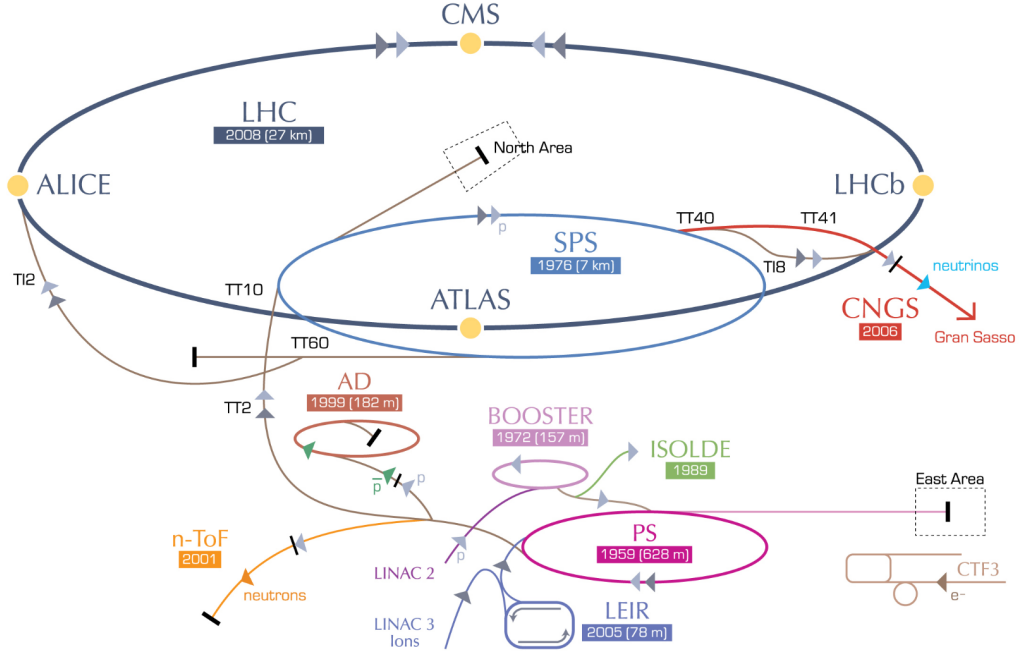


Figure 3.1: The CERN Accelerator Complex [Lef08].

and injected in to the Proton Synchrotron Booster. This synchrotron accelerates the beam to 1.4 GeV, the injection energy of the Proton Synchrotron (PS) which provides acceleration up to 25 GeV. After the subsequent injection into the Super Proton Synchrotron (SPS), the beams are brought to 450 GeV, the injection energy of the LHC [B^{+04b}].

Heavy-ion beams originate from the ion source which is connected upstream of the linear accelerator LINAC3. The ions are generated from a block of isotopically pure Pb²⁰⁸ by means of an Electron Cyclotron Resonance Source [B^{+04b}]. The source delivers ions at a momentum of 2.5 keV/A, which are sent to a spectrometer in order to extract the desired Pb⁺²⁷ charge state. After the filtering, a multi-stage RF system accelerates the selected ion species to a momentum of 4.2 MeV/A. The following 300 nm thick stripper foil removes more electrons, such that an ion beam of Pb⁺⁵³ is extracted from LINAC3 and transferred to the circular accelerator LEIR (Low Energy Ion Ring). In the latter, the ion beams are cooled, e.g. the transverse emittance is reduced by an adiabatic process using electron scattering. In parallel, the beam is accelerated to a momentum of 72 keV/A at which it is extracted and transferred into the PS. In this machine, the ions bunches are re-shaped and accelerated to a momentum of 5.9 GeV/A and sent to the SPS. Another stripper foil in the transfer line between PS and SPS removes the remaining

momentum per nucleon, while for the fully stripped ions, the general convention of using the momentum per charge is followed.

electrons, such that the ion arriving at the SPS is $^{208}\text{Pb}^{82+}$. The SPS provides the acceleration to the energy of $450 Z \text{ GeV}$ at which the beams are injected into the LHC [B^{+04b}].

3.2 LHC Layout

3.2.1 Global Layout

Fig. 3.2 shows the LHC layout with its eight straight insertion regions (IR), four of which host the main experiments (IR1, IR2, IR5 and IR8). The remaining four IRs provide operational functionalities, in particular betatron and momentum cleaning in IR3 and IR7 (see Chap. 3.6), acceleration in IR4 and the beam dump in IR6. The straight sections are separated by eight arc regions, in which the particle beams are transported from IR to IR by means of a periodic array of 1232 superconducting dipole magnets and 392 superconducting quadrupole magnets.

3.2.2 Insertion Region Layout and Optics

Each element of the LHC is associated with a cell number, indicating the number of quadrupoles between the closest IP and the respective location. For example the name MQY.4L5.B1 denotes a quadrupole of the MQY type (see [B^{+04b}]) in cell 4 left of IP5 for Beam 1. The schematic layout of the experimental insertion regions is shown together with the β functions in Fig. 3.3. Downstream of the main arcs (1) in which the beams are transported between the IRs, the dispersion suppressor (DS) region (2) serves the purpose of reducing the periodic dispersion function. This is reached by means of a missing dipole structure, in which one of three dipoles is omitted, compared to the nominal dipole structure in the arcs [B^{+04b}]. In between the surrounding DS regions, the IR is free of the main dipoles and therefore straight. After the DS, the matching section (3) adjusts the β functions to the requirements of the following sections. The separation/recombination dipoles (4) and (5) guide the beams from the separated beam pipes into a common beam pipe. The superconducting triplet magnets (6) provide the final focusing for the experiment at the interaction point (7) (IP) where the beams are brought into collision.

The experiments ATLAS and CMS demand for the highest possible luminosity in order to gain enough statistics for the study of rare processes (see Chap. 3.3). As discussed later, the luminosity is inversely proportional to the β value at the IP (denoted as β^*), thus the optical lattice is optimized to minimize the β^* value. Following Liouville's theorem, small β functions imply a large divergence (large α function) at the IP and, due to the absence of magnets between IP and triplet, the β functions (and associated with it the beam size) at the superconducting triplets increase with smaller β^* . The normalized dimensions of the triplet aperture therefore

impose a lower limit on the achievable β^* . This includes effects of adiabatic damping, such that the transition to the smallest β^* settings (referred to as squeeze) is performed either at top energy or at the end of the energy ramp (see Chap. 3.4). At injection energy, the optics in IR1 and IR5 are set to $\beta^* = 11\text{ m}$ while IP2 and IP8 are set to $\beta^* = 10\text{ m}$. A summary of the β^* values achieved at top energy during the past LHC runs is given in Table 3.1.

In the central part of the experimental insertions both beams are moving in a common vacuum pipe to allow for bringing the beams into collision. In order to avoid unwanted collisions of the counter-rotating beams, a separation bump is applied at every time collisions are not supposed to occur. Furthermore, even when the beams are brought into collision, a crossing bump avoids secondary collisions at parasitic bunch encounters. The crossing and separation bumps are, except in IR8, orthogonal to each other. Both bumps are shown for the example of IR5 in

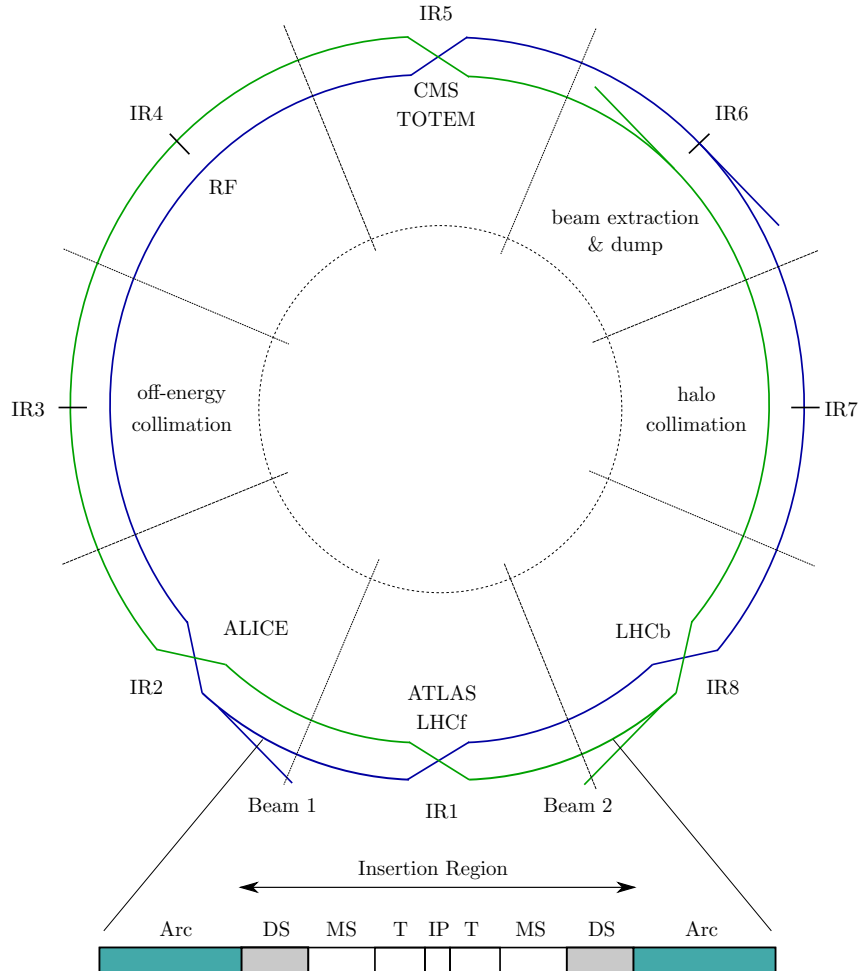


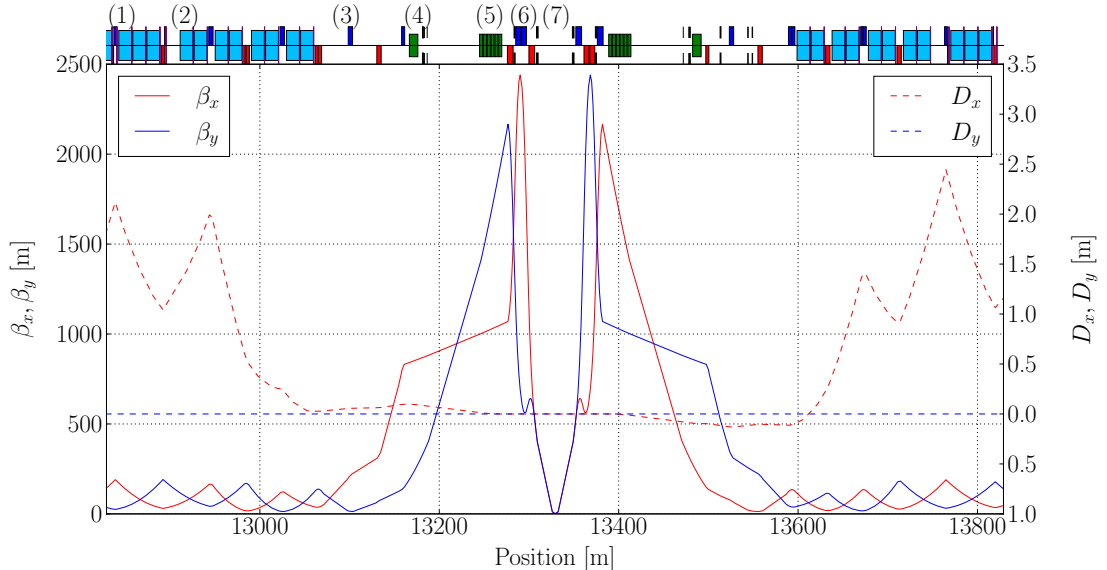
Figure 3.2: The layout of the LHC. Based upon [BBM12, B⁺04b].

Table 3.1: Minimum β^* values in LHC operation compared to the design values.

Configuration	Species	β^* IP1/IP5 [m]	β^* IP2 [m]	β^* IP8 [m]
Design	p	0.55	10.0	10.0
2011	p	1.0	10.0	3.0
2012	p	0.6	10.0	3.0
2015	p	0.8	10.0	3.0
2016	p	0.4	10.0	3.0
Design	Pb	0.5	0.5	10.0
2011	Pb	1.0	1.0	3.0
2013	p -Pb	0.8	0.8	2.0
2015	Pb	0.8	0.8	3.0

Fig. 3.4.

The functional IRs are not equipped with triplet magnets and the optics is adjusted for the purpose of the installed hardware. The layout, functionality and optics of the collimation insertion regions are shown in Chap. 3.6.

Figure 3.3: Optical functions at the experimental insertion IR5 with $\beta^* = 1$ m for a flat machine (no separation or crossing bump).

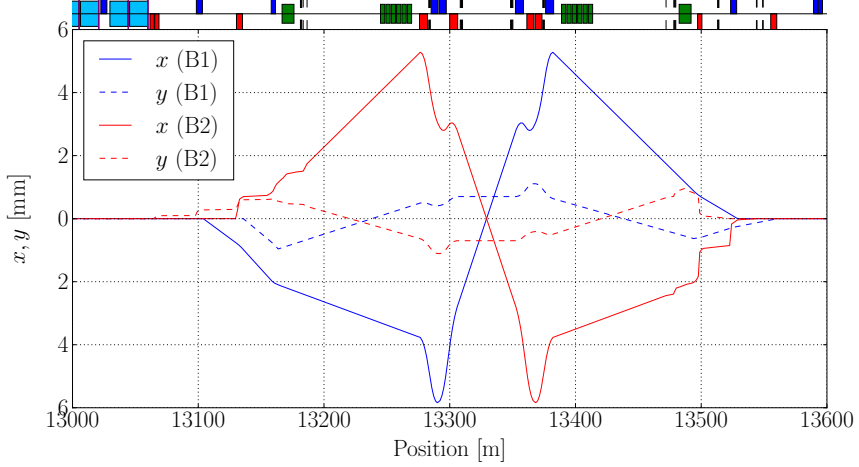


Figure 3.4: Separation and crossing bumps in IR5 during the 2011 heavy-ion run with $\beta^* = 1$ m.

3.2.3 LHC Cycle

The LHC cycle is a defined operational protocol which ensures safe operation and avoids uncertainties of the magnetic fields which could possibly arise from hysteresis. The LHC cycle is shown for an ideal proton physics fill in Fig. 3.5.

In the *injection* mode (1) at a beam energy of $450 Z$ GeV, the machine is ready to receive particle bunches from the injectors. The beams are not squeezed in this configuration, to obey the tight aperture restrictions and the optics in the injection insertions IR2 and IR8 are adjusted to optimize the phase advance between the injection septum the injection protection collimators.

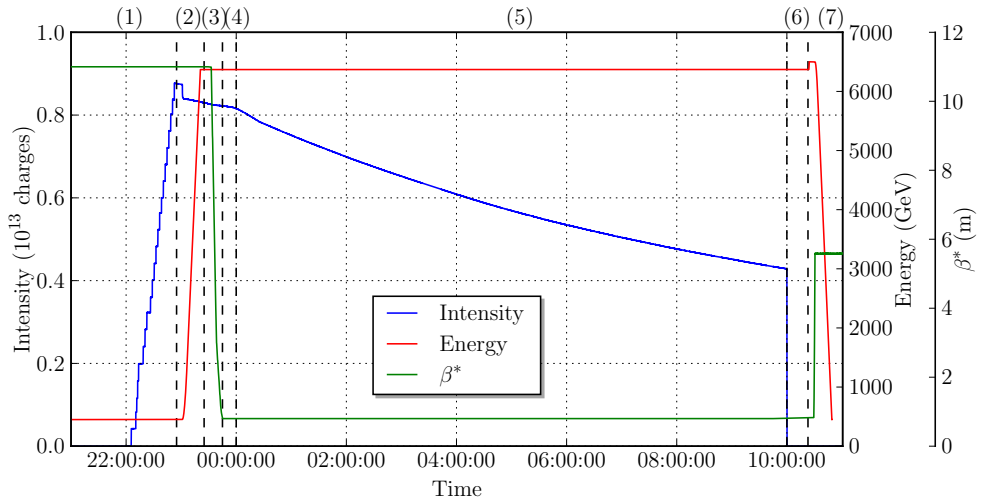


Figure 3.5: Beam energy, intensity and β^* during the LHC cycle.

Once the LHC is filled with beam, the mode is changed to *prepare ramp* (2) in which the injection protection collimators are retracted to allow for the following *ramp* (3), the acceleration to top energy. After the ramp, the *squeeze* (4) is a stepwise optical sequence in which the β^* value in the high luminosity IRs is smoothly reduced to the final value for collision. Finally, the beam mode changes to *adjust* (5), in which the separation bump is collapsed and small additional bumps are introduced to correct for deviations in the closed orbit and maximize the luminosity in the experiments. Once the collisions in the experimental IRs are established, the beam mode is referred to as *stable beams* (6). The stable beam mode is maintained for several hours until the luminosity has decreased. After several hours of stable beams, the beams are dumped (7). The magnets currents are then reduced (ramp down, (7)) to a level below the injection level to eliminate hysteresis effects before the following injection mode. Note that for heavy-ion operation in 2015, the cycle was adopted from the previous proton run in which the protons had larger rigidities. The ramp down therefore included an increase of the magnet currents from the operational setting at $6.37 Z$ TeV to the proton setting at 6.5 TeV.

In 2015, the formerly distinct steps of ramp and squeeze have been merged to reduce the time to set up the stable beams configuration and thus increase the integrated luminosity. This combined ramp and squeeze synchronously accelerates the beams to 6.5 TeV and reduces the β functions at IP1 and IP5 to $\beta^* = 3$ m.

3.3 Luminosity

An important measure for the performance of a collider is the luminosity. The instantaneous luminosity $\mathcal{L}(t)$ is a time dependent proportionality between the cross section σ_p of a physical process and the expected event rate $\frac{dN_p}{dt}$ in a given machine configuration [Wie99]:

$$\frac{dN_p(t)}{dt} = \mathcal{L} \sigma_p. \quad (3.1)$$

The luminosity is proportional to the number of bunches n_b , the square of the number of particles per bunch N_p , the revolution frequency in the machine f , the relativistic γ (to account for the adiabatic damping) and inversely proportional to the β^* value and the normalized emittance:

$$\mathcal{L} = \frac{n_b N_p^2 f \gamma}{4\pi\epsilon_N \beta^*} F. \quad (3.2)$$

The additional factor F takes into account for the luminosity reduction due to the fact that the colliding bunches are not fully overlapping when a crossing angle θ_C is applied. The correction factor depends on the longitudinal r.m.s. beam size σ_l , the transverse beam size at the IP

$(\sigma_x = \sigma_y = \sigma^*)$ and the crossing angle as follows [Her03]:

$$F = \frac{1}{\sqrt{1 + \left(\frac{\sigma^*}{\sigma_l} \tan \frac{\theta}{2}\right)}} \frac{1}{\sqrt{1 + \left(\frac{\sigma_l}{\sigma^*} \tan \frac{\theta}{2}\right)}}. \quad (3.3)$$

Following Eq. (3.2), the luminosity is measured in the unit $\text{cm}^{-2} \text{s}^{-1}$. Note that this corresponds to $10^{24} \text{ b}^{-1} \text{s}^{-1}$. The latter expression in combination with the definition given in Eq. (3.1) elegantly illustrates the dependence of the number of expected events with a cross section σ (measured in barns) per time unit. Even more information on the performance of the accelerator can therefore be obtained if the instantaneous luminosity is integrated over the duty time T , referred to as the integrated luminosity:

$$\mathcal{L}^{\text{int}} = \int_0^T \mathcal{L} dt. \quad (3.4)$$

Obviously, it is of great interest to enlarge the integrated luminosity to the maximum possible extent, to allow for the study of rare events. This can be done either by increasing the instantaneous luminosity (if not restricted by the experiments) or by optimizing the duty cycle of the machine in order to extend the time the machine is operated in its collision mode (see Chap. 3.4).

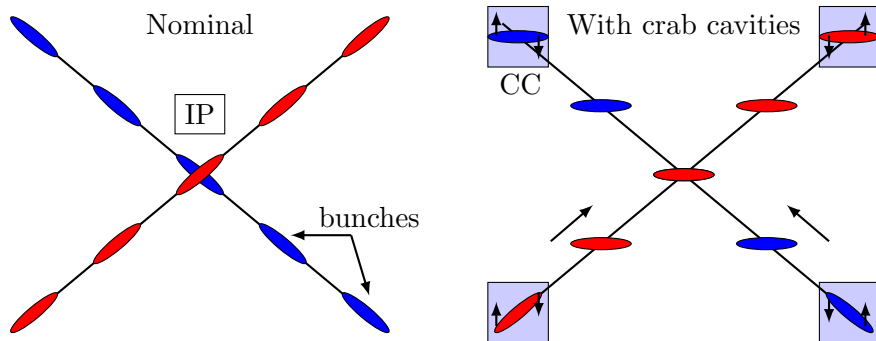


Figure 3.6: Schematic illustration of the functionality of crab cavities (CC). The bunches are tilted to have a larger overlap at the collision point and tilted back after the IP.

The instantaneous luminosity can be increased if smaller β^* values are applied, the emittance is reduced, the stored beam intensity is increased or if the luminosity reduction factor is enlarged. While the achievable emittance, number of bunches and bunch intensity depend strongly on the performance of the LHC injectors, the β^* value is imposed to an inferior limit due to aperture restrictions [BAR15]. The geometrical luminosity reduction factor F could be improved by reducing the crossing angle, which then interferes with the constraints imposed by the long-range

beam-beam interaction.

From the hardware side, the latter can possibly be improved by deciated RF cavities, the crab cavities [], which are to be installed left and right of the collision point in the future HL-LHC []. As shown in Fig. 3.6 they tilt the colliding bunches to increase their overlap at the collision point. This approach reduces the effective crossing angle and so improves the factor F .

TREF: https://cdsweb.cern.ch/record/1493034/files/RC_9_04.pdf

3.4 LHC Performance in Operation

The LHC design beam parameters for proton (p) and $^{208}\text{Pb}^{82+}$ ion operation are summarized in Table 3.2 and Table 3.3, respectively. In this section a brief overview of the beam parameters achieved in LHC operation so far is given.

3.4.1 Proton Beams

The LHC proton program started with the first data taking phase in 2010. In this first operational period the LHC was operated with small beam intensities at 3.5 TeV, half the design energy. With the operational experience gained, the stored beam intensity in 2011 could be increased by almost one order of magnitude and a signficiant amount of integrated luminosity was collected. The 2012 proton operation was fully dedicated to luminosity production and the integrated luminosity could be doubled with respect to the predecedent year. In this year the top energy was increased to 4 TeV [P⁺¹⁶].

Table 3.2: Comparison of the LHC design beam parameters for proton beams []. The data for 2016 is as of July 2016 and may be subject to change.

Year	Nominal	Achieved in the LHC				
		2010	2011	2012	2015	2016
E [TeV]	7	3.5	3.5	4.0	6.5	6.5
γ	7460.5	3730.3	3730.3	4263.2	6927.6	6927.6
n_b	2808	368	1380	1380	2244	2076
n_p [10^{11}]	1.15	1.0	1.3	1.5	1.1	1.1
ϵ_N [$\mu\text{m rad}$]	3.75	2.6	2.4	2.4	3.5	3.4
E_s [MJ]	362	23	112	143	277	266
$\mathcal{L}_{\text{peak}}$ [$10^{34} \text{ cm}^{-2} \text{ s}^{-1}$]	1.0	0.021	0.35	0.77	0.51	1.01
\mathcal{L}_{int} [fb^{-1}]		0.0048	5.5	22.8	4.2	8.1

At the beginning of 2013, LHC operation stopped for long shutdown 1 (LS1), a consolidation and upgrade phase with the main aim to consolidate the superconducting splices in order to reach proton momenta of 6.5 TeV to 7.0 TeV [BBF⁺¹³]. After a successful re-start in 2015, the LHC was operated at an unprecedented proton energy of 6.5 TeV. In the following year the LHC operated the first time at nominal luminosity due to the reduced β^* value and increased bunch intensity.

TREF: <https://hb2016.esss.se/prepress/papers/moam5p50.pdf>

TREF: <https://cds.cern.ch/record/1631030/files/CERN-ACC-Note-2013-0041%20v2.pdf?>

3.4.2 Heavy-Ion Beams

The first LHC run with heavy-ions took place in 2010, in which mostly operational experience at $3.5 Z$ TeV was collected and the produced luminosity was insignificant. The second heavy-ion run in late 2011 was carried out at $3.5 Z$ TeV and delivered half the design luminosity [J⁺¹¹]. In 2013 a mixed particle mode was established, in which protons were collided with $^{208}\text{Pb}^{82+}$ ions at $4 Z$ TeV [J⁺¹³]. This was the first time such asymmetric collisions were achieved in a collider. The 2015 operational period with heavy ions started with a reference proton run at 2.51 TeV per beam in order to obtain the same center of mass energy as in the p-Pb run of 2013. For the same reason, the ensuing Pb-Pb operation was carried out at an energy of $6.37 Z$ TeV, instead of the $6.5 Z$ TeV which would have been possible after the preceding proton operation at

Table 3.3: Comparison of the LHC design beam parameters for heavy-ion beams and proton beams in comparison to the parameters typically achieved in the LHC heavy-ion runs. [B^{+04b}, J⁺¹³, JSV13, J⁺¹¹, J^{+12b}]. The parameters given for p-Pb operation refer to the $^{208}\text{Pb}^{82+}$ beam.

		Nominal	Achieved in the LHC			
Year	Species	Pb-Pb	2010	2011	2013	2015
E	[TeV]	$7 Z$	$3.5 Z$	$3.5 Z$	$4.0 Z$	$6.37 Z$
γ		2963.5	1481.8	1481.8	1693.4	2696.8
n_b		592	137	358	338	518
n_p	[10^8]	0.7	1.12	1.20 ± 0.25	1.40 ± 0.27	2.2 ± 0.3
ϵ_N	[$\mu\text{m rad}$]	1.5	2.0	1.7 ± 0.2	-	1.50 ± 0.15
E_s	[MJ]	3.81	0.71	1.98 ± 0.42	2.18 ± 0.42	9.54 ± 1.30
$\mathcal{L}_{\text{peak}}$	[$10^{27} \text{ cm}^{-2} \text{ s}^{-1}$]	1 (Pb-Pb) 115(p-Pb)	0.03	0.5	110	3.0
\mathcal{L}_{int}	[fb^{-1}]					

equivalent rigidity [JSA⁺16]. This allows the experiments to compare data at the same center of mass energy for three different collision types: p-p, p-Pb and Pb-Pb. In the 2015 Pb-Pb running period, the LHC exceeded the design value of the stored $^{208}\text{Pb}^{82+}$ beam energy more than twice, due to the better-than-nominal performance of the LHC injectors, where the bunch intensity which has tripled with respect to its design value. This remarkable performance led to an excess of the design luminosity by a factor three [JSA⁺16].

3.5 The LHC Magnets

Many different types of magnets provide the guiding and confining forces required for the operation of the LHC. Aside from the magnets in the inner part of the experimental insertions, where the two beams are brought into collision, the LHC magnets are double-bore magnets in which both beams circulate in separated beam pipes as shown in Fig. 3.7. In this chapter, the superconducting LHC main dipoles and quadrupoles are briefly introduced and their superconducting properties are discussed to motivate the LHC collimation system. More extensive information can be found in [B⁺04b].

3.5.1 Main Dipoles

The 1232 superconducting LHC main dipoles are bending magnets of 14.3 m magnetic length capable of delivering a maximum magnetic field of 8.3 T. They are designed for a bending radius

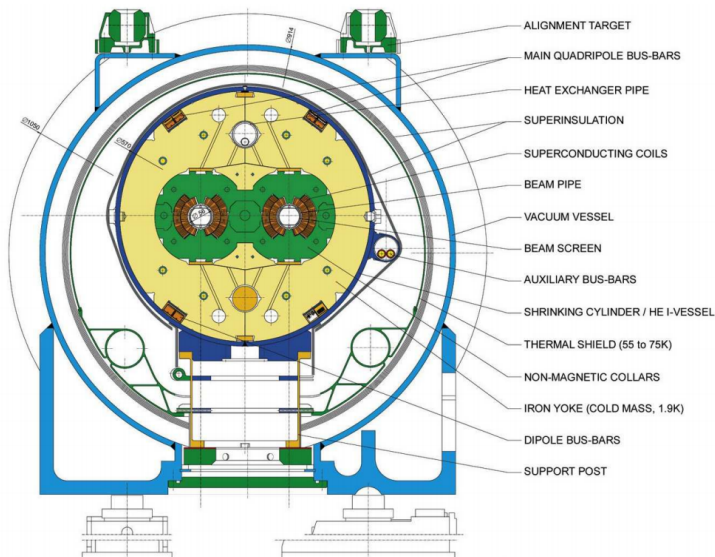


Figure 3.7: Cross section of the LHC double bore main dipole magnet [Duv01].

of $\rho = \frac{1}{h_x} = 2804$ m yielding a maximum particle energy of 7 Z TeV. To keep the NbTi coils in a superconducting state, they are cooled with liquid helium for an operation at a temperature of 1.9 K. More information on the superconducting LHC dipoles can be found in [B⁺04b].

3.5.2 Quadrupoles

The LHC is equipped with many different quadrupoles to provide the focusing required to confine the beams in the LHC arcs and prepare their transverse properties for the collision in the IPs. Depending on their purpose, they are normal or superconducting (and hence provide different field gradients), have different lengths and provide various bore diameters depending on the local aperture requirements [B⁺04b].

The beam transport from IR to IR in the LHC arc regions is provided by a structure of 392 alternating focusing and defocusing quadrupoles, which are referred to as the main quadrupoles (MQ). Their maximum magnetic field gradient is 223 T/m. The superconducting quadrupoles in the matching section of the experimental insertions are of five different types which are summarized in [B⁺04b]. The superconducting triplet magnets MQXA and MQXB provide the final focusing for the experiment with a maximum magnetic field gradient of 215 T/m.

3.5.3 Quench Limit

The superconducting LHC magnets can be operated in a certain dynamic range, in terms of temperature and external magnetic field. Being a type-II superconductor [Tin04], their superconducting state can be maintained if the temperature T , applied magnetic field B and the current density J in the superconducting cable fulfill certain conditions. The latter can be summarized by a critical surface in the (T, B, J) -space underneath of which the magnet is superconducting [Iwa09].

For a given set of two of the three independent parameters, a critical value for the third parameter can be found which then determines the quench limit. As shown in Fig. 3.8, the critical magnetic field for a LHC magnet operated at 1.9 K for a current density of $J = 1.5\text{--}2\text{ kA/mm}^2$ is given by $B_C = 9\text{ T}$, as compared to achievable $B_C = 5\text{ T}$ at $T = 4.2\text{ K}$ [BC07]. Accordingly, the critical temperature is larger if smaller magnetic fields are applied.

The superconducting LHC magnets are sensitive to radiation induced heating of their NbTi-coils. They risk to quench if the energy deposited in their coils by impacting beam particles (or their secondary showers) exceeds a defined threshold, referred to as the quench limit. Assuming that the magnetic field and the current density are fixed, the quench is caused by beam-induced heating of the magnet coil.

Typically, three different loss types are distinguished, depending on the time scale τ at which they occur [A⁺¹⁵]:

- Short duration: $50 \mu\text{s} > \tau$,
- Intermediate duration: $50 \mu\text{s} < \tau < 5 \text{ s}$,
- Steady state losses: $\tau > 5 \text{ s}$.

For every time scale of losses different physical mechanisms are relevant for the quench risk. They are explained in detail in [A⁺¹⁵]. For short and intermediate duration losses, the quench limit is measured in terms of the minimum quench energy density (MQED) in units of mJ/cm^3 . On the other hand, the energy deposited from steady state losses is effectively reduced by heat transfer of the superfluid helium, such that for this scenario the quench limit is quantified by the minimum quench power density (MQPD) in terms of mW/cm^3 [JLO⁺⁹⁶, A⁺¹⁵]. The dependence of these quantities on the loss duration is illustrated in Fig. 3.9.

So far, three beam-induced quenches have occurred in standard proton operation of the LHC, both caused by UFO events [PAA⁺¹⁶]. Furthermore, two beam-induced quenches have occurred with heavy-ion beams in dedicated quench tests with both collimation losses [HAB⁺¹⁶] and BFPP losses (see Chap. ?? and [SAFBC⁺¹⁵]). With the envisaged higher stored beam intensities and constant loss rates, the beam-induced quenches might become a serious issue in the operation of the LHC.

TREF: <https://cds.cern.ch/record/2127951/files/CERN-ACC-Note-2016-0024.pdf>

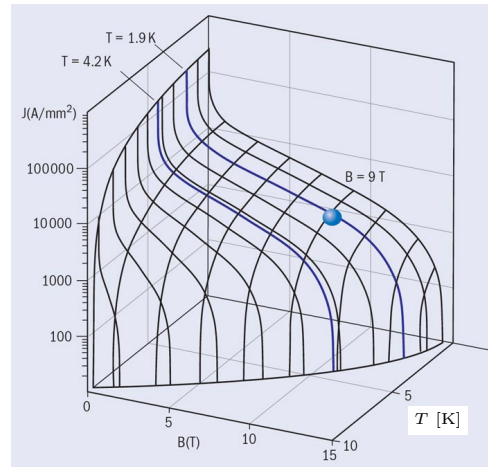


Figure 3.8: Critical surface of the superconducting NbTi coils used for the superconducting LHC magnets operated at 1.9 K [Sie13].

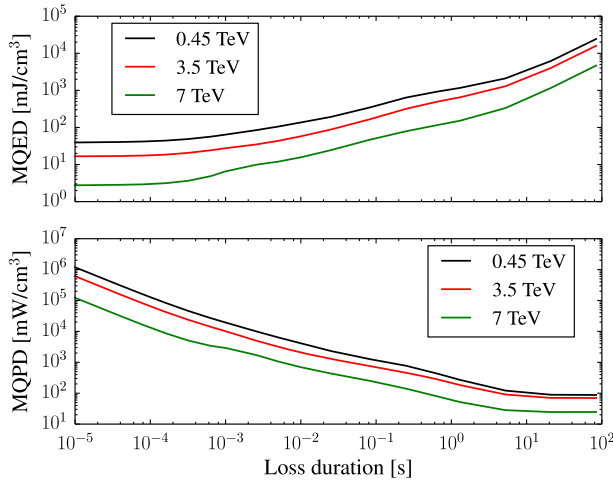


Figure 3.9: Simulated quench limits of LHC main dipoles for different loss durations (courtesy of [A⁺15]).

Table 3.4: Quench limit estimates for steady state losses at 7 TeV for the LHC main dipoles.

Author	Reference	MQPD [mW/cm ³]	Year
Schaumann <i>et al.</i>	[SAFBC ⁺ 15]	13	2016
Auchmann <i>et al.</i>	[A ⁺ 15]	27-49	2015
Granieri <i>et al.</i>	[GvW14]	47-49	2014
Bocian <i>et al.</i>	[BDS09]	12	2008
Jeanneret <i>et al.</i>	[JLO ⁺ 96]	5	1996

Reliable predictions of upper intensity limitations due to the risk of quench require accurate estimates of the quench limit. Theoretically, these are not easy to access, because the effective heat transfer to the superconducting coils depends on their geometry, the type of insulation, their heat capacities, the rate at which the superconducting helium can remove thermal energy from the coils and many more [SRS⁺13]. Accordingly, the estimated quench limits are associated to rather large uncertainties and have changed drastically over time when improved simulation models became available and by taking into account experimental data from quench tests. A non-complete summary of the temporal evolution of the estimated quench limits in the MB coils at 7 TeV is given in Table 3.4.

The threatening of the operational duty time by the risk of quench is one of the motivations for the LHC collimation system aiming to intercept particles which would hit - and potentially quench - the superconducting LHC magnets.

3.6 The LHC Collimation System

The LHC is designed to store particle beams of an unprecedented energy (see Fig. 3.10). At design momentum and intensity, the LHC will store protons of a combined energy of 362 MJ per beam, two orders of magnitude more than in previous accelerators [B⁺04b, A⁺06].

This energy is sufficient to melt 300 kg of copper. Uncontrolled deposition of the beam energy into the machine hardware can cause severe hardware damage. Even tiny fractions of the LHC beams can cause the superconducting magnets to quench. On the other hand, a variety of physical processes inevitably scatters particles to large transverse amplitudes out of the beam core, and they risk to be lost in the aperture of the superconducting magnets. To intercept these particles and remove them from the beam in a safe and controlled manner, the LHC is equipped with a multi-stage collimation system.

The present section describes the design and functionality of the LHC collimation system. Definitions to quantify the cleaning performance are introduced to allow for quantitative comparisons of different operational scenarios. Protons interact differently with the collimator materials than heavy-ions. The heavy-ion-matter interactions lead to fragmentation into other isotopes with rigidities not matched to the accelerator lattice. As it shall be shown in the next chapter, the cleaning performance for heavy-ion beams is therefore worse than for proton beams. It is thus important to describe the particle matter interaction which is done at the end of this section.

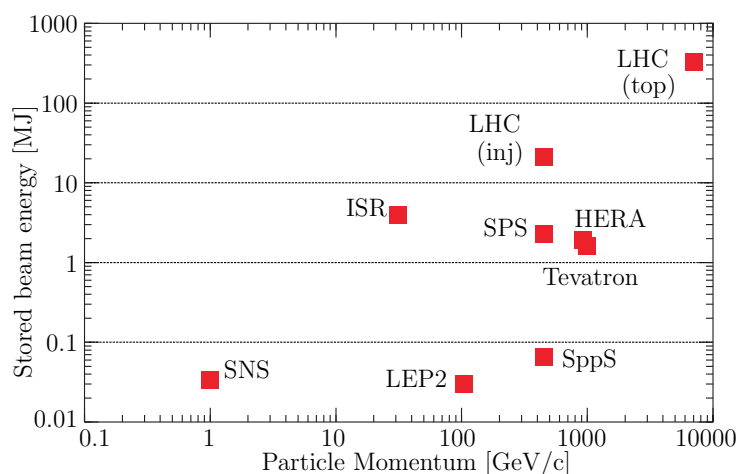


Figure 3.10: Design particle momentum and stored beam energy in different particle accelerators. Figure taken from [A⁺06].

3.6.1 Particle Losses in the LHC

Beam particles are subject to a range of physical processes which increase their betatron amplitude or change their momentum until they are outside of the acceptance of the beam pipes and are lost. Important processes driving particle losses in the LHC are [Lam05]:

- Intrabeam scattering [Piw74, MB83],
- Scattering of colliding particles at the interaction point,
- Orbit instabilities or optics changes with associated resonance crossing,
- Feedback noise,
- Scattering on residual gas molecules,
- Longitudinal drifts out of the RF bucket,
- Energy loss due to synchrotron radiation,
- Abnormal losses due to hardware failure. These include losses from injection failures [S⁺07] and asynchronous beam dump [].

The particles driven to large betatron or momentum amplitudes by the mentioned processes compose a transverse and longitudinal beam halo, which is continuously re-populated during operation. The rate at which particles of the main beam are lost during operation is quantified by the beam lifetime τ , representing the time at which the beam intensity³ $N(t)$ has dropped to $1/e$ of its initial value N_0 :

$$N(t) = N_0 \exp\left(-\frac{t}{\tau}\right). \quad (3.5)$$

The instantaneous loss rate $R_L = \frac{dN(t)}{dt}$ is related to the beam life time (which is in general time dependent) as follows:

$$\tau(t) = \frac{N(t)}{R_L(t)}. \quad (3.6)$$

3.6.2 Collimation Concept

The LHC requires very robust collimators to withstand the impact of the intense bunches with highly energetic particles. On the other hand, the required robustness implies a sufficiently low

³The total number of beam particles.

density of the material with the inevitable consequence of a reduced absorption rate of the beam particles. Therefore, the LHC collimation system relies upon a multi-stage system with different collimators to effectively absorb the beam halo.

The LHC collimators consist of two movable jaws which are adjusted around the beam which passes in between. An example for a collimator jaw and the assembly in a collimator tank is shown in Fig. 3.11. The different types of collimators are presented in Chap. 3.6.3.

The LHC collimation system is schematically illustrated at the example of the betatron cleaning insertion IR7 in Fig. 3.12. An instance of primary collimators (Target Collimator Primary, TCP) serves the purpose of intercepting the primary beam halo (particles of the main beam which are at large amplitudes). In IR7, a horizontal, a vertical and a skew TCP provide betatron cleaning in both transverse planes. The TCPs define the global aperture bottleneck and are the collimators closest to the main beam [B⁺04b]. In order to provide enough robustness to withstand a large power load of impacting protons, the active material of the TCPs is a dedicated carbon-fibre composite (CFC) [B⁺04b]. They can withstand a maximum power load $P_{max} = 500 \text{ kW}$ over 10 s, corresponding to a minimum beam life time of $\tau_{min} = 720 \text{ s}$ at the design energy of 7 TeV [AmBB⁺02].

The multi-stage approach relies upon the particle scattering to even larger amplitudes at their passage through the TCP. If a halo particle receives a sufficiently large transverse kick, it is intercepted by the secondary collimators (abb. Target Collimator Secondary, TCS).

The TCS collimators are retracted with respect to the TCP, thus they should be only exposed to the secondary beam halo with much less intensity than the primary halo. Downstream of

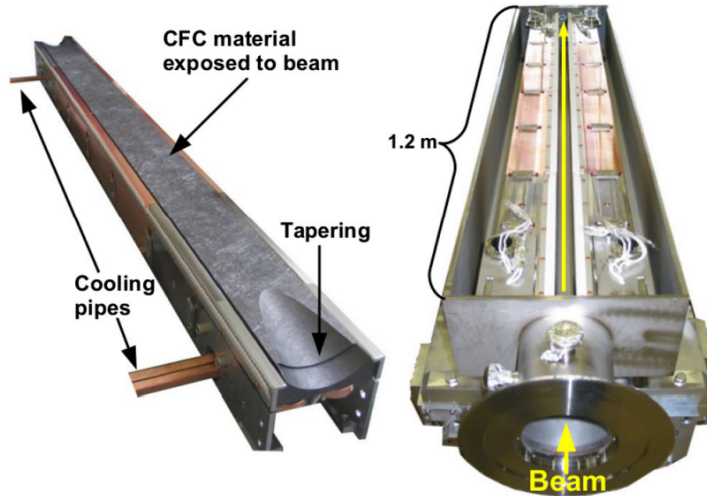


Figure 3.11: Left: Jaw of a secondary collimator. The collimators are water cooled through the copper pipes. Right: Two collimator jaws installed in a collimator tank. Courtesy of [B⁺14c].

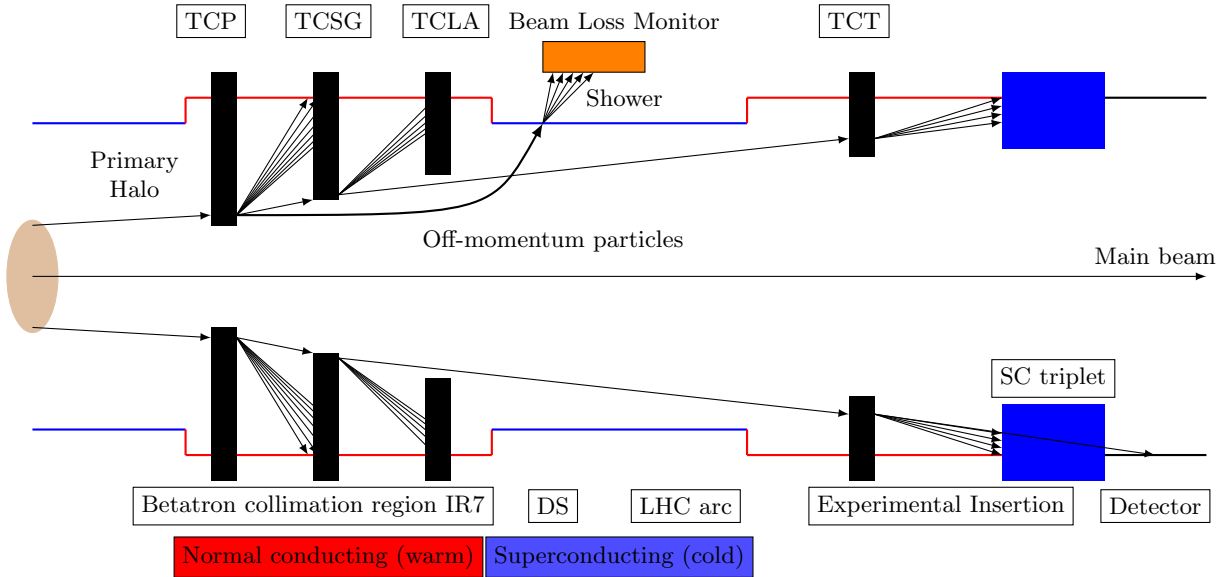


Figure 3.12: Schematic overview of the LHC multi stage collimation system. Based on [Red13].

the TCS collimators, shower absorbers (TCLA) are installed to protect the superconducting magnets downstream of the collimation IRs from from hadronic and electromagnetic showers generated at the TCSG collimators. They intercept also parts of the tertiary beam halo which can still leak out of the TCSG collimators and continue moving inside the machine.

During LHC physics operation, these particles are most likely absorbed in the triplet magnets where the betatronic functions are extreme [R⁺¹²]. In order to avoid beam losses in the triplet magnets, they are protected by the tertiary collimators (abb. Target Collimator Tertiary, TCT). They also provide protection of the experiments from undesired background [B⁺¹³]. The active material of the TCT collimators is a tungsten heavy alloy, INERMET 180 [], providing a high absorption cross section.

The optical functions in IR7 are optimized for small dispersion functions to intercept only particles at large betatron amplitudes. The momentum collimation region IR3 defines the momentum cut and intercepts particles with momentum offsets beyond a defined threshold. In this region, the optics is matched for a large horizontal dispersion function to intercept the off-momentum particles with the TCP. Contrary to the betatron cleaning, which is carried out for the horizontal, vertical and the skew plane with one dedicated primary collimator each, the principle of momentum cleaning requires a primary collimator only in the horizontal plane. The optical functions for the two LHC cleaning insertions are compared in Fig. 3.13.

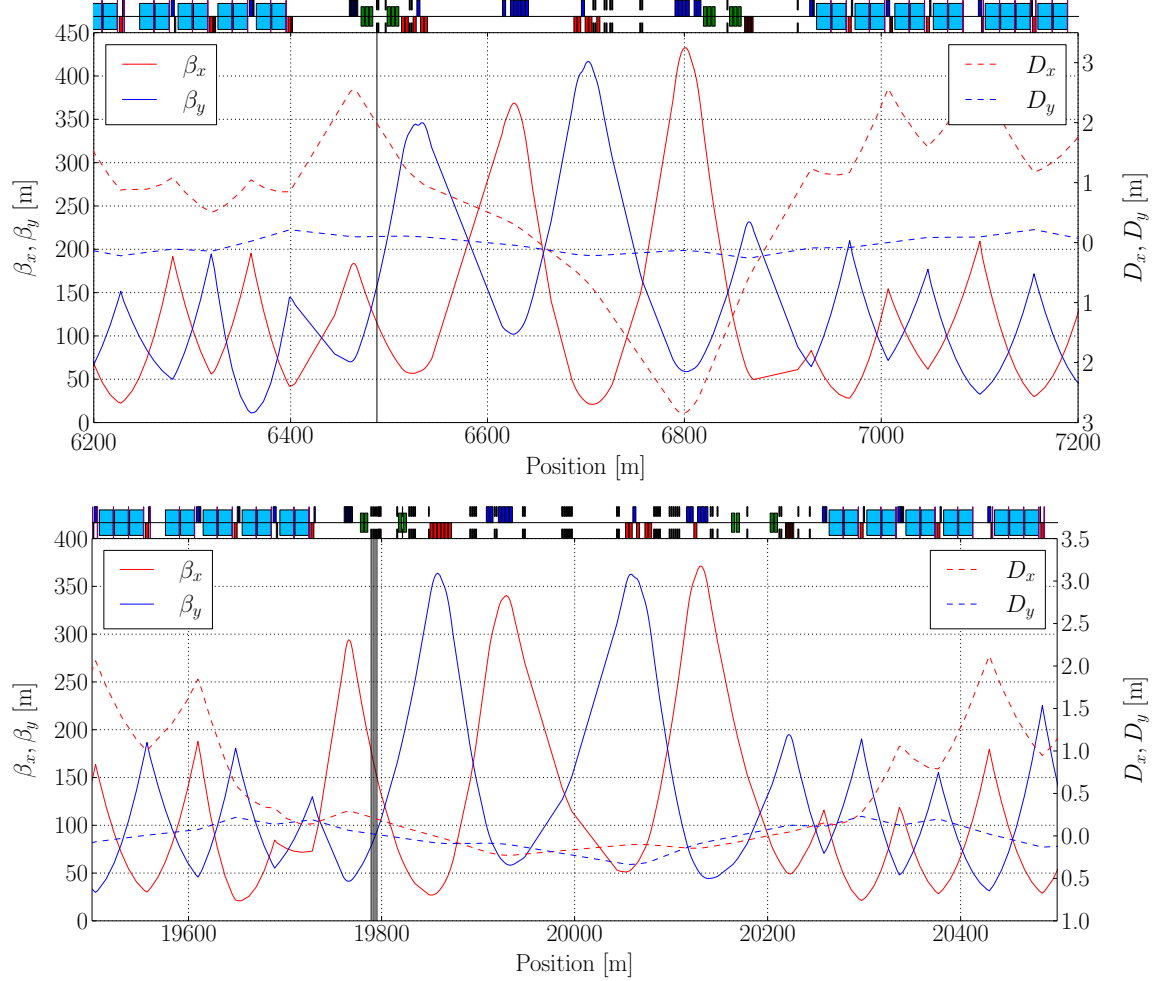


Figure 3.13: Optical functions in the two collimation insertions, IR3 (top) and IR7 (bottom). The vertical black lines represent the locations of the primary collimators

3.6.3 Collimator Types

Aside from the presented primary, secondary and tertiary collimators, additional collimators are installed at strategic locations throughout the ring to prevent from particle losses which are unvulnerable for the collimators installed in IR3 and IR7. A list of all collimator types in the present LHC is given in Table 3.5.

In the high luminosity insertions IR1 and IR5, dedicated physics debris collimators (Target collimator long, TCL) are installed to protect the machine from debris created at the collisions in the IP [Ass05]. Those particles may be scattered and/or off-momentum and would otherwise be likely to be lost at the DS magnets of the experimental insertion.

In case of a beam dump failure, multiple components of the LHC could be seriously damaged, in particular the dumping system, magnets downstream of IP6 or even the detector components in the experimental insertions. Therefore, IR6 is equipped with the single-jaw dump protection collimator TCDQ (Target Collimator Dump Quadruple) and the double-jaw TCSP (Target Collimator Secondary with Pick-up) collimator [Ass05]. The jaw of the TCDQ is composed of graphite and is the longest collimator used in the LHC having a length of 9 m.

The TDI (Target Dump Injection) collimators installed in the two injection insertions IR2 and IR8 protect the LHC hardware from beam loss which could occur due to injection failures. They are composed of graphite in a different composition than CFC. In order to protect a larger area in phase space, the TCLI (Target Collimator Long Injection Protection) collimators are installed downstream of the TDI [B^{+04b}].

3.6.4 Collimator Settings and Alignment

The positions of the movable collimator jaws can be individually adjusted. By convention, the collimator openings are given as the half gap between the jaws in units of the normalized beam size σ . The settings in σ are identical for the individual collimation stages, and can be adjusted to optimize the collimation efficiency. Yet the settings must obey the following constraints:

- The risk of damaging the machine hardware, including collimators, must be minimized.

Table 3.5: Overview of the types of LHC collimators presently installed in the machine (H,V,S: horizontal, vertical, skew) [B^{+04b}].

Type	Region	Name	Plane	Material
Primary	IR3	TCP	H	CFC
Secondary	IR3	TCSG	H	CFC
Shower Absorbers	IR3	TCLA	H,V	W
Primary	IR7	TCP	H,V,S	CFC
Secondary	IR7	TCSG	H,V,S	CFC
Shower Absorbers	IR7	TCLA	H,V	W
Tertiary	IR1/2/5/8	TCT	H,V	W
Physics Debris Absorbers	IR1/5	TCL	H	Cu
Dump Protection	IR6	TCDQ	H	C
Dump Protection	IR6	TCSP	H	CFC
Injection Protection	IR2/8	TDI	V	C
Injection Protection	IR2/8	TCLI/TCLD	V	CFC

- The settings must ensure that the collimation hierarchy⁴ is maintained even under realistic drifts of the orbit or optics. This implies a smallest achievable retraction between the TCP and TCS collimators. In operation, this requirement led to the application of larger retractions between TCS and TCP than initially foreseen in the design phase.
- The triplet aperture must always be protected by the tertiary collimators, which imposes a constraint on the smallest applicable TCT setting.
- The impedance induced by the collimators can change the tune of the individual particles, which must be taken into account for the collimator settings.
- All tungsten collimators and apertures must be sufficiently retracted from the TCDQ/TSP to avoid damaging during an asynchronous dump [AGV⁺⁰²].

The normalized beam size is determined using a normalized emittance of $\epsilon_N^p = 3.5 \mu\text{m rad}$ for proton beams. This value was chosen instead of the design emittance at top energy of $3.75 \mu\text{m rad}$ because the injectors could deliver a significantly better emittance than initially foreseen [?]. This convention provides furthermore simplicity because the same reference emittance applies for the whole cycle and establishes consistency and comparability between the runs.

The collimator setting in terms of the normalized beam size also takes into account the energy dependence of the geometric emittance due to adiabatic damping. With the collimator settings used in 2015, at top energy the TCP is set to values as small as 1.4 mm, compared to 5.6 mm at injection energy. During the ramp, the collimators are synchronously closed to take into account for the decreasing emittance. The geometrical collimator openings in mm for heavy-ion operation are so far adopted from the respective precedent proton runs. The normalized emittance of heavy-ion beams is significantly smaller than for proton beams, mainly due to the electron cooling in LEIR. In the LHC Design Report, a heavy-ion emittance of $\epsilon_N^{\text{Pb}} = 1.5 \mu\text{m rad}$ is foreseen, which yields the same geometrical emittance as for proton beams at the same rigidity. An exception is the 2015 heavy-ion run at $6.37 Z \text{ TeV}$, in which the geometrical emittance of the previous proton run at 6.5 TeV was adopted, corresponding to an equivalent heavy-ion emittance of $\epsilon_N = 1.41 \mu\text{m rad}$. The collimator settings applied during heavy-ion operation with stable beams are compared to the design values in Table 3.6. The settings used so far differ from the design settings and have been modified over the years. The margins between the TCP and TCSG collimators were chosen to be increased in order to mitigate measured hierarchy violations⁵ during proton operation [B^{+14c}]. The retraction of the TCT collimators is mainly

⁴The collimation hierarchy demands that the highest losses occur at the TCP, followed by the TCSGs etc.

⁵This applies for proton beams. Based on the measured loss signals in 2011, 2013 and 2015, the cleaning hierarchy with heavy-ion beams is, however, violated. With the smaller beam intensities, this is not considered critical for heavy ions.

motivated by the risk of material damage related to asynchronous beam dumps. Reasons for such hierarchy violations may be orbit instabilities or beta beating (wrong β functions) [A⁺¹¹]. Starting from the conservative settings applied at the beginning of the LHC operation, the settings were continuously optimized and re-set based on operational experience and on the results of dedicated experiments. This includes tightening of the collimator half gaps to allow for smaller β^* values [BAR15].

The reference orbit is not necessarily at the center of the aperture. One reason for this are the crossing and separation bumps in the experimental IRs. Furthermore, various imperfections cause a non-zero closed orbit around the machine. At the beginning of every run, all collimators are aligned around the beam center and then the collimators are driven back to the found positions at all subsequent physics fills. This procedure relies upon a good reproducability of the machine conditions. Two major methods are used for the collimator alignment, the first being the beam-based alignment [V⁺¹¹] in which the beam edge is defined by the TCP and it is ensured that the beam fills the TCP gap by artificial beam excitations (see Chap. 5.1). Then the collimator jaws of the individual collimators are moved individually towards the beam, until losses are measured with the beam loss monitors close to the collimator (see Chap. 3.6.7). The

Table 3.6: LHC collimator settings applied with squeezed beams at top energy in the LHC heavy ion runs, compared to the design settings. The settings refer to the beam size of proton beams at equivalent energy with a normalized proton beam emittance of $\epsilon_N = 3.5 \mu\text{m rad}$.

Type	Region	Collimator					Half gap (σ) Design ^b
		2010	2011	2013	2015 ^a		
TCP	IR7	5.7	5.7	4.3	5.5	6.0	
TCS	IR7	8.5	8.5	6.3	8.0	7.0	
TCLA	IR7	17.7	17.7	8.3	14.0	10.0	
TCP	IR3	12.0	12.0	12.0	15.0	15.0	
TCS	IR3	15.6	15.6	15.6	18.0	18.0	
TCLA	IR3	17.6	17.6	17.6	20.0	20.0	
TCT	IR1/IR2/IR5	15.0	11.8	9.0	13.7	8.3	
TCT	IR8	15.0	11.8	9.0	15.0	8.3	
Heavy-ion energy [Z TeV]		3.5	3.5	4.0	6.37	7.0	
Proton energy [Z TeV]		3.5	3.5	4.0	6.5	7.0	

^aSettings refer to a proton energy of 6.5 TeV.

^bFor design emittance $\epsilon_N = 3.75 \mu\text{m rad}$.

second method - in the present configuration only implemented for the TCTs - uses beam position monitors [V⁺15] which are integrated in the collimator jaws, measuring the beam position and aligning the collimators accordingly.

3.6.5 Collimation Cleaning Inefficiency

Particles which are not absorbed by the TCPs, but instead outscattered, should be captured by the TCSG collimators. This requires that they receive a sufficient transverse angular kick $\Delta x'$ at the TCP, mathematically expressed by the following inequality [B⁺04a]:

$$\Delta x' > \sqrt{\frac{(N_P^2 - N_S^2) \epsilon_N}{\gamma \beta_x}}. \quad (3.7)$$

Here, β_x is the horizontal betatron function at the TCP and N_P and N_S are the applied half gaps of the TCP and TCS respectively. The formula assumes an ideal betatron phase advance between TCP and TCS, such that the particle amplitude at the secondary collimator is maximized. Particles which do not obey the condition defined in Eq. (3.7), may leave the collimation system and continue moving in the machine. If they have been subject to significant change of rigidity, they are likely to be outside of the rigidity acceptance and absorbed in the aperture of the superconducting magnets where the dispersion increases.

The performance of the collimation system is measured by means of the *local cleaning inefficiency* $\eta(s)$ which quantifies the local loss rate in the machine from collimation debris. For proton losses, it is defined as the number of locally lost protons $N_{\text{loc}}(s)$ in the interval $[s, s + \Delta s]$, normalized by the number of protons lost at the collimators N_{tot} [B⁺14c]:

$$\eta_p(s) = \frac{N_{\text{loc}}(s)}{N_{\text{tot}} \Delta s}. \quad (3.8)$$

As it shall be shown in the next section, the collimation debris for heavy-ion beams is composed of many different isotopes with a large spread in momentum. Therefore, the cleaning inefficiency of heavy-ion beams is defined in a more generic way by integrating the energy E of the particles which are locally lost in the aperture and normalizing by the highest amount of energy lost at one location E_{max} :

$$\eta(s) = \frac{\int_s^{s+\Delta s} E(\tilde{s}) d\tilde{s}}{E_{\text{max}} \Delta s}. \quad (3.9)$$

The local cleaning inefficiency allows a simple scaling of the total loss rate to the amount locally lost energy. Note that the above definition of the cleaning inefficiency considers a particle loss

as the point of interception with the aperture of the beam pipe. In measurements of the losses in the LHC, this definition is not applicable, because secondary showers created by the particles interacting with the material at the location of impact are measured (see Chap. 3.6.7).

Following the definition of $\eta(s)$ and Eq. (3.6), the power $P_L(s, t)$ deposited at the location s with the local cleaning inefficiency $\eta(s)$ is given by

$$P_L(s, t) = \eta(s) \frac{N(t)}{\tau} = \eta(s) P_{TCP}, \quad (3.10)$$

where P_{TCP} is the power load on the primary collimator.

It is the interaction with the primary collimator which determines if a particle is scattered into the secondary collimators or if it receives a rigidity offset and is absorbed in the superconducting magnets. The particle-matter interaction is therefore an important keystone in the understanding of the cleaning inefficiency.

3.6.6 Particle-Matter Interaction and Collision Effects

Relativistic particles traversing matter are subject to different types of interactions. They can often be described on a microscopic scale by the interaction of the moving particle (projectile) with the atoms and/or nuclei (target) of the traversed material. An important quantity in the description of interactions is the minimum transverse distance of the projected projectile trajectory from the target position, the so-called impact parameter b , illustrated in Fig. 3.14. The type of interaction is often determined by the impact parameter with respect to the radii of the target R_T and the projectile R_P .

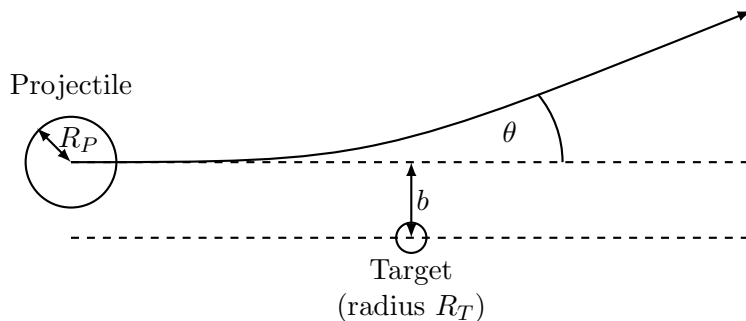


Figure 3.14: Schematic illustration of the impact parameter.

Table 3.7: Properties of the most important collimator materials, including materials foreseen for upgrades of the LHC collimation system. Data taken from [QBM⁺15].

Material	Z_m	A_m	ρ_m [g/cm ³]	X_0 [cm]
C (CFC)	6	12.01	1.67	25.57
Cu	29	63.55	8.96	1.435
W	74	183.85	19.30	0.35
Mo ₂ C	30	67.978	8.40	1.222

Multiple Coulomb Scattering

Coulomb scattering occurs when the projectile is deviated from its trajectory while interacting with the coulomb field of the atoms in the collimator material [J⁺12a].

Throughout the passage of the material, the particle can be repeatedly subject to small angular Coulomb scattering and so accumulate an angular deviation significantly larger than from the individual interactions. This process, referred to as Multiple Coulomb Scattering (MCS), leads to a wide distribution of scattering angles. It can be quantified by the RMS scattering angle θ_0 which is well-described the Molière formula [J⁺12a]

$$\theta_0 = \frac{13.6 \text{ MeV}}{\beta c P} Z \sqrt{\frac{d}{X_0}} \left[1 + 0.038 \ln \left(\frac{d}{X_0} \right) \right], \quad (3.11)$$

where d is the distance the particle traversed inside the material and X_0 is the radiation length that is a characteristic quantity for the target material.

The radiation length is accessible via tabulated data or by means of the approximated formula depending on the charge Z_m , nucleon number A_m and density ρ_m of the target material [J⁺12a]

$$X_0 = \frac{716.4 \text{ g cm}^{-2} A_m}{\rho_m Z_m (Z_m + 1) \ln(287/\sqrt{Z_m})}. \quad (3.12)$$

The radiation length for the most important collimator materials is given in Table 3.7.

Energy Loss from Ionization

Particles at the passage through matter can interact inelastically with the electrons of the atoms constituting the target material. At such encounters, a fraction of the projectile's kinetic energy is disposed into the energy required to dislodge an electron from an atom of the target material. Quantitatively, the mean energy loss per traversed length unit (or stopping power) in the material

is described by the Bethe-Bloch formula [J⁺12a]:

$$-\frac{1}{\rho} \left\langle \frac{dE}{dx} \right\rangle = \frac{4\pi}{\rho m_e c^2} \cdot \frac{nq^2}{\beta^2} \cdot \left(\frac{e}{4\pi\varepsilon_0} \right)^2 \cdot \left[\ln \left(\frac{2m_e c^2 \beta^2}{I \cdot (1 - \beta^2)} \right) - \beta^2 \right], \quad (3.13)$$

where I is the mean excitation energy (which is tabulated for different materials), m_e is the electron rest mass, q is the particle charge, ρ is the density of the traversed material and n is the electron density in the material. The stopping power is shown as a function of $\beta\gamma$ of the particle in Fig. 3.15. It increases quadratically with the particle charge. This means that the stopping power for $^{208}\text{Pb}^{82+}$ ions is larger by a factor of 6724 than for protons with the same speed. Energy loss from ionization is therefore significantly more important for $^{208}\text{Pb}^{82+}$ ions than for protons.

Electromagnetic Interactions

Electromagnetic Dissociation in Collimators

Electromagnetic dissociation (EMD) is a photonuclear reaction that occurs at ultraperipheral collisions of the involved nuclei ($b > R_1 + R_2$). The Lorentz contracted electric fields lead to the exchange of a large number of virtual photons which can induce the nuclear excitation of one or

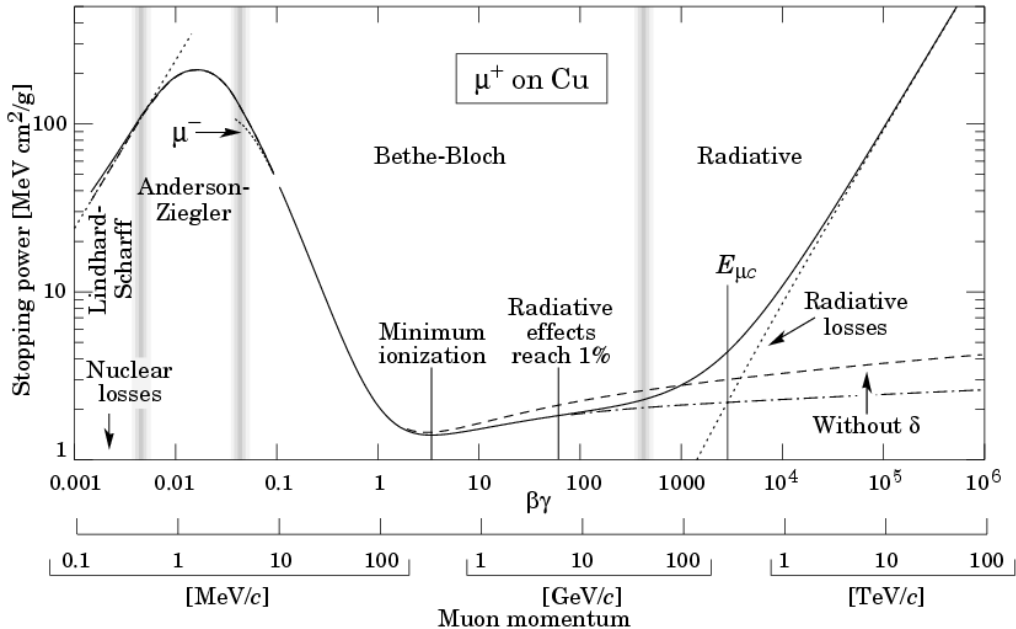
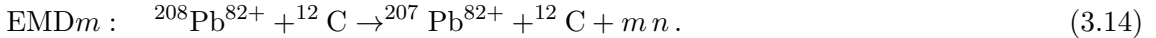


Figure 3.15: Stopping power as described by the Bethe-Bloch formula [J⁺12a]. Compared to Eq. (3.13), the mean energy loss per traversed length is normalized by the density of the material.

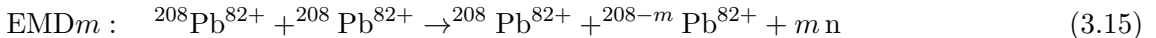
both of the involved nuclei [BFF⁺¹⁴]. The cross section of the EMD process scales logarithmically with the relativistic γ factor of the impacting nucleus [BFF⁺¹⁴]. The excited nuclei dissipate the energy under the emission of one or more nucleons, where the emission of neutrons has the largest cross section for heavy nuclei such as $^{208}\text{Pb}^{82+}$. The process of neutron emission of m -th order is summarized by the following reaction formula:



Also higher order EMD processes with the emission neutrons and protons are possible, but have a lower cross section. Overall, the EMD process is very important to consider in the picture of heavy-ion collimation, because the residual ions have rigidities very close to the main beam. As it is demonstrated in Chap. 8.2, they can travel through the magnetic lattice of the LHC over large distances and may cause distinct losses at given LHC elements. Photonuclear reactions with proton beams are suppressed by a factor of $1/Z^2$ with respect to heavy-ion beams [BFF⁺¹⁴].

Electromagnetic Dissociation in Interaction Points

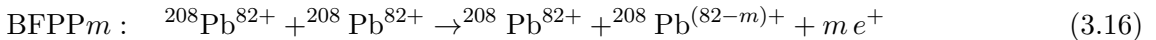
EMD can also occur from the interaction of colliding particles at the IP. The reaction chain for neutron emission of m -th order is the following:



Again, higher order processes are possible, but the emission of a single neutron has the largest cross section. The emission of one neutron and one proton is suppressed by two orders of magnitude compared to the single neutron emission [Psh16].

Bound-Free Pair Production

The photon exchanged in ultra-peripheral collisions $b > 2 \times R_P$ of two ions can create a virtual pair of leptons from which the negatively charged particle may be captured by one of the interacting nuclei. Of practical relevance in terms of cross-section are BFPP processes in which electrons are captured. The BFPP process of m -th order for LHC $^{208}\text{Pb}^{82+}$ ions is summarized as follows [Ast08]:



The cross-section for BFPP processes can be approximated by the formula:

$$\sigma_{\text{BFPP}} = Z_P^5 Z_T^2 a \log \left(\frac{\gamma_{\text{cm}}}{\gamma_0} \right), \quad (3.17)$$

where Z_P and Z_T are the charge numbers of the projectile and target, γ_{cm} is the relativistic Lorentz factor in the center of mass frame and a, γ_0 are tabulated values with a small dependence on Z_T [MHH⁺01]. This equation also shows that, compared to processes at the IP, the BFPP cross section for interactions at the collimators is significantly smaller because of the quadratic dependence on Z_T and the reduced γ_{cm} for the fixed target interaction.

Compared to the fully stripped nucleus, the $^{208}\text{Pb}^{(82-m)+}$ ion has a different mass to charge ratio and is therefore subject to dispersion. Already the secondary beam generated from first order BFPP (in $^{208}\text{Pb}^{82+}$ - $^{208}\text{Pb}^{82+}$ collisions the dominating process with a cross section of 281 b, see Table 3.8) is outside the momentum acceptance of the LHC arcs and hence lost at the DS at the end of the IR in which it is produced. The cross sections for the most important electromagnetic interactions of $^{208}\text{Pb}^{82+}$ ions colliding at the IP at 7 Z TeV are summarized together with the χ factor quantifying their mass to charge ratio in Table 3.8.

Table 3.8: Cross sections and relative mass to charge ratio of interaction products for electromagnetic and photonuclear interactions of colliding $^{208}\text{Pb}^{82+}$ beams at 7 Z TeV [Sch15].

	Unit	BFPP1	BFPP2	EMD1	EMD2	\sum EMD
σ	[b]	281	0.006	96	29	226
$\chi - 1$	$[10^{-3}]$	-12.2	-24.4	4.84	9.72	-
Source		[MHH ⁺ 01]	[ASS14]		[BBG ⁺ 09]	

With the presented cross section and considering the design luminosity, the secondary BFPP beam carries a power of 26 W. With its distinct rigidity change, the secondary BFPP beam impacts the DS magnets in a very localized manner. This leads to a locally high power density in the magnet coils that may cause a quench, as demonstrated in a dedicated BFPP quench test [SAFBC⁺15]. In 2015 dedicated orbit bumps were used in IR1 and IR5 to steer the secondary BFPP beam into an empty cryostat where the lost particles cannot cause a magnet quench. In the region around the ALICE experiment this solution is not applicable, such that for future operation in HL-LHC, the installation of additional collimators in the IR2 DS is envisaged [B⁺15].

Nuclear Interactions

Nuclear Interactions in Collimators

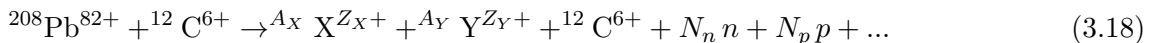
Nuclear encounters with impact parameters smaller or equal than the sum of the radii of the involved nuclei can lead to interactions over strong force. The gluon exchange implies large momentum transfers which may lead to the production of new particles or nuclear fragmentation subsequent to the nuclear excitation of one or both nuclei.

Table 3.9: Cross sections for EMD and nuclear interactions of $^{208}\text{Pb}^{82+}$ ions for different fixed target materials at the 2011 LHC energy of $3.5 Z \text{ TeV}$ and its design energy $7.0 Z \text{ TeV}$ [BFF⁺¹⁴].

Target	σ [b]		σ [b]	
	$3.5 Z \text{ TeV}$	$7.0 Z \text{ TeV}$	EMD	$Nuclear$
C	0.471	3.24	0.498	3.26
Cu	10.16	5.09	11.05	5.11
W	63.52	6.92	68.91	6.95

A very important nuclear process for protons interacting with the collimator material is single diffractive scattering. In this process, the proton interacts with a nucleus of the collimator material and is excited to a higher nuclear state. This excited state decays into a proton and other particles and the momentum of the outgoing proton is reduced with respect to the incident proton [S^{+14b}].

For heavy-ions, the associated nuclear excitation of either the target and/or the projectile and their subsequent disintegration leads to a spectrum of residual nuclei much wider than that of EMD processes [Bar09]. Typically residual ion fragments from nuclear interactions can cover the full isotope spectrum and therefore produce particles with rigidities far from the main beam. For the materials used in primary LHC collimators nuclear interactions occur with cross sections almost one order of magnitude above the one for EMD processes (see Table 3.9) making them an important component in the study of loss patterns of heavy-ion collimator debris. The mechanism of nuclear fragmentation of $^{208}\text{Pb}^{82+}$ ions in the TCP collimator material is summarized by the following reaction formula:



Here, A_X, A_Y are the nuclear mass numbers of the fragment X and Y , Z_X, Z_Y are their charge numbers and N_n, N_p are the number of produced neutrons and protons.

Processes of fragmentation, either from EMD or nuclear interactions, cause also deviations in angle and transfer of transverse and longitudinal momentum. The created fragments thus populate not only a wide spectrum in terms of mass and charge, but also of angular coordinate (which can be superior to angular scattering from MCS) and momentum, which leads to additional smearing of the distribution of magnetic rigidities [BFF⁺¹⁴].

Nuclear Interactions at the IP

Nuclear fragmentation processes at the IP are the main interest of the LHC experiments. At a momentum of $7 Z \text{ TeV}$, the total cross section for such hadronic interactions of two $^{208}\text{Pb}^{82+}$ ions is 8 b [Col95]. Debris from nuclear fragmentation of $^{208}\text{Pb}^{82+}$ ions at the IP is a negligible process compared to the secondary BFPP beam, because the cross section is significantly smaller and the broad spectrum of generated χ -values leads to large spread of loss locations.

For proton operation at high luminosity, physics debris from nuclear interactions can lead to significant losses rates at magnets close to the IP, which motivates the installation of the TCL collimators because the Q5 in IR1 or IR5 could quench otherwise.

Nuclear Evaporation and Statistical Fragmentation

The residual heavy ions generated at a cascade of interactions of either nature may still be in a nuclear charge state above the ground level. Depending on the mass of the fragment two physical processes of energy dissipation can be distinguished.

Heavy nuclei can decay into their ground state by either nuclear fission, the emission of nucleons or γ rays, a process referred to as nuclear evaporation [FSB⁺03]. Proton emission from nuclear evaporation is suppressed as compared to neutron emission because of the Coulomb barrier [FSB⁺03].

Light residual ions are subject to fragmentation which can be statistically described by the Fermi breakup model [CDS⁺12]. In this model, significant momentum can be transferred to the fragments originating from this process.

Summary and Conclusion

Interactions of heavy-ions with the collimator material can cause changes in transverse and longitudinal momentum, as well as changes in rigidity due to processes changing mass and charge of heavy-ions. A summary of the most important processes for the study of the heavy-ion collimation efficiency is given in Table 3.10. The mean free path λ for nuclear interactions and EMD describes the mean distance a particle traverses in the material before it interacts via the respective reaction channel.

The comparison to protons clearly shows that the nuclear interaction length λ_{nuclear} for $^{208}\text{Pb}^{82+}$ ions is smaller by more than one order of magnitude compared to protons. In addition, the EMD process generates off-rigidity ion fragments. The higher production rate of off-rigidity particles with heavy-ion beams compared to proton beams is the origin of the worse cleaning inefficiency. A dedicated simulation to understand the effect in more detail is presented in Chap. 6.1.

Table 3.10: Characteristic quantities for the most important physical processes of protons and lead ions traversing CFC at 7 Z TeV. Data taken from [B⁺04a] and scaled to the density of CFC.

Physics Process	Unit	Proton	²⁰⁸ Pb ⁸²⁺
$-\frac{dE}{E dx}$	[10^{-5} m^{-1}]	11	917
θ_{MCS}	[$\mu\text{rad}/\sqrt{m}$]	4.0	4.0
λ_{nuclear}	[cm]	47.9	3.1
λ_{EMD}	[cm]	-	23.9

3.6.7 Measurement of Losses in LHC Operation

The LHC is equipped with more than 4500 ionization chambers, the beam loss monitors (BLM) [H⁺05, H⁺08], installed at the outer side of superconducting magnets, collimators and other locations, in order to keep track of the particle losses throughout the ring. The ionization chambers are gas filled cylinders housing a structure of parallel electrodes with opposite voltages (see Fig. 3.16). Charged particles traversing the detector ionize the gas particles and the created ions and their electrons are captured by the electrodes, which is measured as a drop of the high voltage at which the BLMs are operated. The measured signal is proportional to the radiation dose.

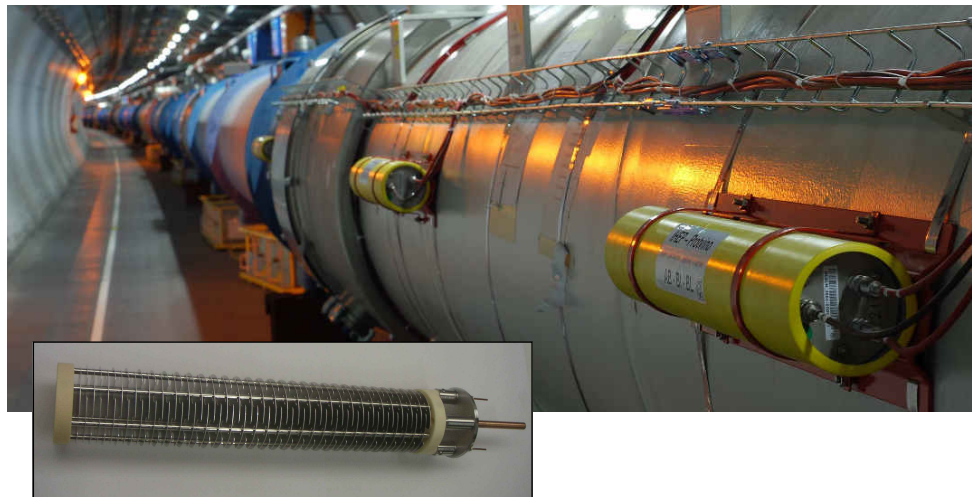


Figure 3.16: Top: Ionization chambers of the LHC BLM system, mounted at the LHC Magnets. Bottom: Inner structure of an ionization chamber. Figures taken from [BLM16].

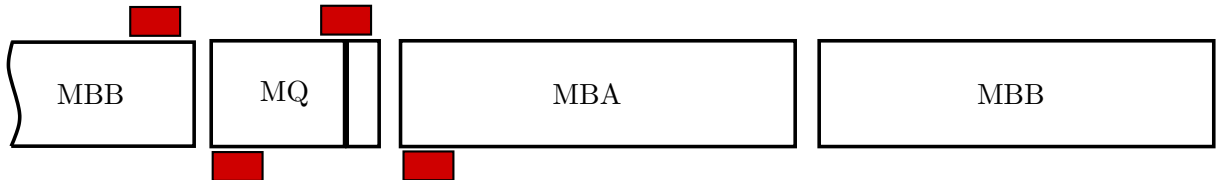


Figure 3.17: BLM positioning around a MQ magnet [Lec14].

The BLMs measure the secondary particle showers from the interaction of beam particles with the material of collimators or with the beam pipes and surrounding components. Given their small size, the positioning of the BLMs is essential to monitor losses at strategic locations at which high losses are expected. A schematic illustration of the BLM positioning around the superconducting magnets is shown in Fig. 3.17.

It is not straight-forward to deduce the number of locally lost particles and the energy deposition in the magnet coils from measured BLM signals. With the small azimuthal coverage, the different response function to upstream particle impacts at the beam pipe, the distinct longitudinal distribution of the BLMs and the different loss types throughout the ring, the BLM signals shall be interpreted in the global scale to identify critical loss locations in the machine, rather than deducing quantitative information about energy deposition. The latter requires dedicated simulations, including the shower propagation from the point of primary particle impact [BAB⁺⁰⁹, B^{+14c}, A⁺¹⁵].

Such shower propagation simulations can be combined with quench limit estimates to derive operational thresholds for the BLMs to reduce the risk of undesired quenches or even hardware damage. The BLM data is continuously monitored by the LHC interlock system which triggers a beam dump if these thresholds are exceeded [Gua05]. Both the quench limit and the intensity limit at which the physical integrity of the collimators is endangered by beam induced plastic deformations, depend on the time scale at which the losses occur [BBC⁺¹¹, RBB⁺¹⁴]. Therefore the signals of the ionization chambers are sampled over twelve different integration time scales reaching from $40\ \mu\text{s}$ to $83.89\ \text{s}$, denominated as the running sums RS01 to RS12. With increasing integration times, the BLM thresholds are set to larger values, accounting for the larger quench limit with increasing loss duration.

The longitudinal distribution of losses in the LHC ring is referred to as a loss map. The constant loss monitoring in operation (physics loss map) delivers a convolution of all losses presently occurring, whatever their origin might be. The qualification of the LHC collimation system is therefore carried out in dedicated measurements, presented in the next section.

4. Simulation Tools

Important contributions to the excellent performance of the LHC came from theoretical simulations. Many tools have been developed and used to predict various physics aspects of the machine. For collimation, particularly software for particle tracking and simulations of particle-matter interaction are important. The former requires also a detailed model for optics computation, as the configuration of the magnetic lattice is crucial for the particle motion in the machine. In order to have a complete picture of the collimation efficiency, information must be exchanged between the tracking tool and the particle-matter interaction, which can be realized in different manners. In this chapter, different software tools important for the development of the heavy-ion collimation simulation tools are presented.

4.1 MAD-X

MAD-X (Methodical Accelerator Design) [MAD] is the standard tool at CERN to simulate beam dynamics and compute beam optics in particle accelerators. The software is a complete migration of MAD-8 (written in FORTRAN77) to C++ and was introduced in 2002 for the design and simulation of the LHC optics [Sch06].

The software computes the global Twiss parameters by means of transfer matrices for the individual lattice elements. The structure of the machine and the strengths of the magnets are given by the user by means of dedicated input files. A matching function provides the functionality to adjust specific variables such that previously defined constraints are fulfilled. An aperture model of the machine can be processed and compared with the beam position and dimensions to evaluate the available normalized aperture throughout the machine. A dedicated function produces the required optics input for SixTrack (see next Chapter).

4.2 FLUKA

FLUKA (FLuktuierende KAskade) is a fully integrated Monte-Carlo package to simulate particle transport and the interaction of particles with matter [FSF⁺05, B⁺14b]. The package

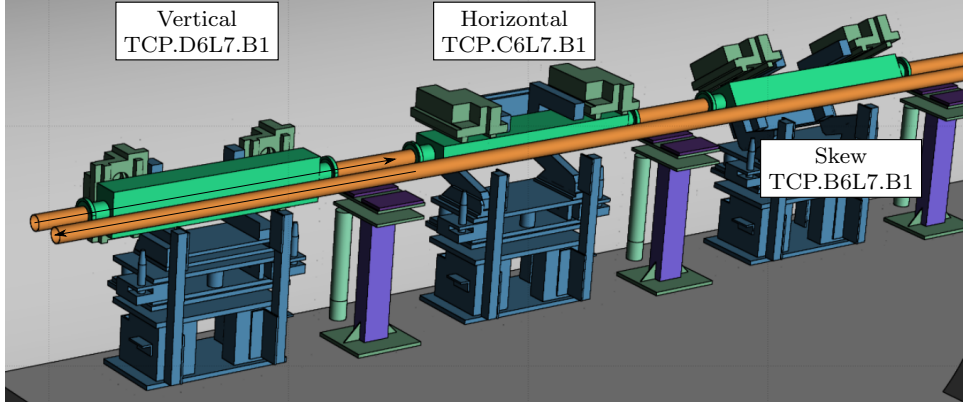


Figure 4.1: FLUKA geometry of the three primary collimators in IR7 for B1 [SCL⁺13].

simulates the interaction of a primary beam particle with the nuclei of the traversed material in a user-defined 3D geometry. It simulates and tracks the particles generated in electromagnetic or hadronic cascades. The software uses regularly updated physics models derived from experimental data and is used for a variety of applications, including particle shower simulations and energy deposition studies in the LHC.

The species, energy and direction of the incident particles are given by the user in a dedicated input file. The geometry can be defined manually with a dedicated synthax or generated from the FLUKA element database (fdb) which contains LHC elements which may be assembled [MBC⁺12]. The full geometry of the different LHC IRs is available as a FLUKA model and is regularly used to study energy deposition, activation or shower propagation for different beam loss scenarios. As an example, the geometry of three primary LHC collimators, including their supports, is shown in Fig. 4.1.

The FLUKA user input file is a sequence of command lines (called *cards*), which define the simulation setup via different available options. The required output information can be selected, post-processed and written to dedicated files via 38 different user routines that can be linked to the FLUKA executable. Each user routine consists of FORTRAN code that can be adjusted to the specific requirements of the user. The options for pre-defined output can be set in the FLUKA input file by means of the respective card linked to a specific user routine.

4.3 SixTrack

4.3.1 Tracking in SixTrack

SixTrack [Sch94, RD⁺05a, TJ94, Tam14] is designed to provide symplectic (see Chap. 7.2.1) six-dimensional tracking of relativistic proton beams in high energy synchrotrons over many

turns. Initially developed for dynamic aperture studies, the software is subject to regular updates providing new features for dedicated functions or improved physics models. The tracking algorithm is based on symplectic transfer maps derived from the accelerator Hamiltonian, which are implemented in both thick lens model and thin lens approximation. Based on these tracking maps, the array $[x, x', y, y', \sigma, p_\sigma, P]$ is transported through the magnetic lattice of the accelerator. The symplecticity makes SixTrack an excellent tool to provide accurate tracking over a large number of turns. The tracking is performed around the reference orbit which is known from the optics computation.

4.3.2 Collimation SixTrack

SixTrack is equipped with a collimation subroutine [RD+05b, Web12] providing an integrated environment for 6D thin-lens tracking together with a Monte-Carlo Module to simulate the interaction of the protons with the material of the collimation devices. For this purpose, physics models and cross-sections for different types of interactions are implemented for different collimator materials. The SixTrack particle-matter interaction simulation includes energy loss via ionization, multiple Coulomb scattering, and nuclear interactions at the passage of the protons through the collimator. Both elastic and inelastic nuclear interactions are simulated, where the proton is considered to be lost when the interaction is inelastic, except in the case of single diffractive scattering. For particles having undergone single diffractive and elastic scattering, the tracking is continued when the particle has left the collimator.

In order to identify the loss distribution in the ring, the individual particle tracks are compared to a detailed model of the LHC aperture. If the track of a beam particle is identified to intercept the aperture, the loss location is identified with a precision of 0.1 m and the information is saved in a dedicated output file. The aperture check is first carried out at dedicated aperture markers to reduce the required computing time. Beginning from the marker, particle track is then reversely extrapolated as a straight line and the aperture check is iteratively repeated in steps of 10 cm until the loss location is identified. In the current SixTrack release version ¹, this algorithm is executed on a post-processing level by means of the software BeamLossPattern [RARD05] (see Fig. 4.2). Given that all particle tracks have to be saved and analyzed in this approach, this method of loss detection is very time- and space-consuming.

An important recent extension of SixTrack is an on-line aperture check during the tracking instead of computing the aperture losses on a post-processing level. With this algorithm SixTrack continuously compares the particle coordinates to a detailed model of the LHC aperture while tracking. With the initial aperture check carried out at the markers, the losses are precisely localized by backwards extrapolation, equivalent to the aperture check with `BeamLossPattern`.

¹SixTrack Version 4.5.34 from 20.04.2016

The approach significantly reduces the required CPU time and reduces the amount of produced data generated.

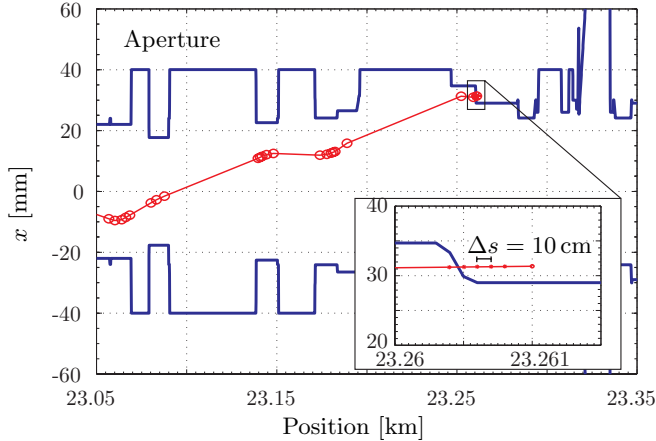


Figure 4.2: Illustration of the `BeamLossPattern` backtracking algorithm to identify aperture losses from particle tracks simulated with SixTrack. Figure taken from [RARD05].

Options and input for the execution of Collimation SixTrack are given via dedicated input files:

- `fort.2`: Defining the optical configuration of the accelerator. This file can be automatically generated from MAD-X.
- `fort.3`: Selection of options and beam settings via dedicated blocks. The most relevant options for collimation studies are the number of tracked particles, number of turns through the machine, particle energy, RF settings, collimator settings and initial distribution.
- `CollDB`: Collimator database file, containing information on the name, length and material of the different collimators.
- `allapert`: Contains detailed information about the beam pipe aperture throughout the ring.

The `COLLIMATION` block in the `fort.3` file contains information about the settings of the different collimator families. The classification of the collimator family is conducted by the prefix of the collimator name and the region where the collimator is installed.

The initial particle distribution can be selected from different options. In the framework of this document, two of them are of major importance: the annular halo and the direct halo [B⁺14c], as shown in Fig. 4.3. The annular halo is a hollow ellipse in the horizontal or vertical phase space with a normalized amplitude between N_P and $N_P + \bar{\epsilon}$, where N_P is the normalized half gap of the primary collimator and $\bar{\epsilon}$ is a small quantity. The quantity $\bar{\epsilon}$ accounts for the diffusion

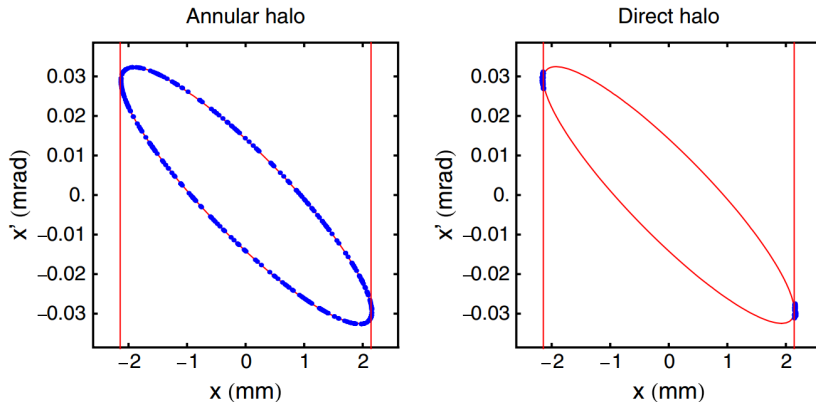


Figure 4.3: Initial distribution sampled as an annular halo (left panel) and as a direct halo (right panel). Figure courtesy of [B⁺14c].

which is not taken into account in SixTrack, in order to save computing time [B⁺14c]. The annular halo is sampled at IP1, with a Gaussian distribution in the other plane. The particles hit the primary collimator within several turns, depending on their initial betatron phase. The selection of an appropriate value for $\bar{\epsilon}$ requires to assume the impact parameter at the collimator jaw (the transverse distance of the impacting particle from the edge of the collimator jaw). It is, however, altered by non-linearities in the machine from higher order fields than quadrupoles which deform and shift the phase space ellipse [B⁺14c]. This effect is discussed in more detail in Chap. 7.6.1. The direct halo is simulated to impact immediately at the TCP jaws, which allows for a direct control of the impact parameter and reduces the number of turns required for the tracking.

Besides these halo types which can be generated by SixTrack, the software is capable of reading an input file containing the 6D coordinates of the particle distribution to be tracked.

Collimation simulations with SixTrack are usually carried out for 200 turns with an initial sample of 6.4 million protons to gain enough statistics. In this scenario, one proton lost in the aperture leads to a cleaning inefficiency of $1.5 \cdot 10^{-6} \text{ m}^{-1}$ over a 10 cm bin, about one order of magnitude below the estimated quench level during the design of the LHC. Given the large amount of required space which has to be allocated for the aperture loss detection, and the high amount of required CPU time, the simulations are split into 1000 sub-simulations which are submitted to the CERN batch computing service in which they are processed in parallel, if possible [Dep16]. The post-processing is carried out on the virtual machine of the cluster, such that only the relevant output is saved back in the user directory and the required disk space is reduced by several orders of magnitude.

Additional information can be obtained by a subsequent shower propagation simulation with

FLUKA. This allows for the study of energy deposition in the machine hardware, in particular the superconducting magnets, including contributions from hadronic and electromagnetic showers. The input for the subsequent simulation is obtained by SixTrack, which saves the information on particles having undergone inelastic interactions in the collimators to a dedicated file. Furthermore, the shower simulations can be used to quantitatively predict the resulting BLM signals. Compared to the nominal cleaning simulations with SixTrack these simulations are extensive in terms of time and space consumption and are therefore rather carried out for dedicated configurations, e.g. when experimentally measured quench limits shall be theoretically accessed.

4.4 SixTrack-FLUKA Coupling

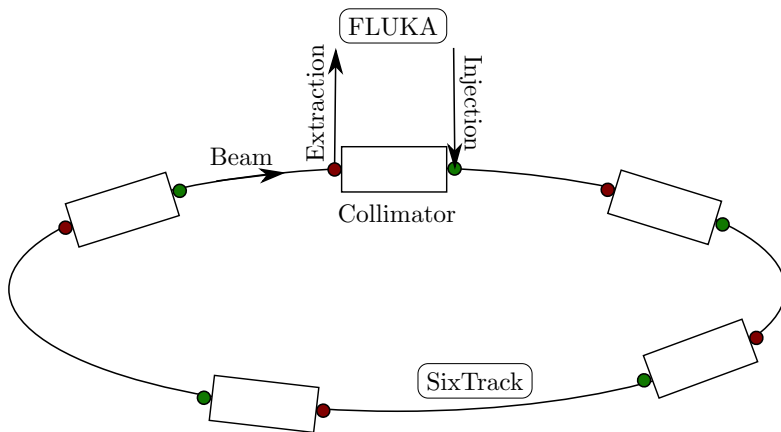


Figure 4.4: Principle of the SixTrack-FLUKA coupling. At every collimator extraction marker (red) the particle bunch is sent to FLUKA where the interaction with the collimator is simulated. The resulting distribution is then re-injected in SixTrack at the injection marker (green), from where the tracking is continued.

The SixTrack-FLUKA online coupling [M⁺13a] is a dedicated framework in which the two simulation codes SixTrack and FLUKA are run in parallel to simulate the cleaning performance of the collimation system by complementary tracking and particle-matter interaction at the collimators. It was developed as an alternative to using the built-in scattering in SixTrack and instead simulate the proton-matter interaction with FLUKA. It combines the advantages of both codes with their detailed and regularly updated physics models. The backbone of the particle exchange is a network port which transfers particle information between the two codes while both of them keep running in the background. This shortens the time required compared to if each code would have to be re-initialized after each particle exchange, and post-processing of

data becomes unnecessary.

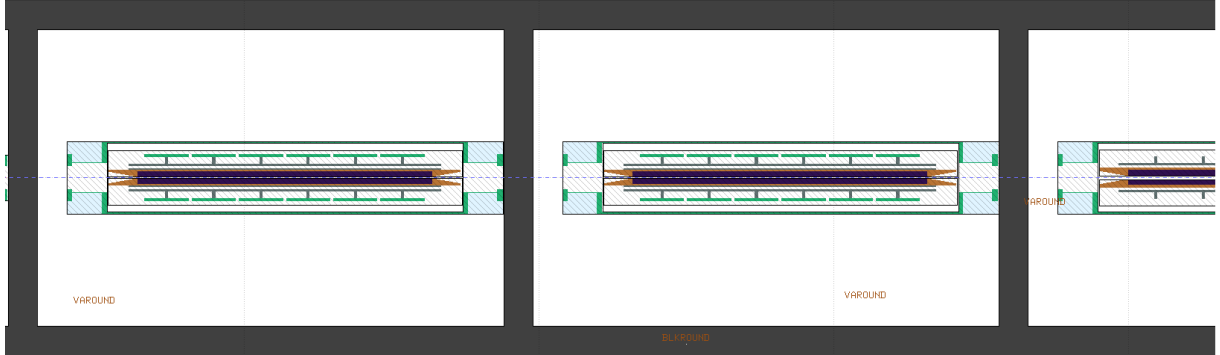


Figure 4.5: Collimator models in the FLUKA input file used for the SixTrack-FLUKA coupling.

The basic principle of the SixTrack-FLUKA coupling is illustrated in Fig. 4.4. The magnetic lattice used in SixTrack is expanded by additional collimator extraction markers at which SixTrack sends the particle distribution to FLUKA, where the interaction with the collimator is simulated. Conversely, at the end of the collimator, the distribution of residual particles is sent back to SixTrack and re-injected into the lattice at a dedicated injection marker from which the tracking is continued.

The marker locations correspond to the beginning and end of the collimator tanks. The FEDB stores detailed models of each collimator type (see Fig. 4.5) and the settings of the individual collimators are applied in a dedicated pre-processing algorithm in which the FLUKA input file, required for the coupling simulation, is produced. Residual protons which are not identical to the incoming protons (e.g. those produced in nuclear interactions) are assigned to a new particle ID, which can take values up to 2000.

Losses at the aperture of the LHC magnets are identified by the on-line aperture check. The input for subsequent shower propagation simulations can be obtained in full analogy to that of SixTrack. In addition, a `toucMap` file can be generated, which contains information on the impact position at every collimator. This data can be used to produce input for subsequent shower propagation simulations, starting from the surface of the collimator.

4.5 ICOSIM

It was yet anticipated in the LHC design phase that the interaction of the heavy ions with the collimator material can lead to fragmentation into other isotopes, with consequences on the cleaning inefficiency. This was incorporated into a dedicated simulation software for heavy-ion collimation cleaning, Ion Collimation Simulation (ICOSIM) [B⁺04a, Hol08].

It is an integrated program for particle tracking with a Monte-Carlo module to simulate the interaction of heavy-ions with the collimator materials. The tracking routine is split in two stages: First, the impact distribution at the TCPs is determined by a linear transformation between them. Every 100 turns, random transverse kicks are applied to the particles to simulate diffusion. When all particles have impacted the TCPs, the tracking of the residual fragments is continued based on a matrix multiplication with chromatic modelling in linear approximation and sextupole fields in thin-lens approximation. The information about the magnetic lattice is read from MAD-X output. Along with the tracking, the particle amplitudes are compared to a simplified aperture model, in which the aperture cross sections are approximated by an ellipse. Once the aperture is identified to be intercepted at the end of an element, the exact location is determined by extrapolation, as described in the previous chapter.

The Monte-Carlo module simulates the interaction of the ions with matter, including energy loss from ionization via the Bethe-Bloch equation and multiple Coulomb scattering, as well as fragmentation processes from EMD and NF [B⁺04a]. The latter is computed using tabulated cross-section information for the two processes which is generated beforehand with FLUKA or the Pshenichnov model [B⁺04a]. When a particle is subject to fragmentation in the collimator, the heaviest fragment is given back to the tracking routine. Momentum transfers (both transverse and longitudinal) from the fragmentation process are not taken into account [B⁺04a]. At the time of development, these simplifications were considered to be of small importance for the simulation result, because the transverse momentum transfer from the fragmentation process and the energy loss related to it are small [B⁺04a].

5. Collimation of Heavy-Ion Beams

This chapter points out the challenges that are related to the operation with heavy-ion beams and the simulation of the heavy-ion collimation performance.

5.1 Heavy-Ion Qualification Loss Maps

The LHC BLM system is also used to study the efficiency of the collimation system for a given machine configuration. Such analyses are mainly carried out when new optics, collimator settings or particle momenta are commissioned. The cleaning performance must be validated in every possible machine configuration before they are permitted for the injection of high intensity beams [BAF⁺⁰⁶].

Strategies to increase the emittance have been developed and are regularly used for loss map measurements. Early loss map measurements have been carried out by means of optics changes that led to tune resonance crossing which induced fast beam losses at the collimation system. From 2012 on, the beam excitation is carried out using the transverse damper (ADT) [M^{+13b}] which is capable of introducing white noise excitation such that the beam particles receive random transverse kicks resulting in an effective increase of emittance. The latter is distinguished by the better controllability of the excitation and is done selectively for both planes of both beams with a selectable loss rate [M^{+13b}].

Such loss map measurement campaigns are carried out with very low intensity (maximum $3 \cdot 10^{11}$), compared to the nominal intensity for stable beams. The excited beam particles are intercepted by the collimation system and the collimation debris is measured with the BLMs. This approach produces loss patterns significantly different from nominal operational losses, in which the losses occur for both planes of both beams, indistinguishable with respect to their origin. In the latter scenario, another loss type could be dominating the global loss pattern and the collimation losses could be too small to be above the background signal of the BLM system.

The B1H qualification loss maps measured in the 2011 configuration with protons and $^{208}\text{Pb}^{82+}$ ions at a momentum of $3.5 Z \text{TeV}/c$ are directly compared in Fig. 5.1. The optics

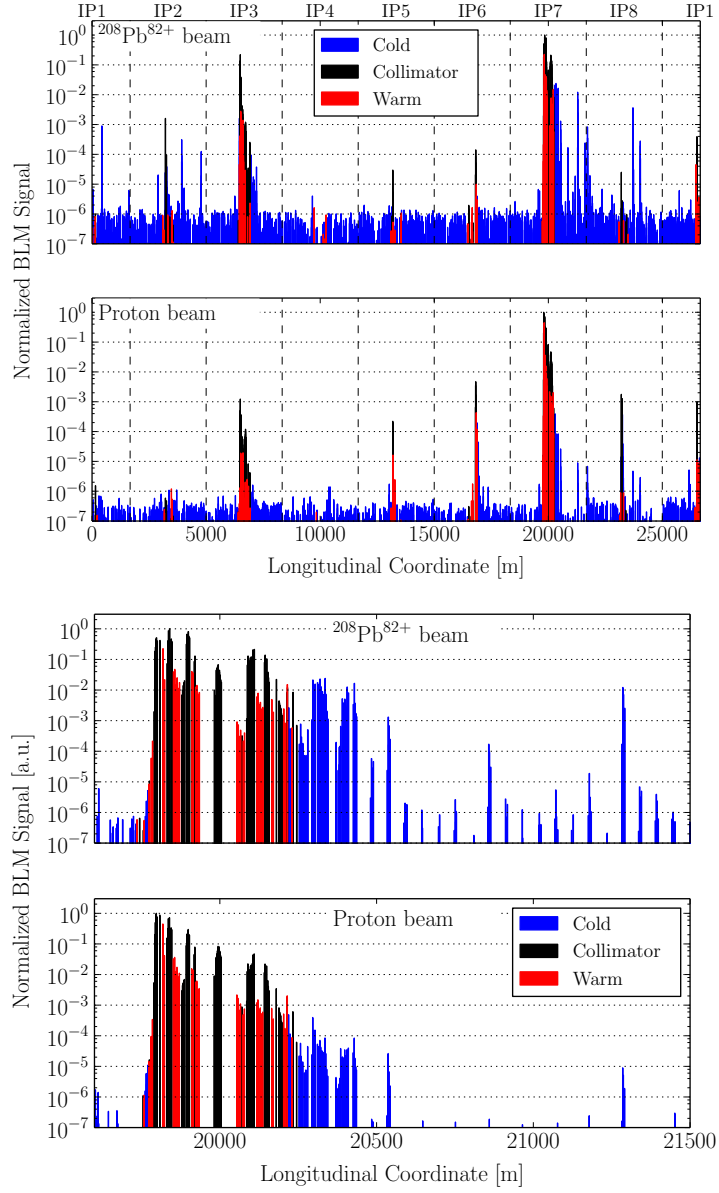


Figure 5.1: Qualification loss maps measured in 2011 with proton [B⁺14c] and ²⁰⁸Pb⁸²⁺ beams [H⁺14] at 3.5 Z TeV with identical collimator settings and optics, except in IR2. The vertical dashed lines mark the LHC octants. The upper plots show the full LHC ring, the bottom plots a zoom to IR7.

settings are squeezed with the β^* values listed in Table 3.1. Note the difference in IP2, where the injection settings with $\beta^* = 10\text{ m}$ are maintained for protons and the beams are squeezed to $\beta^* = 1\text{ m}$ for heavy-ions. The collimator settings are listed in Table 3.6.

In both qualification loss maps the collimation regions capture the largest fraction of losses, where the peak loss rate at the TCP in the momentum cleaning insertion IR3 is two orders of magnitude higher for $^{208}\text{Pb}^{82+}$ ions than for protons. While the proton loss signals are beyond the noise level only in regions close to collimators, the loss distribution of heavy-ion beams shows pronounced peaks at amplitudes up to 10^{-2} in superconducting regions across the LHC ring. In both measurements the highest loss signal is measured in the DS region downstream of IR7 with amplitudes of $3 \cdot 10^{-4}$ for protons and $2 \cdot 10^{-2}$ for $^{208}\text{Pb}^{82+}$ ions, so the cleaning performance with heavy-ion beams is almost two orders of magnitude worse than for protons. Additional losses in cold regions are measured with heavy-ion beams in the arc region between IR7 and IR8 and in the cold regions downstream of IP8, IP1 and IP2.

This finding and its consequences on the feasibility of heavy-ion operation should be regarded in the context of the stored heavy-ion beam energy which is two orders of magnitude below that of protons. It shows that heavy-ion operation in the LHC is viable in principle, but the collimation system should be evaluated with the same thoroughness as it is for proton beams. Particularly the cleaning performance should be theoretically accessible by means of simulation tools to allow for potential optimizations and to study the potential benefit by hardware upgrades.

5.2 Simulation with ICOSIM

Fragments scattered out of the collimators are in this model absorbed closely to the collimators where the fragmentation occurred and do not continue moving inside the machine for long distances. Losses in warm regions are visible only in IR3 but not in IR7. The mass number of the heaviest created and tracked fragment is $A_{\max} = 90$ which can be traced back to the simplified fragmentation algorithm. The high measured loss peaks (see bottom row in Fig. 6.7) in the arcs between IR7 and IR8 are, with one exception, not reproduced by ICOSIM. The most critical losses in the dispersion suppressor (DS1 and DS2) located in the cells 8 and 9 of IR7 are visible in the simulated loss map. The local cleaning inefficiency in this region peaks at approximately $\eta = 10^{-2}$, which is comparable to the measured loss distribution. However, it shall again be emphasized that the BLM signals with limited coverage can not be compared quantitatively to the simulated loss maps (see Chap. ??). The longitudinal extensions of the loss clusters in the DS do not fully match with the ones of the measured losses.

5.3 Conclusions

6. SixTrack with Ion-Equivalent Rigidities

The benchmarking of ICOSIM against measured LHC data unveiled that the simulation result shows discrepancies and that important loss patterns in the ring are not simulated by the software. Based on this, the development of a new improved simulation tool was initiated which is presented in this document.

The new simulation software for heavy-ion collimation shall be easy to use, well-benchmarked and contain accurate physics models. As a first step in this development the requirements of an improved simulation tool have to be determined. One important hypothesis is that the discrepancy between ICOSIM and the measured loss map might arise from the fact that the transverse momentum transfer and kicks in kinetic energy in the fragmentation process is not included in ICOSIM. Contributions to the real loss patterns could also come from light ions which are omitted in ICOSIM.

To study these hypotheses, the simulation tool SixTrack with Ion-Equivalent Rigidities (STIER) was developed. The loss maps are compared to the simulations with the previous standard simulation tool ICOSIM and, based on the results, the requirements for a further improved collimation simulation software are outlined. The content of this chapter has partly been published in [H⁺14, HBJ⁺16].

6.1 Efficiency of Staged Collimation for Heavy-Ions

The loss locations of residual particles that inevitably leave the primary collimator in IR7 depend on the type of interaction the particles have undergone. By virtue of its design, the collimation system is most efficient if the particles have been subject only to small changes in rigidity but received transverse momentum transfers large enough to scatter them into the secondary collimators, as described by Eq. (3.7). Losses in the IR7 DS are therefore associated with angular kicks $\Delta x'$ inside the angular acceptance and rigidity changes $\delta_{\text{eff}} = (1 + \delta)/\chi$ outside the rigidity

acceptance of the DS magnets. A rough estimate for the latter is given by

$$\delta_{\text{eff}}^{\max} = \pm A_g D_x^l. \quad (6.1)$$

where A_g is the horizontal aperture in the magnet (approximately 24 mm in the IR7 DS) and D_x^l is the dispersion generated locally between the TCP and the considered DS magnet. This relation is valid in linear approximation for a particle without betatron offset. For real particles with betatron offsets, the acceptance may be reduced or enhanced, such that the expression in Eq. (6.1) is only approximate and the real value for $\delta_{\text{eff}}^{\max}$ becomes a distribution, rather than a constant.

To study the difference between the distribution in angle and energy of $^{208}\text{Pb}^{82+}$ ions and protons after interactions with the primary collimators, two dedicated simulations were carried out with FLUKA. In both cases, a particle beam with an energy of $3.5 Z \text{ TeV}$ is simulated to perpendicularly hit a carbon target of 10.3 cm thickness. This compares to the typical distances particles traverse in the collimator material with impact parameters of $3 \mu\text{m}$ at an angle of $29.1 \mu\text{rad}$.

The resulting distribution in terms of the momentum per nucleon and the scattering angle $\Delta x'$ of all out-coming particles is shown for both simulations in the top and middle plot of Fig. 6.1. The horizontal lines show the minimum angular kick $\Delta x'$ required such that a particle intercepts the secondary collimator. The vertical lines show the rigidity acceptance of the MQ.11R7.B1 around the nominal beam energy of $3.5 Z \text{ TeV}$, assuming an aperture of $A_g = \pm 24 \text{ mm}$ and a local dispersion fuction of $D_x^l = 2.4 \text{ m}$. Particles passing this magnet are not lost in the DS any more. Note also that the dispersion function in this magnet is larger than in the previous MQ.9R7.B1 at the DS1 cluster, so the presented rigidity acceptance is rather conservative.

The comparison demonstrates that the number of particles outside the rigidity acceptance of the DS magnets but inside the angular acceptance of the TCSG is significantly larger for the heavy-ion distribution than for protons. The bottom plot of Fig. 6.1 shows the projected number of nucleons inside the angular acceptance of the TCSG collimators. For rigidities beyond $\pm \delta_{\text{eff}}^{\max}$, the fraction of heavy-ions (black line) is larger by up to three orders of magnitude compared to the proton distribution.

The integral of the distribution outside the rigidity acceptance in the bottom plot of Fig. 6.1 yields $(5.1 \pm 0.5) \cdot 10^{-3}$ for protons and $(863.0 \pm 0.2) \cdot 10^{-3}$ for heavy-ions. This finding is the origin of the measured cleaning inefficiency, which is two orders of magnitude higher for heavy-ions than for proton beams. Given the drastic impact on the cleaning inefficiency, the effect of fragmentation and the motion of the ion fragments in the LHC must be accurately modelled in a simulation tool for heavy-ion collimation.

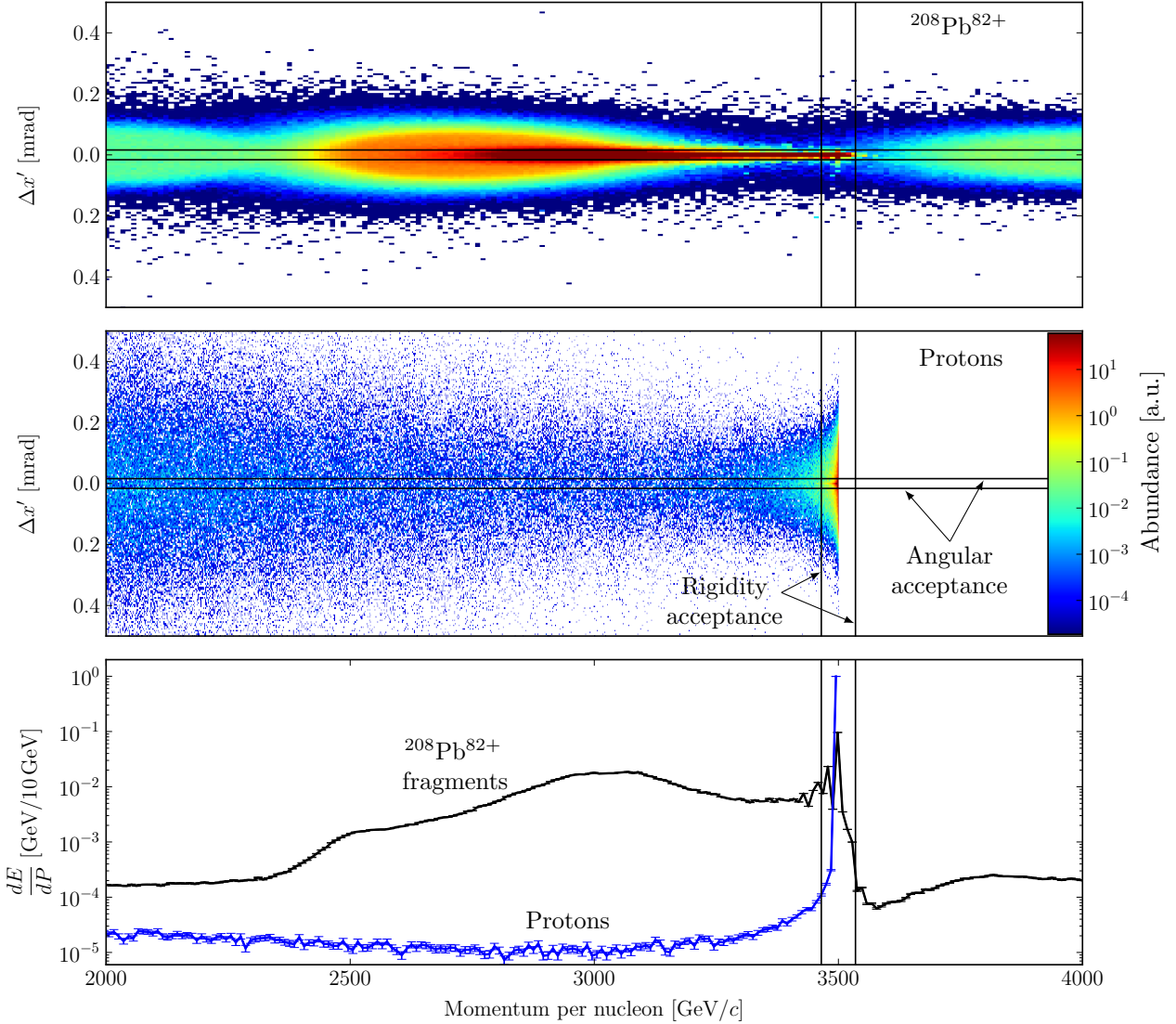


Figure 6.1: Top and middle plot: FLUKA simulated heat map of transverse angular kick received at the passage through a 10.3 cm thick carbon target vs particle momentum per nucleon for an initial beam of $^{208}\text{Pb}^{82+}$ ions (top) and protons (middle). The horizontal lines represent the TCSG acceptance and the vertical lines the rigidity acceptance of the MQ.11R7.B1. All data points are weighted with the number of nucleons per bin, roughly proportional to the energy per bin. The bottom plot shows a projected and weighted histogram of all particles inside the TCSG acceptance as a function of the momentum per nucleon.

6.2 The STIER Simulation Tool

The design of the LHC collimation system foresees the TCPs in the betatron cleaning insertion IR7 as the first collimators in the cleaning hierarchy. For every plane (H,V,S), the respective TCP should be the only collimator exposed to particles of the main beam and is under normal circumstances the location with the highest amount of lost particles in the LHC ring. The simulation presented in the previous section shows that most of the heavy-ion fragments generated at the TCP are within the acceptance of the TCSG collimators but outside of the momentum acceptance of the DS magnets. The most critical losses at the DS should hence be described very accurately by a simulation model which takes into account only the fragmentation at the primary collimators.

Based on these assumptions, a simulation tool for heavy-ion cleaning was established to investigate the impact of the approximations in ICOSIM on the simulated loss maps. Instead of using a simplified fragmentation model for all collimators, this approach relies upon a detailed fragmentation simulation at the TCP, including all generated fragments and all kicks in energy and angle from the fragmentation process. The particle-matter interaction with other collimators is neglected and they are treated as perfect absorbers. The resulting heavy-ion distribution starting at the TCP is tracked as protons with equivalent momenta in SixTrack, to take into account the rigidities of the different heavy ions. The approach is referred to as SixTrack with Ion-Equivalent Rigidities (STIER). Initially developed to study the effect of the simplifications in ICOSIM and to determine the requirements for an improved simulation tool, STIER simulations proved to be in good agreement with the measured losses. It was used in the 2015 heavy-ion run to validate the collimator settings and to develop loss mitigation strategies, which were successfully tested in operation (see Chap. 8).

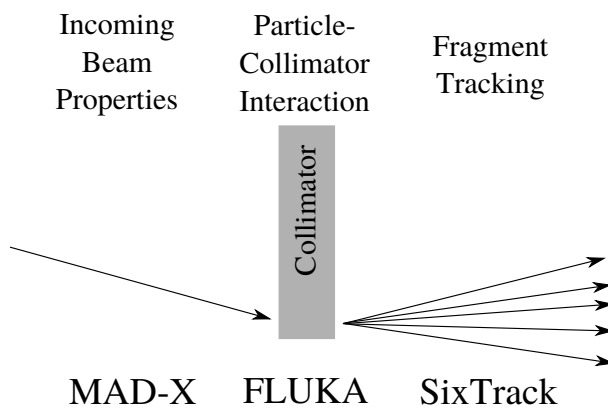


Figure 6.2: Three stages of the STIER simulation setup.

STIER relies upon three consecutive simulation steps shown in Fig. 6.2. In the first step, the phase space properties of the particles impacting the collimator jaws are determined by means of MAD-X. The angle of incidence is then used as an input for the following simulation step in which the interaction of the primary heavy-ion beam with the material of the primary collimator is simulated using FLUKA. The information about the outcoming ion fragments is then converted to input for SixTrack where the ions are tracked as protons with specific momenta to match the rigidities of the individual isotopes.

In the following sub-sections, the three STIER stages are described in detail and important simulation results for every stage are summarized. Some of the results are important also for the development of the advanced heavy-ion collimation tool described in Chap. 7.

6.2.1 Optics Calculation

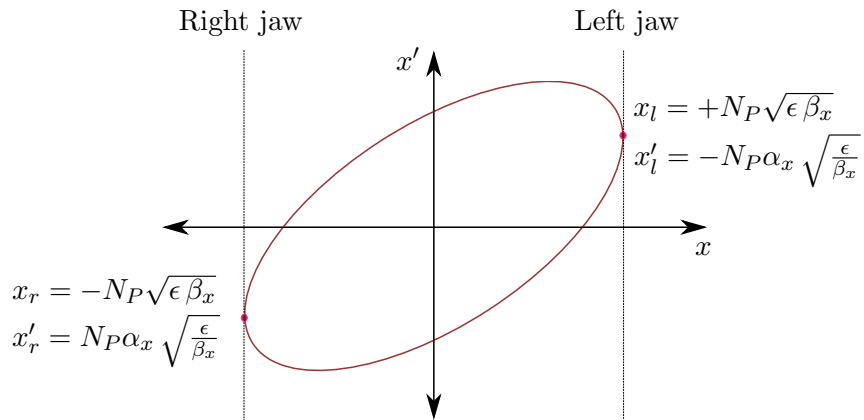


Figure 6.3: Phase space diagram of particles at a maximum normalized betatron amplitude N_P . Particles hitting the left and right jaw of the TCP have specific coordinates in phase space.

As a first step of the STIER simulation approach, the optical functions are computed with MAD-X. This simulation delivers both the phase space parameters at the TCP and the fort.2 optics input required for SixTrack.

Particles impacting the primary collimator have specific properties in phase space, as illustrated in Fig. 6.3. The collimator jaw is assumed to have no inclination (i.e. it is not aligned to align with the divergence of the beam envelope). Furthermore, it is assumed that the diffusion is slow enough for particles to hit the TCP close to their maximum spacial amplitude. Then one can conclude from Fig. 6.3 that the particles impacting the collimator do so with a non-zero angle of incidence, if $\alpha \neq 0$. This is illustrated in Fig. 6.4.

The angle of incidence $x'_{r/l}$ at the left and right collimator jaw is defined by the normalized half gap N_P , the geometric emittance ϵ_x and the Twiss parameters β_x, α_x at the location of the TCP

as follows [Wie99]

$$x'_{r/l} = \pm N_p \alpha_x \sqrt{\frac{\epsilon_x}{\beta_x}}. \quad (6.2)$$

For LHC emittances and collimator settings, the distance the primary beam particles travel through the collimator material scales, in good approximation, linearly with the impact parameters. They were found in SixTrack simulations for protons to be between $1\text{ }\mu\text{m}$ and $10\text{ }\mu\text{m}$ [B⁺14c]. Assuming that the diffusion for heavy-ion beams is similar, and taking into account the angle of incidence for $3.5 Z\text{ TeV}$ presented in Table 6.1, the travelled lie in the range from $\approx 3\text{ cm}$ to 30 cm , which is in the same order of magnitude as the nuclear fragmentation length (see Table 3.10). The isotopic composition of the outcoming heavy-ions thus strongly depends on the angle of incidence.

A summary of the Twiss parameters at the TCP, the collimator opening and the resulting angles of incidence for different scenarios are shown in Table 6.1. Note that the optics in IR7 remains unchanged during the LHC cycle and for the different configurations.

6.2.2 Fragmentation Simulation

Simulation Setup

A Monte-Carlo event generator is used to simulate the interaction of the heavy-ion beam with the material of the primary collimator. In the STIER simulations presented, FLUKA is employed for this purpose.

The primary collimator is modelled as a simple rectangular carbon cuboid of 60 cm length (see Fig. 6.4). Alternatively, the more accurately modelled collimator geometry of the FEDB can be used. Comparisons between fragmentation simulations using the two geometries have

Table 6.1: Summary of the parameters used to calculate the angle of incidence at the primary collimator for the LHC machine configurations used in different years. The Twiss parameters β_x and α_x are computed using MAD-X. The angle x' is calculated by means of Eq. (6.2) with $\epsilon_N = 1.4 \times 10^{-6}\text{ }\mu\text{m rad}$.

Year	E [Z GeV]	β_x [m]	α_x []	ϵ_N [$\mu\text{m rad}$]	γ []	N_p [σ]	x' [rad]
2010/2011	3500	148.46	2.04	1.50	1482.8	5.7	-2.9×10^{-5}
2015	6370	148.46	2.04	1.41	2696.8	5.5	-2.1×10^{-5}
Design	7000	148.46	2.04	1.50	2964.5	5.7	-2.1×10^{-5}

shown no significant discrepancy in the resulting spectrum of heavy-ion fragments. The density of the carbon composite is set to a density of 1.61 g/cm^3 to account for the CFC material used for the TCPs. Species, energy and transverse momentum of the heavy-ions passing the boundary crossing at the end of the collimator jaw are saved to an output file. Other particles, such as electrons, pions, mesons, etc. are ignored because they are lost most probably in the warm aperture immediately downstream of the TCP. While this approximation is valid for cleaning simulations, in which the global cleaning inefficiency is simulated, detailed shower simulations of energy deposition and radiation dose in the collimation region IR7 take them into account [B⁺14a].

The FLUKA simulation input file is adjusted to take into account for electromagnetic dissociation, nuclear fragmentations using the DPMJET-III model [R⁺00] as well as subsequent nuclear evaporation.

In the presented simulations of the 2011 cleaning performance, the primary beam is simulated as 10^7 particles of $^{208}\text{Pb}^{82+}$ at an energy of $3.5 Z \text{ TeV}$, impacting the TCP at an angle of incidence of $x'_{r,l} = \pm 2.91 \times 10^{-5} \text{ rad}$. They have been carried out for three different impact parameters: $b = 1 \mu\text{m}$, $b = 3 \mu\text{m}$ and $b = 10 \mu\text{m}$. The beam is simulated to impact with fixed x, x' (in contrast to a distribution in x, x') and no amplitude in y, y' . This setup is called pencil beam.

Isotope Spectrum

From the FLUKA simulations for the three impact parameters $1 \mu\text{m}$, $3 \mu\text{m}$ and $10 \mu\text{m}$, the isotope spectra in terms of mass number A can be derived for the three different simulation cases. In Fig. 6.5, the distribution of A , weighted with the particle momentum, is shown for the simulations with the three impact parameters.

With an impact parameter of $b = 1 \mu\text{m}$ the distribution is clearly dominated by heavy fragments,

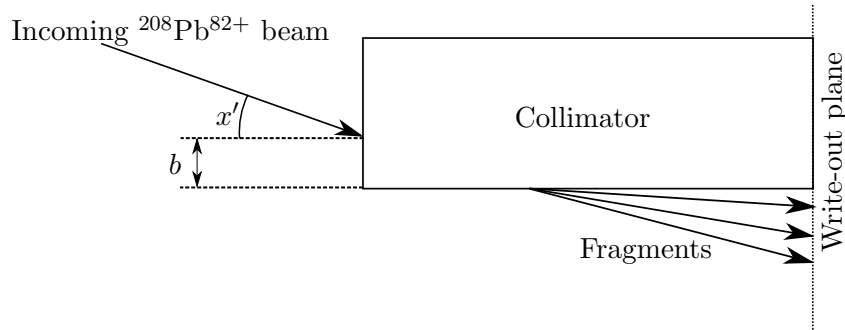


Figure 6.4: Geometry used for the FLUKA simulation of the fragmentation at the TCP.

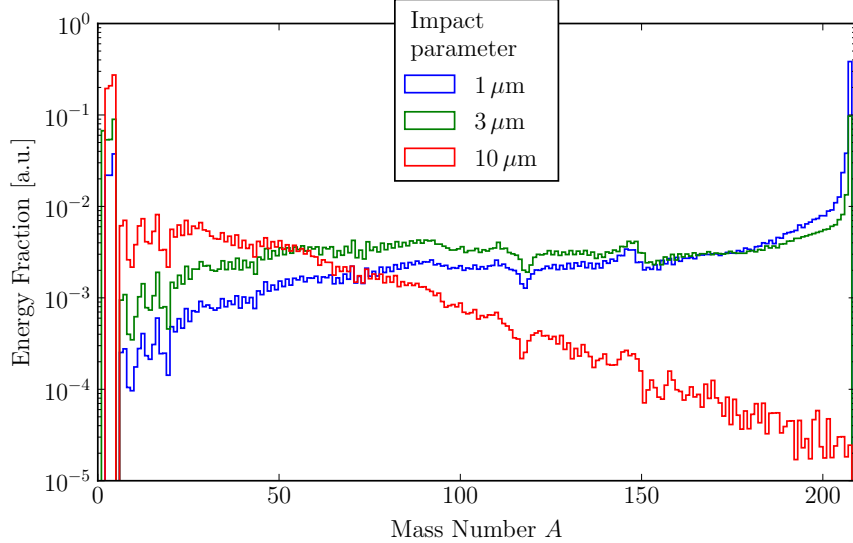


Figure 6.5: FLUKA simulation results for different impact parameters: mass numbers for heavy-ion fragments leaving the TCP weighted with their momentum.

with masses closely to that of the main beam. For $b = 3 \mu\text{m}$, the production yield of lighter ion fragments increases, and for $b = 10 \mu\text{m}$ the spectrum is clearly dominated by very light fragments such as helium nuclei, tritium, deuterium and protons. In all simulations, the ions carrying the most fraction of energy are either those with A, Z close to the main beam and very light ion fragments. A detailed overview of the energy fraction carried by the most important isotopes is given for different impact parameters in Table 6.2.

Table 6.2: Isotopes with the largest energetic fractions leaking out the collimator material from the initial fragmentation simulation.

Isotope	Energetic Fraction		
	$b = 1 \mu\text{m}$	$b = 3 \mu\text{m}$	$b = 10 \mu\text{m}$
${}^1\text{H}^{1+}$	4.7×10^{-2}	6.3×10^{-2}	4.0×10^{-1}
${}^2\text{H}^{1+}$	2.1×10^{-2}	2.5×10^{-2}	1.2×10^{-1}
${}^3\text{H}^{1+}$	1.5×10^{-2}	1.7×10^{-2}	7.4×10^{-3}
${}^3\text{He}^{2+}$	5.8×10^{-3}	8.1×10^{-3}	4.9×10^{-3}
${}^4\text{He}^{2+}$	3.6×10^{-2}	4.2×10^{-2}	1.6×10^{-1}
${}^{205}\text{Pb}^{82+}$	7.1×10^{-3}	2.3×10^{-3}	1.1×10^{-5}
${}^{206}\text{Pb}^{82+}$	1.7×10^{-2}	5.0×10^{-3}	1.4×10^{-5}
${}^{207}\text{Pb}^{82+}$	3.3×10^{-2}	8.4×10^{-3}	1.0×10^{-5}
${}^{208}\text{Pb}^{82+}$	3.6×10^{-1}	3.6×10^{-2}	1.4×10^{-5}

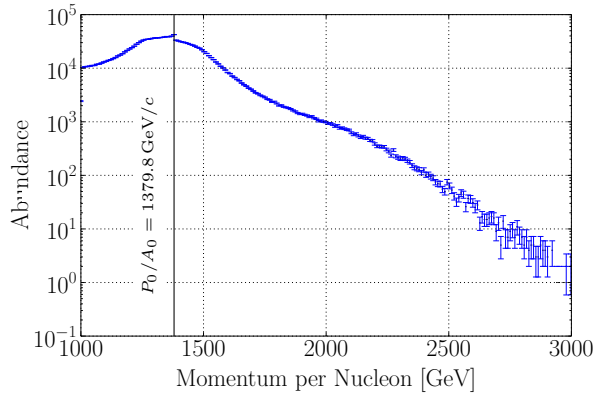


Figure 6.6: Momentum per nucleon of the ion fragments in the fragmentation simulation.

The reason for the increasing number of light ion fragments with larger impact parameters is the linear relation between the impact parameter and the distance the particles travel through the material. Therewith, the probability of fragmentation increases exponentially. As shown in Table 6.2, for an impact parameter of $b = 1 \mu\text{m}$, the amount of energy carried by protons is approximately one order of magnitude below that carried by $^{208}\text{Pb}^{82+}$ ions. At $b = 10 \mu\text{m}$, approximately 40% of the outgoing beam energy is carried by protons and 16% by $^4\text{He}^{2+}$ ions, while the contribution of particles of the main beam is smaller by four orders of magnitude. Therefore, the impact parameter plays an important role for the isotopic spectrum generated in the process of heavy-ion fragmentation. The impact on the resulting loss distribution is studied in the following chapters.

In the ICOSIM tool it is assumed that the momentum per nucleon of the fragments generated in NF and EMD processes is similar to p_A of the main beam ($\delta \approx 0$). The fragmentation simulation for STIER allows for the analysis of the p_A spectrum for the outgoing ions, shown in Fig. 6.6. Most of the ions have p_A close to that of the incoming $^{208}\text{Pb}^{82+}$ beam, which is at $1379.8 \text{ GeV}/A$. Parts of the fermi-motion in the nucleus can be transferred to individual ion fragments, such that the fragment can have significantly larger momentum per nucleon. The largest p_A that was obtained from the FLUKA simulation is approximately $3200 \text{ GeV}/A$. This broad spectrum of momenta indicates that an improved heavy-ion collimation tool should include the change of kinetic energy from the fragmentation process, especially if light fragments shall be included in the simulation.

6.2.3 Heavy-Ion Tracking in SixTrack

SixTrack is designed for the tracking of protons, so the tracking does not include effects of isotopic dispersion. Based on Eq. (2.16), the effective momentum offset δ_{eff} of an ion of the

reference species to have the same magnetic bending behaviour as an arbitrary ion with δ, χ , is given by

$$\delta_{\text{eff}} = \frac{(1 + \delta)}{\chi} - 1. \quad (6.3)$$

If the reference species is a proton of momentum P_0 , the applicable effective proton momentum to simulate the tracking behaviour of an ion with mass and charge m and Z is given by:

$$P_E = P_0 (1 + \delta_{\text{eff}}) = \frac{P}{Z}. \quad (6.4)$$

The isotopic dispersion of heavy-ion species not matched to the magnetic lattice can therefore be accurately simulated by assigning the ion-equivalent momentum P_E to the tracked proton. From the FLUKA simulation data on the ion fragments leaving the primary collimator, the momentum and charge are easily extracted and converted into the momenta used for the initial distribution in STIER. Furthermore, the transverse angles x' and y' and positions x, y' are incorporated into the initial conditions.

In order to take into account the different energy deposited from heavy nuclei compared to light nuclei, the losses on the aperture in the tracking and the cleaning inefficiency must be calculated taking into account the physical momentum of the impacting nuclei. Given that the losses are not to be compared quantitatively to the measured loss signals, this approximation is acceptable. The aperture losses are identified with `BeamLossPattern`, in a manner fully identical to that used for proton studies with SixTrack. The Monte-Carlo routine implemented in SixTrack to simulate the proton interaction with the collimators must be evaded because it is not adapted to heavy-ions. The collimators in the STIER approach are therefore set to perfect absorbers. This approach will lead to an overestimation of the collimator losses which should be considered in the analysis of the simulated loss pattern.

The accelerating RF cavities are switched off in STIER because the acceleration depends on Z which is not incorporated. However, it is expected that the number of turns that a heavy-ion fragment can perform in the machine without being lost is very small compared to the synchrotron period (≈ 500 turns).

6.3 Simulation Results

6.3.1 Full Heavy-Ion Loss Map Simulations

In this section the simulation results in the 2011 configuration (see Table 3.1 and Table 3.6) are compared between ICOSIM and STIER. Both simulations are carried out with an impact

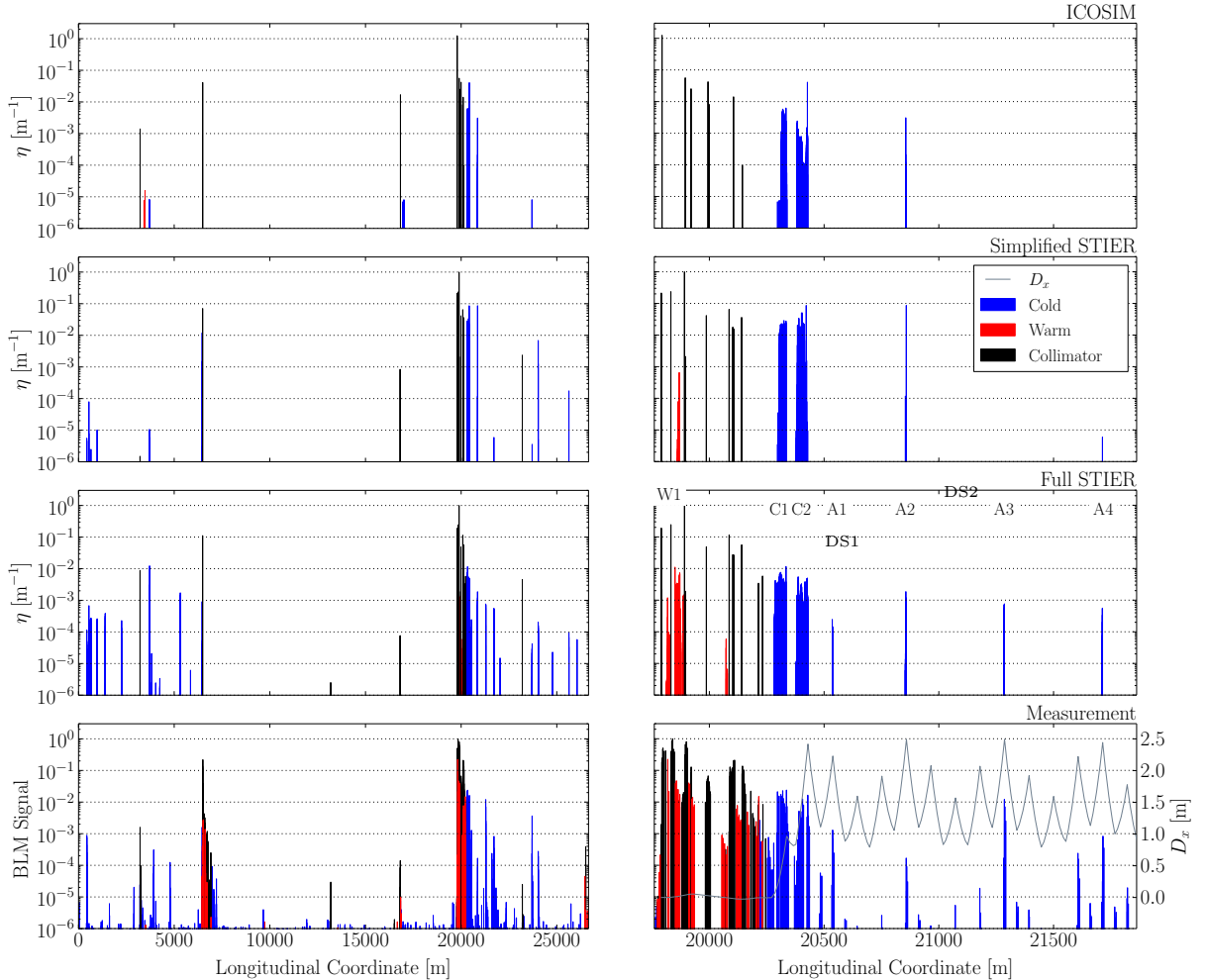


Figure 6.7: Comparison of loss map simulations using ICOSIM (top row), a simplified STIER approach (second row), a full STIER simulation (third row) and the measured loss maps during the 2011 LHC heavy-ion run at $3.5 Z \text{ TeV}$. The right graph in the bottom row also shows the locally generated dispersion function D_x starting at $D_x = 0$ at the TCP. The left column shows the loss map over the full LHC ring, while the right column shows the same loss map zoomed into the betatron collimation region IR7. The STIER simulations are carried out assuming an impact parameter of $b = 3 \mu\text{m}$. The losses in the DS are denominated DS1 and DS2, those in the arc A1 to A4.

parameter of $3\mu\text{m}$, and the same initial distribution is loaded in the two approaches to provide comparability. In addition to the full STIER simulation (which is the approach described above), a simulation with simplified outscattering from the TCP is carried out, in which angular and energetic kicks from the fragmentation simulation are not taken into account. This approach, here called simplified STIER, allows to benchmark the STIER simulation result against ICOSIM. However, ICOSIM and the simplified STIER approach are not fully comparable because of the different aperture checks, and the losses from subsequent fragmentation processes included in ICOSIM but not in STIER. Furthermore, simplified STIER includes light ion fragments, but their contribution to the loss pattern is studied separately later-on in this chapter.

The result of the ICOSIM simulation presented before in Chap. ?? is shown in the first row of Fig. 6.7 for the full LHC ring (left) and zoomed into IR7 and the following arcs (right). The loss maps from the simplified STIER simulation are shown in the second row of Fig. 6.7. The losses are more broadly distributed over the LHC ring when the full spectrum of fragments is included. This indicates that light isotopes are by no means only lost locally in the secondary collimators or in the warm regions surrounding them. Parts of the losses in the warm region of IR7 are reproduced in this simulation approach, originating mainly from very light isotopes at $|\delta_{\text{eff}}| \gg 0$. The two clusters of losses in the IR7 DS are increased in their intensity and longitudinal extension, since the isotopes which are neglected in ICOSIM are now included and are lost in these regions. The loss peak with the largest amplitude is still in the IR7 DS but is increased to $\eta_{\text{max}} = 10^{-1}$. One of the loss peaks in the arcs is, as in ICOSIM, reproduced in this simulation. Also here, the simulated peak intensity is increased with respect to ICOSIM.

The loss maps generated with the full STIER simulation are shown in comparison to the measurement and the ICOSIM loss map in the third row of Fig. 6.7. This approach shows the best agreement with the measured loss distribution. The four highest loss peaks in the arcs become visible when the angles and energies of the fragments are included. A larger amount of the

Table 6.3: STIER simulated contributions on the total deposited energy at the warm magnets in IR7 (W1), the two loss clusters in the IR7 DS (C1 and C2) and in the arcs downstream of IR7 (A1,A2,A3,A4) as shown in Fig. 6.7

W1		DS1		DS2		A1		A2		A3		A4	
Ion	(%)	Ion	(%)	Ion	(%)	Ion	(%)	Ion	(%)	Ion	(%)	Ion	(%)
$^1\text{H}^{1+}$	57.0	$^3\text{H}^{1+}$	8.6	$^{206}\text{Pb}^{82+}$	34.0	$^{204}\text{Tl}^{81+}$	61.0	$^{204}\text{Tl}^{81+}$	74.6	$^{204}\text{Tl}^{81+}$	86.6	$^{204}\text{Tl}^{81+}$	86.7
$^3\text{H}^{1+}$	38.0	$^4\text{He}^{2+}$	4.5	$^{205}\text{Pb}^{82+}$	16.2	$^{206}\text{Pb}^{82+}$	18.7	$^{206}\text{Pb}^{82+}$	10.3	$^{199}\text{Au}^{79+}$	6.7	$^{199}\text{Au}^{79+}$	7.2
$^2\text{H}^{1+}$	2.6	$^2\text{H}^{1+}$	3.2	$^{204}\text{Pb}^{82+}$	11.6	$^{199}\text{Au}^{79+}$	7.4	$^{199}\text{Au}^{79+}$	5.7	$^{206}\text{Pb}^{82+}$	2.2	$^{206}\text{Pb}^{82+}$	1.7
$^3\text{He}^{2+}$	1.4	$^{203}\text{Pb}^{82+}$	3.2	$^{203}\text{Tl}^{81+}$	8.7	$^1\text{H}^{3+}$	3.5	$^{201}\text{Hg}^{80+}$	2.3	$^{194}\text{Ir}^{77+}$	1.2	$^{202}\text{Hg}^{80+}$	1.6

losses in the warm IR7 magnets (W1) is visible, coming mainly from the very light fragments scattered out of the collimator (see Tab. 6.3 for the mainly contributing isotopes). The two loss clusters (C1 and C2) in the IR7 DS are modeled with a correct longitudinal extension and order of magnitude (the mainly contributing isotopes to C1 and C2 are also listed in Tab. 6.3). It is remarkable that the second loss cluster C2 is dominated by heavy fragments of Pb, created by electromagnetic dissociation (the three isotopes contribute to 61.8 % of the total deposited energy), while the highest fraction of C1 is due to very light isotopes (H and He ions) where the four most important isotopes only compose only 19.5 % of the energy deposited in C1. With 1227 different isotope species lost in C1, the deposited energy is shared between a much larger number of isotopes than at C2, where only 334 different isotopes are absorbed. The distributions of the quantity χ for the isotopes lost in the regions C1,C2 are graphically represented in Fig. 6.8. As expected, the aperture in the cold region C1 captures a very broad range of isotopes. In the cold region C2, mostly isotopes with mass to charge ratios close to the reference ion species contribute to the total deposited energy. The graph at the right bottom of Fig. 6.7 shows also the locally generated dispersion function D_x starting at the primary collimator. The dispersion increases from $D_x \approx 0$ m in the warm IR7 magnets to $D_x \approx 1$ m at the end of the C1. At the second loss cluster C2, the dispersion increases to even $D_x = 2.4$ m. We conclude that the isotope distribution shown in Fig. 6.8 can be explained by the fact that the isotopes with large momentum offsets are removed from the beam already in the C1, while the isotopes with rigidities closer to the main beam are not sufficiently off-momentum to be intercepted by the aperture at this location. When the dispersion further increases at C2, also the isotopes with smaller $|\delta_{\text{eff}}|$ are lost in the aperture, while the isotopes with $A < 190$ have already been removed from the beam in C1. Here it shall be pointed out that the fraction of light isotopes depends strongly on the chosen impact parameter for the fragmentation simulation.

Contrary to this, the isotope composition at the arc loss peaks (A1,A2,A3,A4) is very homogeneous (see Tab. 6.3). At the passage through the arcs, the locally generated dispersion function is beating with amplitudes between $0.8 \text{ m} < D_x < 2.5 \text{ m}$. The loss peaks A1-A4 are located at local maxima of the function D_x . The similarity of their isotopic composition can be explained by the fact that, especially for isotopes with rigidities closely to the main beam, the individual starting conditions at the TCP (starting angle and collimator jaw) can partly add or subtract to dispersive effects, thus some ions of the same species can travel for longer distances than others. It shall be emphasized that except $^1\text{H}^{3+}$, all isotopes listed for A1-A4 in Tab. 6.3 are also included in the ICOSIM simulation. We conclude that the decisive properties determining at which of the four locations a particle is absorbed are the angle and momentum at which the particle is emitted at the TCP, which are not included in ICOSIM. Hence, an accurate simulation of heavy ion loss patterns requires inevitably the incorporation of angular and energetic shifts

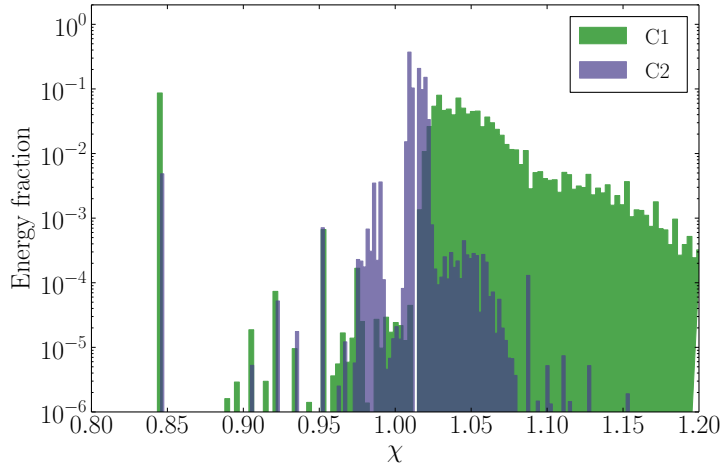


Figure 6.8: Fractions of the total deposited energies in the regions C1 and C2 as a function of the relative mass to charge ratio χ . The data is extracted from the full STIER simulation with $b = 3 \mu\text{m}$.

by fragmentation at the collimator, which should be considered for future simulations. The fraction of nucleons which is absorbed in the aperture was calculated to be $f_{\text{glob}} = 0.167$ almost two orders of magnitude larger than for comparable simulations with proton beams where this quantity takes typically values in the order of $f_{\text{glob}} = 0.002$ [B⁺14c].

Parts of the losses far downstream of the TCP are longitudinally shifted with respect to the measured loss peaks in the same region of the LHC. These shifts could come from small aperture displacements in the real machine, or offsets of the closed orbit by the same amount. An analysis of the particle trajectories at the corresponding loss locations shows that displacements as small as $\Delta a = 300 \mu\text{m}$ are sufficient to shift the loss location of the impacting ions, while at the loss peaks A1-A4 displacements of $\Delta a > 600 \mu\text{m}$ are required for a significant reduction of the loss peak amplitude. In operation, orbit drifts in the order of $500 \mu\text{m}$ have been observed [BAR15]. Furthermore, the measured aperture profile in the magnets varies up to 1.2 mm [].

Another possible explanation is that a non-equal amount of secondary ion fragments is produced at the two collimator jaws, which is studied in the next sub-chapter.

6.3.2 Dependence on the starting Collimator Jaw

STIER can be used to study the loss behaviour of isotopes starting at the individual collimator jaws. So far, all STIER results assume the same amount of ions impacting on the two TCP jaws. However, SixTrack studies with proton beams have shown that the beam halo can impact the two collimator jaws asymmetrically, as discussed in [B⁺14c] and in Chap. 7.6.1. This process is

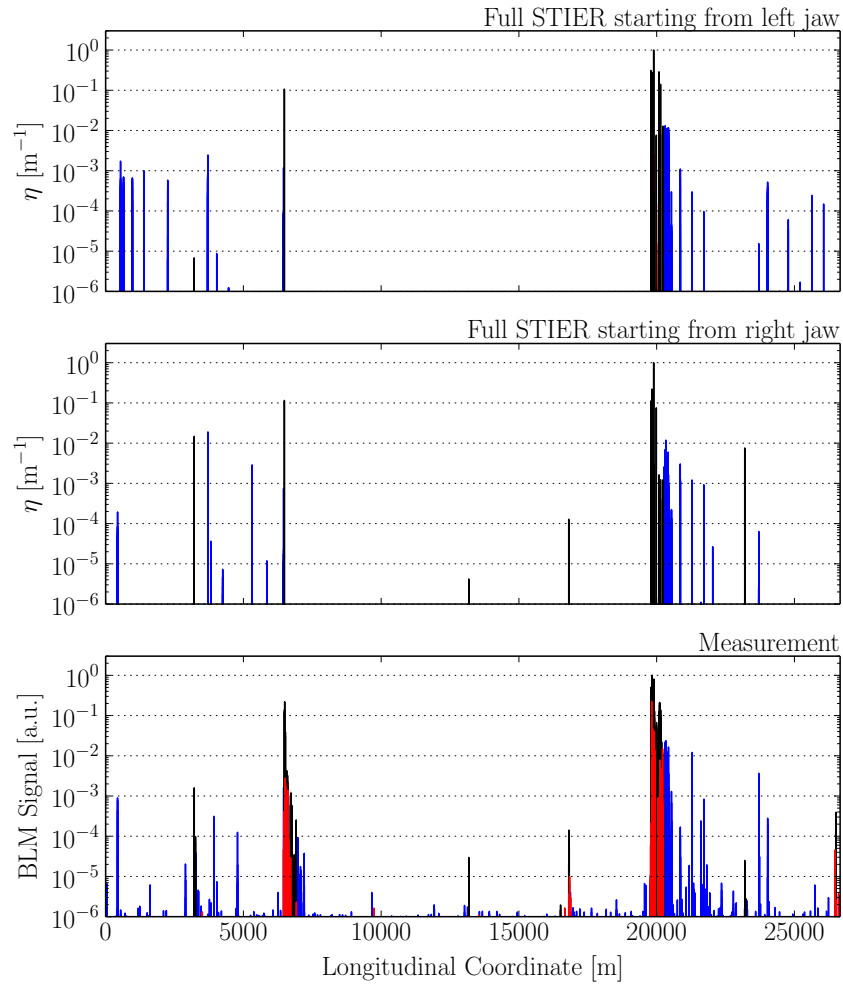


Figure 6.9: STIER simulations in the 2011 configuration with $^{208}\text{Pb}^{82+}$ beams at $3.5 Z \text{ TeV}$ starting at the left and right collimator jaw, shown in comparison to the measured loss map. The simulations are carried out considering an impact parameter of $3 \mu\text{m}$.

very hard to model accurately in simulations, as it depends on the interplay of a large number of machine imperfections that are not well known. In Fig. 6.9, the loss map is shown, as simulated with STIER with the same settings as above for particles starting at the left and right collimator jaw separately. A different behaviour of the losses can be expected because the betatronic motion and the dispersion can add or subtract, depending on the starting conditions of the ion. From the obtained loss maps it can be seen that the simulation result for the particles starting at the right collimator jaw is in much better agreement with the measured data than the simulation of particles starting at the left jaw. The largest fraction of the loss peaks between IR8 and IR1

as well as between IR1 and IR2 which are not observed in the measurement but visible in STIER come from particles starting at the left jaw. However, still one intense peak, visible in the simulation for the right jaw, is not observed in the measurement, which might come from aperture or orbit displacements as discussed above. In conclusion, the discrepancies of STIER in the regions far downstream of the TCP might come from both, asymmetric losses at the two collimator jaws and small beam displacements relative to the aperture.

6.3.3 Loss locations of individual isotopes

STIER allows the study of the distribution of losses for the individual isotopes. With the previous studies it became apparent that the measured loss pattern may be affected by light ion fragments not only in the warm regions just downstream of the collimators but also in the superconducting magnets. The STIER simulation result allows for the study of loss locations for any of the isotopes created in the TCP. In Fig. 6.10 the loss maps for five individual isotopes are compared. Note that the loss peaks are normalized with respect to the total number of ions of the respective species lost in the ring. The first plot shows the loss pattern for the isotope $^{207}\text{Pb}^{82+}$ with a rigidity offset $\delta_{\text{eff}} = 0.0048$. This isotope is generated via EMD with a relatively high cross section and has a small offset in rigidity compared to the main beam, hence it can travel in the machine over long distances. As expected, the losses are globally distributed, showing that the isotope is within the momentum acceptance of the arcs. The losses are mainly localized at collimators, few of them at the secondary collimators in IR7 and the dominating part at the TCP in IR3 and the TCTs in IR2 and IR8. It shall be shown later that for a different particle momentum and different optics, a significantly larger fraction of this isotope is lost at the TCT in IR2 (see Chap. 8.2).

The isotope $^{204}\text{Tl}^{81+}$ is the dominant species lost at the A1 loss peak with $\delta = 0.0072$. The global distribution for this isotope shows a defined peak at the horizontal TCT in IR8 and significant losses in superconducting magnets from IR7 to IR2. Again, the TCP in IR3 captures a large fraction of this isotope. These losses disappear if the rigidity offset is further increased to $\delta = 0.0097$ as it is visible in the loss pattern of the isotope $^{206}\text{Pb}^{82+}$. This isotope is generated via second order EMD or two sub-sequent first order EMD processes and dominates the losses in the DS2. Most of these ion fragments are lost at the TCSGs, in the IR7 DS magnets and in the arc region between IR7 and IR8. Their rigidity is too different from that of the main beam to reach IR3.

In the domain of more extreme rigidity offsets the losses are mostly localized in IR7 as shown for $^4\text{He}^{2+}$ and $^1\text{H}^{1+}$. Most of the prior isotope are lost in the IR7 collimators, with small fractions intercepted in the IR7 DS. All protons are lost in the IR7 collimation system, so they are not contributing to the losses in cold regions.

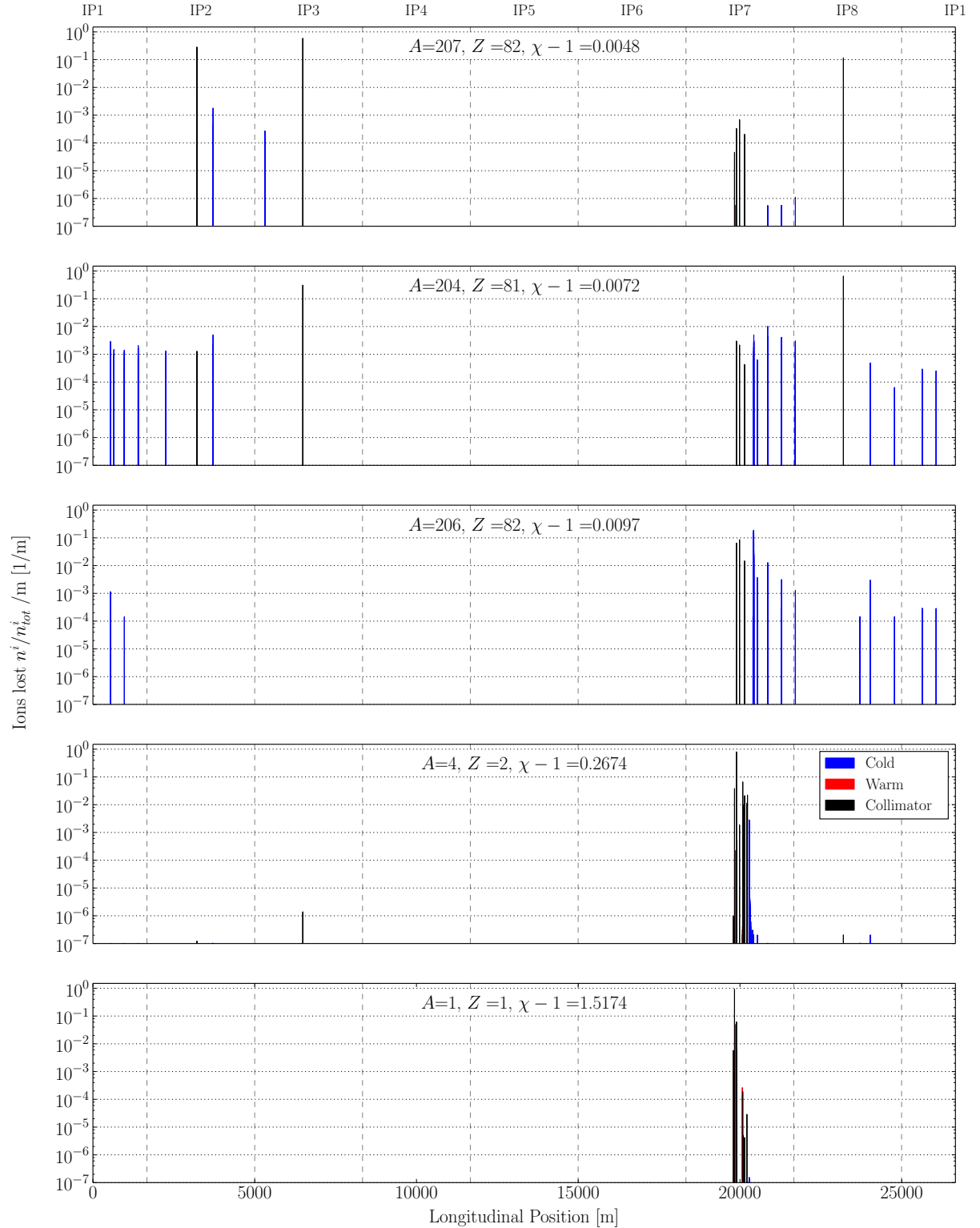


Figure 6.10: STIER simulated loss locations of the isotopes $^{207}\text{Pb}^{82+}$, $^{204}\text{Tl}^{81+}$, $^{206}\text{Pb}^{82+}$, $^4\text{He}^{2+}$, $^1\text{H}^{1+}$ (from top to bottom) in the 2011 heavy-ion configuration at $3.5 Z \text{ TeV}$. The vertical axis describes the number of ions n^i lost, normalized by the total number of ions n_{tot}^i of the species i .

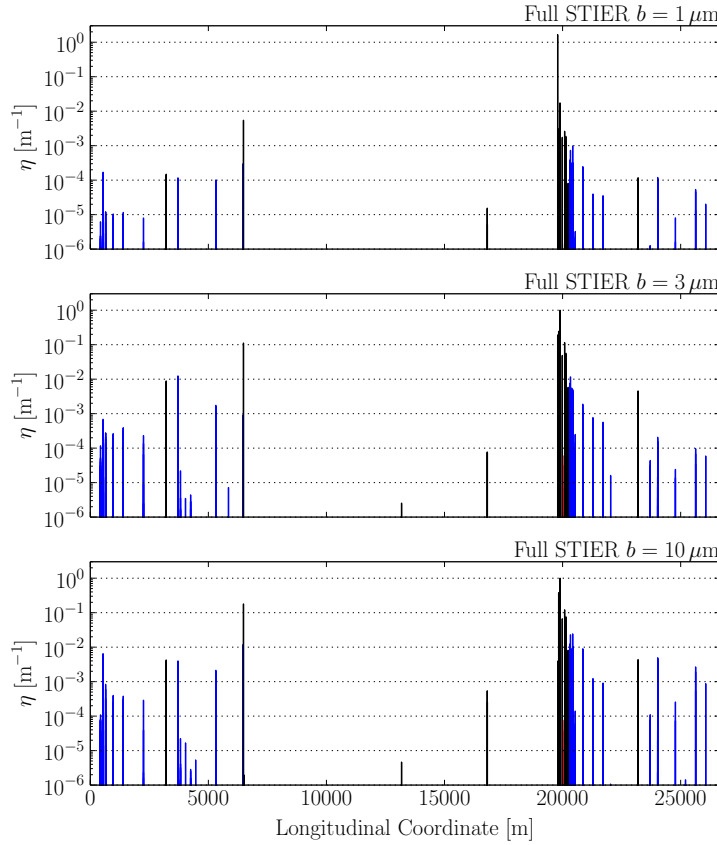


Figure 6.11: Ion loss maps as simulated with the full STIER approach for three different impact parameters $b = 1 \mu\text{m}$, $b = 3 \mu\text{m}$, $b = 10 \mu\text{m}$.

6.3.4 Dependence on the Impact Parameter

In the real machine, the impact parameter b of the ions hitting the collimators may vary. For the STIER simulations presented so far, an impact parameter of $3 \mu\text{m}$ was assumed, based on previous proton studies. With increasing impact parameter, the traversed distance of the heavy-ion beam inside the material increases, leading to a drastic change of the fragmentation rates into the different isotopes. In particular the production of very light ion fragments, such as protons, α -particles and neutrons increases, while the rate of surviving ions of the main beam drops significantly with increasing b . An overview of the energetic fraction carried by different out-coming isotopes after the ion-collimator interaction is given in Tab. ???. Note that the values are scaled with the ion mass, so the ion abundance is reduced by a factor of A with respect to the given values. With an impact parameter of $b = 3 \mu\text{m}$, the two most important isotopes are protons and α particles followed by $^{208}\text{Pb}^{82+}$ ions of the initial species.

The loss maps as simulated with STIER for the three different impact parameters are compared in Fig. 6.11. The loss patterns are qualitatively similar but the loss peak intensities differ quantitatively. For the smallest impact parameter, the highest losses occur at the primary collimator in IR7. The main contribution of these losses comes from $^{208}\text{Pb}^{82+}$ ions that were not fragmented but scattered at small angles in the TCP. They move inside the machine for one or multiple turns until they are intercepted by the global bottleneck, which is the primary collimator. In reality, however, these ions are again subject to fragmentation and scattering inside of the TCP, which is not considered in the presented simulation. The losses at the DS region peaks at $\eta = 10^{-3}$, which is smaller than in the other simulations, due to the large amount ions of the main beam surviving the initial passage through the TCP. The remaining losses in the aperture and the other collimators are located at elements which are also subject to losses for the other impact parameters, but the loss amplitudes are smaller. For the cases of $b = 3\ \mu\text{m}$ and $b = 10\ \mu\text{m}$ the highest losses are visible at the secondary collimator, which is consistent with the loss pattern measured during operation. Both simulated loss patterns are dominated by ion fragments instead of ions of the main beam. The losses in the DS clusters peak at $\eta = 10^{-2}$ for $b = 3\ \mu\text{m}$ and are larger by a factor of 3 for the case of $b = 10\ \mu\text{m}$. In the latter case, the production yield of effectively off-momentum isotopes is highest among the studied scenarios, which becomes apparent by the comparatively small amount of fragments captured by the collimation system.

We conclude that the impact parameter does seem to influence the cleaning inefficiency but not on the longitudinal distribution of the losses.

6.3.5 Loss Classification of Residual Heavy-Ion Fragments

- **Elastic scattering:** The particle rigidity is very close to the rigidity of the main beam. In the case of heavy ions, the particle species has not changed. The particle is scattered to larger transverse betatron amplitudes. If the transverse angular kick is sufficient, the particle is intercepted by the secondary collimators. Otherwise, they are intercepted by the TCP or a TCSG on a subsequent turn.
- **Inelastic interactions with small rigidity change:** Particles leaving the TCP with small momentum offsets and scattered at small angles continue moving through the magnetic lattice. Many of them are intercepted by the TCP in the momentum collimation region IR3, but - depending on their initial conditions - they can also be lost at other locations, such as TCT collimators. Typical rigidity offsets for such particles are in the order of 10^{-4} . An important example for such particles in $^{208}\text{Pb}^{82+}$ operation are $^{207}\text{Pb}^{82+}$ ions, which can continue to move in the machine for several km.

- **Inelastic interactions with large rigidity change:** Residual particles produced in nuclear interactions (single diffractive dissociation for protons and nuclear fragmentation or multiple EMD for heavy ions) can have rigidity offsets in the order of 10^{-3} or above. Depending on their initial conditions they may be beyond the momentum acceptance of the DS region in IR7 and therefore lost in these magnets. The losses from these particles compose the characteristic DS clusters in this region. The transverse momentum can partly compensate for the dispersive effect, such that the loss location for particles of the same rigidity may alter. In ICOSIM the latter effect was considered negligible, but in the studies presented in the following chapters it is demonstrated to have a considerable influence on the real loss distribution.
- **Inelastic interactions with extreme rigidity change:** Heavy-ion fragments with mass to charge ratios very different from the main beam (significantly above 10^{-1}) are subject to large dispersive offsets already after the passage of the normal conducting magnets in the straight section of IR7. Typically these ions are very light (protons, deuterium, tritium, ${}^4\text{He}^{2+}, \dots$) and have large transverse momenta compared to the main beam. In consequence, these particles are lost in IR7, partly in the secondary collimators, partly in the aperture of the normal conducting elements and the surrounding beam pipes.

6.4 Chromatic Tracking in ICOSIM and SixTrack

ICOSIM tracks off-momentum heavy ions by means of a matrix formalism with chromatic effects modelled in linear order. This approximation implies only small errors for small rigidity offsets,

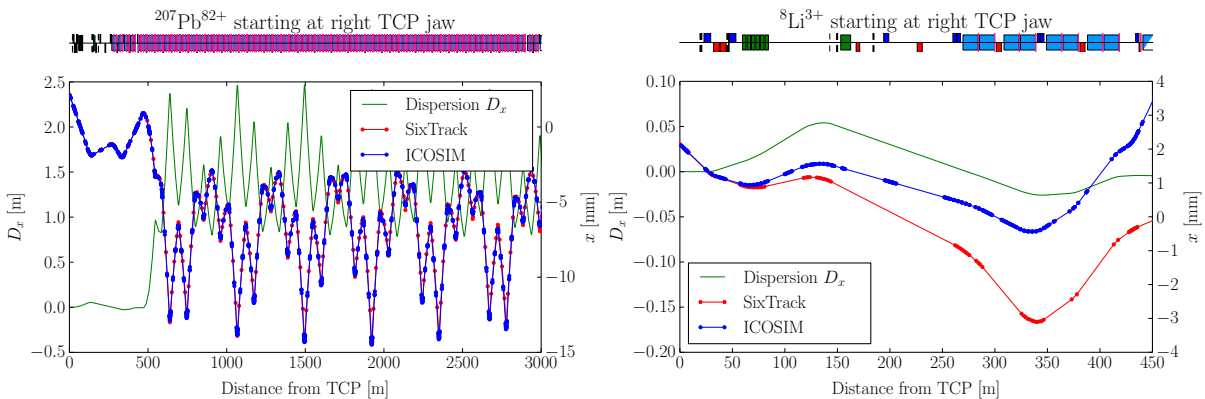


Figure 6.12: Comparison of the tracking behavior of ICOSIM and SixTrack for the two isotopes ${}^8\text{Li}^{3+}$ (left) and ${}^{207}\text{Pb}^{82+}$ (right) with identical starting conditions at the right jaw of the IR7 horizontal TCP. Note the different scales for the dispersion function and the computed horizontal position. The elements of the LHC beam line are shown on top of the graphs.

but becomes important when δ_{eff} increases. SixTrack on the other hand provides full symplectic tracking with magnetic multipole fields modelled up to 20th order.

To study the relevance of the chromatic modelling dedicated tracking simulations of the isotopes $^8\text{Li}^{3+}$ (with $\delta_{\text{eff}} = 0.054$) and $^{207}\text{Pb}^{82+}$ (with $\delta_{\text{eff}} = -0.005$) are carried out with identical optics and initial conditions in SixTrack and ICOSIM. Assuming that the chromatic modelling in SixTrack is superior to that of ICOSIM, this comparison allows to quantify the error implied by the linear truncation of the equation of motion in the ICOSIM implementation.

The simulations are launched at the edge of the right jaw of the TCP.C6L7.B1 with a starting angle identical to the angle of incidence at the collimator derived from the phase space parameters. The simulated tracks are compared in Fig. 6.12. For the isotope $^{207}\text{Pb}^{82+}$, the tracks simulated with SixTrack and ICOSIM are nearly identical. At a distance of 2 km from the TCP, the horizontal positions simulated with the two codes differ by $200 \mu\text{m}$, a small deviation compared to the orbit fluctuations in the machine. On the contrary, for the isotope $^8\text{Li}^{3+}$ the horizontal position differs by 3 mm already after a longitudinal distance of 450 m, demonstrating the drastic impact of the linear approximation on the simulated track for particles with large rigidity offsets. Thus, in spite of the fact that these ions are lost closely to the TCP, the error on the simulated track may cause a shift in their simulated loss position that could be of practical relevance for whatever reason. From the previous analysis of the loss locations for different isotopes it becomes apparent, that particles with rigidity offsets of which underlines their importance for the simulated loss pattern.

In conclusion, the accurate simulation of particles with large rigidity offsets requires to take into account higher order chromatic effects in the tracking routine.

6.5 Summary and Conclusions

The STIER simulation tool proved that the discrepancy between measured and simulated loss pattern can be traced back to the simplified fragmentation routine and that a significantly improved agreement can be achieved if the kicks in transverse momentum and kinetic energy are included in the simulation framework. Also the study of loss locations of light ion fragments not included in ICOSIM has shown that their loss locations may be in the regions of interest, in particular in the superconducting IR7 DS magnets. With the improved accuracy of cleaning simulations, STIER was used for many LHC studies, including operational preparation and the development of loss mitigation strategies, described in Chap. 8.

The comparison of the chromatic tracking in ICOSIM and SixTrack demonstrates that the purpose of accurate tracking of off-rigidity ions can be best served by SixTrack. A further improved simulation tool for heavy-ion collimation should therefore be based on SixTrack. The

development of a new version of SixTrack, adapted for the tracking of multi-isotopic heavy-ion beams is described in the next chapter.

7. Heavy-Ion SixTrack

Introduction

The previous study with the STIER simulation tool shows that SixTrack can serve the purpose of accurately tracking of multi-isotopic heavy-ion beams. However, in the STIER approach the different heavy-ions are tracked as protons. In order to keep track of the particle species, extensive pre- and post-processing is required.

Furthermore, the active coupling with a software for particle-matter interaction such as FLUKA requires to track the physical heavy-ions in SixTrack to allow for the exchange of information on the particle species. In this chapter, the implementation of the new heavy-ion SixTrack is described, including the derivation of symplectic tracking maps for multi-isotopic particle beams, the modification of the SixTrack tracking routine to account for the isotopic dispersion and the linking to the SixTrack-FLUKA active coupling to allow for fragmentation simulations at all collimators. The tracking and the fragmentation routine are individually benchmarked against STIER and the main version of FLUKA.

7.1 Requirements and Implementation Strategy

The following list summarizes the implementation tasks to be carried out in order to make heavy-ion SixTrack (hiSixTrack) operationable for heavy-ion collimation simulations.

- hiSixTrack must provide additional arrays storing information about the particle mass m , charge Z , and nuclear mass number A . In the present implementation it is assumed that the particle charge corresponds to the nuclear charge number (e.g. nuclei from which all electrons are removed). For the heavy-ion beams circulating in the LHC this is a valid assumption. If required, an adequate extension to define the particle charge differently than the nuclear charge number is fairly easy to implement.
- The reference species must be defined in a designated input option, preferably given in

the fort.3 file. Furthermore, the particle species of the initial bunch to be tracked must be read from an initial distribution file.

- The tracking maps must be modified to take into account the change of magnetic rigidity for different ions. Instead of using effective proton momenta as it was done for STIER, the tracking maps should be implemented such that the momentum of the tracked ion conforms to the physical momentum.
- The on-line coupling between SixTrack and FLUKA must be adapted to allow for the exchange of ions different than protons. The FLUKA input must be changed to take into account fragmentation processes by EMD, NF, and nuclear evaporation.
- The dump of particle losses must be changed to include information of the ions lost at the collimators and at the aperture. This will allow for studies of loss locations of individual isotopes and analysis of the isotopic composition of losses.

Even though collimation simulations are typically carried out for some hundreds of turns, other simulations of the particle behaviour in a high energy ring can require 10^6 turns or even more. The demand on hiSixTrack is thus above the typical requirements on a collimation simulation software for which it would suffice to have enough numeric precision for a tracking over 500 turns and without the need to include RF cavities. The software is therefore going enable the possibility for many different studies with heavy-ion beams.

7.2 Magnetic Tracking of Multiple Isotopes

The tracking maps for multi-isotopic particle beams can be derived from an appropriate Hamiltonian which incorporates information about the particle mass and charge with respect to the reference species. In this section, a consistent mathematical framework for the derivation of tracking maps is introduced based on a generalized Hamiltonian applicable for particles different from the reference species. The derivation of this Hamiltonian follows the same approach as for the mono-isotopic Hamiltonian, under consideration of the mathematical description of the magnetic rigidities treated in Chap. ???. Once derived, the multi-isotopic Hamiltonian is applied to vector potentials specific to the LHC beam line elements, to derive the corresponding tracking maps for multi-isotopic particle beams.

7.2.1 Hamiltonian Formalism of Particle Motion

A particle moving in the accelerator lattice has three degrees of freedom $i = 1, 2, 3$. The dynamical behaviour is thus described by a set of six coordinates, three of which being the generalized

position coordinates $\mathbf{q} = \{q_i\} = (x, y, z)$. In the studied scenario, the latter are identical to the coordinates of the reference frame previously defined in Chap. 2.1.1. The canonical conjugate is the generalized momentum $\mathbf{p} = (p_x, p_y, p_z)$. For convenience, the generalized velocities are defined as $\dot{\mathbf{q}} = (\dot{x}, \dot{y}, \dot{z})$, where $\dot{q}_i = \frac{dq_i}{dt}$ and the time t is the independent variable.

The temporal evolution of the particle coordinates during their motion in electromagnetic fields obeys Hamilton's equation of motion, so it can be described by the Hamiltonian formalism. In the Hamiltonian formulation of mechanics the motion of a particle with N degrees of freedom is described by the time evolution of a set of the $2N$ variables:

$$\mathbf{x} = (q_1, p_1, q_2, p_2, \dots, p_N, q_N)^T. \quad (7.1)$$

The longitudinal coordinate $s(t)$ is monotonically and smoothly raising in time, so that Hamilton's equations can also be expressed using s as the independent parameter [FLS65, Ree03]:

$$\frac{dq_k}{ds} = \frac{\partial H}{\partial p_k} \quad \frac{dp_k}{ds} = -\frac{\partial H}{\partial q_k} \quad k = 1, 2, \dots, N, \quad (7.2)$$

where q_k, p_k is the set of canonically conjugate variables corresponding to the degree of freedom k and $H = H(p_k, q_k, s)$ is the Hamiltonian with the independent variable s . Using the vector notation introduced in Eq. (7.1), Hamilton's equations can be expressed in a simple manner:

$$\frac{d\mathbf{x}}{ds} = \mathbf{S} \frac{\partial H}{\partial \mathbf{x}}, \quad \text{with} \quad \left(\frac{\partial H}{\partial \mathbf{x}} \right)_i = \frac{\partial H}{\partial x_i}. \quad (7.3)$$

where \mathbf{S} is a rearranging matrix, the so-called *symplectic matrix*:

$$\mathbf{S} = \begin{pmatrix} \mathbf{s} & \mathbf{0} & \cdots & \mathbf{0} \\ \mathbf{0} & \mathbf{s} & & \mathbf{0} \\ \vdots & & \ddots & \vdots \\ \mathbf{0} & \cdots & \mathbf{0} & \mathbf{s} \end{pmatrix}, \quad \text{with} \quad \mathbf{s} = \begin{pmatrix} 0 & 1 \\ -1 & 0 \end{pmatrix} \quad \text{and} \quad \mathbf{0} = \begin{pmatrix} 0 & 0 \\ 0 & 0 \end{pmatrix}. \quad (7.4)$$

The particular shape of this matrix is determined by the specific ordering used for \mathbf{x} and the representation of Hamilton's equations in Eq. (7.3) are referred to as their *symplectic form*. Frequently, the set of canonical variables is subject to transformations \mathcal{T} :

$$\mathcal{T}: \quad \mathbf{x} = (q_1, p_1, q_2, p_2, \dots, p_N, q_N)^T \quad \rightarrow \quad \mathbf{X} = (Q_1, P_1, Q_2, P_2, \dots, P_N, Q_N)^T. \quad (7.5)$$

The transformation is called canonical or symplectic if the new set of variables \mathbf{X} is also obeying

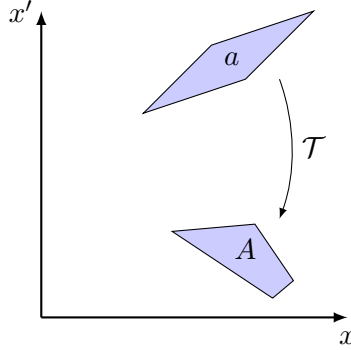


Figure 7.1: Illustration of symplecticity

Hamiltonian's equations with respect to a new Hamiltonian $\mathcal{K}(Q_k, P_k, s)$:

$$\frac{dQ_k}{ds} = \frac{\partial \mathcal{K}}{\partial P_k} \quad \frac{dP_k}{ds} = -\frac{\partial \mathcal{K}}{\partial Q_k} \quad k = 1, 2, \dots, N, \quad (7.6)$$

This new Hamiltonian can be derived through a generating function as described in detail in []. The Jacobian matrix \mathcal{J} of the transformation \mathcal{T} is defined by [RS95]

$$\mathcal{J}_{ij} = \left(\frac{\partial \mathbf{X}}{\partial \mathbf{x}} \right)_{i,j} = \frac{\partial X_i}{\partial x_j}, \quad i, j = 1, 2, \dots, N. \quad (7.7)$$

One can show, that a given transformation is symplectic (or canonical) if the Jacobian matrix obeys the *symplectic condition* [RS95]:

$$\mathcal{J}^T \mathbf{S} \mathcal{J} = \mathbf{S}. \quad (7.8)$$

Thus, the symplectic condition provides a tool for direct testing of the canonicity of a transformation or mapping. Symplecticity corresponds to a conservation of phase space volume throughout the transformation of a particle bunch [Wol14], as illustrated in Fig. 7.1 and in line with Liouville's theorem.

7.2.2 The Accelerator Hamiltonian for Multi-Isotopic Ion Beams

Prologue

Literature [Rip85, BRS87, RS95, HRS95, Wol14] has so far discussed the accelerator Hamiltonian and the resulting equations of motion in the mono-isotopic scenario, which is a valid approximation for pure proton, electron or positron beams, as well as for heavy-ion beams in

which only a small fraction of ions different from the reference species are present. In heavy-ion collimation studies with a large fraction of energy carried by isotopes of a particle species unmatched to the magnetic lattice, a more generic approach should be chosen.

The derivation of the generalized multi-isotopic accelerator Hamiltonian follows the same approach as the mono-isotopic derivation presented in [Pro95]. If not indicated differently, the basic definitions used below are taken from this reference. Fundamental differences are introduced with the normalization of the dynamic variables and the re-definition of δ to be in line with Eq. (2.13).

In the following derivation, the particle mass, charge and nuclear mass number of the tracked particle are given as $m, q = Z e, A$, while the equivalent quantities for the reference particle are given as m_0, q_0, A_0 . Eventual ambiguities between the particle charge q and canonical coordinate \mathbf{q} shall be ruled out by using the vector notation for the latter, or well q_i when referring to one particular coordinate.

Derivation of the Multi-Isotopic Hamiltonian

The generic Hamiltonian H is given by [BMW15]:

$$H(\mathbf{p}, \mathbf{q}, t) = p_i \dot{q}_i - \mathcal{L}(\mathbf{q}, \dot{\mathbf{q}}, t), \quad (7.9)$$

where \mathcal{L} is the Lagrangian of the particle. For an arbitrary particle of the species ${}^A X^{Z+}$ moving in an electromagnetic field defined by the magnetic vector potential \mathbf{A} and the electric (scalar) potential ϕ , the Lagrangian is given by

$$\mathcal{L}(\mathbf{q}, \dot{\mathbf{q}}, t) = -\frac{mc^2}{\gamma} - q\phi + q\dot{\mathbf{q}}\cdot\mathbf{A}. \quad (7.10)$$

The canonical momentum is then defined by Hamilton's variational principle:

$$p_i = \frac{\partial \mathcal{L}}{\partial \dot{q}_i} = m\dot{q}_i\gamma + qA_i. \quad (7.11)$$

Merging the Eqs. (7.9) and (7.10) yields for the Hamiltonian:

$$H(\mathbf{p}, \mathbf{q}, t) = \sqrt{(\mathbf{p} - q\mathbf{A})^2 + m^2c^4} + q\phi. \quad (7.12)$$

The Hamiltonian represents the total energy of the particle. It is advantageous to transform the independent variables from t to $s(t)$, which is valid because $s(t)$ is continuously increasing with t . The new dynamic variables can be obtained by comparing the action functional S before and after the transformation. Following the Euler-Lagrange equations, the temporal evolution of

the canonical coordinates is such that the action functional is minimized. The action functional is given by the expression:

$$S = \int_{t_0}^{t_1} \mathcal{L}(\mathbf{q}, \dot{\mathbf{q}}, t) dt. \quad (7.13)$$

With the relation defined in Eq. (7.9), the action functional yields:

$$S = \int_{t_0}^{t_1} (p_x \dot{x} + p_y \dot{y} + p_z \dot{z} - H) dt, \quad (7.14)$$

for the set of canonical coordinates

$$(x, p_x), (y, p_y), (z, p_z). \quad (7.15)$$

After the transformation of the independent variable $t \rightarrow s$, the action functional is given by

$$S = \int_{s_0}^{s_1} (p_x x' + p_y y' - H t' + p_z) ds, \quad (7.16)$$

where $q'_i = \frac{dq_i}{ds}$. The direct comparison of the original and the transformed action functional shows that the new set of canonical coordinates is given by

$$(x, p_x), (y, p_y), (-t, H), \quad (7.17)$$

with respect to the transformed Hamiltonian \tilde{H} :

$$\tilde{H} = -p_z. \quad (7.18)$$

Elementary transformations of Eq. (7.12) and taking into account that H represents the full ion energy E , the new Hamiltonian yields:

$$\tilde{H} = -p_z = -\sqrt{\frac{(E - q\phi)^2}{c^2} - m^2 c^2 - (p_x - qA_x)^2 - (p_y - qA_y)^2 - qA_z}. \quad (7.19)$$

The Hamiltonian should be expandable to allow for the analytical treatment of complex vector potentials. This requires the dynamic variables in the square root to be small, which can be

achieved with the following set of transformations:

$$\begin{aligned} p_i \rightarrow \tilde{p}_i &= \frac{p_i}{P_0} \frac{m_0}{m} & \tilde{H} \rightarrow \bar{H} &= \frac{\tilde{H}}{P_0} \frac{m_0}{m}, \\ qA_i \rightarrow \chi a_i &= \chi \frac{q_0 A_i}{P_0} & E \rightarrow \tilde{E} &= \frac{E}{P_0} \frac{m_0}{m}, \end{aligned} \quad (7.20)$$

Note that this is a different definition than usually given in literature [Pro95], and takes into account that the momentum of the tracked ion may be significantly different from the reference momentum. The chosen definition with the ratio of mass with respect to the mass of the reference particle takes into account for these difference and delivers small quantities even for a large spread of masses.

Expressed in terms of the new coordinates, and assuming that a gauge can be found such that $\phi = 0$, the transformed Hamiltonian is given by

$$\bar{H} = -\sqrt{\frac{m_0^2}{m^2} \left(\frac{E^2 - m^2 c^4}{P_0^2 c^2} \right) - (\tilde{p}_x - \chi a_x)^2 - (\tilde{p}_y - \chi a_y)^2 - \chi a_z}. \quad (7.21)$$

Using Eq. (??) and the relativistic energy-momentum relation the latter can be simplified to

$$\bar{H} = -\sqrt{(1 + \delta)^2 - (\tilde{p}_x - \chi a_x)^2 - (\tilde{p}_y - \chi a_y)^2 - \chi a_z}. \quad (7.22)$$

The longitudinal motion can be described in a more convenient manner by means of another transformation to new canonical variables:

$$(x, \tilde{p}_x), (y, \tilde{p}_y), (-t, \tilde{E}) \rightarrow (X, P_x), (Y, P_y), (\sigma, p_\sigma). \quad (7.23)$$

The transformation can be provided using the generating function of the second order

$$F_2 = xP_x + yP_y + (s - \beta_0 ct) \left(p_\sigma + \frac{E_0}{\beta_0 P_0 c} \right), \quad (7.24)$$

from which the transformed variables Q_i, P_i and the new Hamiltonian K follow from the following relations [Pro95]:

$$\tilde{p}_i = \frac{\partial F_2}{\partial q_i} \quad Q_i = \frac{\partial F_2}{\partial P_i} \quad K = \bar{H} + \frac{\partial F_2}{\partial z} = \bar{H} + p_\sigma. \quad (7.25)$$

The transformed coordinates are then related to the initial coordinates as

$$X = x, \quad Y = y, \quad \sigma = s - \beta_0 c t, \quad (7.26)$$

$$P_x = \tilde{p}_x, \quad P_y = \tilde{p}_y, \quad p_\sigma = \frac{\frac{m_0}{m} E - E_0}{\beta_0 P_0 c}. \quad (7.27)$$

with the new Hamiltonian

$$K = p_\sigma - \sqrt{(1 + \delta)^2 - (P_x - \chi a_x)^2 - (P_y - \chi a_y)^2} - \chi a_z. \quad (7.28)$$

The new longitudinal coordinate σ with the canonical conjugate p_σ describes the difference in arrival time with respect to the reference particle. After a last transformation for convenience: $P_i \rightarrow p_i$, $K \rightarrow H$, the final generic accelerator Hamiltonian is written as

$$H = p_\sigma - \sqrt{(1 + \delta)^2 - (p_x - \chi a_x)^2 - (p_y - \chi a_y)^2} - \chi a_z. \quad (7.29)$$

In the general case of a curved coordinate system, the Hamiltonian changes to [F+13]

$$H = p_\sigma - (1 + h_x(s) x) \left(\sqrt{(1 + \delta)^2 - (p_x - \chi a_x(s))^2 - (p_y - \chi a_y(s))^2} + \chi a_s(s) \right), \quad (7.30)$$

where $h_x(s) = \frac{1}{\rho(s)}$ is the radius of curvature of the particle trajectory. The longitudinal magnetic vector potential with respect to s is defined by the following relation:

$$p_s = \frac{m_0 \gamma \dot{s}}{P_0} (1 + h_x x)^2 + q(1 + h_x x) \chi a_s. \quad (7.31)$$

For the case of a straight coordinate system with $h_x = 0$, the quantity p_s is identical to p_z . In the mono-isotopic limit of $m \rightarrow m_0$ and $q \rightarrow q_0$, all derived equations converge into the standard expressions derived from the mono-isotopic Hamiltonian [RS95].

Expansion

The Hamiltonian presented in Eq. (7.30) is exact, thus without the usage of approximations. Depending on the complexity of the electromagnetic field of the beam-line element and the corresponding boundary conditions it can be useful to expand the square root in $\frac{(p_x - \chi a_x)^2 + (p_y - \chi a_y)^2}{(1 + \delta)^2}$. By virtue of the normalization applied in Eq. (7.20), this is a small quantity, such that the

second order Taylor expansion delivers a good approximation of the physical problem:

$$H \approx p_\sigma - (1 + h_x(s)x) \left[(1 + \delta) \left(1 - \frac{1}{2} \frac{(p_x - \chi a_x(s))^2 + (p_y - \chi a_y(s))^2}{(1 + \delta)^2} \right) + \chi a_s(s) \right]. \quad (7.32)$$

The accuracy of tracking maps derived from the expanded Hamiltonian is studied for the example of the drift space in [F⁺13].

7.3 Tracking Maps for Beam-Line Elements

Based on the Hamiltonian for multi-isotopic particle beams, in this chapter the tracking maps for the individual beam line elements are derived. The technical implemenetation of the individual maps into hiSixTrack is presented in Chap. A.5.4. Their symplecticity is demonstrated by means of the Jacobian matrix in Chap. A.1.

7.3.1 Drift Space

Exact Hamiltonian

A drift space is defined by the absence of electromagnetic fields, thus the vector potential is zero in all directions. With regard to Eq. (7.30), the Hamiltonian is then given by

$$H = p_\sigma - \sqrt{(1 + \delta)^2 - p_x^2 - p_y^2} = p_\sigma - p_z. \quad (7.33)$$

The equations of motion derived from this Hamiltonian are

$$x' = \frac{dx}{dz} = \frac{\partial H}{\partial p_x} = \frac{p_x}{\sqrt{(1 + \delta)^2 - p_x^2 - p_y^2}} = \frac{p_x}{p_z} \quad p'_x = -\frac{\partial H}{\partial x} = 0, \quad (7.34)$$

$$y' = \frac{dy}{dz} = \frac{\partial H}{\partial p_y} = \frac{p_y}{\sqrt{(1 + \delta)^2 - p_x^2 - p_y^2}} = \frac{p_y}{p_z} \quad p'_y = -\frac{\partial H}{\partial y} = 0, \quad (7.35)$$

$$\sigma' = \frac{d\sigma}{dz} = \frac{\partial H}{\partial p_\sigma} = \left(1 - \frac{\beta_0}{\beta_z} \right) \quad p'_\sigma = -\frac{\partial H}{\partial \sigma} = 0, \quad (7.36)$$

where β_z is defined as

$$\beta_z = \beta \frac{p_z}{1 + \delta}. \quad (7.37)$$

Starting from the equations of motion, the transformation of the initial set of coordinates $(\mathbf{q}^I, \mathbf{p}^I)$ at the beginning of the drift space is related to their final coordinates $(\mathbf{q}^F, \mathbf{p}^F)$ by the following set of equations, referred to as the transfer map:

$$x^F = x^I + x^I L \quad p_x^F = p_x^I, \quad (7.38)$$

$$y^F = y^I + y^I L \quad p_y^F = p_y^I, \quad (7.39)$$

$$\sigma^F = \sigma^I + \left(1 - \frac{\beta_0}{\beta_z}\right) L \quad p_\sigma^F = p_\sigma^I, \quad (7.40)$$

where, L denotes the length of the drift space.

Expanded Hamiltonian

Combining Eq. (7.32) and Eq. (7.33) yields for the expanded Hamiltonian

$$H \approx p_\sigma - \delta + \frac{1}{2} \frac{p_x^2 + p_y^2}{(1 + \delta)}. \quad (7.41)$$

Hamilton's equations of motion are

$$x' = \frac{dx}{dz} = \frac{\partial H}{\partial p_x} = \frac{p_x}{(1 + \delta)} \quad p'_x = -\frac{\partial H}{\partial x} = 0, \quad (7.42)$$

$$y' = \frac{dy}{dz} = \frac{\partial H}{\partial p_y} = \frac{p_y}{(1 + \delta)} \quad p'_y = -\frac{\partial H}{\partial y} = 0, \quad (7.43)$$

$$\sigma' = \frac{d\sigma}{dz} = \frac{\partial H}{\partial p_\sigma} = 1 - \frac{\beta_0}{\beta} \left(1 + \frac{1}{2} \frac{p_x^2 + p_y^2}{(1 + \delta)^2}\right) \quad p'_\sigma = -\frac{\partial H}{\partial \sigma} = 0, \quad (7.44)$$

Note the different definition of x' with respect to the exact Hamiltonian. The resulting tracking map for the drift space from the expanded Hamiltonian yields:

$$x^F = x^I + \frac{p_x^I}{1 + \delta} L \quad p_x^F = p_x^I, \quad (7.45)$$

$$y^F = y^I + \frac{p_y^I}{1 + \delta} L \quad p_y^F = p_y^I, \quad (7.46)$$

$$\sigma^F = \sigma^I - L \frac{\beta_0}{\beta} \left(1 + \frac{1}{2} \frac{(p_x^I)^2 + (p_y^I)^2}{(1 + \delta)^2}\right) \quad p_\sigma^F = p_\sigma^I. \quad (7.47)$$

The comparison of x' for the expanded and the exact drift space unveils that they agree in the limit of small p_x and p_y . A detailed analysis is presented in [F+13]. Since 2013, the exact Hamiltonian is implemented in SixTrack.

The modification of tracking maps for the drift space is not necessary for hiSixTrack, because the key quantity β_0/β is defined in SixTrack as follows:

$$\frac{\beta_0}{\beta} = \frac{E}{pc} \frac{p_0 c}{E}, \quad (7.48)$$

which is also applicable for multi-isotopic heavy-ion beams.

7.3.2 Dipole

For simplicity, parts of the following derivations are only considered for a horizontal bending, but they are also valid for vertical bendings by permuting x and y . The uniform magnetic field in a horizontal bending dipole can be described by the vector potential [Wol14]

$$A_x = 0, \quad A_y = 0, \quad A_s = -B_y x \left(1 - \frac{h_x x}{2(1 + h_x x)} \right). \quad (7.49)$$

Ideally, the vertical magnetic field B_y is matched to the reference momentum and charge such that the bending radius of the reference particle yields $\rho_0 = h_x^{-1}$. In reality, the magnet strength may differ from the reference, such that the ideal particle is bent with the radius $\rho^i = k_0^{-1}$ and

$$B_y = \frac{P_0 k_0}{q_0}. \quad (7.50)$$

The resulting exact Hamiltonian is then given by

$$H = p_\sigma - (1 + h_x x) p_z + \chi k_0 \left(x + \frac{h_x x^2}{2} \right), \quad (7.51)$$

with

$$p_z = \sqrt{(1 + \delta)^2 - (p_x - \chi a_x)^2 - (p_y - \chi a_y)^2}. \quad (7.52)$$

Omitting non-linear and constant terms delivers for the expanded Hamiltonian

$$H \approx p_\sigma - \delta - (h_x x)(1 + \delta) + \frac{1}{2} \frac{p_x^2 + p_y^2}{(1 + \delta)} + \chi k_0 \left(x + \frac{h_x x^2}{2} \right). \quad (7.53)$$

Thick Dipole

With the expanded Hamiltonian and considering that δ is a function of p_σ with the derivative $\frac{d\delta}{dp_\sigma} = \frac{\beta_0}{\beta}$, the equations of motion become

$$x' = \frac{\partial H}{\partial p_x} = \frac{p_x}{1 + \delta} \quad p'_x = -\frac{\partial H}{\partial x} = h_x (1 + \delta) - \chi k_0 (1 + h_x x), \quad (7.54)$$

$$y' = \frac{\partial H}{\partial p_y} = \frac{p_y}{1 + \delta} \quad p'_y = -\frac{\partial H}{\partial y} = 0, \quad (7.55)$$

$$\sigma' = \frac{\partial H}{\partial p_\sigma} = 1 - \frac{\beta_0}{\beta} \left(1 + h_x x + \frac{1}{2} \frac{p_x^2 + p_y^2}{(1 + \delta)^2} \right) \quad p'_\sigma = -\frac{\partial H}{\partial \sigma} = 0. \quad (7.56)$$

In the vertical direction, the dipole acts like a drift space in the vertical direction where no bending force is present.

Starting from Eq. (7.54), the horizontal motion can be described by the differential equation

$$x''(s) + \frac{\chi h_x k_0}{(1 + \delta)} x = \frac{h_x \delta}{(1 + \delta)} + \frac{h_x - \chi k_0}{(1 + \delta)}. \quad (7.57)$$

The homogenous part of the equation describes an oscillation with frequency $\omega_x = \sqrt{\frac{\chi h_x k_0}{1 + \delta}}$. Note that the inhomogeneous part of the differential equation Eq. (7.57) represents the dispersion in the magnet. Compared to the corresponding mono-isotopic equation presented in [HRS95], an additional term proportional to $(\chi - 1)$ appears, which takes account for the isotopic dispersion. For particles of the reference species this term vanishes.

The following quantities are defined for convenience:

$$S_x = \sin \omega_x L \quad C_x = \cos \omega_x L \quad (7.58)$$

$$\omega_x^2 = \frac{\chi h_x k_0}{1 + \delta} \quad \Omega_x = \frac{1 + \delta}{k_0 \chi} - \frac{1}{h_x}. \quad (7.59)$$

The transfer map is then given by

$$x^F = x^I C_x + p_x^I \omega_x^{-1} \frac{S_x}{(1+\delta)} + \Omega_x (1 - C_x) , \quad (7.60)$$

$$p_x^F = -x^I \omega_x (1+\delta) S_x + p_x^I C_x + (1+\delta) \Omega_x \omega_x S_x , \quad (7.61)$$

$$y^F = y^I + (y')^I L , \quad (7.62)$$

$$p_y^F = p_y^I . \quad (7.63)$$

$$\sigma^F = \sigma^I + L \left[1 - \frac{\beta_0}{\beta} - \frac{\beta_0}{\beta} \frac{1}{2} \left(\frac{p_y^I}{1+\delta} \right)^2 \right] - \quad (7.64)$$

$$\frac{\beta_0}{\beta} \left[\frac{S_x}{\omega_x} (x^I - \Omega_x) + \frac{p_x^I (1 - C_x)}{(1+\delta) \omega_x^2} + L \Omega_x \right] - \quad (7.65)$$

$$\frac{1}{8} \frac{\beta_0}{\beta} \frac{1}{(1+\delta)^2} \left[-2 p_x^I (1+\delta) (x^I - \Omega_x) + \right. \quad (7.66)$$

$$2 L \left((p_x^I)^2 + (1+\delta)^2 \omega_x^2 (x^I - \Omega_x)^2 \right) + \quad (7.67)$$

$$2 p_x^I (1+\delta) (x^I - \Omega_x) \cos(2 \omega_x L) +$$

$$\left. \frac{\sin(2 \omega_x L)}{\omega_x} \left((p_x^I)^2 - (1+\delta)^2 \omega_x^2 (x^I - \Omega_x)^2 \right) \right] \quad (7.68)$$

$$p_\sigma^F = p_\sigma^I . \quad (7.69)$$

Thin Dipole

Thick lens tracking is very demanding in terms of time and computing power. Also, the exact motion of the particle inside the magnet is often not required and the global tracking through a large accelerator like the LHC can be well approximated by thin lenses. The tracking routine used in SixTrack for collimation studies is based on thin lens tracking, so the derivation of thin lens tracking maps is of particular interest.

The Hamiltonian in Eq. (7.53) can be decomposed into the expanded Hamiltonian of a drift H_D , defined in Eq. (7.41), and the contribution from electromagnetic fields H_L as follows:

$$H = H_D - h_x x (1+\delta) + \chi k_0 \left(x + \frac{h_x x^2}{2} \right) = H_D + H_L . \quad (7.70)$$

In the thin lens approximation, this Hamiltonian is changed to [HRS95]:

$$H = H_D + \bar{\delta}(s - s_0) L H_L , \quad (7.71)$$

where $\bar{\delta}(s - s_0)$ is the δ distribution which is non-zero only at the center s_0 of the magnet [Dir58]. Starting from this Hamiltonian, the equations of motion are given by:

$$x' = \frac{p_x}{(1 + \delta)}, \quad (7.72)$$

$$p'_x = L \bar{\delta}(s - s_0) [h_x(1 + \delta) - \chi k_0 (1 + h_x x)], \quad (7.73)$$

$$y' = \frac{p_y}{(1 + \delta)}, \quad (7.74)$$

$$p'_y = 0, \quad (7.75)$$

$$\sigma' = 1 - \frac{\beta_0}{\beta} - \frac{\beta_0}{\beta} \left[\frac{1}{2} (x'^2 + y'^2) \right] - \frac{\beta_0}{\beta} h_x x (1 + \delta) \bar{\delta}(s - s_0) L, \quad (7.76)$$

$$p'_\sigma = 0. \quad (7.77)$$

The solution of the differential equations in the thin lens approximation are obtained by integrating from $s - \epsilon$ to $s + \epsilon$ in the limit of $\epsilon \rightarrow 0$. The tracking map for x with the equation of motion given in Eq. (7.72) is obtained as follows:

$$x^F - x^I = \lim_{\epsilon \rightarrow 0} \left[\int_{s_0 - \epsilon}^{s_0 + \epsilon} \frac{p_x}{(1 + \delta)} ds \right] = 0. \quad (7.78)$$

Applying the same approach for the remaining quantities, the transformation rules for the dipole in thin lens approximation are given by:

$$x^F = x^I, \quad (7.79)$$

$$p_x^F = p_x^I + L [h_x (1 + \delta) - k_0 \chi (1 + h_x x^I)], \quad (7.80)$$

$$y^F = y^I, \quad (7.81)$$

$$p_y^F = p_y^I, \quad (7.82)$$

$$\sigma^F = \sigma^I - \frac{\beta_0}{\beta} h_x x^I L, \quad (7.83)$$

$$p_\sigma^F = p_\sigma^I. \quad (7.84)$$

The transverse kick depends on the initial horizontal offset x^I , which is known as weak focusing [Wol14]. Two particles with the same set of χ and δ are bent differently in the same magnet when they have two different initial offsets x_1, x_2 , as illustrated in Fig. 7.2. Weak focusing refers to the effect that the trajectories of two particles starting at different positions are focussed to a defined focal point.

The effect of dispersion is taken into account by the dependence on δ and χ . The chromatic dispersion, which is a pure function of the particle velocity, and the isotopic dispersion which

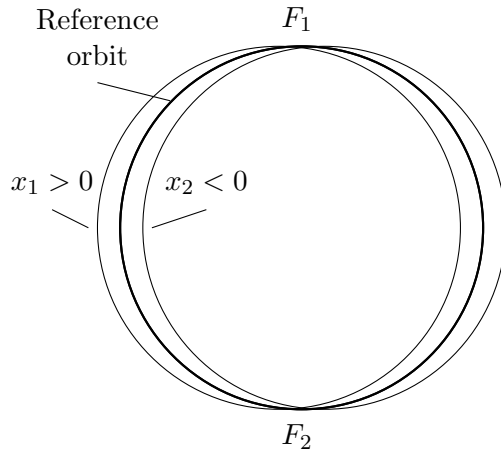


Figure 7.2: Weak focusing in a transverse magnetic dipole field. Two particles starting with different initial offsets x_1 and x_2 are focused to two distinct focal points F_1 and F_2 .

only depends on the mass to charge ratio are independent effects which can compensate or enhance each other. In the mono-isotopic case $\chi \rightarrow 1$, and with perfectly matched magnetic field $k_0 = h_x$, the Eq. (7.87) yields the well known shape (see [RS95])

$$p_x^F = p_x^I + \delta h_x L - h_x^2 L x^I. \quad (7.85)$$

7.3.3 Thin Transverse Kicker Magnet

Transverse kicker magnets are used in accelerators as the LHC to control the beam orbit. Technically they are identical to bending magnets, with the exception that $h_x = 0$, so the reference trajectory in these magnets is not bent. The Hamiltonian for a transverse kicker magnet in thin

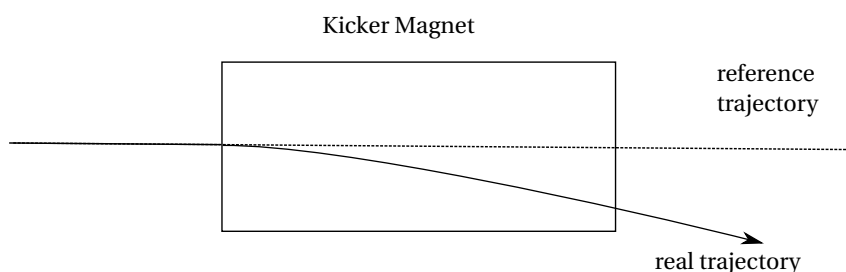


Figure 7.3: Schematics of a transverse kicker magnet. Kicker magnets are dipole magnets with unbent reference trajectory, thus $h_x = 0$.

lens approximation is given by:

$$H = H_D + \chi k_0 L \bar{\delta}(s - s_0). \quad (7.86)$$

The resulting equations of motion lead to the following transport map:

$$p_x^F = p_x^I - k_0 \chi L, \quad (7.87)$$

$$p_y^F = p_y^I, \quad (7.88)$$

$$p_\sigma^F = p_\sigma^I. \quad (7.89)$$

7.3.4 Quadrupole

The vector potential of a quadrupole magnet is given by [RS95]:

$$A_x = 0 \quad A_y = 0 \quad A_s = -\frac{1}{2} g (y^2 - x^2). \quad (7.90)$$

Expressed in the normalized coordinates, the longitudinal vector potential becomes

$$a_s = -\frac{1}{2} \frac{q_0}{P_0} g (y^2 - x^2) = -\frac{1}{2} k (y^2 - x^2). \quad (7.91)$$

The quantity $k = \frac{q_0}{P_0} g$ is the normalized quadrupole gradient which has the unit $[k] = \text{m}^{-2}$. The optics of a machine in a certain configuration is defined by a full set of k_i with $i = 1, \dots, N_q$, where N_q is the number of quadrupoles in the machine. Thanks to the definition of the normalized quadrupole strength, the machine optics can be described by identical values valid for different energies, even if in reality the magnet currents are ramped with increasing beam energy.

The reference trajectory passes through the center of the quadrupole where no magnetic field is present and is hence straight with $h_x = 0$. The exact Hamiltonian of a quadrupole yields

$$H = p_\sigma - \sqrt{(1 + \delta)^2 - p_x^2 - p_y^2} + \frac{1}{2} k \chi (x^2 - y^2). \quad (7.92)$$

Thick quadrupole

For the solution of the equations of motion, the following quantities are defined:

$$K = k \chi, \quad \omega^2 = |K|. \quad (7.93)$$

The expanded Hamiltonian for the quadrupole is then given by

$$H = p_\sigma + \frac{1}{2} \frac{p_x^2 + p_y^2}{(1 + \delta)} + \frac{1}{2} K (x^2 - y^2) - \delta. \quad (7.94)$$

Hamilton's equations deliver the following equations of motion

$$x' = \frac{\partial H}{\partial p_x} = \frac{p_x}{(1 + \delta)} \quad p'_x = -\frac{\partial H}{\partial x} = -Kx, \quad (7.95)$$

$$y' = \frac{\partial H}{\partial p_y} = \frac{p_y}{(1 + \delta)} \quad p'_y = -\frac{\partial H}{\partial y} = Ky, \quad (7.96)$$

$$\sigma' = \frac{\partial H}{\partial p_\sigma} = 1 - \frac{\beta_0}{\beta} \left[1 + \frac{1}{2} \frac{p_x^2 + p_y^2}{(1 + \delta)^2} \right] \quad p'_\sigma = -\frac{\partial H}{\partial \sigma} = 0. \quad (7.97)$$

Using these relations, the transverse motion can be described by two differential equations of the same type

$$x'' + \frac{K}{1 + \delta} x = 0, \quad (7.98)$$

$$y'' - \frac{K}{1 + \delta} y = 0. \quad (7.99)$$

This is the well-known Hill equation. The transverse transport map is the general solution of the two differential equations

$$x^F = C_x x^I + S_x \frac{p_x^I}{(1 + \delta)} \quad p_x^F = C_x p_x^I - S_x \omega^2 x^I (1 + \delta), \quad (7.100)$$

$$y^F = C_y y^I + S_y \frac{p_y^I}{(1 + \delta)} \quad p_y^F = C_y p_y^I + S_y \omega^2 y^I (1 + \delta), \quad (7.101)$$

The quantities C_u and S_u are defined as follows:

$$C_x = \begin{cases} \cos(\omega L) & \text{if } K > 0 \\ \cosh(\omega L) & \text{if } K < 0 \end{cases} \quad S_x = \begin{cases} \omega^{-1} \sin(\omega L) & \text{if } K > 0 \\ \omega^{-1} \sinh(\omega L) & \text{if } K < 0 \end{cases}, \quad (7.102)$$

$$C_y = \begin{cases} \cosh(\omega L) & \text{if } K > 0 \\ \cos(\omega L) & \text{if } K < 0 \end{cases} \quad S_y = \begin{cases} \omega^{-1} \sinh(\omega L) & \text{if } K > 0 \\ \omega^{-1} \sin(\omega L) & \text{if } K < 0 \end{cases}, \quad (7.103)$$

Thin Lens Approximation

Following the Eqs. (7.71) and (7.94), the following Hamiltonian can be derived for the quadrupole in thin lens approximation:

$$H = H_D + \frac{1}{2} \bar{\delta}(s - s_0) L K (x^2 - y^2). \quad (7.104)$$

The corresponding transfer map becomes:

$$x^F = x^I, \quad p_x^F = p_x^I - KL x^I, \quad (7.105)$$

$$y^F = y^I, \quad p_y^F = p_y^I + KL y^I, \quad (7.106)$$

$$\sigma^F = \sigma^I, \quad p_\sigma^F = p_\sigma^I. \quad (7.107)$$

This transfer map corresponds to a focusing lens in horizontal and a defocusing lens in vertical direction. Compared to the transverse kick $\Delta p_x = -k L x^I$ of the reference isotope, the kick for arbitrary ions scales linearly with χ :

$$\Delta p_x = -\chi k L x^I. \quad (7.108)$$

The focal length for the different isotopes varies with χ , in line with the expectation.

7.3.5 Thin Multipole

Higher order magnetic fields than the presented dipole and quadrupole fields are described in a more generic way:

$$B_y + iB_x = \sum_{n=1}^{\infty} (b_n + ia_n) \left(\frac{x + iy}{\rho_0} \right)^{n-1}. \quad (7.109)$$

In this context, n the multipole order, b_n, a_n are the multipole coefficients which describe the field orientation for the contribution of each multipole order [Wol12] and the quantity ρ_0 is a reference radius. The well-known dipole and quadrupole fields described in the previous chapters correspond to the multipole orders $n_D = 1$ and $n_Q = 2$. In a perfect multipole of the order n , all multipole coefficients $m \neq 0$ yield zero.

The magnetic field described in Eq. (7.109) corresponds to the following vector potential:

$$A_x = 0, \quad A_y = 0, \quad A_z = -\text{Re} \sum_{n=1}^{\infty} (b_n + ia_n) \frac{(x + iy)^n}{n \rho_0^{n-1}}. \quad (7.110)$$

Inserting this vector potential the Hamiltonian in thin lens approximation yields

$$H = H_D - \frac{q_0}{P_0} \chi L \bar{\delta}(s - s_0) \operatorname{Re} \left[\sum_{n=1}^{\infty} (b_n + i a_n) \frac{(x + iy)^n}{n \rho_0^{n-1}} \right] \quad (7.111)$$

The resulting tracking map for the thin multipole is:

$$x^F = x^I, \quad p_x^F = p_x^I - \chi L \operatorname{Re} \left[\sum_{n=1}^{\infty} (k_n + i \hat{k}_n) (x + iy)^{n-1} \right] \quad (7.112)$$

$$y^F = y^I, \quad p_y^F = p_y^I - \chi L \operatorname{Re} \left[\sum_{n=1}^{\infty} i(k_n + i \hat{k}_n) (x + iy)^{n-1} \right] \quad (7.113)$$

$$\sigma^F = \sigma^I, \quad p_{\sigma}^F \rightarrow p_{\sigma}^I, \quad (7.114)$$

where k_n and \hat{k}_n are defined as:

$$k_n = \frac{q_0}{P_0} \frac{a_n}{\rho_0^{n-1}} \quad \text{and} \quad \hat{k}_n = \frac{q_0}{P_0} \frac{b_n}{\rho_0^{n-1}}. \quad (7.115)$$

7.3.6 Accelerating RF Cavity

The energy gain ΔE a particle receives at the position s inside an accelerating cavity operated at frequency f and wave number $k = \frac{\omega}{c} = 2\pi f$ can be approximated by:

$$\Delta E = qV(s) \sin \left(k \frac{\sigma}{\beta_0} + \phi \right). \quad (7.116)$$

Where $V(s)$ is the longitudinal electric field acting on the particle at the position s . The dependence of V on s complicates the solution of the equations of motion and is therefore not explicitly considered in the magnetic vector potential. Rather, the electric field is averaged over the length of the cavity which is summarized in the mean electric field U [Wol14]:

$$U = \frac{1}{L} \int_{-L/2}^{L/2} V(s) ds. \quad (7.117)$$

This approximation leads to the following vector potential for a cavity [RS95]:

$$A_x = A_y = 0 \quad A_s = \frac{U}{\omega} \cos \left(k \frac{\sigma}{\beta_0} + \phi \right). \quad (7.118)$$

The resulting expanded Hamiltonian for a thin cavity is then given by:

$$H = H_D + \chi \frac{q_0}{P_0} \frac{U}{\omega} \cos \left(k \frac{\sigma}{\beta_0} + \phi \right) L \bar{\delta}(s - s_0). \quad (7.119)$$

Using the substitution $\tilde{U} = \frac{q_0}{P_0} U$, the transfer map can be deduced as:

$$x^F = x^I, \quad p_x^F = p_x^I \quad (7.120)$$

$$y^F = y^I, \quad p_y^F = p_y^I \quad (7.121)$$

$$\sigma^F = \sigma^I, \quad p_\sigma^F \rightarrow p_\sigma^I + \chi U_n \frac{1}{\beta_0} \sin \left(k \frac{\sigma^I}{\beta_0} + \phi \right). \quad (7.122)$$

The change in p_σ is, as expected, proportional to $q \frac{m_0}{m}$.

7.4 Multi-Isotope Tracking in hiSixTrack

Based on the presented tracking maps derived from the generic Hamiltonian, the proton tracking software SixTrack is made compatible with multi-isotope tracking. Contrary to the STIER approach, hiSixTrack is developed with the aim to track the heavy-ions as the physical particles instead of tracking protons with rigidities corresponding to the different ions. Essential physics parameters are therefore modified in hiSixTrack, as described in the following. However, as demonstrated above, these parameters converge to their mono-isotopic counterpart if the tracked particle is identical to the reference particle.

The new implementation hiSixTrack is similar to use as the standard SixTrack-FLUKA coupling with minor changes required for the simulation set up. In this section, the changes introduced in hiSixTrack are discussed qualitatively while a more detailed technical overview of the implementation is given in the Appendix.

7.4.1 Multi-Isotope Tracking

To allow for the tracking of multiple different isotopes, additional arrays containing information about the particle mass, charge number and nucleon number are implemented in hiSixTrack. For the definition of the reference ion species, a dedicated block is introduced in the `fort.3` file. In this block the nuclear charge number, mass number and physical particle mass (in GeV/c^2) is given by the user. Combining this information allows for the definition of χ of each particle, which is also stored in a dedicated array.

The definition of δ is changed to obey the multi-isotopic definition given in Eq. (2.13):

$$\delta = \frac{P - P_0}{P_0} \quad \rightarrow \quad \delta = \frac{P^{\frac{m_0}{m}} - P_0}{P_0}. \quad (7.123)$$

With the re-definition of δ and the information on χ available, the tracking maps implemented in SixTrack are modified to include the isotopic dispersion. The implementation follows the tracking maps derived from the generalized Hamiltonian presented in the previous chapter. For collimation studies the thin lens implementation of SixTrack is used and accordingly all thin-lens tracking maps are modified to allow for the multi-isotopic tracking. Note that instead of the canonic momenta p_x and p_y , SixTrack computes the evolution of x', y' , such that the corresponding tracking map for a thin-lens quadrupole is modified for hiSixTrack as follows:

$$(x')^F = (x')^I + \frac{k L}{1 + \delta} \quad \rightarrow \quad (x')^F = (x')^I + \frac{\chi k L}{1 + \delta}. \quad (7.124)$$

Further details on the implementation are given in Chap. A.5.4.

7.4.2 Definition of the Heavy-Ion Species

The algorithm to load the initial distribution in the SixTrack-FLUKA coupling was already prepared, though not completely set up, for the eventual input of the particle species. The general structure of input therefore includes by default not only the six-dimensional particle coordinates but also information on the particle species. In the sampling of the initial distribution file, the information on A, Z, m is accordingly adjusted.

The subroutine initializing the particle properties in the standard SixTrack-FLUKA coupling ignores this information. For heavy-ion applications this algorithm is adjusted to populate the respective arrays with the isotope information. With this change, hiSixTrack is capable to load an initial bunch of arbitrary ions and store information on the particle type throughout the tracking and send this information from hiSixTrack to FLUKA and back.

Note that the mass of both reference particle and tracked particle must coincide with their associated masses in FLUKA. If this is not respected, the hiSixTrack-FLUKA coupling refuses their exchange between the codes.

7.4.3 Benchmarking of Ion Tracking in hiSixTrack

The updated tracking algorithm can be benchmarked against heavy-ion tracking in the STIER approach. Taking into account that STIER provides symplectic tracking with multipole contributions to the same order as it is implemented in hiSixTrack, a full agreement of the particle

tracks computed in the two approaches can be expected. In the following, different simulation cases are discussed to study the accuracy at which isotopic and chromatic dispersion are computed in hiSixTrack:

1. Study of the betatron motion for particles of the reference species with perfect momentum ($\delta = 0; \chi = 1$),
2. Tracking of different isotopes with ideal momentum to study the modelling of the isotopic dispersion ($\delta = 0, \chi \neq 1$)
3. Tracking of off-momentum particles of the reference species to study the modelling of the chromatic dispersion ($\delta \neq 0, \chi = 1$)
4. Tracking of off-momentum particles of an unmatched species ($\delta \neq 0, \chi \neq 1$)

Especially if the particle tracks are observed over many turns, small numeric imprecisions induced by improper implementation (wrong setting of brackets etc.) of the tracking maps may lead to significant changes of the particle tracks. All simulations assume the reference isotope to be $^{208}\text{Pb}^{82+}$ with a rest mass of $m_0 = 193.68769 \text{ GeV}/c^2$. The collimators are removed from the simulation, such that the tracking result can not be adulterated by scattering in the collimators. Furthermore, the RF cavities are not included since the momentum kicks for ions and protons deliver different kicks in δ .

Betatron Motion without Dispersion

The simulated betatron motion in hiSixTrack is benchmarked against STIER by means of comparing on-momentum particles ($\delta = 0$) of the respective reference species ($\chi = 1$) with identical initial conditions in IP1. As an example, the betatron oscillations simulated for ten on-momentum particles, randomly generated at IP1 at the surface of a horizontal annular halo in x, x' at an amplitude of 5.7σ , is shown in Fig. 7.4.

For the benchmarking of the tracking algorithm in hiSixTrack, the simulated tracks of 100 particles with $\chi = 1$ and different betatron amplitudes starting in IP1 are compared to the tracks extracted from STIER. The tracking is performed over 10^6 turns through the magnetic lattice of the LHC, in the 2011 configuration with crossing and separation bumps switched on in all experimental IRs, except IR1.

The comparison of the simulated tracks shows, within the precision of the floating point numbers dumped from SixTrack, no difference between the two tracking approaches. This proves the consistency of the tracking maps derived in Chap. 7.3 with the ion-equivalent proton tracking used in STIER.

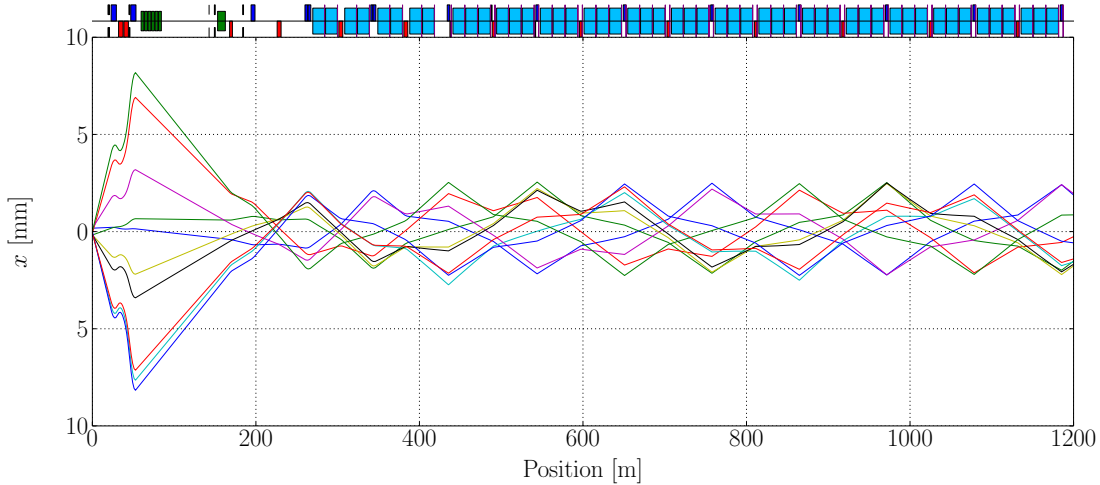


Figure 7.4: Tracks of on-momentum particles of the reference species starting from IP1 on an horizontal annular halo at an amplitude of 5.7σ , as simulated with hiSixTrack.

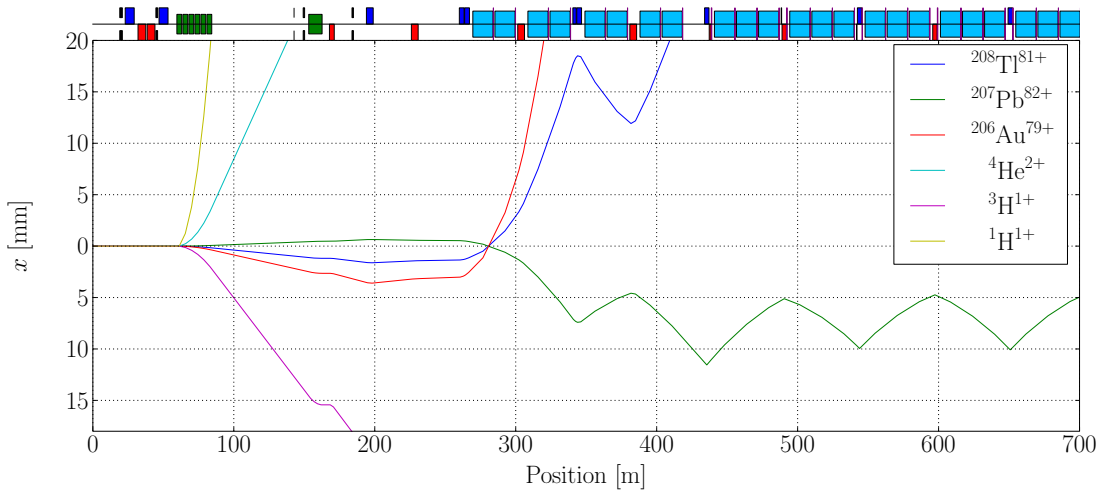


Figure 7.5: Simulated heavy-ion tracks for different on-momentum ($\delta = 0$) isotopes starting with the same initial conditions in IP1.

Tracking of different Isotopes without chromatic Dispersion

To benchmark the isotopic dispersion without the influence of betatron motion and chromatic dispersion, different isotopes to which the magnetic lattice is not matched ($\chi \neq 1$) are simulated to start in IP1 without momentum per mass offset $\delta = 0$ and betatron amplitude $x = y = x' = y' = 0$. The resulting tracks from hiSixTrack and STIER are compared in Fig. 7.5 for the isotopes listed with their χ values and the resulting δ_{eff} in Table 7.1.

While the study case is unphysical and without correspondence in the real machine, it is well

suites for the study of the isotopic dispersion. In the simulated scenario the particle motion is undisturbed of initial betatron offsets and chromatic dispersion, which can enhance or reduce the effect of the isotopic dispersion on the particle tracks.

The particle tracks of all isotopes except $^{207}\text{Pb}^{82+}$ were simulated for less than one turn through the LHC, because the strong dispersion leads to very large horizontal amplitudes after only a few magnets. The isotope $^{207}\text{Pb}^{82+}$ is tracked over 10^6 turns. Also in this scenario, the tracks simulated by hiSixTrack and STIER are identical, confirming the accuracy of the implementation in hiSixTrack.

Tracking of the Reference Isotope with Momentum Offset

To confirm the accuracy of the chromatic tracking without isotopic dispersion and betatron offset, the tracking is benchmarked for particles of the reference species ($\chi = 0$) with momentum deviations relative to the reference particle ($\delta \neq 0$). With each tool, 100 initial particles are simulated starting at IP1 with different momenta and initial amplitudes of $x = y = 0$ and $x' = y' = 0$. The tracking is carried out for a maximum of 10^6 turns, which can only be achieved if the chosen momentum offsets are small enough. The tracks simulated with both tools are in full agreement.

Unmatched Isotope with Momentum Offset

Figure 7.6 shows the simulated track of a $^{207}\text{Pb}^{82+}$ ion starting from IP1 in a LHC lattice matched for $^{208}\text{Pb}^{82+}$ with $\delta \neq 0$ and an initial betatron offset. This scenario is studied for 200 particles of the species $^{207}\text{Pb}^{82+}$ with different values of $-5 \cdot 10^{-4} < \delta < 5 \cdot 10^{-4}$ and starting conditions in x, x', y, y' randomly sampled from a Gaussian distribution in IP1. The comparison

Table 7.1: Isotopes used for the benchmarking of the heavy-ion tracking. Values for χ and δ_{eff} are computed by means of Eqs. ?? with respect to the reference isotope $^{208}\text{Pb}^{82+}$. The masses correspond to the fully stripped ions and were extracted from FLUKA.

Element	A	Z	m [GeV/ c^2]	χ	δ_{eff}
H	1	1	0.93827	2.51744	-0.6030
H	3	1	2.80892	0.84090	0.1892
He	4	2	3.72738	1.26740	-0.2110
Au	206	79	191.833	0.97273	0.0280
Pb	207	82	192.755	1.00484	-0.0048
Tl	208	81	193.693	0.98778	0.0124

of the tracking in hiSixTrack and SixTrack with ion-equivalent rigidities shows a full agreement of the simulated tracks. The tracking of this isotope is limited to a maximum of five turns due to the large transverse offsets reached.

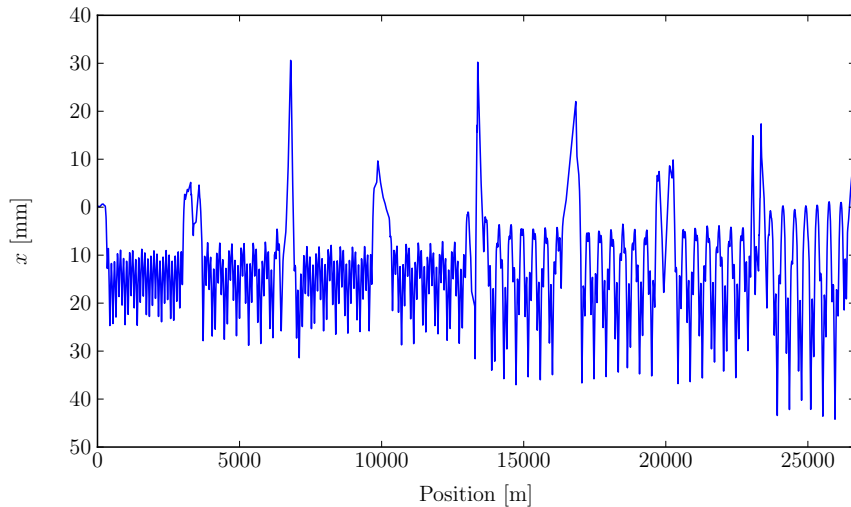


Figure 7.6: Horizontal motion of $^{207}\text{Pb}^{82+}$ with momentum offset $\delta \neq 0$ starting from IP1.

Symplecticity

With the symplecticity for the individual beam line elements already proven analytically (see Chap. A.1), the global implementation in hiSixTrack can be studied for its symplecticity. For this purpose a bunch of on-momentum particles of the reference species starting as an annular halo at IP1 is tracked over 10^6 turns. Sextupoles are switched off, such that the phase space ellipse should remain constant and not be shifted by non-linear forces. The study case is the LHC configuration of the 2015 heavy-ion run at $6.37 Z$ TeV and the particle distribution in phase space is compared with itself every turn at the TCP.C6L7.B1.

The simulation result is shown in Fig. 7.7 proving that the volume of the phase space ellipse remains constant even after the large number of turns the particles are tracked through the LHC. This finding confirms the global symplecticity of the implementation in hiSixTrack and is in line with the symplecticity check carried out for the transport maps of the individual beam line elements. Together with the tracking benchmarking presented above, this result allows the conclusion that the implementation in hiSixTrack is accurate and trustworthy.

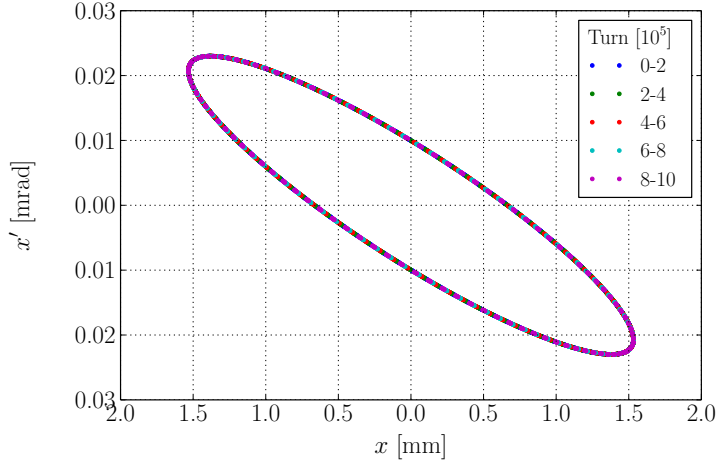


Figure 7.7: Phase space parameters of an initial beam halo at 5.5σ at the location of the TCP.C6L7.B1 over 10^6 turns, simulated with hiSixtrack. The volume covered in phase space remains constant.

7.5 The hiSixTrack-FLUKA Coupling

With the native heavy-ion tracking established in hiSixTrack, the on-line coupling for fragmentation simulations with FLUKA becomes possible. The algorithms which enable the particle exchange are adapted for heavy-ion applications and additional output data is produced to accurately account for heavy-ion losses simulated in the framework of the hiSixTrack-FLUKA coupling. In this chapter the essential modifications are qualitatively described.

7.5.1 Heavy Ion Exchange between hiSixTrack and FLUKA

In the nominal framework of the SixTrack-FLUKA coupling, with a defined particle species (protons), it is sufficient to send the proton energy and coordinates to FLUKA and back, with a transfer of information defining the particle type being not required. For the implementation of the hiSixTrack-FLUKA coupling, the inclusion of the particle species (defined by A, Z) and mass m is important to ensure the use the correct physics models in both FLUKA and hiSixTrack. Every particle is identified in SixTrack by its particle ID, which is unique for each initial particle and each residual fragment. The hiSixTrack-FLUKA coupling assigns the new particle ID automatically to a newly created fragment.

The particles sent back to the tracker are selected by means of their FLUKA particle ID which classifies them into different particle categories. For the heavy-ion coupling, the selection of protons is replaced by heavy ions (describing all fully stripped ions beyond ${}^4\text{He}^{2+}$), deuterons, tritium, ${}^3\text{He}^{2+}$ and ${}^4\text{He}^{2+}$. Protons are by default not sent back to hiSixTrack, but this feature

can easily be activated with a minor modification of the corresponding FLUKA subroutine `fluscw.f`. The multi-isotopic modifications in hiSixTrack can in principle eligible support to the tracking of all other charged particles which are now excluded from the tracking (protons, pions, Δ -baryons, ...). However, they are not included in the tracking, because with their extreme rigidity offset with respect to the main beam they are absorbed very locally, as it was demonstrated for the residual protons tracked in STIER (see Fig. 6.10). In real operation these losses in the warm regions close to the collimators are shadowed by particle showers which are not modelled in the presented framework, such that their inclusion into the simulation would most probably not lead to conclusive findings.

In addition, the simulations with the hiSixTrack-FLUKA coupling are space- and time-consuming due to the large number of different fragments produced. The total number of particles which can be tracked in one hiSixTrack simulation (the number of different particle IDs) is limited to 2000 due to limitations in working memory in the CERN cluster, imposing an upper boundary for the number of initial particles used per job. In the mentioned configuration a reasonable number of initial particles per job is 140, leaving enough margin for the production of more than 13 residual particles from each initial $^{208}\text{Pb}^{82+}$ ion. The sole inclusion of protons requires a significant reduction of the number of initial particles per job: the study with impact

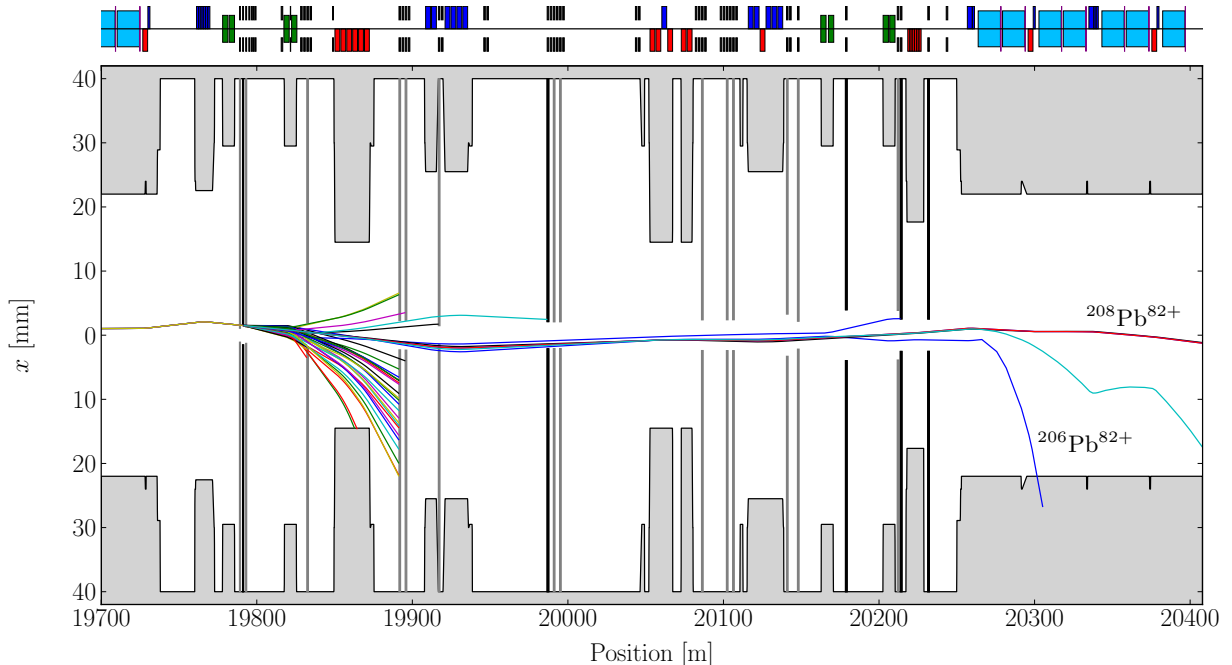


Figure 7.8: Simulated fragmentation of four $^{208}\text{Pb}^{82+}$ ions at the TCP and the subsequent motion of their residual fragments, as simulated with the hiSixTrack-FLUKA coupling.

parameters between 1 and $10\text{ }\mu\text{m}$ in the 2011 configuration showed that a large enough margin constraints the number of initial particles to be below 40 (which is in line with the production yield of 40% at $b = 10\text{ }\mu\text{m}$ that was found in the STIER simulations, see Table 6.2, and considering the effect of fragmentation at subsequent collimators). In conclusion, the selection of heavy ions in the hiSixTrack-FLUKA coupling serves the purpose of reducing the required space and running time without a significant impact on the simulated loss pattern in regions beyond the normal conducting cleaning insertions IR7 and IR3.

The particle exchange in the hiSixTrack-FLUKA coupling was extensively tested to ensure that the correct particle species and properties are transferred between the codes. The output of both hiSixTrack and FLUKA can be adjusted to save information about the particle species and their six-dimensional phase space parameters. The tests carried out with 1 million particles demonstrate the accuracy of particle exchange.

Details on the technical implementation in the FLUKA subroutines and the SixTrack code is given in Chap. ??.

7.5.2 Benchmarking of the Fragmentation Simulation

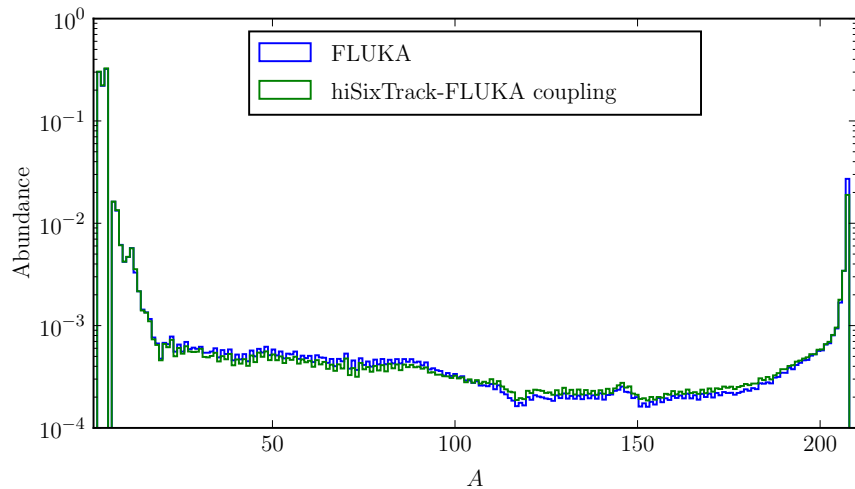


Figure 7.9: Heavy-Ion spectrum of particles leaving the TCP for an initial $^{208}\text{Pb}^{82+}$ beam at $7Z\text{ TeV}$ as simulated with FLUKA and with the hiSixTrack-FLUKA coupling.

The accuracy of the fragmentation simulation is studied by a comparison of the heavy-ion spectrum coming out of the primary collimator between FLUKA and the hiSixTrack-FLUKA coupling. The geometry used in FLUKA is identical to the setup used for the STIER simulations. The impacting beam consists of 10^6 particles of the isotope $^{208}\text{Pb}^{82+}$ with a momentum of $7Z\text{ TeV}/c$ with $b = 1\text{ }\mu\text{m}$. In the hiSixTrack-FLUKA coupling the primary beam is simulated

to impact the TCP at an impact parameter between $0.9 \mu\text{m}$ and $1.1 \mu\text{m}$. In both methods, the nuclear evaporation model of FLUKA is switched on and the material is set to graphite with the density of CFC. A major difference between the simulations is the fact that the beam used in FLUKA is on-momentum, while the particles used in the hiSixTrack-FLUKA have a momentum spread.

The spectrum of nuclear mass numbers simulated with the two approaches is shown in Fig. 7.9. Both histograms are normalized such that the values integrated over all bins yields one. Note that only the abundance of isotopes is given, so the data is not weighted with A . Overall, the two fragment spectra show an excellent agreement, with minor discrepancies for intermediate mass number, which lie within the expected statistical fluctuations. The rate of surviving $^{208}\text{Pb}^{82+}$ ions is slightly higher FLUKA, which can be traced back to the spread of impact parameters and energies in the hiSixTrack-FLUKA coupling. The latter leads to a spread of the angle of incidence increasing the mean traversed distance in the collimator material and thus the fragmentation rate.

7.5.3 Collimator Losses

The proton implementation of SixTrack and the SixTrack-FLUKA coupling consider particles to be lost in a collimator if they undergo inelastic nuclear interactions with large momentum transfer. In the heavy-ion SixTrack framework, the underlying physical processes are different, such that collimator losses have to be counted differently.

The basic idea behind the loss scaling in hiSixTrack is the comparison of the total energy entering each collimator with the energy leaving it. Therefore, the coupling framework is modified to integrate the total ion energy every time the particle bunch is sent to FLUKA and when it is sent back from FLUKA to hiSixTrack. The difference is then considered as the energy lost at this collimator. This information is written to the dedicated output file `fort.208`.

Considering that the particles sent back to hiSixTrack are exclusively heavy-ions while all other particles (neutrons, pions, Δ -baryons, ...) are invisible in this approach even though they may have left the collimator carrying significant energies, the collimator losses derived from the mentioned approach are likely to be overestimated. Therfore the FLUKA subroutines are adapted to store information about all particles leaving the collimator which are not sent back to hiSixTrack into the output file `fort.66`.

In practice the collimator losses at the TCP, taking into account the correction factor, are reduced by approximately 20%. More information on the implementation and the structure of the `fort.208` and `fort.66` files is given in Chap. ??.

7.5.4 Simulation Output

Specific simulation output is required for the study of heavy-ion losses. The hiSixTrack-FLUKA coupling is adapted to provide additional information about the lost isotopes via new output files and by the modification of output files already implemented before.

- **fort.999:** default output file from the online aperture check; modified to save also information on A, Z, m of the impacting particle.
- **fort.208:** stores information on collimator losses. This includes the number of nucleons and total particle energy lost at each collimator, without providing information about the individual particles lost.
- **fort.209:** relates the collimator losses to individual particles. For every particle lost at a collimator the collimator ID is saved. The collimator losses can so be drawn back to the individual isotopes.
- **fort.822:** Ion fragments produced at the collimator. Every residual ion produced at any collimator is listed with its particle ID, the parent particle ID, the ID of the collimator at which it is produced and its mass, charge and energy.
- **fort.66:** Correction file for collimator losses.

7.6 Loss Map Simulation with the hiSixTrack-FLUKA coupling

To validate the accuracy of full cleaning simulations with hiSixTrack, the measured BLM pattern in the 2011 heavy-ion run is compared to simulation results obtained with hiSixTrack and STIER. Fig. 7.11 shows the resulting loss patterns.

7.6.1 Initial Distribution

Cleaning simulations with hiSixTrack can in principle be initiated similarly to proton simulations with SixTrack. In this approach the initial distribution is sampled as an annular halo at a betatron amplitude in the interval $[N_P, N_P + \epsilon]$, where ϵ is a small number and determines the thickness of the sampled ellipse in phase space. The latter is related to the maximum impact parameter which can be achieved if the phase space is conserved. In this approach, the particles continue moving in the machine until they hit the primary collimator after some turns. If non-linear elements, such as sextupoles, are present in the machine, the phase space ellipse is slightly shifted and tilted which can enlarge the impact parameter and lead to non-symmetric impacts on

the two collimator jaws (see Fig. 7.10). This should not be confused with a lack of symplecticity, because the volume enclosed by the annular halo remains constant. For protons, this behaviour is acceptable because the scattering in the collimator is not strongly dependent on the impact parameter [B⁺14c]. As discussed in earlier chapters, for heavy-ions the spectrum of outgoing ion fragments is strongly dependent on the impact parameter, such that in cleaning simulations it must be better controlled than in the proton case.

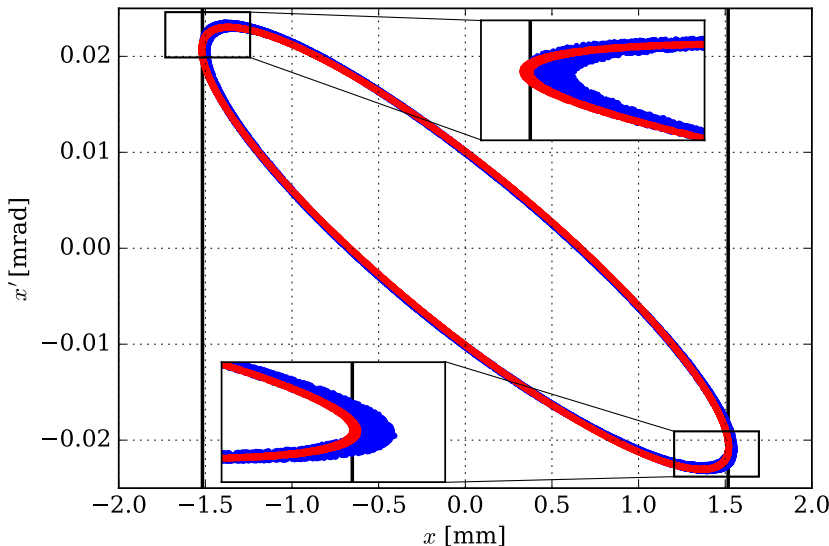


Figure 7.10: Annular halo of on-momentum particles tracked from the TCP to the TCP.C6L7.B1 over ten turns with sextupoles (blue) and without sextupoles (red). The black horizontal lines indicate the TCP jaw edges.

Instead, a preliminary approach to control the impact parameter at the primary collimators is used the cleaning simulations with hiSixTrack. In an initial high statistics simulation over one turn through the LHC, the impact coordinates on the collimator jaws of the respective TCP (depending on the beam and the transverse directin) are determined. Based on this simulation result the initial conditions can be associated to impact parameters and the impacting jaw. Finally, the initial coordinates resulting in impacts at the desired jaw with the chosen impact parameter can be sampled and multiplied to the required number of initial particles. In terms of computing time the initial simulation and the subsequent sampling of the initial distribution file requires less than one hour, which is negligible to a total simulation time for a full hiSixTrack cleaning simulation of 24 h for 6.5 million particles. The loss maps presented in the following sections are generated with this approach.

Future upgrades of hiSixTrack may include input options for pencil beams, which impact directly on a dedicated collimator with a defined impact parameter. This feature, already implemented

in the standard collimation version of SixTrack [Bru14], is not available in the framework of the SixTrack-FLUKA coupling. The simulation is in this case not initiated at IP1 but directly at the TCP with the subsequent fragmentation simulation, comparable to the approach used in STIER. It allows precise studies on the behaviour of the cleaning system with given impact parameters.

7.6.2 Loss Map Benchmarking

The full cleaning simulation with hiSixTrack is benchmarked against the measured data of the 2011 heavy-ion run and compared also to the STIER simulation result. The hiSixTrack simulation presented is carried out for B1H with 6.5 million initial $^{208}\text{Pb}^{82+}$ ions which start at IP1 and are intercepted by the TCP on the first turn in the machine. The impact parameter at the latter is continuously distributed between $1\mu\text{m}$ and $10\mu\text{m}$.

The loss maps are shown in the Figs. 7.11 (full LHC), 7.12 (zoom to IR7) and 7.13 (zoom to IR3). The global loss pattern simulated with the hiSixTrack-FLUKA coupling is very similar to the STIER simulation. While the loss peak distribution is quantitatively in good agreement, the amplitude of the losses is different in the two simulations. This can be drawn back to the different impact parameter and residual particles emitted from collimators downstream of the TCP. As expected, they become visible in the hiSixTrack-FLUKA coupling while they are not simulated in STIER. The most remarkable are the losses downstream of the momentum cleaning region IR3.

The losses in the warm elements of IR3 and IR7 are, as expected, not modelled accurately in either simulation because the secondary particle showers are not included in the simulation. The general shape of the collimator losses in IR7 is different between the two simulation tools. Note in particular the different ratio of losses at the primary collimator and the TCSG collimators immediately downstream. This difference can be drawn back to two effects: first, the TCP losses in STIER are uniquely originating from out-scattered $^{208}\text{Pb}^{82+}$ ions surviving one or multiple turns and then impact on the TCP again. The energy lost in the TCP at the initial passage is not included in STIER, with the evident consequence of a significant reduction of simulated losses at the TCP. Secondly, the STIER simulation includes protons, which are mostly lost at the TCSG collimators and therefore change the loss ratio between TCP and TCSG in favour of the TCSG. This assumption is supported by low statistics hiSixTrack simulations including protons.

One additional loss peak in the arc between IR8 and IR1 (marked as A8 in Fig. 7.11) is simulated in hiSixTrack. Further investigation shows that this additional peak is indeed generated from multiple collimator interactions. A more detailed analysis is shown in the next section.

The direct comparison of the simulated global heavy-ion beam loss pattern shows that the loss

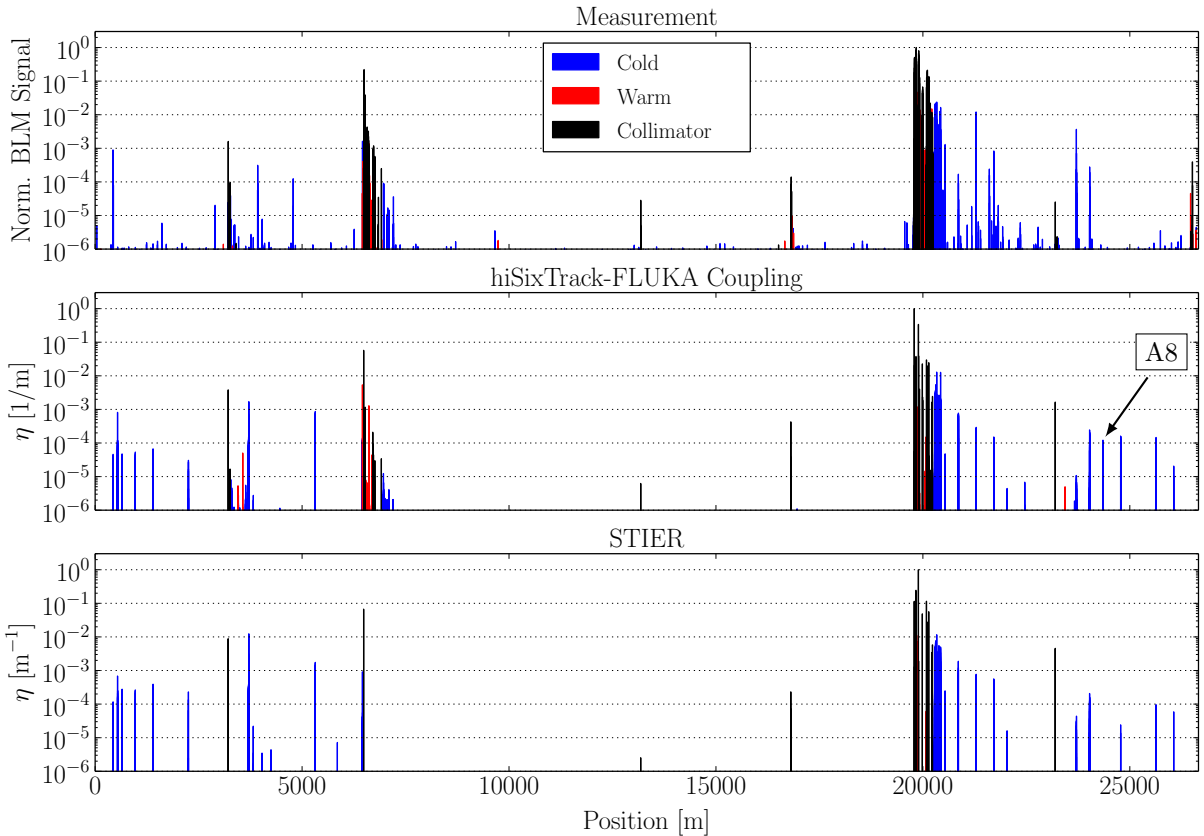


Figure 7.11: B1H betatron loss maps measured in the 2011 heavy-ion run compared to simulations with the hiSixTrack-FLUKA coupling and STIER.

distribution is dominated by particles starting from the IR7 TCP. The difference between the resulting loss pattern from STIER and hiSixTrack are mainly visible at regions downstream of the collimators in IR3 and IR2. This finding is in line with the assumption under which the STIER tool was developed and supports the accuracy of the loss maps simulated with it.

The following conclusions are drawn from the benchmarking of the loss maps simulated with hiSixTrack.

- The accuracy of global loss simulations is improved with respect to STIER by the inclusion of scattering and fragmentation at all collimators. This can become of interest for the study of TCLD collimators, where ions scattered out of secondary collimators or the TCLD collimators themselves may lead to losses in the DS region of IR7 and therefore reduce their efficiency.
- The most critical losses at the IR7 DS are simulated similarly as in STIER. This demon-

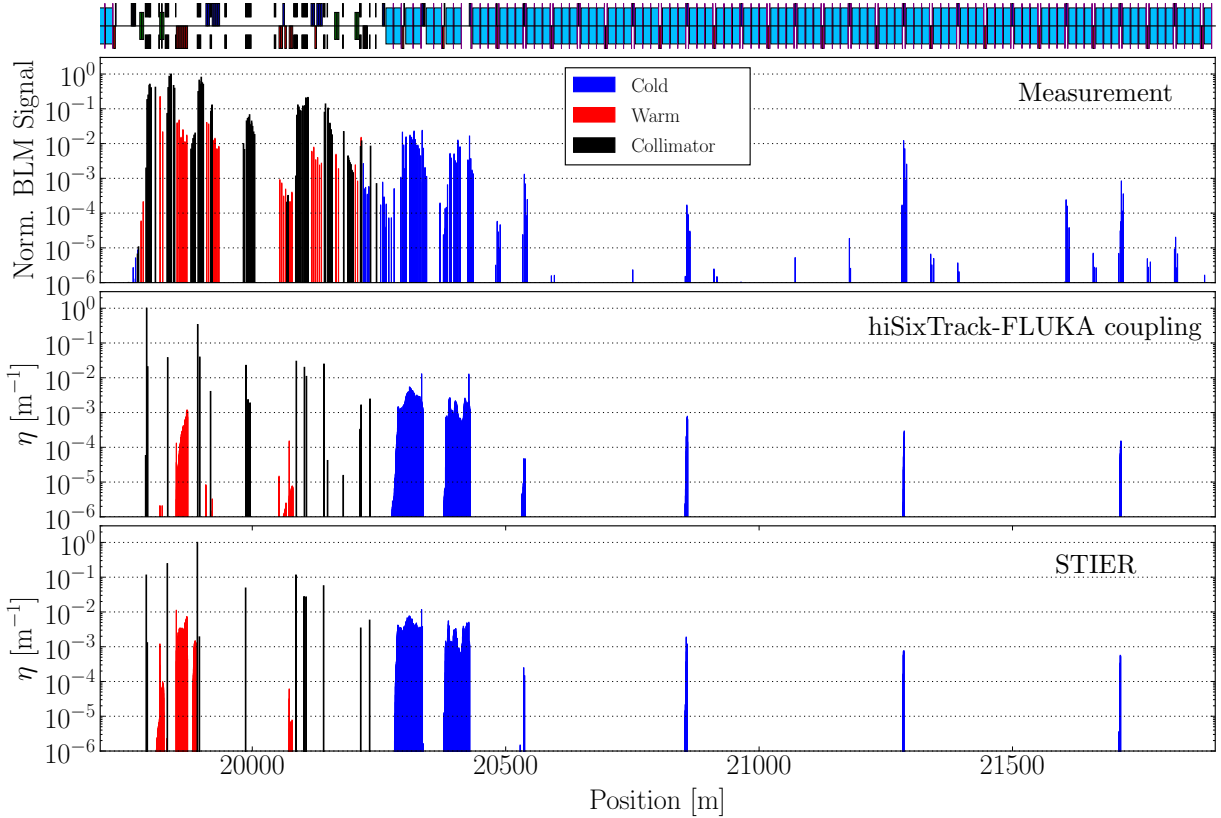


Figure 7.12: B1H betatron loss maps measured in the 2011 heavy-ion run compared to simulations with the hiSixTrack-FLUKA coupling and STIER, zoomed to IR7.

strates that the assumptions used for the set up of the STIER simulation tool are valid and the simulation results obtained with it are accurate within its limitations.

7.6.3 Contribution of Secondary Fragmentation

With the inclusion of secondary fragmentation in hiSixTrack the impact of the latter on the final loss map can be studied. The simulation of the 2011 heavy-ion run can be analyzed for the contribution of secondary ion fragments to the final loss pattern. The result of this analysis is given in terms of the integrated losses η_{sec}^{int} of particles generated at collimators different from the IR7 TCP normalized by the total amount of losses η_{tot}^{int} integrated for the region of interest. The comparison is shown for the two IR7 DS loss clusters, the four arc cluster A1 to A4 downstream of IR7 in Table 7.2 and for all aperture losses in the LHC ring.

The simulation data shows that only minor contributions to all loss peaks arise from these secondary fragmentation processes. The highest contribution in the concrete simulation case is reached at the A1 cluster where 3% of the losses are caused by these heavy-ion fragments. On

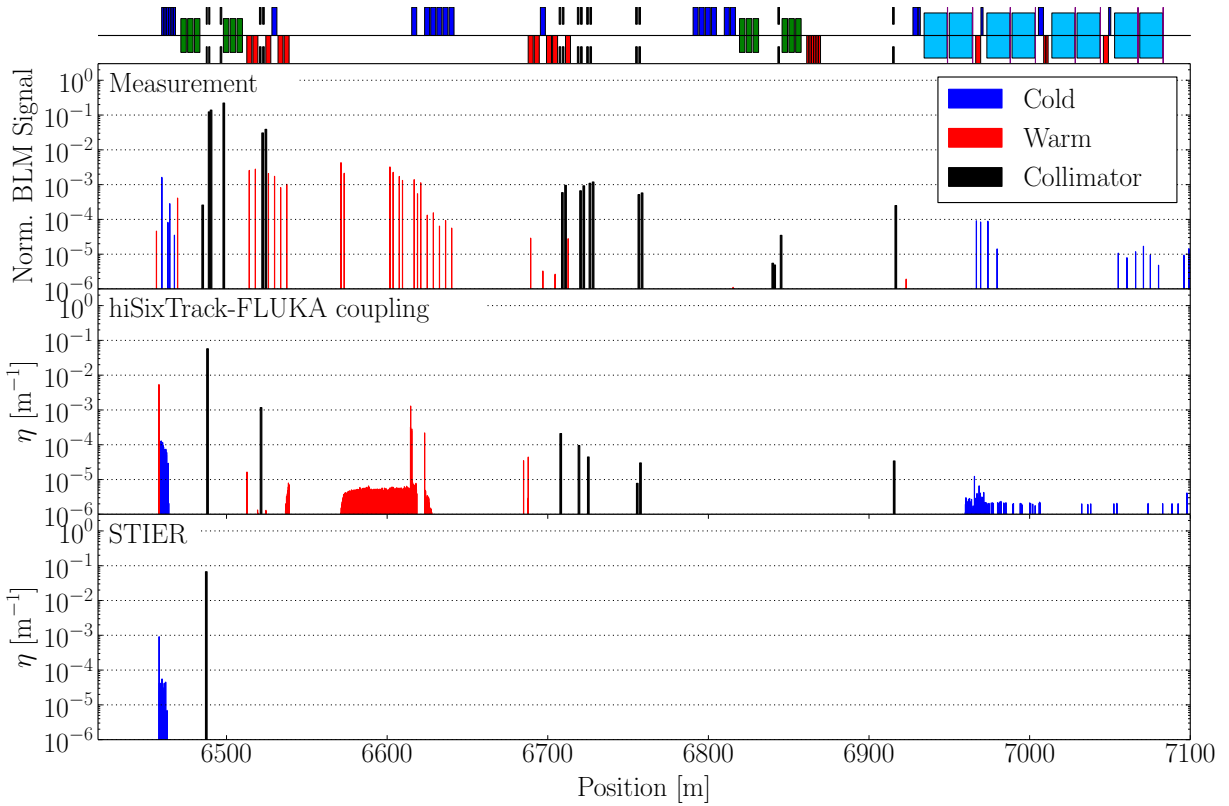


Figure 7.13: Comparison of the measured loss map in the 2011 heavy-ion run to simulations with STIER and hiSixTrack, zoomed to IR3.

a global scale, approximately 0.8% of aperture losses arise from these ions.

While the losses in the regions mentioned above are affected only insignificantly by secondary fragmentation processes, in the arc region between IR7 and IR8 a new loss peak A8 is simulated in hiSixTrack. The STIER simulation does not predict any losses at this location.

Further analysis shows that mainly particles of the species $^{206}\text{Pb}^{82+}$ generated at the TCP are lost at A8. All of the studied particles are generated at secondary interactions of $^{208}\text{Pb}^{82+}$ ions with the TCP after being scattered in it in a previous turn. The scattered $^{208}\text{Pb}^{82+}$ ions have lost some of their initial momentum and impact the TCP again with different angle or impact

Table 7.2: Energy fraction of ion fragments generated at secondary interactions collimators with respect to the total integrated energy lost in different LHC regions.

	DS1	DS2	A1	A2	A3	A4	Global
$\eta_{\text{sec}}^{\text{int}} / \eta_{\text{tot}}^{\text{int}}$	$5 \cdot 10^{-3}$	$3 \cdot 10^{-3}$	$3 \cdot 10^{-2}$	$1 \cdot 10^{-4}$	$6 \cdot 10^{-4}$	$1 \cdot 10^{-3}$	$8 \cdot 10^{-3}$

parameter than the particles of the primary halo. The residual $^{206}\text{Pb}^{82+}$ ions generated at the second interaction at the TCP have considerably different starting conditions than those generated during the primary fragmentation which leads to a different loss location.

Evidently, the loss peak can not be simulated with STIER because secondary fragmentation at the TCP is not included in the simulation framework.

In conclusion, ions generated from fragmentation at subsequent collimator interactions may lead to additional features of the simulated loss pattern, although, compared to the losses from the primary TCP interaction, their contribution is small. Around 0.8% of the global aperture losses simulated in hiSixTrack arise from particles generated in secondary fragmentation processes. Note that this conclusion might not be valid for other study cases at different particle momenta, with other heavy-ion species or collimator settings.

8. Simulations and Measurements

Alongside with the comparison of simulated and measured loss patterns for benchmarking of the simulation tools, such comparisons allow the study of potential strategies of loss reductions. In this chapter, different studies carried out with STIER and hiSixTrack related to operational aspects are outlined and discussed.

8.1 Preparation of the Heavy-Ion Operation in 2015

With the $^{208}\text{Pb}^{82+}$ ion operation in late 2015, the LHC advanced into regimes of unprecedented heavy-ion momenta and stored beam energies [JSA⁺16]. The collider reached a particle momentum of $6.37 Z \text{ TeV}$ and a stored beam energy of approximately 9.5 MJ , the latter being more than twice beyond the design value. While the number of injected bunches ($k_b = 426$) was still below the design value of $k_b^d = 518$, the injector chain upgrades performed in the past led to a significant increase of the energy per bunch []. Altogether with the small emittances achieved,

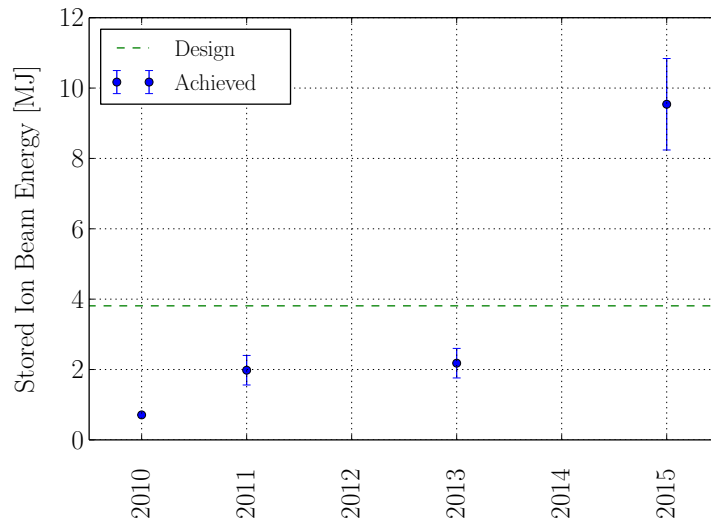


Figure 8.1: Stored heavy-ion beam energy in the past LHC heavy-ion runs.

these improvements enabled luminosities surpassing the design value by a factor of 3.6 [JSA⁺¹⁶], in spite of the rather large $\beta^* = 0.8$ m applied in ATLAS, CMS and ALICE.

The large beam intensity was highly challenging for the LHC collimation system. Occasionally, the amount of collimation cleaning debris absorbed in the IR7 DS exceeded the allowed threshold and led to protection dumps triggered by the BLM system. Furthermore, secondary losses at the tertiary collimators led to particle showers which produced perturbing background in the experiments, especially in ALICE.

Alongside the physics program, which was accomplished with great success and unprecedented integrated luminosities collected [JSA⁺¹⁶], various dedicated machine experiments were carried out with the LHC. These included the study of new collimation devices (crystal collimation [MRS⁺¹⁵]) and two quench tests: one in which a main dipole was quenched with the secondary BFPP beams generated in IP5 [SAFBC⁺¹⁵], and a collimation quench test with collimation debris generated at the TCP in IR7, described in Chap. ??.

In this section, cleaning simulations carried out for the preparation and optimization of the collimation system in the 2015 configuration are presented together with loss patterns measured during operation.

8.1.1 Validation of Collimator Settings

In preparation of the heavy-ion run, the tool STIER was used to give an estimate about the expected cleaning performance and to study possible strategies to reduce the amount of losses at the IR7 DS magnets. This includes the study of different collimator settings, in particular different retractions of the TCSG collimators, to validate the collimation system and give estimates about the expected loss reduction in case of tighter settings.

With the geometrical collimator settings taken from the precedent proton operation, the TCSG collimators are retracted by $\Delta N_{S,P} = 2.5 \sigma$ with respect to the primary collimators. STIER was employed to simulate the cleaning inefficiency for the reference settings and in addition with retractions of $\Delta N_{S,P} = 2.0 \sigma, 1.5 \sigma$ and 1.0σ .

In the fragmentation simulation, the $^{208}\text{Pb}^{82+}$ beam is simulated to impact the carbon target in the same geometry already used for the simulations presented in Chap. ?? at an impact parameter of $b = 2 \mu\text{m}$. With an initial sample of 5×10^6 heavy-ions impacting the TCP jaw, the fragment distribution obtained from FLUKA is processed into initial coordinates in B1H for the tracking simulation as protons with equivalent rigidity performed with SixTrack. The simulation is carried out for both jaws individually to disentangle the losses arising from particles starting at each individual jaw. This approach turned out to be very useful for the analysis and mitigation of the losses at the TCT in IR2, as discussed in Chap. 8.3. For the four simulations with different TCSG retractions, the same sample of initial coordinates is used, so the obtained

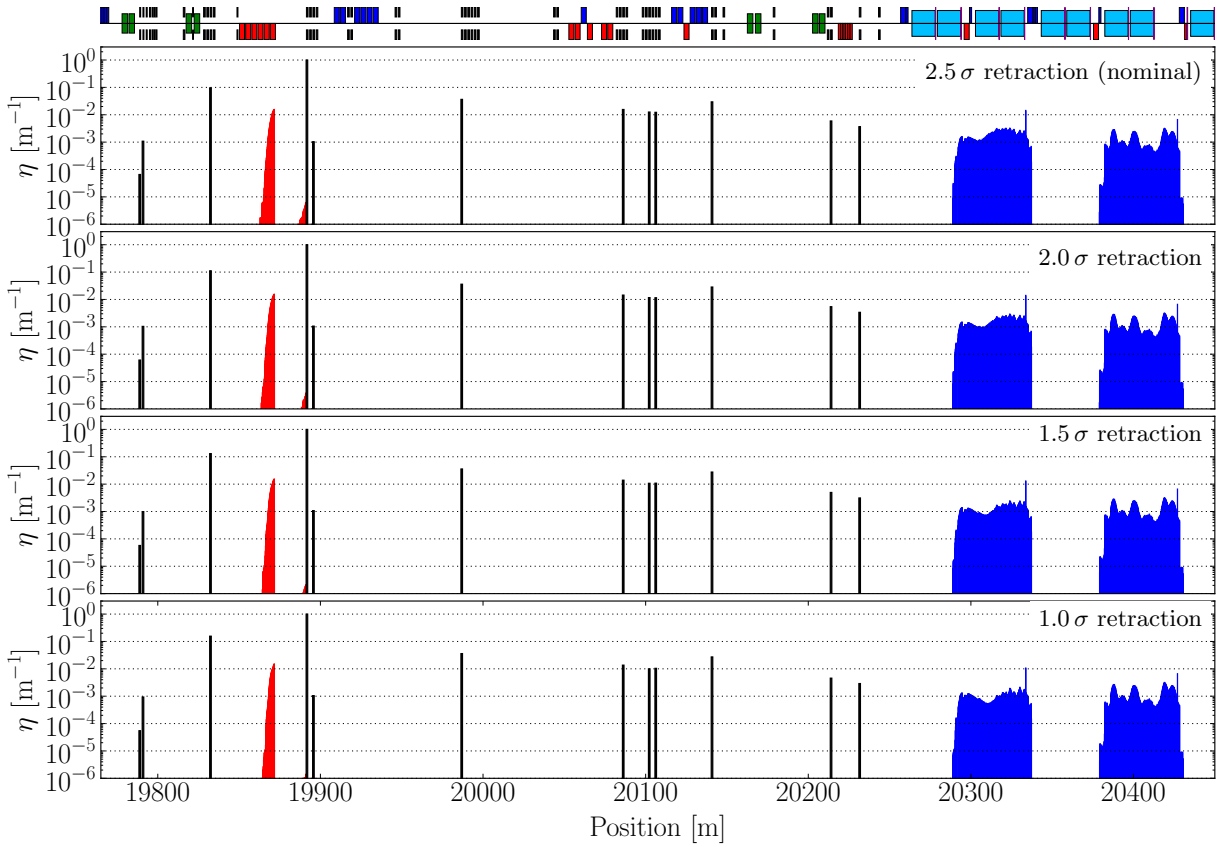


Figure 8.2: IR7 view of the STIER simulated loss maps for $^{208}\text{Pb}^{82+}$ ions at 6.37 TeV in the configuration of the 2015 heavy-ion run for different retractions of the TCSG collimators with respect to the primary collimators.

loss patterns are quantitatively comparable without the need to consider statistical fluctuations of the loss pattern.

The loss maps generated from the STIER simulations are shown for the full ring in Fig. A.3 in the appendix and zoomed to IR7 in Fig. 8.2. With the smaller TCSG opening, additional losses occur only at the TCSG.A6L7.B1 which is the first TCSG downstream of the primary collimators. For the tightest setting studied, the losses in the latter are increased by 60% with respect to the nominal case.

The tightening of the TCSG settings does not lead to a significant change of the simulated loss pattern. The losses in the warm region downstream of the TCP can be slightly reduced. For the critical losses in the IR7 DS, slight differences in the loss pattern are visible for the different scenarios. A quantitative comparison of the cleaning performance with nominal retraction and the with tightest setting is shown in Fig. ???. Also, selected numeric key quantities as a measure of the evolution of cleaning performance with decreasing TCSG retraction are listed in Table 8.1.

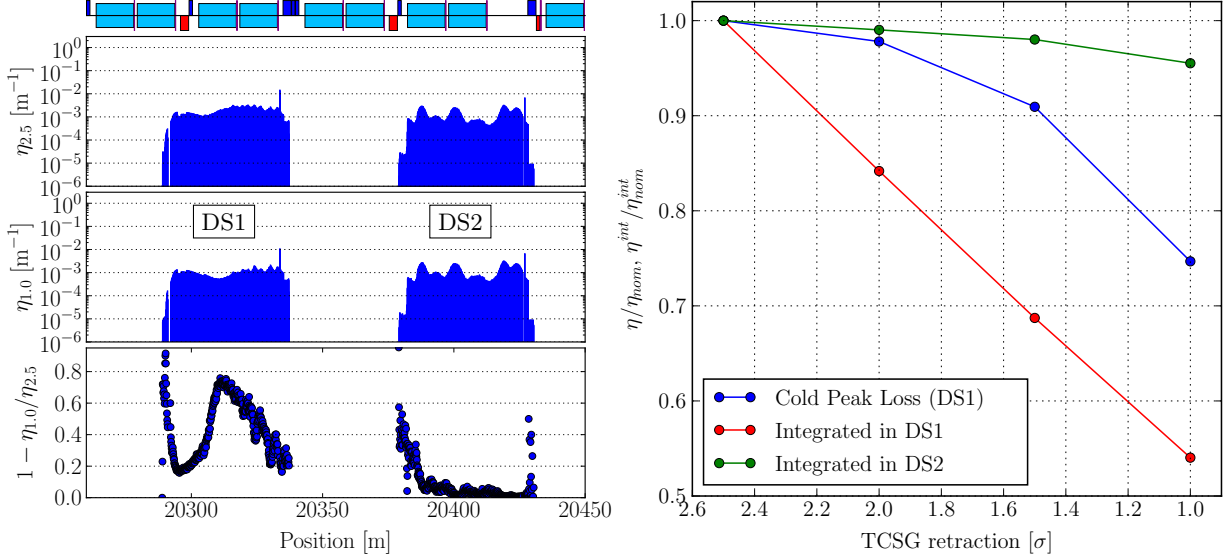


Figure 8.3: Left: Dispersion suppressor loss clusters with nominal TCSG retraction (top plot), with 1.0σ TCSG retraction (middle plot). Right: Evolution of the highest cleaning inefficiency and the integrated losses in DS1 and DS2 as a function of the applied TCSG retraction.

Table 8.1: STIER simulation results quantifying the cleaning performance as a function of the applied TCSG retraction $N_S - N_P$ for the 2015 heavy-ion run.

$N_S - N_P$ [σ]	η_{cold}^{max} [$10^{-2}/\text{m}$]	η_{DS1}^{int} [10^{-2}]	η_{DS2}^{int} [10^{-2}]	η_{cold}^{int} [10^{-2}]
2.5	1.44	8.1	5.5	14.0
2.0	1.41	6.8	5.5	12.7
1.5	1.31	5.6	5.4	11.3
1.0	1.07	4.4	5.3	10.0

The comparison shows that, with tighter setting, the TCSG captures particularly ion fragments which are lost in the first DS loss cluster otherwise. In terms of integrated losses η^{int} , a reduction of almost 50% is simulated in the DS1, compared to a reduction of only 4% in the DS2. The highest loss peak in the superconducting LHC regions is found in the DS1 for all simulations, and is predicted to be reduced by approximately 25% by applying the tightest setting. The loss distribution in the remaining LHC ring is not changed in a significant way. Further analysis of the loss pattern outside IR7 is presented in Chap. 8.2.

In conclusion, the analysis shows that a significant reduction of the DS losses (at least one order of magnitude) can not be achieved by varying the TCSG settings. Given the low potential for

improvement by closing the TCSG collimators, the nominal retraction was maintained.

8.1.2 Orbit Bumps in the IR7 DS

The loss location of off-momentum particles lost due to magnetic dispersion can be modified by means of dedicated orbit changes. The losses due to BFPP, for example, were in the 2015 heavy-ion run shifted into the empty connection cryostat between two superconducting magnets, which reduced the amount of energy lost in the coils of the superconducting magnets and thus also the risk of a magnet quench.

Such shifts of the loss position can be achieved if the theoretical particle trajectory (without aperture restrictions) is beating and the projected penetration depth d_p into the aperture is not too large. The latter is the difference between the dimension of the aperture and the maximum amplitude a particle would reach at the dispersive peak downstream of the loss location, as illustrated in Fig. 8.4. If the loss location of an off-momentum particle is known and d_p is small enough to be compensated by a moderate orbit bump in the opposite direction, the loss location can be shifted towards the next dispersive peak, as shown in Fig. 8.5. Additional bumps in the machine reduce the normalized aperture at the bump location and introduce additional dispersion in the machine, which must be taken into account and limits the achievable bump amplitude. The peak transverse amplitude of the BFPP bump applied in 2015 is $x_b = 3$ mm.

The potential reduction of collimation losses by compensating bumps is limited by the asymmetry of the loss distribution in x . The maximum relative reduction of the cleaning inefficiency $\Delta\bar{\eta}_{max}$ as a function of the cleaning inefficiency from particles impacting on the right side of the beam pipe η_R and those impacting at the left side η_L is given by

$$\Delta\bar{\eta}_{max} = \frac{\eta_R}{\eta_L + \eta_R}, \quad (8.1)$$

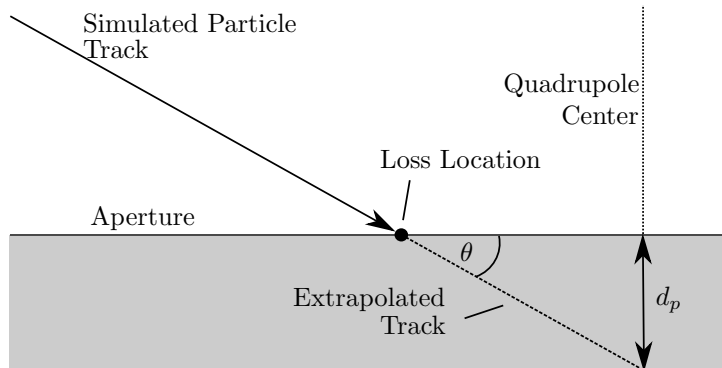


Figure 8.4: Projected penetration depth from the extrapolated particle track in the aperture.

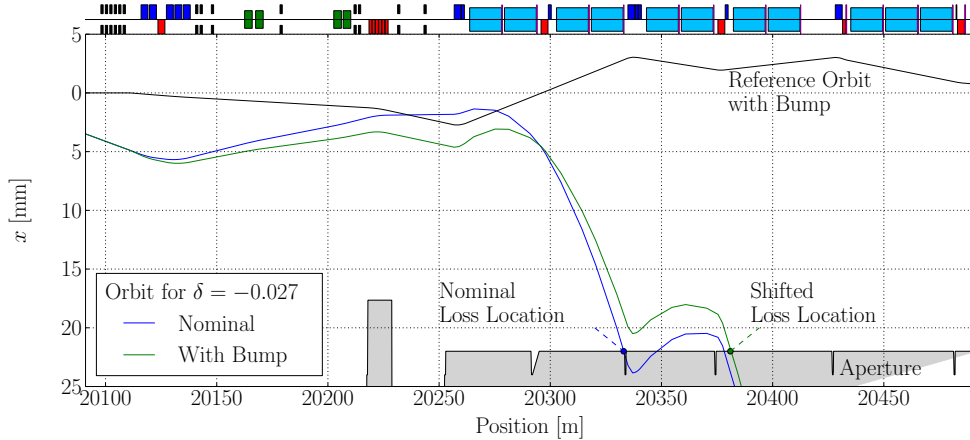


Figure 8.5: Loss location shift of an off-momentum particle by a compensating orbit bump.

assuming that more particles impact the right side of the beam pipe. In case of a full asymmetry of the losses, they can in theory be fully shifted by a dedicated bump.

The possibility of collimation loss mitigation with orbit bumps in the IR7 DS is explored in a dedicated STIER simulation for B1H in the 2015 heavy-ion run configuration. The fragmentation simulation setup and the reference simulation are taken over from the settings validation simulation presented in the previous chapter.

The simulation data unveils that in the DS1 75% of the collimation debris impacts the aperture on the left hand side of the beam pipe, while in the DS2 it is 97%. This finding is in line with the asymmetry in χ observed for the fragments leaving the primary collimator (see Fig. 8.7). These numbers also describe the maximum potential for reduction, which is fully exploited if all losses at the dominating side of impact are alleviated.

Using the STIER simulation data, the possible loss reduction by an orbit bump is studied by means of the projected penetration depth of the isotopes impacting at the two DS clusters. The quantity d_p is extracted from the simulation data by a linear extrapolation of the particle trajectory on the basis of the longitudinal distance between impact location and quadrupole center (in which both betatron function and dispersion are maximum) and the impacting angle at the aperture. This method allows to relate a target loss reduction to the required bump amplitude at the loss location. The distribution of the projected penetration depth of particles impacting the DS is shown for the two different loss clusters in Fig. 8.6. Both clusters show a broad distribution of d_p reaching to values up to more than 25 mm. On the bottom row of Fig. 8.6 the integrated losses are shown as a function of the projected penetration depth, which can be interpreted as the achievable loss reduction with respect to a given bump amplitude. Both integrated loss curves are calculated with respect to the highest achievable loss reduction,

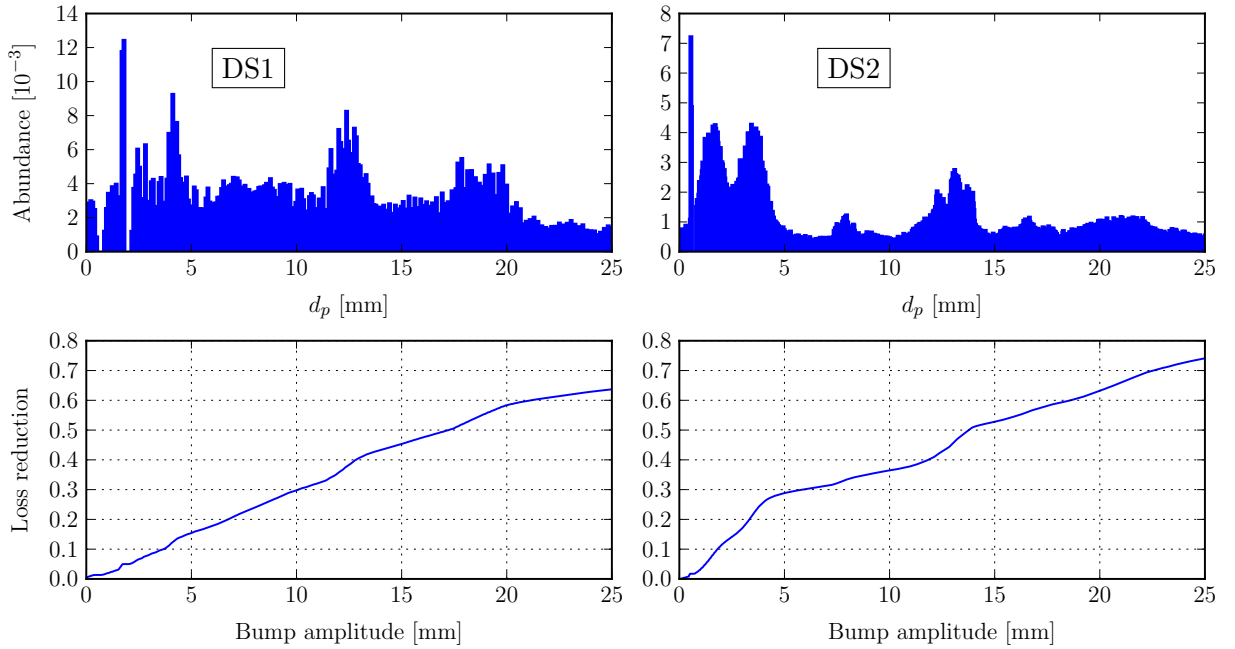


Figure 8.6: Top row: Projected penetration depth of the different isotopes impacting the left side of the beam pipe in DS1 and DS2. Bottom row: Potential loss reduction as a function of the bump amplitude applied at each loss region.

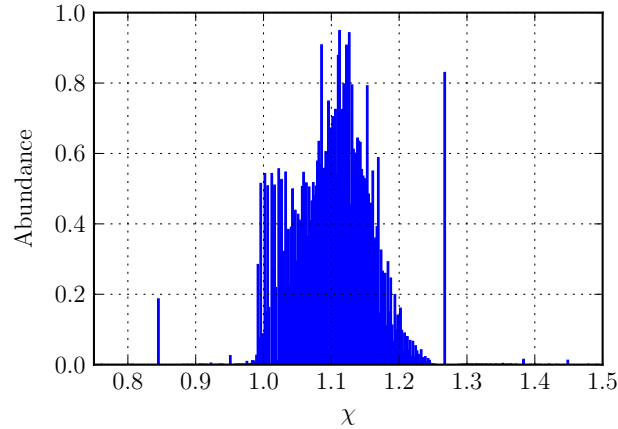


Figure 8.7: Distribution in χ for the particles leaving the primary collimator simulated with FLUKA for $^{208}\text{Pb}^{82+}$ at 6.37 ZTeV .

determined from the loss asymmetry.

The bump amplitude required to alleviate 50% of the losses yields approximately 17 mm in the DS1 and 13.7 mm in the DS2. Both bump amplitudes are beyond acceptable values because the reduction of normalized aperture they imply are unacceptable. Rather, applicable bump

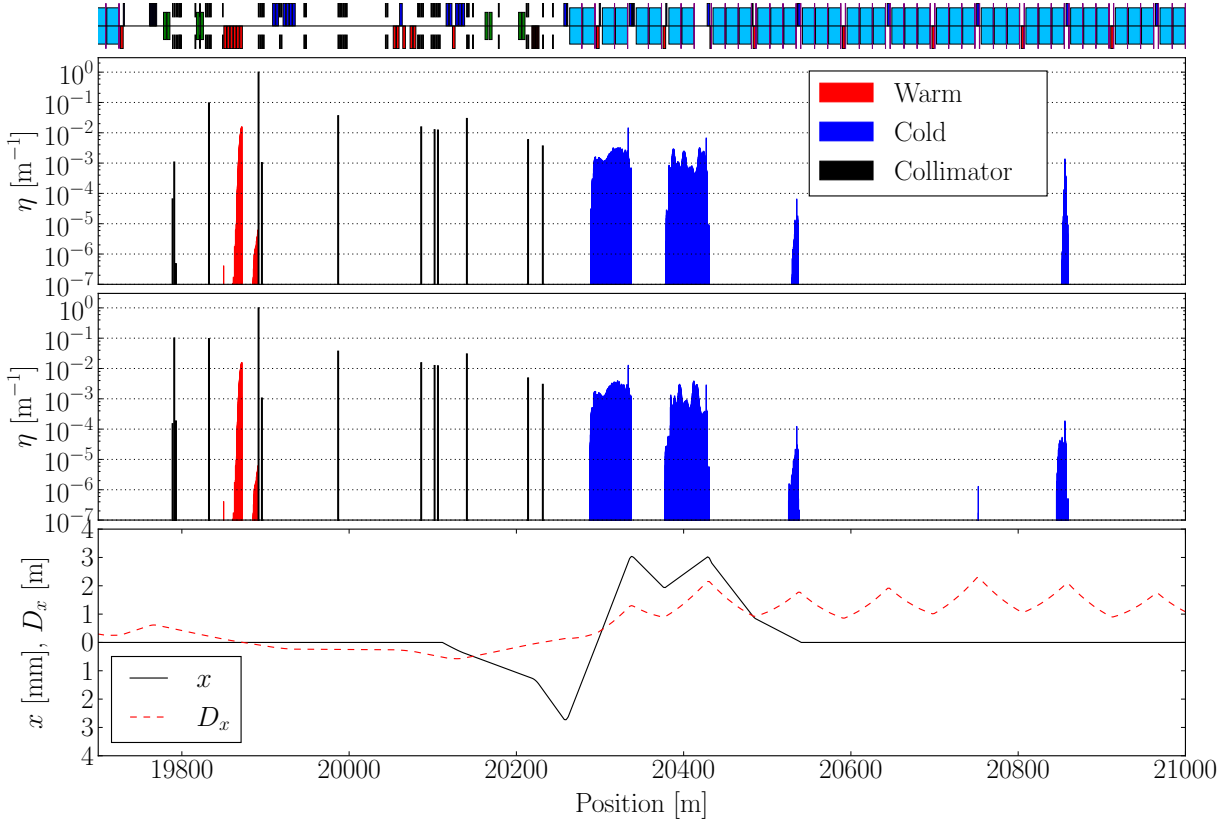


Figure 8.8: Top row: nominal cleaning inefficiency in the 2015 heavy-ion configuration as simulated with STIER. Middle row: simulated cleaning inefficiency with an additional orbit bump having a maximum amplitude of $x_b = +3$ mm at the DS2. Bottom row: beam orbit and periodic dispersion function with the applied bump.

amplitudes are in the order of 3 mm as done for the BFPP loss shift. With this value as a baseline, the reachable loss reduction yields only 6% in the DS1 and 14% in the DS2.

This conclusion is supported by the outcome of a dedicated STIER simulation with an additional bump in positive direction which peaks at an amplitude of $x_b = 3$ mm in the DS2. Besides the additional orbit bump applied, the configuration is identical to the reference simulation of the 2015 heavy-ion run. Compared to the reference simulation, the loss pattern is changed in the DS2 but the peak amplitude in the latter is almost unchanged, as shown in Fig. 8.8. Given the small bump amplitude at the DS1 cluster, these losses are almost unchanged. The losses within the DS2 cluster are re-ordered because the loss location of the individual isotopes is shifted to the right. This is especially true for the losses at the right bound of the DS2, which are shifted into the first loss peak of the LHC arc region as becoming apparent through the increased loss rate at this location. The integrated losses in the DS2 are reduced by approximately 14% in this

scenario which is in excellend agreement with the prediction made on the basis of the projected penetration depth, supporting the accuracy of this method.

In conclusion, the analysis of the projected penetration depth shows that the alleviation of the DS losses would require very large bump aplitudes, which are not compatible with safe operation of the LHC. Also the shift of losses towards the connection cryostat, as it is done for the BFPP losses, is not possible within the available margins of bump amplitudes, because the effective momentum offset of the impacting particles is too large. On the contrary, the loss reduction that is achievable with reasonable bump amplitudes is not sufficiently beneficial to justify the additional efford of integrating it into the operational configuration.

8.2 Suppression of Losses at the IR2 TCT

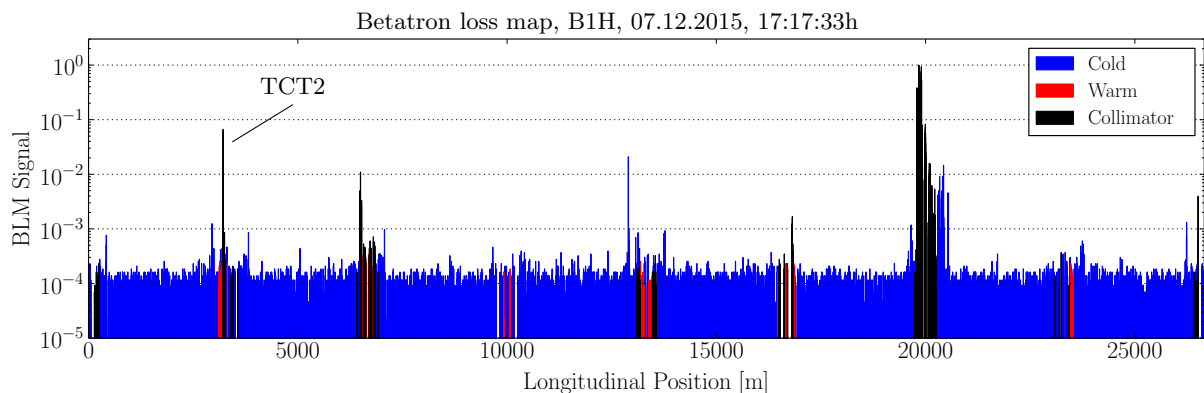


Figure 8.9: Beam 1 horizontal qualification loss map measured in the 2015 heavy-ion run.

The global B1H betatron qualification loss map measured in this operational period is shown in Fig. 8.9. The cleaning inefficiency in the IR7 DS reaches $\eta_{DS} \approx 10^{-2}$, comparable to the 2011 heavy-ion run. The locations in the arc between IR7 and IR8, where high losses were measured in 2011, are free of loss signal above the background level. Very high loss signals with $\eta_{TCT2} \approx 6.6 \times 10^{-2}$ were measured at the horizontal tertiary collimator for Beam 1 in IR2, TCTPH.4L2.B1 (abbreviated TCT2).

The high collimation losses at the TCT2 where present during operation even without additional excitation from the ADT (see Fig. ??). Subsequently, the losses at the TCT2 caused a radiation background and hence distorted the operation of ALICE experiment. The STIER output data was consulted to understand these losses and work out possible strategies to reduce them.

Table 8.2: STIER simulated composition of losses on the TCT2 in the 2015 configuration.

Isotope (A,Z)	TCP jaw	Fraction (%)
(207,82)	left	92.5
(204,81)	right	3.6
(202,80)	left	2.2
(199,79)	right	0.3

8.2.1 Situation and Analysis

Considering that the losses occur at the horizontal TCT for B1, the STIER reference simulation presented in Chap. 8.1.1 can be taken as a baseline for the analysis. The global loss map as simulated with STIER is shown, disentangled for the particles starting at the left and the right TCP jaw, in Fig. 8.10. With the TCT2 losses clearly visible in both simulations, the comparison unveils that the larger fraction originates from the left TCP jaw. The fragments starting from the left jaw cause 20 times more losses than those starting from the right jaw.

The quantitative analysis summarized in Table 8.2 shows that the isotope $^{207}\text{Pb}^{82+}$ starting at the left TCP jaw is clearly dominating over all other isotopes lost at the TCT2. About 92.5% of

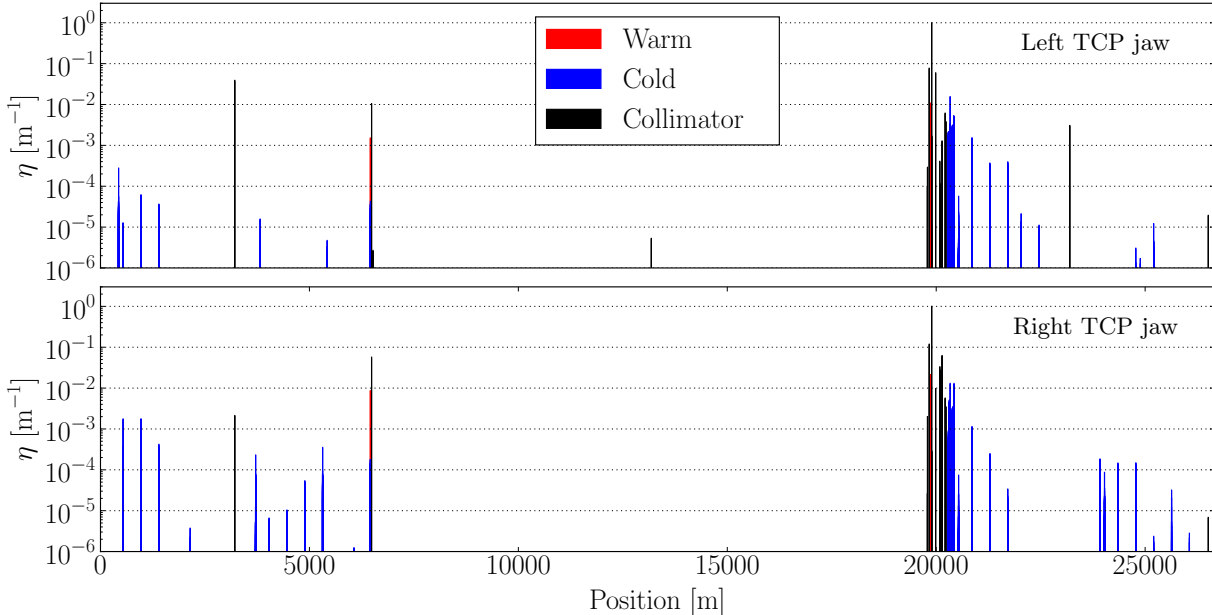


Figure 8.10: STIER simulation result in the 2015 configuration.

the TCT2 loss is caused by this single isotope. Note, however, that the production rate of this isotope and therefore also the loss composition at the TCT2 depends on the impact parameter at the TCP which is $2\mu\text{m}$ in this simulation.

An even better understanding of the situation can be obtained from the horizontal trajectory of the secondary $^{207}\text{Pb}^{82+}$ beam which is generated by EMD in the TCP. The simulated horizontal track of this isotope starting from the left TCP jaw is shown with the machine aperture and the collimators in Fig. 8.11. The secondary beam of the un-matched isotope is not intercepted by the TCSG collimators in IR7 and passes the edge of the right TCTH.4L8.B1 (TCT8) jaw at a small distance. It finally impacts the left jaw of the TCT2 with an impact parameter of several mm. STIER predicts the secondary $^{207}\text{Pb}^{82+}$ beam starting from the right TCP jaw to be intercepted by the momentum collimators in IR3.

These findings allow for two different mitigation strategies which have been tested during the 2015 heavy-ion run with beam in the LHC.

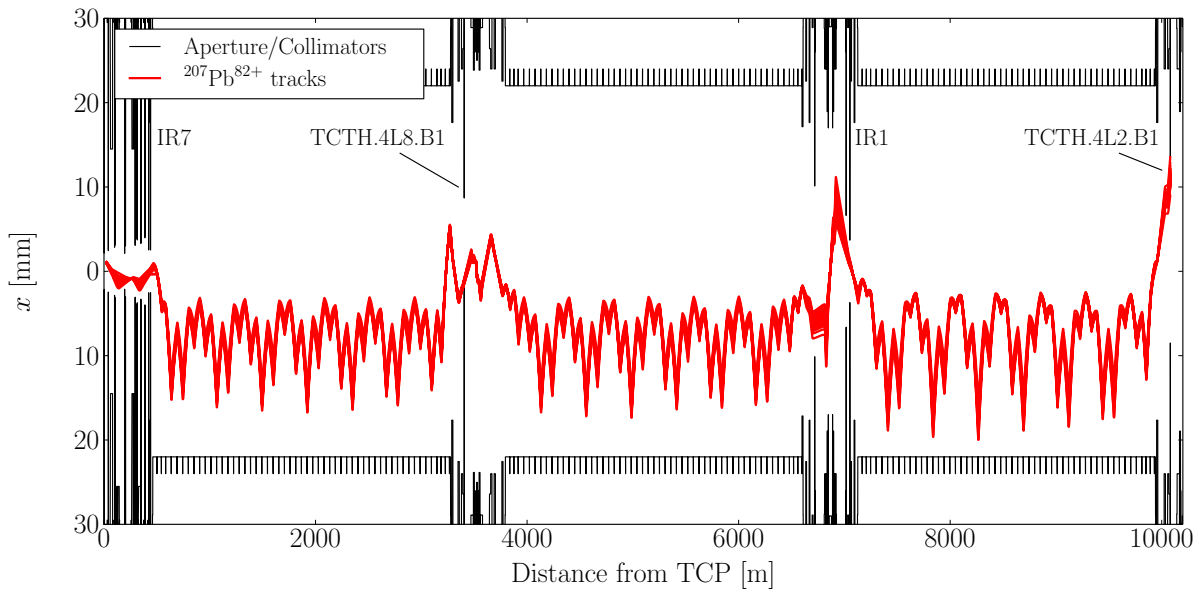


Figure 8.11: Tracks of the secondary $^{207}\text{Pb}^{82+}$ beam starting at the left jaw of TCP.C6L7.B1 and intercepted by the TCTH.4L2.B1. In the STIER model, 92.5% of the losses at the TCTH.4L2.B1 are caused by this secondary ion beam.

8.2.2 Mitigation Strategies and their Application in the LHC

Retraction of the left TCP jaw

The asymmetry in the origin of the TCT2 losses can be exploited by means of asymmetric collimator settings. Given that the majority of losses is caused by particles starting from the left TCP jaw, a significant reduction of these losses can be expected if the latter is retracted. The primary losses in this case are shifted to the right TCP jaw and, at full retraction of the left jaw, the TCT2 losses should be reduced from $\eta_{\text{TCT}} = 6.6 \cdot 10^{-2}$ to $\eta_{\text{TCT}} = 5 \cdot 10^{-3}$. Note that in this case the simulation result can only be compared quantitatively to the measurement because the initial BLM signal is known and scaled with the reduction factor calculated with STIER.

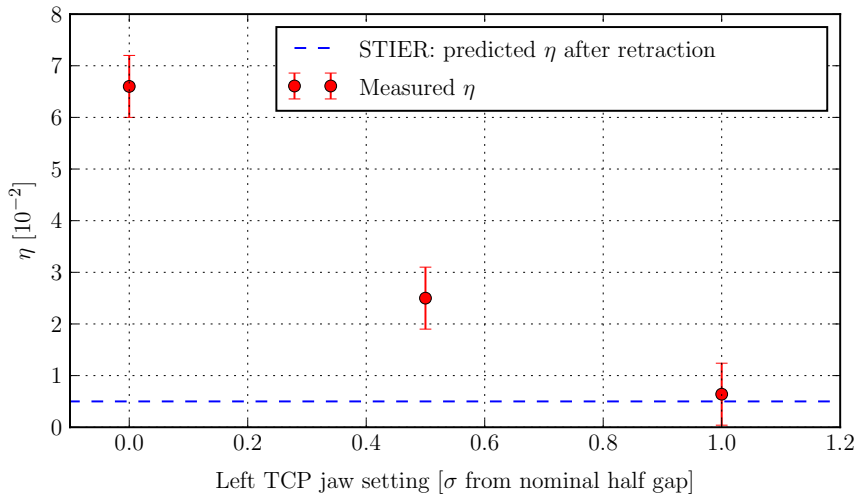


Figure 8.12: Measured BLM Signal (RS09) at the TCT2 for different settings of the left TCP jaw.

The operational test of the mitigation strategy was carried out the 07.12.2015. In this experiment with low intensity beams circulating in the machine at 6.37 TeV with squeezed optics, the left TCP jaw was stepwise retracted and the ADT used to induce the primary losses at the TCP. The individual loss maps measured for this experiment are shown in Fig. A.2. The measured signal¹ at the TCT2 is shown as a function of the left TCP jaw position in Fig. 8.12. During the experiment, the loss signal indeed decreased with increasing retraction of the left TCP jaw and yielded $\eta_{\text{TCT2}} = (6 \pm 6) \cdot 10^{-3}$ at the most extreme scenario of a full retraction. This result is in excellent agreement with the prediction made by STIER. As a consistency check, the same experiment was repeated with the left TCP jaw in place and the right TCP jaw retraction,

¹The error bars are estimated from variations of the measured η_{TCT2} in different measurement campaigns. It corresponds to the difference between the largest and the smallest η_{TCT2} measured.

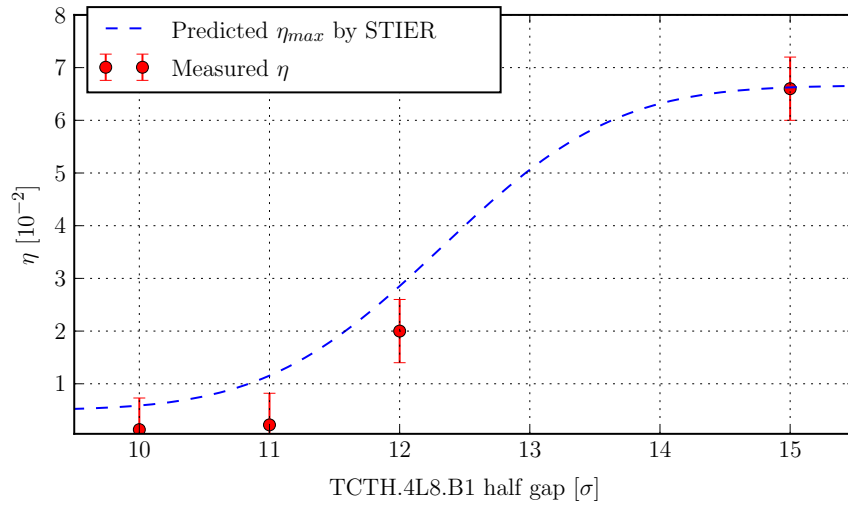


Figure 8.13: Measured signal RS09 signal at the BLMTI.04L2.B1E10_TCTPH.4L2.B1 (normalized to the highest loss singal in the ring) as a function of the TCTH.4L8.B1 half gap. The blue line shows the predicted upper boundary of the cleaning inefficiency η_{max} as simulated with STIER.

with the result that no loss reduction was achieved. The outcome of this experiment confirms that the assumption that the collimation losses are dominated by secondary particles generated at the TCP is valid.

Tightening the TCT in IR8

The track shows that the secondary ion beam passes the horizontal TCT8 at a very small distance in x . In a second experiment this prediction was studied by closing the TCT8 in steps. The measured loss maps for the individual steps are shown in Fig. A.1. For this experiment, STIER can be used to determine expected loss signal at the TCT2 as a function of the TCT8 half gap. To do so, the beam size of the secondary $^{207}\text{Pb}^{82+}$ beam must be determined, which can be done with a dedicated MAD-X simulation in which the betatron function is calculated taking into account the offset in rigidity with respect to the main beam². Assuming that the emittance is not significantly different than that of the main beam, the rms beam size is used to predict the transverse particle distribution, modelled as a Gaussian that is superimposed to the particle track predicted by STIER. With this model, the fraction of the secondary $^{207}\text{Pb}^{82+}$ beam that is intercepted by the TCT8 can be determined and converted into the expected loss reduction at the TCT2. The latter requires to take into account that the studied isotope is not the only one lost at the TCT2, thus the predicted reduction of the secondary $^{207}\text{Pb}^{82+}$ beam intensity

²The betatron function is momentum-dependent.

must be scaled with its contribution to the TCT2 losses, which yields 0.925. Furthermore, the remaining isotopes may also be intercepted by the TCT8 which would also reduce the TCT2 loss signal. This is not modelled in this approach, such that the result indicates only an upper boundary η_{\max} of the expected TCT2 signal.

The measured TCT2 signals as a function of the TCT8 half gap is shown together with η_{\max} predicted by STIER in Fig. 8.13. Also this experiment shows an excellent agreement with the prediction made by STIER.

8.2.3 Conclusions

Both mitigation strategies derived from the STIER simulation data have been proven to be effective and the predicted loss levels are quantitatively supported by the measured experimental data. This result underlines the importance of heavy-ion collimation simulation tools, which are essential to optimize the collimation system if the stored beam energy shall be further increased. After the successful test the application of asymmetric TCP settings to reduce the background at the ALICE experiment was under discussion. The decision was taken to accept the TCT2 losses and maintain the nominal collimator configuration to save the time otherwise required for a re-commissioning of the new configuration.

8.3 Heavy-Ion Collimation Quench Test

To exploit the full potential of the LHC and achieve the highest possible (integrated) luminosity, the intensity has to be pushed to the maximum which is compatible with safe and uninterrupted operation. Limitations on the achievable beam intensity are mainly imposed by the quench limit in the superconducting DS magnets downstream of IR7. As shown in Chap. 3.5.3, the quench limit of the latter is not well understood and subject to large uncertainties. They also depend on the loss scenario, which reflects in the fact that the BLM thresholds are set with respect to the expected quench limit for UFO³ events [].

The quench limit for other loss scenarios, such as the impact of collimation debris on the superconducting magnets must be experimentally accessed in operational conditions. Very high losses are produced at the primary collimator in dedicated tests with the aim to quench the IR7 DS magnets with the collimation debris in a controlled manner.

Multiple of such dedicated collimation quench tests have been carried out in the past to get experimental input for quench test analyses. They are summarized in Table 8.3. The measurements are complemented by theoretical simulations of the experimental set up which allow for

³Unidentified Falling Objects in the beam pipe. Their interaction with the circulating beam causes secondary showers which can quench the superconducting magnets.

detailed shower propagation and energy deposition studies and hence the interrelation of the measured BLM signal to the energy deposited in the magnet coils [SBC⁺15]. The so obtained information gives indispensable input for the study of potential collimator upgrades required to further push the luminosity.

Table 8.3: Key parameters of collimation quench tests carried out at the LHC.

Year	Energy [Z GeV]	Particle	Method	P_{\max} [kW]	loss duration [s]	Quench	Ref.
2011	3.5	p	tune	500	1	No	
2013	4.0	p	ADT	1050	5-10	No	
2015	6.5	p	ADT	585	4	No	
2011	3.5	$^{208}\text{Pb}^{82+}$	tune	151	0.075	No	
2015	6.37	$^{208}\text{Pb}^{82+}$	ADT	15	14	Yes	

The worse cleaning performance with heavy-ion beams implies smaller loss rates than with proton beams as can be seen in Table 8.3. Also the loss duration is of great importance for the quench limit. While the quench tests in early operation used tune resonance crossing methods which induces fast losses at the primary collimators, the tests from 2013 on could make use of the transverse damper. This led to a much better controllability of the losses and came along with a significant increase of the loss duration enabling to study the quench limit with steady state losses. The presented 2015 heavy-ion collimation quench test is the first collimation quench test in which a quench was achieved. The following analysis is partly presented in [HAB⁺16].

TREF: <https://accelconf.web.cern.ch/accelconf/HB2012/papers/mop245.pdf>

8.3.1 Preparation & Experimental Schedule

The preparation of the test includes to determine the beam parameters, target loss rates and machine modifications required for the successful realization of the experiment. The quench limit in the DS magnets downstream of IR7 is probed with collimation debris which is lost immediately after its generation in the primary collimators. Therefore, the quench limit in operational conditions can be tested with un-squeezed beams in the IRs (flat top at 6.37 Z TeV). Accordingly the collimator settings correspond to the operational settings in the collision mode, except for the TCTs and physics debris collimators (see Table 8.4).

The beam and plane to be used for the test can in principle be freely chosen, where preference should be given to the horizontal plane in which the DS losses are typically higher (see Chap. ??).

Table 8.4: Collimator settings in σ applied in the collimation quench test.

	IR7	IR3		IR1/2/5/8/6	
TCP	5.5	TCP	15.0	TCT	37.0
TCSG	8.0	TCSG	18.0	TCL	out
TCLA	14.0	TCLA	20.0	TCDQ	9.1

The decision was taken to use B2H for the test to potentially benefit from synergies with the precedent proton quench test.

Target Beam Loss Rate

The target loss rate at the primary collimator is an important measure which must be defined before the experiment is started. The loss rate imposes a lower limit on the number of bunches that must be excited simultaneously. Furthermore, the BLM thresholds have to be adjusted to allow for the high amount of losses which would trigger a beam dump otherwise.

As explained before, the quench limit is related to many uncertainties. The preparation target loss rate was therefore based on the operational BLM thresholds. The latter are set to 1.5 times the assumed quench limit for UFO events, which is taken as a baseline, in spite of the different loss mechanism due to the lack of more accurate approaches. The qualification loss map for B2H measured in the 2015 heavy-ion run is shown in Fig. ???. The highest BLM signal at the superconducting LHC magnets is measured at the `BLMQI.09L7.B2I10.MQ`. The measured cleaning inefficiency (RS09) at this BLM is $\eta = (1.6 \pm 0.2) \times 10^{-2}$. At the beam excitation associated with this loss map measurement, an intensity drop equivalent to a peak primary beam loss of $P_l = 123$ W was measured with the beam current transformers (BCT) []. Taking into account the fact that the peak BLM signal B_m at the loss map measurement is related to the assumed quench limit B_q of the concerned BLM as

$$\frac{B_m}{B_q} = (8.8 \pm 1.1) \cdot 10^{-3}, \quad (8.2)$$

the BLM signal equivalent to the assumed quench limit for UFO events yields

$$P_q^T = \frac{B_q}{B_m} P_l = (13.9 \pm 1.8) \text{ kW}. \quad (8.3)$$

This number should, however, only be regarded as rough estimate because the loss mechanism is different from the UFO scenario to which the BLM threshold is adjusted. Furthermore, even for the UFO event the quench limit is related to uncertainties such that the primary loss rate at

which a quench occurs might be above or below. For this reason, it was decided to prepare for a target beam loss rate significantly above this value and, during the experiment, increase the loss rate in steps to narrow down the real quench limit.

The upper boundary for the achievable loss rate is given by the power load the primary collimators can resist. Being designed to withstand continuous proton losses of 487 kW, the analysis of the 2013 proton collimation quench test demonstrated that their physical integrity is not endangered by losses up to 1 MW [S⁺14a].

The dominating process of energy deposition in the collimator is different for protons and heavy-ions. The power deposited by an impacting proton and $^{208}\text{Pb}^{82+}$ ion at 7 Z TeV along the primary collimator is shown in Fig. 21.7 in [B⁺04b]. The charge dependence of the Bethe-Bloch formula indicates that the energy deposited by the $^{208}\text{Pb}^{82+}$ ions is much more driven by ionization losses than for protons with the peak energy deposited from $^{208}\text{Pb}^{82+}$ being approximately 57 GeV/cm³/charge. For protons it is approximately 6.5 GeV/cm³/charge, mainly due to hadronic showers produced during the passage through the collimator. Based on this finding, the peak loss rate at the primary collimator was conservatively limited to 100 kW, leaving enough margin to significantly outreach the power load derived in Eq. (8.3).

From the envisaged peak power load, the number of bunches required can be deduced. Conservatively assuming that one ion bunch carries 10^{10} charges with an energy of 6.37 TeV per charge, the energy per bunch yields $E_B = 10$ kJ. The LHC interlock system triggers a beam dump if the bunch intensity of a circulating bunch is below 30% of its nominal value, because the beam position monitors (BPM) [] require sufficiently populated bunches to accurately measure their position. With this information included, the required number of bunches for continuous losses over 10 s yields $n_B^P = 1.4$ bunches/kW.

BLM Thresholds

From the qualification loss map and the loss rate associated, the expected BLM signals at a peak loss rate of 100 kW can be estimated for the full ring. This data is used to derive the increase of BLM thresholds required to permit the target loss rate during the experiment without triggering a beam dump. In the preparation phase of the experiment the required modifications on the BLM thresholds (mainly the BLMs in IR7) were prepared and presented in [Kal15].

8.3.2 Realization

From the n_B^P parameter, the required number of bunches to achieve a given loss rate can be deduced. The chosen approach of a stepwise increase of the loss rate at the primary collimators reflects in the filling schedule that was foreseen for the experiment, shown in Table 8.5. An

Table 8.5: Proposed and realized fills for the MD. The quench occurred in the first ramp.

Fill	Bunches	E [Z TeV]	P_{max} [kW]
Planned			
1	8	0.45	≈ 0.1
2	$8 + 4 \times 24$	6.37	13.5
3	8×24	6.37	50
4	8×24	6.37	100
Realized			
1	3×24	0.45	0.6
2	$2 + 12 \times 24$	6.37	15.0

initial fill at injection energy was dedicated to the set-up of the ADT. The control software of the latter is designed for the excitation of single bunches and had to be adjusted to allow for the excitation of the many bunches required to achieve the target loss rate. Also the time profile of the losses was adjusted to flatten the loss profile with continuous losses at a given level. More details on the ADT modifications are given in [HAB⁺16].

In the second fill four bunch trains of 24 bunches as well as 8 individual bunches were foreseen to be accelerated to top energy for a first quench attempt with a peak loss rate around 13.5 kW. This approximately corresponds to the loss rate required to reach the BLM signal equivalent to the assumed quench limit for UFO events. The individual bunches allowed a first test of the ADT excitation at top energy for small intensities and hence without the risk of outreaching the envisaged loss rate. The bunch trains carry enough particles to allow multiple attempts at a peak loss rate of approximately 13.5 kW. In case a quench could not have been achieved, two optional fills were foreseen to increase the loss rate to 50 kW and 100 kW respectively.

The heavy-ion collimation quench test was carried out the 13.12.2015 from 17:00h and ended with the quench at 22:08 h (fill numbers 4722 & 4723). The filling scheme and the envisaged peak loss rates were slightly modified during the experiment due to time constraints (see Table 8.5). After the set up of the ADT in fill 1, the machine was filled with 12 bunch trains of 24 bunches and 2 single bunches which were accelerated to 6.37 Z TeV. At the first excitation of 6 bunch trains, the MBB.9L7 quenched at a peak power loss of approximately

$$P_q \approx (15 \pm 1) \text{ kW}. \quad (8.4)$$

The beam was subsequently dumped by the quench protection system (QPS). The intensity and

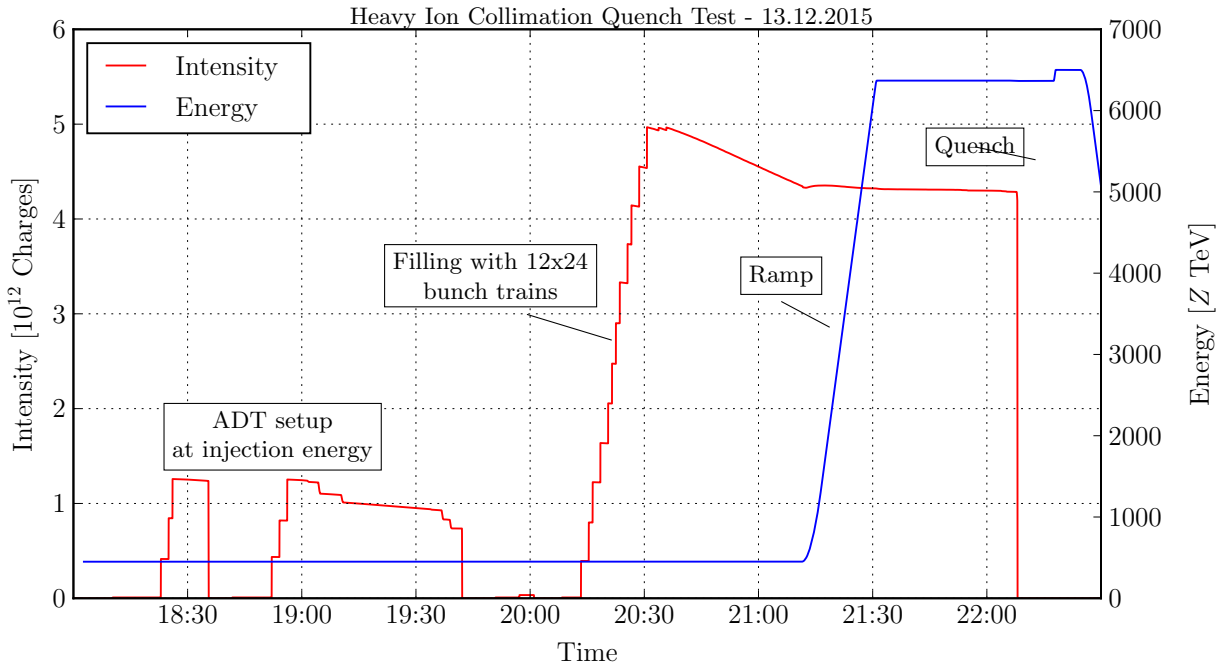


Figure 8.14: Intensity and particle energy evolution during the quench test.

energy evolution throughout the experiment is shown in Fig. 8.14.

8.3.3 Data Analysis

The evolution of the beam intensity, the power loss derived from it and the BLM signal at the quench location during the final excitation which quenched the magnet is shown in Fig. 8.15. The error bar on the beam intensity derived from the standard deviation of the BCT signal is negligible. The uncertainty on the peak power loss which is derived from the latter is therefore estimated based upon the fluctuations visible in the rising power load evolution. The loss rate increased continuously over approximately 14 s when the peak power load was achieved and the quench occurred. Note that the apparent agreement with P_q^T is coincidental because the loss scenario from which the latter is derived is fundamentally different.

In lack of better estimates, the measurement result can be used to scale the permitted stored beam energy in the LHC on the basis of the minimum beam lifetime. In this analysis it must be taken into account that the quench limit at design rigidity is going to be lower than at $6.37 Z \text{ TeV}$. Presently, no accurate estimate on the scaling of the quench limit with higher magnetic field is available, such that the total stored beam energy which can be derived from the quench test result represents only an upper limit. Considering the design value of $\tau = 12 \text{ min}$ for minimum

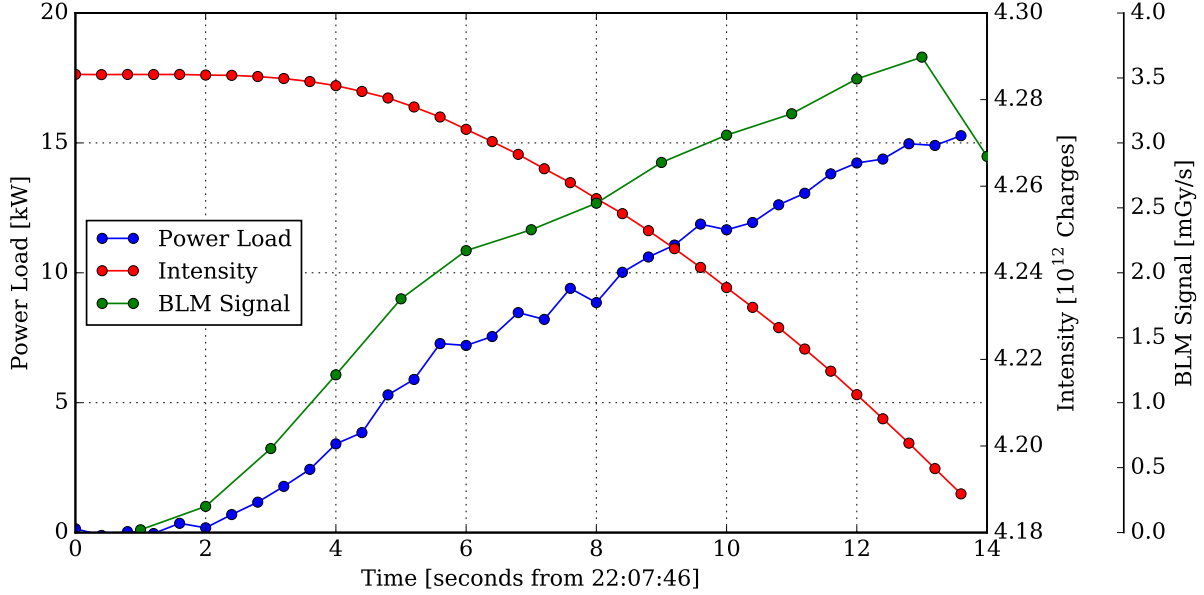


Figure 8.15: Power load on the TCP, intensity evolution and measured BLM signal (BLMEI.09L7.B2I30, RS09) during the final beam excitation in which the quench was achieved in cell 9 L7.

beam life time, the maximum stored beam energy at $7 Z$ TeV yields

$$E_{\max}^{\text{tot}} < P_q \tau = (10.8 \pm 0.8) \text{ MJ}. \quad (8.5)$$

This value is very close to the stored beam energy already achieved in the 2015 heavy-ion run and therefore imposes a serious limitation for the achievable luminosity in future operation. Eventual upgrades of the collimation system and studies of the cleaning inefficiency in future LHC configuration should take this limitation into account. From the measured cleaning inefficiency at the MBB.9L7 and the known peak power loss at the TCP, a rough estimate of the peak power deposited in the latter can be extracted as:

$$P_{\text{MBB}} = \eta_Q P_q = (330 \pm 30) \text{ W}. \quad (8.6)$$

This value should be regarded with caution, knowing that the energy deposited is related to the BLM signals via a response function which is unknown. Better estimates for the power deposited can be obtained with the detailed shower deposition study carried out with FLUKA on the basis of a dedicated hiSixTrack simulation in which the toucMap data is used for a subsequent FLUKA simulation.

The hiSixTrack simulation is carried out with $6.8 \cdot 10^6$ initial $^{208}\text{Pb}^{82+}$ ions starting at IP1 for

B2H. The simulated optics and collimator settings are identical to the settings applied in the measurement. The impact parameter at the TCP.C6R7.B2 was set to $0.5 \mu\text{m}$ to $2.0 \mu\text{m}$ on both collimator jaws. The simulated loss pattern is compared to the loss map measured during the quench test and the qualification loss map used for the preparation in Fig. 8.16 (full ring) and Fig. 8.17 (zoom to IR7). The highest loss signal in the cold regions was measured at the time of the quench at the MBB.9L7 with a loss signal of $\eta_Q = (2.2 \pm 0.4) \cdot 10^{-2}$, while in the loss map the highest loss signal was measured at the MQY in the same cell, with a slightly lower cleaning inefficiency. This discrepancy is not considered grave because the impact parameter might be different in the two measurements.

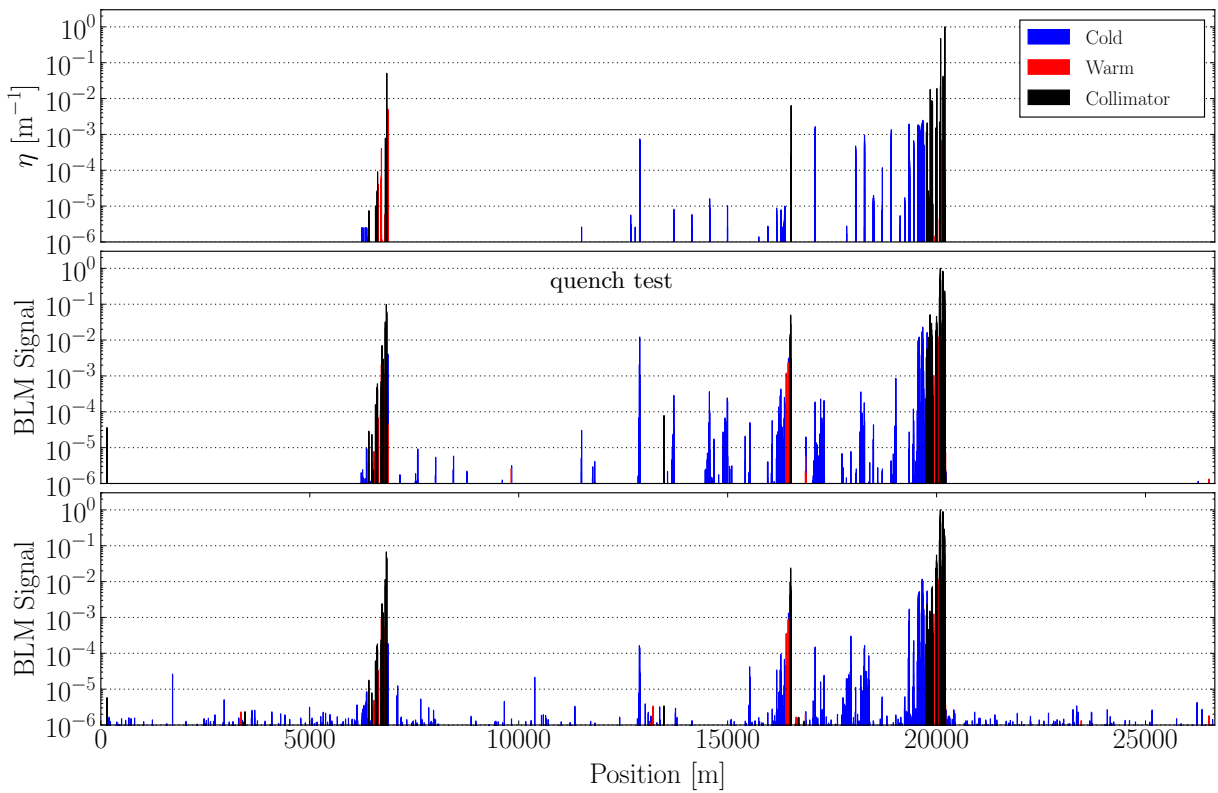


Figure 8.16: Measured and simulated B2H loss maps for the B2H collimation quench test (full ring).

The qualification loss map simulated with hiSixTrack shows a good overall agreement with the measured loss maps. The dominating losses in IR7, IR6, and IR3 are well modelled in the simulation and also the loss peak C5 (see Fig. ??) in the cold region downstream of IR5 is well predicted in hiSixTrack. Remarkable differences arise in the arcs between IR5 and IR6 as well as IR6 and IR7. The loss peaks in the prior are only visible in the loss map measured during the quench test, while they are neither simulated nor measured in the qualification loss

map, even though their amplitude should be above the noise level. The same applies for the pronounced loss peaks in the arc between IR6 and IR7, where some of them are simulated in hiSixTrack, but not measured in the qualification loss map. These discrepancies are not understood and subject to further investigation. Possible reasons could be orbit fluctuations between the different measurements.

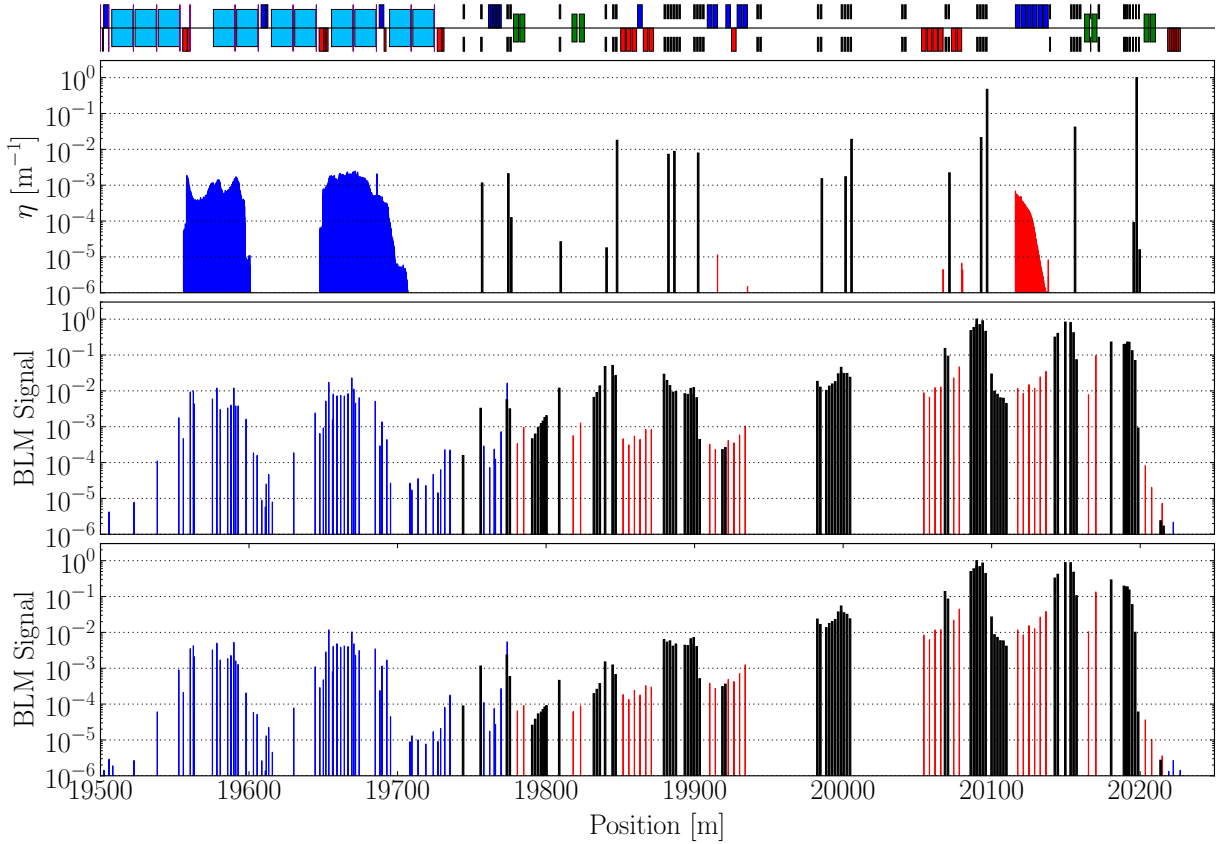


Figure 8.17: Figure caption

With hiSixTrack, the highest loss peak in the cold regions is located at the MBB.9L7, in line with the measurement and the quench location. At this location, the simulated cleaning inefficiency is $\eta_{\text{MBB}}^S = 2.4 \cdot 10^{-3} \text{ m}^{-1}$. As explained before this value should not be compared quantitatively to the measured cleaning inefficiency. The loss composition in the DS1 and DS2 is listed in Table ???. While the losses in the DS1 are composed of many different isotopes with rather small contributions of single ion species, compared to the DS2. In the latter, more than one third of the losses are induced by $^{205}\text{Pb}^{82+}$. As shown in previous chapters, this diverse composition of the losses in the DS makes it difficult to mitigate these losses without hardware modifications.

Table 8.6: Isotope composition in the DS clusters in the quench test simulation.

DS1		DS2	
Isotope (A,Z)	Fraction[%]	Isotope (A,Z)	Fraction[%]
203, 82	7.7	205, 82	36.8
202, 82	6.9	206, 82	21.3
201, 81	5.3	203, 81	17.3
200, 81	4.5	200, 80	6.8
199, 81	4.1	202, 81	6.6

BLM Signals

An important outcome of the experiment are the measured BLM signals at quench with respect to the BLM thresholds. The BLM signals at the BLMEI.09L7.B2I30 at the moment of the quench are shown, normalized to the operational BLM thresholds, for all running sums in Fig. 8.18. The highest signal is measured for RS10 with a factor 3.5 of the applied threshold. For RS09 and RS11, the thresholds were exceeded by 60% and 110% respectively [HAB⁺16]. This is an important information for the setting of BLM thresholds in future heavy-ion runs.

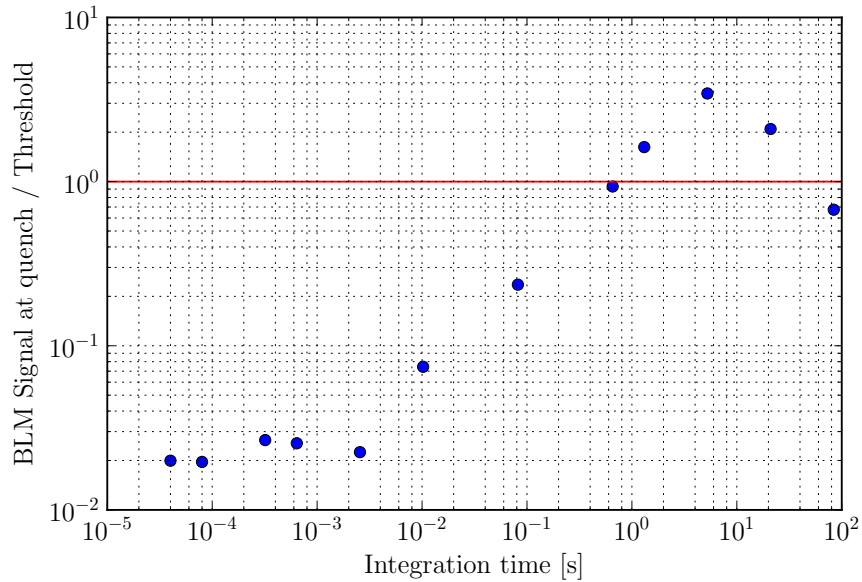


Figure 8.18: Figure caption

8.3.4 Summary and Outlook

The LHC heavy-ion collimation quench test was the first collimation quench test in which a quench was achieved. With the collimation debris generated in the horizontal TCP for B2, the MBB.L7 was quenched when a power of (15 ± 1) kW was deposited at the primary collimator. Extrapolating from the TCP power load and the minimum beam life time, the upper limit for the achievable stored beam energy is 10.8 MJ. As shown in the next chapter, the beam intensities foreseen for the future LHC operation after the LIU upgrade in the HL-LHC era are significantly above this value. In combination with the results of Chap. 8.1, the most important conclusion of the heavy-ion collimation quench test is that the envisaged intensities can not be achieved without an upgrade of the LHC collimation system. A possible upgrade with additional collimators in the DS region is studied in the next chapter.

9. Future LHC Configurations

9.1 Heavy-Ion Operation in 2016

9.2 HL-LHC Upgrade with TCLD Collimators

9.2.1 LIU and High Luminosity LHC

For the future of the LHC, a drastic increase of the luminosity is foreseen to increase the potential for discoveries. The current baseline foresees the commissioning of the High Luminosity LHC (HL-LHC) adapted for a luminosity five times beyond the design value as of 2025, after a period of dedicated hardware upgrades [BR16]. An essential keystone for this aim is the increase of the bunch intensity and the possible number of bunches that can be stored in the machine. This is made possible by the LHC injectors upgrade (LIU) [GGG⁺¹¹, MCD⁺¹⁵], a modification of the injector chain with hardware upgrades and even the replacement of LINAC2 by a new H⁻ accelerator LINAC4 [MCD⁺¹⁵]. The schedule to reach the HL-LHC parameters foresees a stepwise luminosity increase in which double of the design luminosity shall be reached after the LIU in long shutdown 2 [BR16].

For the HL-LHC upgrade additional physics debris collimators, TCLX are foreseen to be installed

Table 9.1: Comparison of heavy-ion beam parameters: design parameters [B^{+04b}], achieved in the 2015 heavy-ion run, envisaged parameters for LIU [GGG⁺¹¹, MCD⁺¹⁵] and HL-LHC []

	E [Z TeV]	n_B μm rad	ϵ_N	I_B [10 ⁷ ions]	E^{tot} [MJ]
Design	7.0	592	3.75	7	3.81
2015	6.37	518	1.5±0.15	22±3	9.54±1.30
LIU baseline	7.0	1152	1.2	17	18.0
HL-LHC request	7.0	1248	1.3	21	24.1

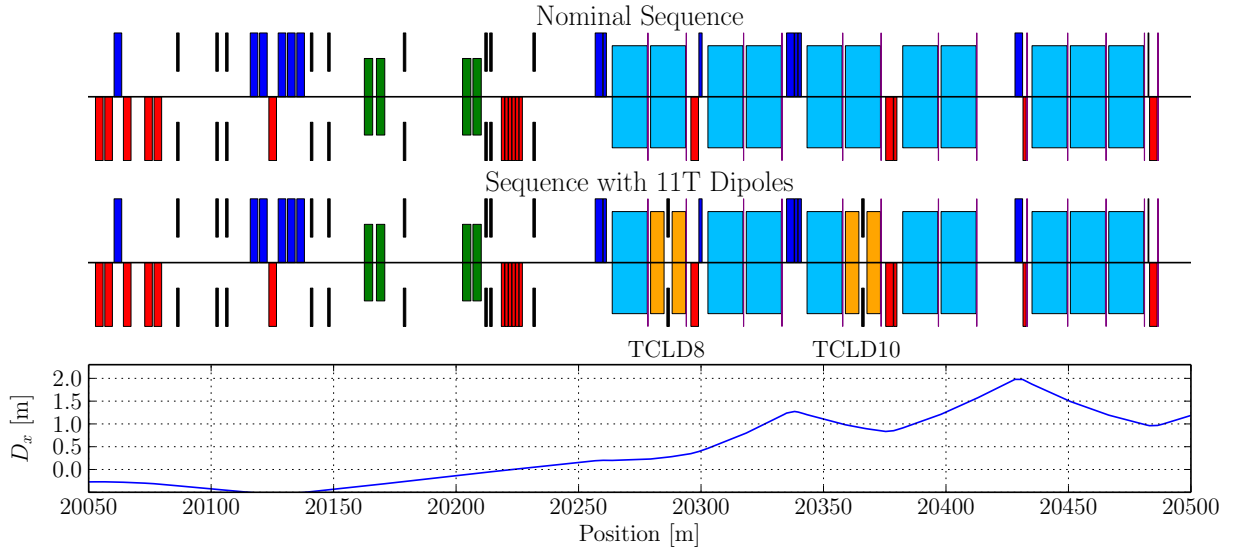


Figure 9.1: LHC beam line sequence in IR7. Top: Nominal sequence. Middle: sequence with the main dipoles in cell 8 and cell 10 replaced by two 11 T dipoles and the TCCLD collimators in between. Bottom: horizontal dispersion function.

in the experimental insertions. Furthermore, new TCSP collimators with CFC as the active material are to be installed in IR6.

Crab cavities are not installed in the present LHC configuration, but their installation is foreseen for HL-LHC (see Chap. 9.2).

The luminosity increase is envisaged for both, proton and heavy-ion beams. The relevant parameters are compared for the design values, the values achieved in 2015 and present optimistic estimates for the LIU and HL-LHC upgrade in Table 9.1.

This comparison makes apparent that the stored beam energies are envisaged to increase drastically to values more than six times the design values. Note that the target bunch intensity for LIU has already been exceeded in the 2015 heavy-ion run. Inevitably, the increased stored beam energy will increase the collimation losses, especially in the IR7 DS regions. The collimation quench test unveiled that with the present collimation system the largest acceptable stored beam energy is very close to the values yet achieved in the 2015 heavy-ion run.

The safe and uninterrupted operation with HL-LHC intensities shall be ensured by means of additional collimators in the DS region downstream of IR7. The required space would be made available by replacing a main dipole with a maximum magnetic field of 8.3 T dipole by two stronger dipoles (with a maximum field strength of 11 T). In the center of the two dipoles a new collimator, denominated TCCLD, could be installed (see Fig. 9.1). To provide a large cross section for absorption, the present layout foresees tungsten as the active material of the TCCLD

collimators. In view of the two most critical loss locations in the cells 9 and 11 downstream of IR7, the proposal foresees the new collimators to be installed immediately upstream of them in the cells 8 and 10 [W⁺08, BMR14].

As presented in [BMR14], the TCLD collimators have been demonstrated to significantly improve the cleaning inefficiency for proton beams. In this chapter the cleaning inefficiency in the HL-LHC configuration is studied with STIER and hiSixTrack for heavy-ion beams with and without the TCLD collimators. Given that especially the construction of the stronger dipole magnets requires significant financial resources, the present estimate for the integrated cost of the installation of one TCLD is presently approximately 7 mio CHF. Therefore, a solution in which only one TCLD is required (installed in cell 8), is desirable. The presented simulations are therefore carried out for three cases to compare the limiting cleaning inefficiency and evaluate the risk of quenches for the three scenarios:

- 0 TCLDs: reference simulation for the present layout without additional collimators,
- 1 TCLD: layout with an additional TCLD collimator in cell 8,
- 2 TCLDs: two TCLD collimators are installed cell 8 and cell 10.

9.2.2 Consistency Check with STIER

The first simulation of the cleaning inefficiency with heavy-ions in the HL-LHC configuration was conducted with the STIER simulation tool. The optics used for the simulation is identical to the settings used in the 2011 heavy-ion run, due to a lack of concrete optics proposals at the time the simulation was conducted. Hitherto a change of the optics in IR7 is not envisaged. Therefore, the cleaning inefficiency simulated in the IR7 DS should not be affected by eventual optics changes coming up in the experimental IRs. The collimator half gaps applied in the simulation are the design settings summarized in Table 3.6 and the TCLD collimators set to a half gap of 10σ . The presented simulations are carried out for B1H with 10^6 initial $^{208}\text{Pb}^{82+}$ ions at an energy of 7 Z TeV, impacting the TCP at an impact parameter of $10\ \mu\text{m}$. The STIER simulation with these parameters predicts a significant improvement of the cleaning performance with the TCLD collimators, as presented in detail in [HBJ⁺15]. In this section, only the simulation result without DS collimators is presented to validate the hiSixTrack simulations. In the next sections the cleaning performance with TCLD collimators shall be presented in a more thorough analysis with hiSixTrack, based on more recent estimates for the collimator settings, optics and including also secondary particles generated in the TCLDs.

The cleaning inefficiency in the HL-LHC configuration without TCLD collimators as simulated with STIER and hiSixTrack is shown in Fig. 9.2. Both simulations take into account identical

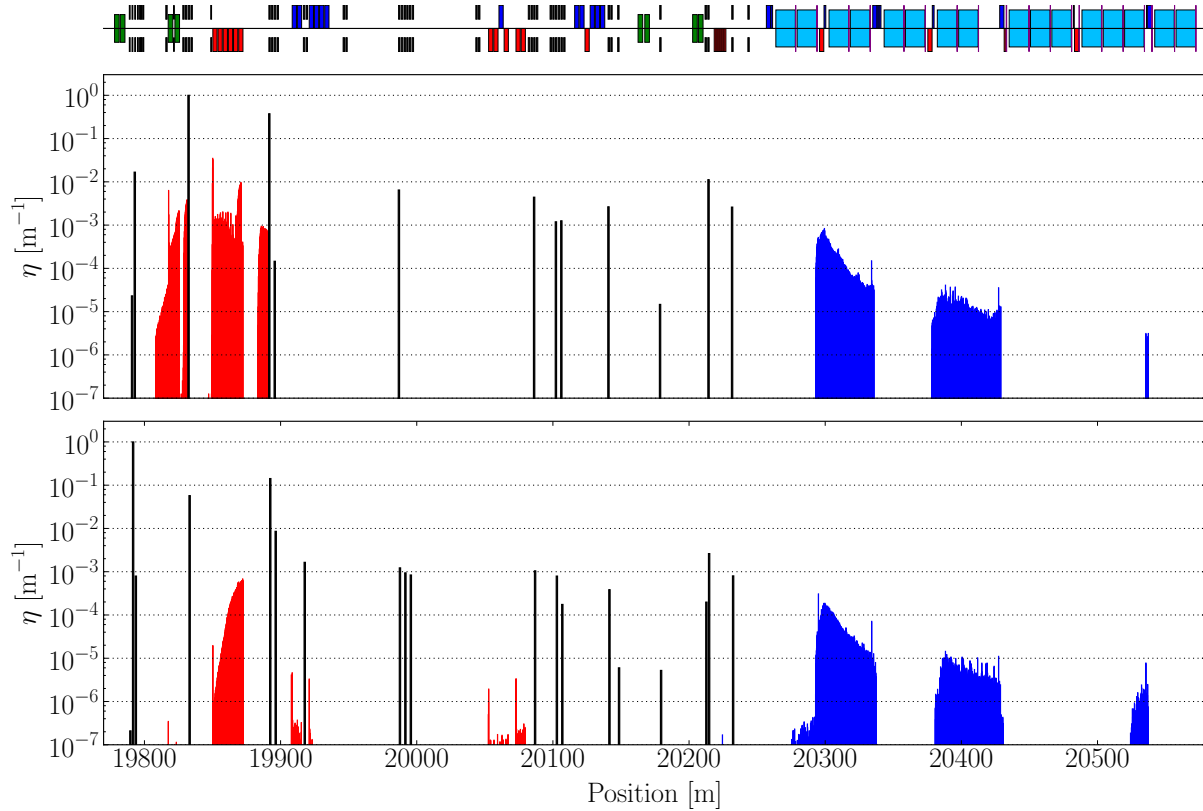


Figure 9.2: Cleaning inefficiency of HL-LHC at 7 Z TeV simulated with STIER (top) and hiSixTrack (bottom).

settings of the collimators with the TCP at 6.0σ and the same impact parameter $b = 10\mu\text{m}$ at the TCP jaw. The simulated losses at the TCP and the TCSG collimators downstream is different between the two simulations, with the reasons discussed in Chap. 7.6.2. The same reason applies for the apparent discrepancy of the loss rate in the IR7 DS clusters, which are simulated to be smaller in hiSixTrack than in STIER. The more accurate accounting of the TCP losses leads to a higher loss rate at the latter, leading to an apparent reduction of the losses at the remaining locations.

The shape of the DS loss clusters is, however, similar in both simulations confirming the accuracy of hiSixTrack. Additional losses are simulated with the latter slightly upstream of the DS1 cluster, which could be traced back to secondary fragments generated in the TCSG collimator. The same applies for the apparent broadening of the A1 loss peak in hiSixTrack. In conclusion, the STIER result can be reproduced with hiSixTrack with additional features expected from the changed simulation approach.

9.2.3 Simulation with hiSixTrack

Table 9.2: Collimator settings in σ used for the HL-LHC simulations in hiSixTrack.

	IR7		IR3		IR1/2/5/8/6
TCP	5.7	TCP	15.0	TCT	10.9
TCSG	7.7	TCSG	18.0	TCL	12.0
TCLA	10.0	TCLA	20.0	TCDQ	9.0
				TCSP	8.5

Compared to the STIER simulation that was carried out for one particular plane, with a defined impact parameter and fixed TCLD settings [HBJ⁺15], the hiSixTrack simulation is carried out for a variety of different settings to define the worst case scenario and thoroughly study the cleaning performance for this case. First, the cleaning performance without TCLD collimators is evaluated for a defined impact parameter for the both planes and beams. The most critical plane is chosen and the cleaning inefficiency is systematically evaluated for different impact parameters. Again the most critical impact parameter is selected and the cleaning inefficiency is compared with and without one or two TCLD collimators. The study is conducted for different possible half gaps of the TCLD collimators. At the time of study, the decision of installing one TCLD collimator was already taken, based on the requirements for proton beams.

The main aim of this study is thus to clarify whether the heavy-ion losses can be reduced to a satisfactory low extent with only one TCLD, such that the target beam intensity can be achieved. All simulations are carried out with the HL-LHC optics V.1.2 and the collimator settings summarized in Table 9.2.

Selection of Beam and Plane

Impact Parameters

Based on the results of the previous simulations, the simulation is carried out for B1H with different impact parameters. The IR7 loss maps simulated for $b = 0.1 \mu\text{m}$, $1.0 \mu\text{m}$, $10.0 \mu\text{m}$ and $100 \mu\text{m}$ are shown in Fig. 9.3.

The comparison shows, as for the STIER study case at $3.5 Z \text{ TeV}$ qualitatively similar loss patterns, which are quantitatively different. The worst cleaning inefficiency with the highest losses at the IR7 DS magnets is obtained for an impact parameter of $b = 1.0 \mu\text{m}$. In Fig. 9.4, the distribution of χ and A in both loss clusters DS1 and DS2 is shown for the four impact parameters. Both distributions are normalized to yield one if the values of all data points

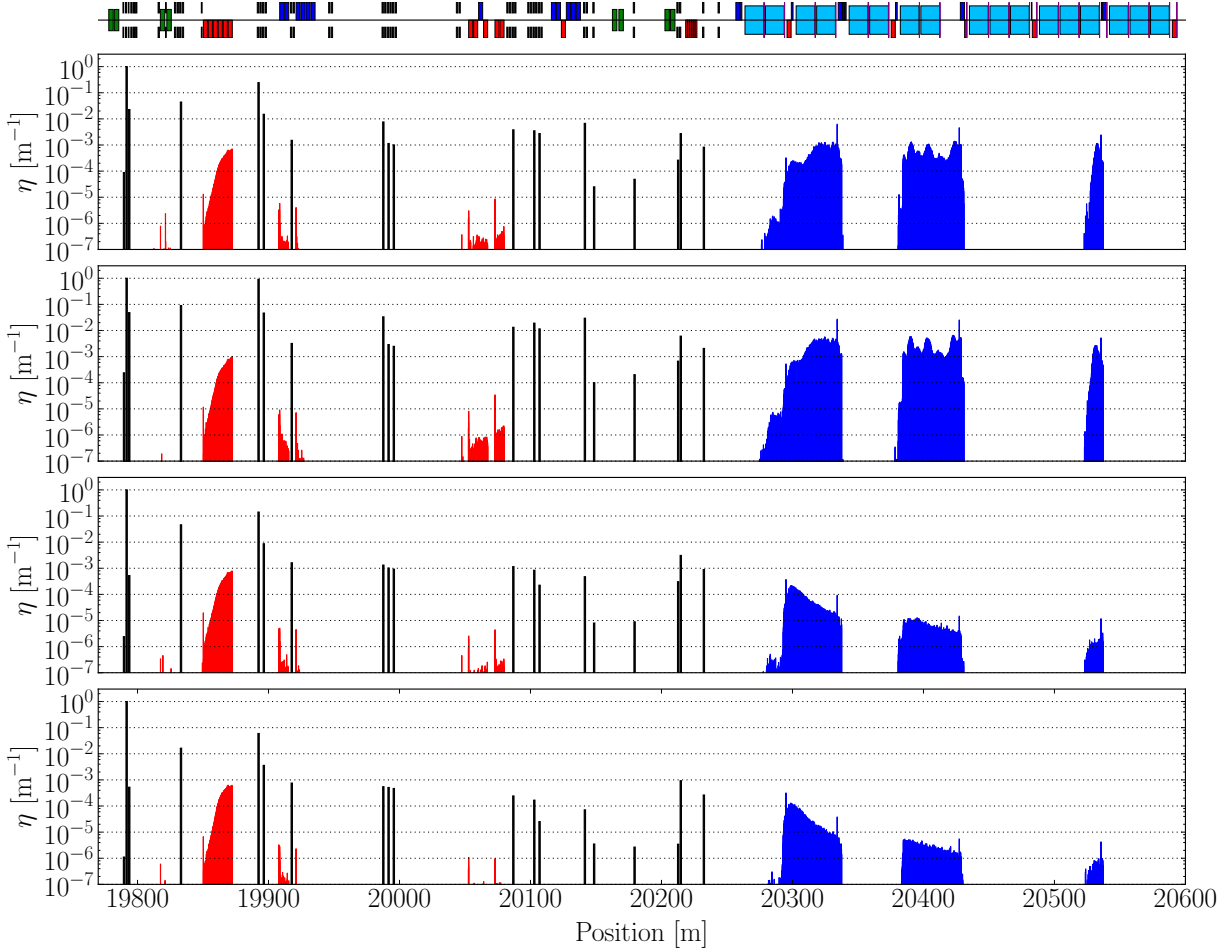


Figure 9.3: Comparison of the cleaning inefficiency simulated with the hiSixTrack-FLUKA coupling for four different impact parameters $b = 0.1\mu\text{m}$, $1.0\mu\text{m}$, $10.0\mu\text{m}$, $100.0\mu\text{m}$.

are integrated. In all studied cases, the distribution of χ in the DS1 cluster is broader than in the DS2 cluster, in line with the observation made in the STIER simulation in the 2011 configuration. Pronounced peaks are visible in all simulations from the isotope ${}^3\text{H}^{1+}$ with an amplitude increasing from $b = 1\mu\text{m}$ to $b = 100\mu\text{m}$, but larger for $0.1\mu\text{m}$ than for $1.0\mu\text{m}$. This observation is, like the better cleaning inefficiency for $0.1\mu\text{m}$ than with $1.0\mu\text{m}$ unexpected, because the fragmentation rate should be lower for smaller impact parameters. This behaviour is studied in detail later-on in this section.

A further observation is the diminished density in the χ histogram with increasing impact parameter. The losses for the larger impact parameters are caused by less different isotopes which is also visible in the distribution of nuclear mass numbers. For the largest impact parameter, the largest fraction of the losses arises from tritium ions with the spectrum of isotopes lost

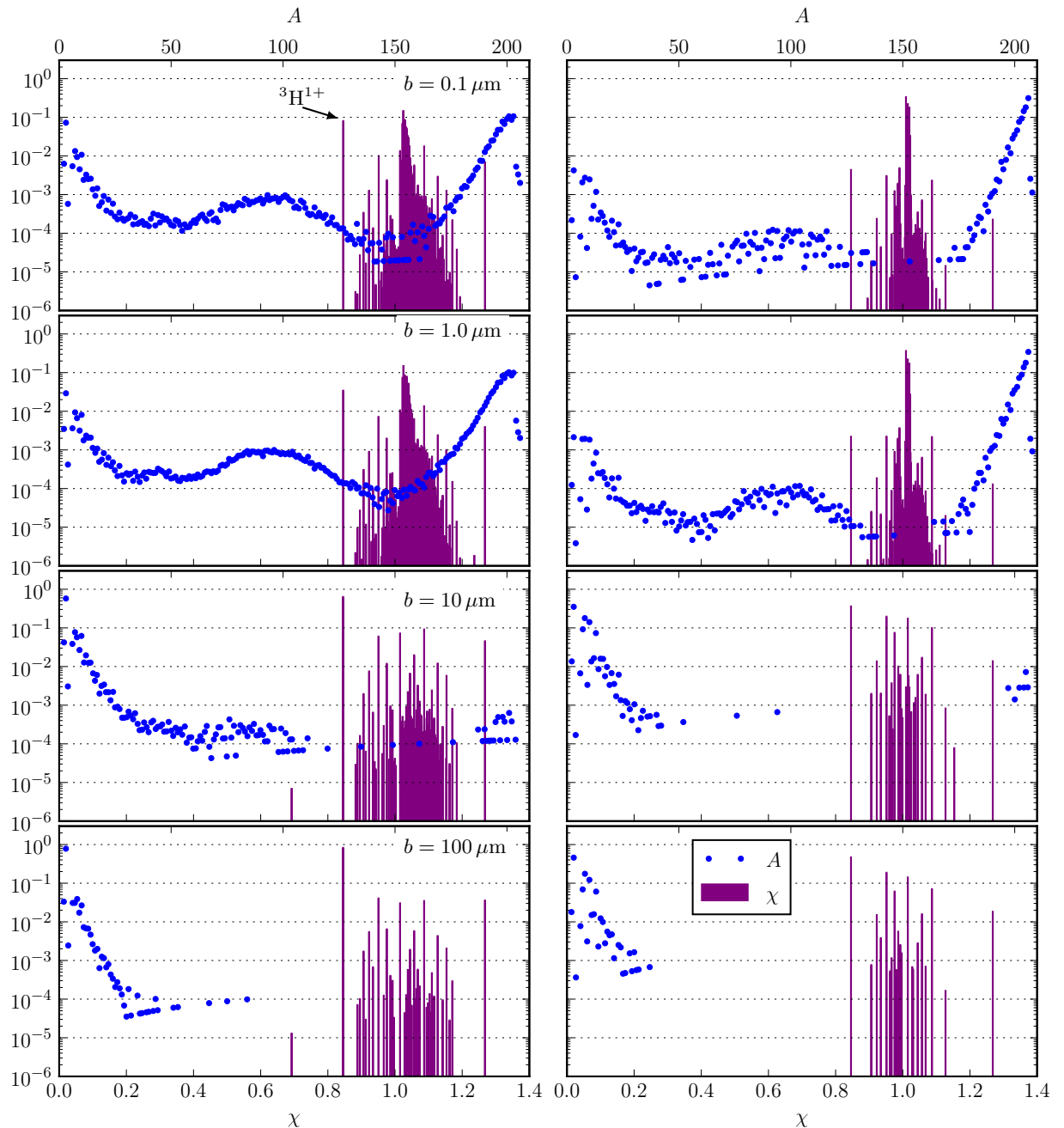


Figure 9.4: Distribution of χ and A in the DS1 (left) and DS2 (right) clusters with different impact parameters from $b = 0.1 \mu\text{m}$ to $100 \mu\text{m}$.

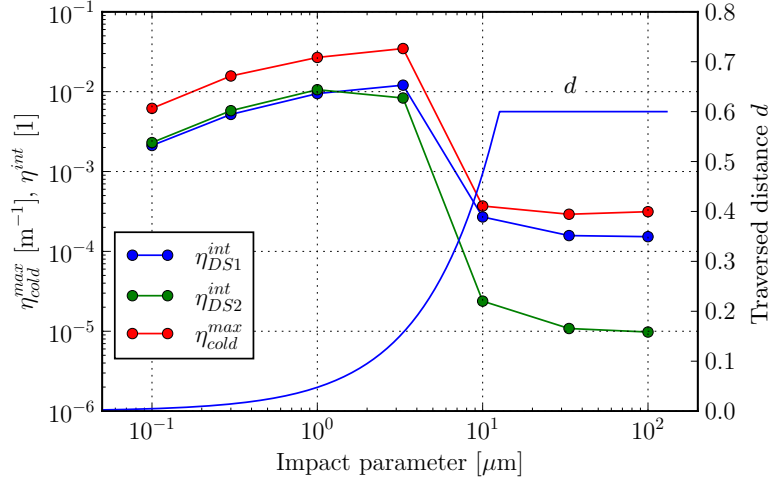


Figure 9.5: Cleaning inefficiency for B1H for different impact parameters.

in the DS ending at $A = 85$. Along with this observation comes the larger amount of energy lost in the TCP, leading to a reduced cleaning inefficiency in the DS clusters. The cleaning inefficiency does not change significantly from $b = 10 \mu\text{m}$ to $100 \mu\text{m}$, because at $10 \mu\text{m}$ the primary heavy-ions traverse almost the full length of the collimator (for the presented setup they do so at $b = 13 \mu\text{m}$).

Additional cleaning simulations show a complete picture of the cleaning evolution with the impact parameter. The result is shown in Fig. 9.5 and confirms the expectation of better cleaning performance at larger impact parameters. However, the better cleaning performance at $b = 0.1 \mu\text{m}$ than at $1.0 \mu\text{m}$ is not understood.

In the assumption that the underlying physical process is related the secondary impact of out-scattered $^{208}\text{Pb}^{82+}$ ions at the TCP in subsequent turns, a dedicated simulation was conducted. To avoid eventual effect of the phase space shift with the associated increase of the impact parameter (see Chap. 7.6.1), the simulations are repeated for $0.1 \mu\text{m}$ and $1.0 \mu\text{m}$ with the sextupoles switched off. In this scenario, the cleaning inefficiency for $b = 1.0 \mu\text{m}$ is still worse than for $0.1 \mu\text{m}$. The distribution of impact parameters at the TCP for impacts at subsequent turns is shown in Fig. ??.

9.3 Operation with other Heavy-Ion Species

The LHC injectors are capable of providing heavy-ions of species different from $^{208}\text{Pb}^{82+}$ to the LHC. The NA61/Shine experiment has so far received $^{40}\text{Ar}^{18+}$ ions for fixed target experiments and $^{129}\text{Xe}^{54+}$ ions are scheduled for future operation [Scr15, Man14].

The cleaning simulations with these ion species are carried out in the HL-LHC configuration with the optical and collimator settings identical to those used in Chap. 9.2 with the primary beam impacting the TCP with $b = 1\mu\text{m}$. The loss maps simulated for the different heavy-ion species and for protons are compared in Fig. 9.6 (zoom to IR7) and Fig. 9.7 (full LHC ring).

The proton simulation result (courtesy of D. Mirarchi [M⁺16]) is obtained with the standard proton SixTrack using the `BeamLossPattern` aperture check.

The losses in the IR7 region are very similar for $^{208}\text{Pb}^{82+}$ ions, $^{129}\text{Xe}^{54+}$ ions, and $^{40}\text{Ar}^{18+}$ ions. Slight differences in terms of shape of the loss patterns in the DS clusters are visible between the different heavy-ion species but the simulated cleaning inefficiency is in the same order of magnitude, as summarized in Table 9.3. Unsurprisingly, the loss peaks in the remaining ring are at the same locations where the dispersion function takes local maxima. They are, however, at different amplitudes due to differences in the fragmentation spectra for the different isotopes. The beam loss pattern of $^4\text{He}^{2+}$ shows significantly less losses at in the DS clusters and at all other aperture loss locations. Compared to the proton simulation the DS losses with $^4\text{He}^{2+}$ are higher by one order of magnitude.

The worst cleaning inefficiency in terms of peak loss and integrated loss in the DS1 is simulated for $^{129}\text{Xe}^{54+}$, but the difference to the cleaning inefficiency for $^{208}\text{Pb}^{82+}$ is small (see Table 9.3). A remarkable difference between $^{208}\text{Pb}^{82+}$ and the lighter heavy-ion species is the ratio of the integrated losses in the DS1 and DS2. While for $^{208}\text{Pb}^{82+}$ the quantities η_{DS1}^{int} and η_{DS2}^{int} take similar values with a slight overweight towards DS2, the lighter ion fragments have a clear tendency to have higher integrated losses in the first DS cluster. For $^{40}\text{Ar}^{18+}$, the integrated

Table 9.3: Cleaning inefficiency for different isotopes in the HL-LHC configuration.

Isotope	η_{cold}^{max} [$10^{-2}/\text{m}$]	η_{DS1}^{int} [10^{-2}]	η_{DS2}^{int} [10^{-2}]	η_{cold}^{int} [10^{-2}]
$^{208}\text{Pb}^{82+}$	2.7	9.5	10.6	22
$^{129}\text{Xe}^{54+}$	3.5	12.0	8.3	28
$^{40}\text{Ar}^{18+}$	2.5	11.1	4.6	17
$^4\text{He}^{2+}$	0.07	0.6	0.2	0.9
p	$7 \cdot 10^{-3}$	$4 \cdot 10^{-2}$	$4 \cdot 10^{-2}$	$9 \cdot 10^{-2}$

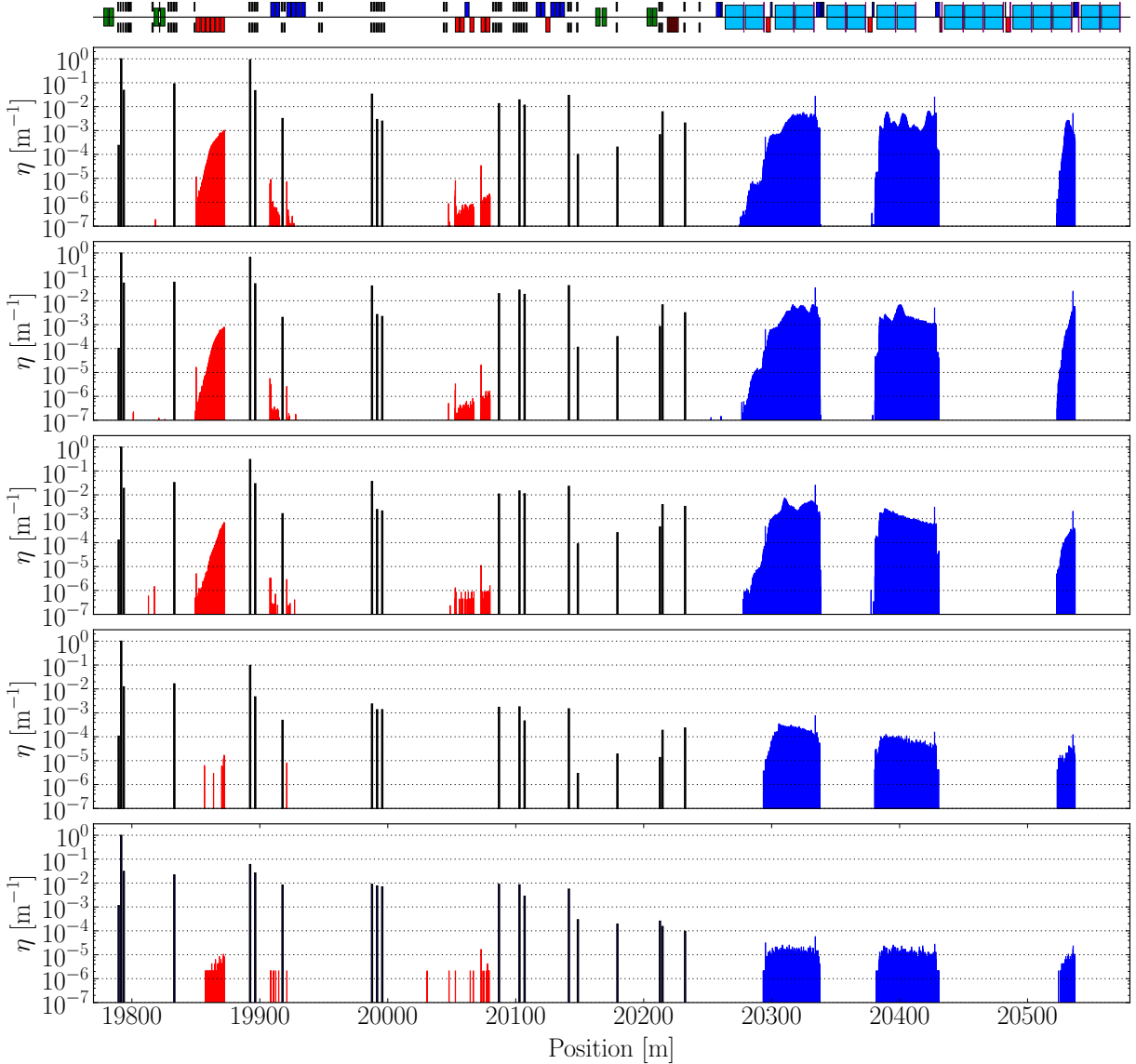


Figure 9.6: Loss maps zoomed to IR7 simulated for the HL-LHC configuration with $^{208}\text{Pb}^{82+}$ ions, $^{129}\text{Xe}^{54+}$ ions, $^{40}\text{Ar}^{18+}$ ions, $^4\text{He}^{2+}$ ions and protons.

losses in the DS1 are more than twice as high as in the DS2. For $^4\text{He}^{2+}$ the ratio is approximately three. This observation is an inevitable consequence of the quantization of nucleons in the nuclei, which implies a larger rigidity offset for the same amount of neutron loss for lighter isotopes.

In Table 9.4, the $\chi - 1$ -values of particles generated from EMD1 and EMD2 are summarized as a measure of the rigidity offset for the different reference species. Furthermore, $\chi - 1$ for the EMD1 and EMD2 isotopes is given as a function of A for different isotopes in Fig. 9.8. The

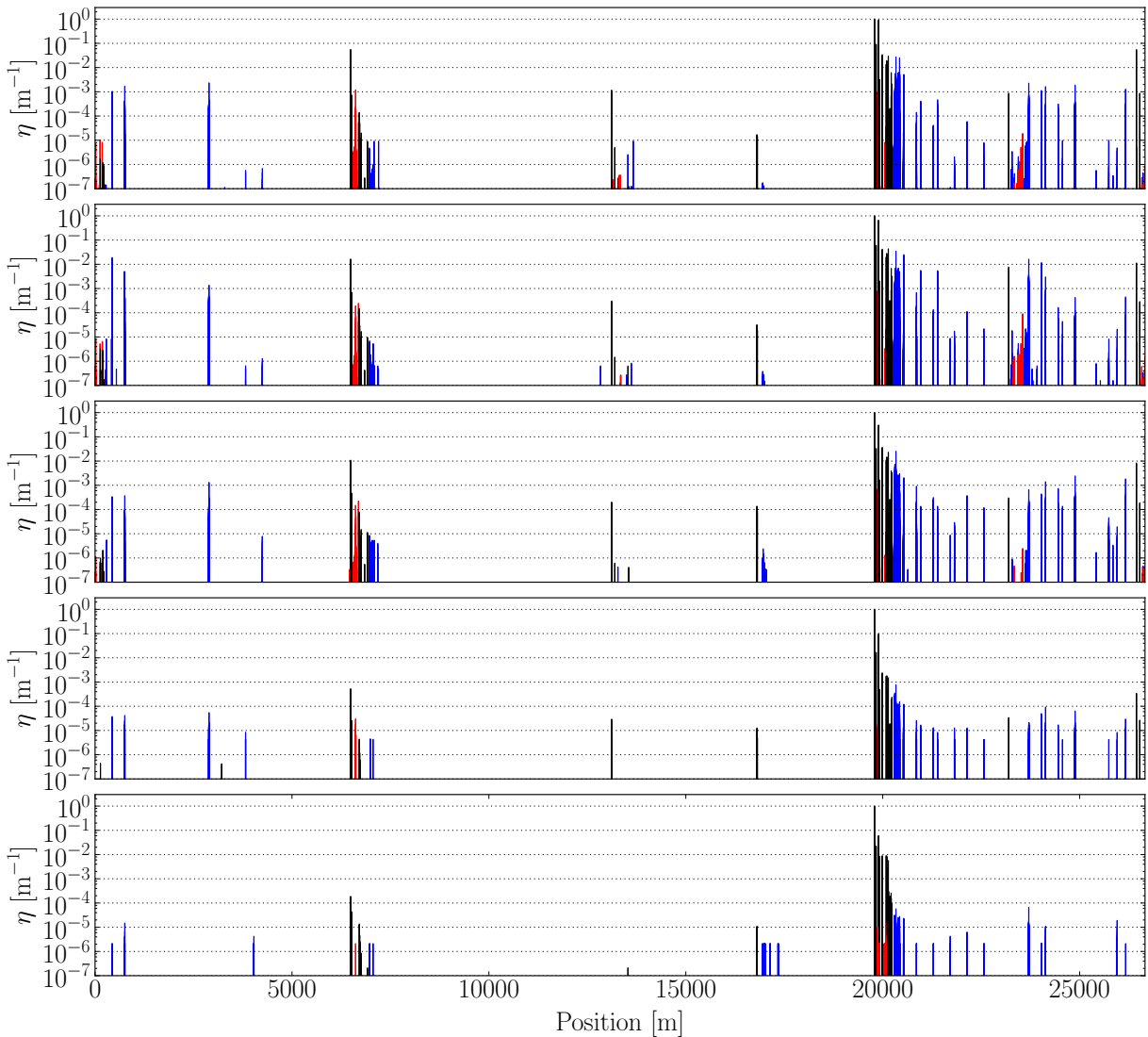


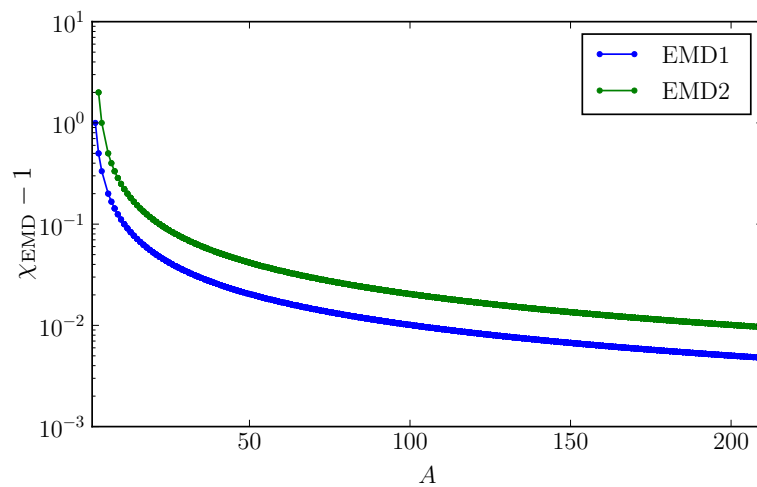
Figure 9.7: Full ring loss maps simulated for the HL-LHC configuration with $^{208}\text{Pb}^{82+}$ ions, $^{129}\text{Xe}^{54+}$ ions, $^{40}\text{Ar}^{18+}$ ions, $^4\text{He}^{2+}$ ions and protons.

$\chi - 1$ value for the EMD isotopes increases continuously with decreasing mass number of the reference isotope. With increasing rigidity offset, the probability that the residual heavy-ion fragment is lost at the first DS cluster increases. The finding confirms the observation made with the simulated loss patterns.

In conclusion, the simulation with hiSixTrack shows that the cleaning inefficiency for other heavy-ion species that could be possibly injected into the LHC is comparable or better to that of $^{208}\text{Pb}^{82+}$. Therefore, the same limitations in terms of stored beam energy apply similarly for the other ion species.

Table 9.4: Cleaning inefficiency for different isotopes in the HL-LHC configuration.

Ref. species	$\chi_{\text{EMD1}} - 1 [10^{-2}]$	$\chi_{\text{EMD2}} - 1 [10^{-2}]$
$^{208}\text{Pb}^{82+}$	0.48	0.97
$^{129}\text{Xe}^{54+}$	0.78	1.57
$^{40}\text{Ar}^{18+}$	2.56	5.27
$^4\text{He}^{2+}$	33.3	-

Figure 9.8: $\chi_{\text{EMD}} - 1$ as a function of A for all isotopes lighter than $^{208}\text{Pb}^{82+}$.

10. Outlook

10.0.1

10.1 Heavy-Ion Loss Maps with Aperture and Orbit Uncertainties

11. Summary and Conclusions

Appendix A.

A.1 Tracking Map Symplecticity

The symplecticity can be probed with the Jacobian of the tracking map. It can be shown [RS95] that a tracking map is symplectic if its Jacobian matrix \mathcal{J} fulfills the symplectic condition:

$$\mathcal{J}^T S \mathcal{J} = S. \quad (\text{A.1})$$

The Jacobian matrix is related to the initial coordinates and the final coordinates as follows:

$$\mathcal{J} = \frac{\partial(x^f, p_x^f, y^f, p_y^f, \sigma^f, p_\sigma^f)}{\partial(x^i, p_x^i, y^i, p_y^i, \sigma^i, p_\sigma^i)} = \begin{pmatrix} \frac{\partial x^f}{\partial x^i} & \frac{\partial x^f}{\partial p_x^i} & \frac{\partial x^f}{\partial y^i} & \frac{\partial x^f}{\partial p_y^i} & \frac{\partial x^f}{\partial \sigma^i} & \frac{\partial x^f}{\partial p_\sigma^i} \\ \frac{\partial p_x^f}{\partial x^i} & \frac{\partial p_x^f}{\partial p_x^i} & \frac{\partial p_x^f}{\partial y^i} & \frac{\partial p_x^f}{\partial p_y^i} & \frac{\partial p_x^f}{\partial \sigma^i} & \frac{\partial p_x^f}{\partial p_\sigma^i} \\ \frac{\partial y^f}{\partial x^i} & \frac{\partial y^f}{\partial p_x^i} & \frac{\partial y^f}{\partial y^i} & \frac{\partial y^f}{\partial p_y^i} & \frac{\partial y^f}{\partial \sigma^i} & \frac{\partial y^f}{\partial p_\sigma^i} \\ \frac{\partial p_y^f}{\partial x^i} & \frac{\partial p_y^f}{\partial p_x^i} & \frac{\partial p_y^f}{\partial y^i} & \frac{\partial p_y^f}{\partial p_y^i} & \frac{\partial p_y^f}{\partial \sigma^i} & \frac{\partial p_y^f}{\partial p_\sigma^i} \\ \frac{\partial \sigma^f}{\partial x^i} & \frac{\partial \sigma^f}{\partial p_x^i} & \frac{\partial \sigma^f}{\partial y^i} & \frac{\partial \sigma^f}{\partial p_y^i} & \frac{\partial \sigma^f}{\partial \sigma^i} & \frac{\partial \sigma^f}{\partial p_\sigma^i} \\ \frac{\partial p_\sigma^f}{\partial x^i} & \frac{\partial p_\sigma^f}{\partial p_x^i} & \frac{\partial p_\sigma^f}{\partial y^i} & \frac{\partial p_\sigma^f}{\partial p_y^i} & \frac{\partial p_\sigma^f}{\partial \sigma^i} & \frac{\partial p_\sigma^f}{\partial p_\sigma^i} \end{pmatrix}. \quad (\text{A.2})$$

A.1.1 Thick Dipole

For simplicity and due to the lack of relevance for hiSixTrack, the symplecticity of the thick dipole is here only discussed in two dimensions. Following the tracking map shown in the Eqs. (7.60) to (7.63), the two-dimensional Jacobian matrix yields:

$$\mathcal{J} = \begin{pmatrix} C_x & \frac{S_x}{(1+\delta)\omega_x} & 0 & 0 \\ -S_x(1+\delta)\omega_x & C_x & 0 & 0 \\ 0 & 0 & 1 & \frac{L}{1+\delta} \\ 0 & 0 & 0 & 1 \end{pmatrix}. \quad (\text{A.3})$$

The symplectic condition $\mathcal{J}^T \mathbf{S} \mathcal{J} = \mathbf{S}$ is fulfilled.

A.1.2 Thin Dipole

From the tracking map for the thin dipole, presented in the Eqs. (7.79) to (7.84), the following Jacobian can be derived:

$$\mathcal{J} = \begin{pmatrix} 1 & 0 & 0 & 0 & 0 \\ -L k_0 \chi h_x & 1 & 0 & 0 & \frac{\beta_0}{\beta} L h_x \\ 0 & 0 & 1 & 0 & 0 \\ 0 & 0 & 0 & 1 & 0 \\ -\frac{\beta_0}{\beta} L h_x & 0 & 0 & 0 & 1 - h_x x L \frac{d}{dp_\sigma} \frac{\beta_0}{\beta} \\ 0 & 0 & 0 & 0 & 1 \end{pmatrix} \quad (\text{A.4})$$

This Jacobian fulfills the symplectic condition.

A.1.3 Thick Quadrupole

The Jacobian matrix of the thick quadrupole in four dimensions is given by:

$$\mathcal{J} = \begin{pmatrix} \cos(\omega_x L) & \frac{\sin(\omega_x L)}{(1+\delta)\omega_x} & 0 & 0 \\ -(1+\delta)\omega_x \sin(\omega_x L) & \cos(\omega_x L) & 0 & 0 \\ 0 & 0 & \cosh(\omega_x L) & \frac{\sinh(\omega_x L)}{(1+\delta)\omega_x} \\ 0 & 0 & (1+\delta)\omega_x \sinh(\omega_x L) & \cosh(\omega_x L) \end{pmatrix}. \quad (\text{A.5})$$

The symplectic condition is fulfilled.

A.1.4 Thin Quadrupole

From the tracking map for the thin quadrupole, presented in the Eqs. (1) to (4), the following Jacobian can be derived:

$$\mathcal{J} = \begin{pmatrix} 1 & 0 & 0 & 0 & 0 & 0 \\ -KL & 1 & 0 & 0 & 0 & 0 \\ 0 & 0 & 1 & 0 & 0 & 0 \\ 0 & 0 & KL & 1 & 0 & 0 \\ 0 & 0 & 0 & 0 & 1 & 0 \\ 0 & 0 & 0 & 0 & 0 & 1 \end{pmatrix} \quad (\text{A.6})$$

This Jacobian fulfills the symplectic condition.

A.2 IR2 Loss Mitigation Experiment - Loss Maps

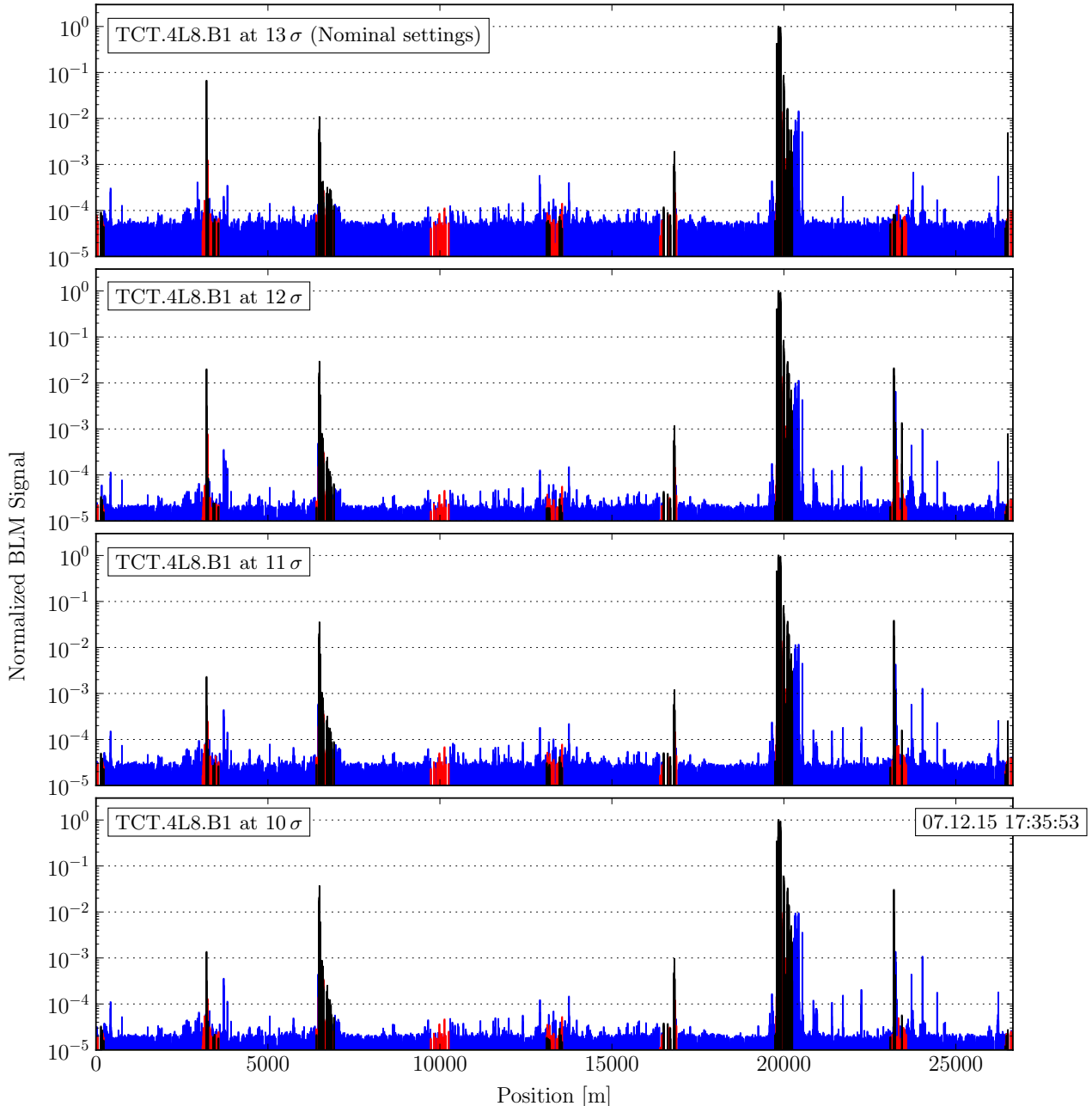


Figure A.1: Loss maps measured in the 2015 heavy-ion run with different settings of the TCTH.4L8.B1. Each loss map was measured the 07.12.2015

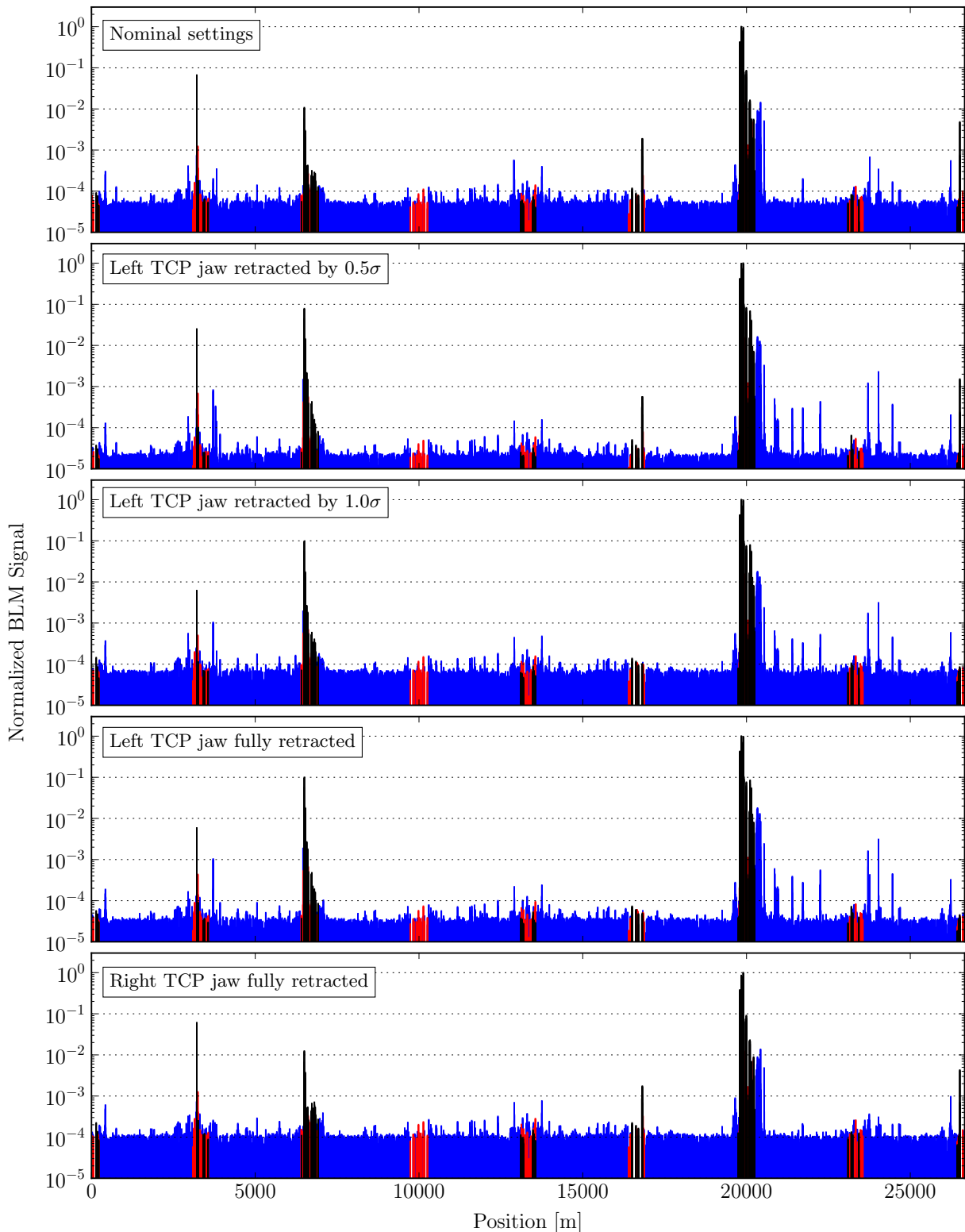


Figure A.2: Loss maps measured in the 2015 heavy-ion run with different TCP configurations. Each loss map was measured the 07.12.2015 at the times indicated at top right of each plot.

A.3 STIER Loss Maps

A.3.1 Settings validation for the 2015 heavy-ion run

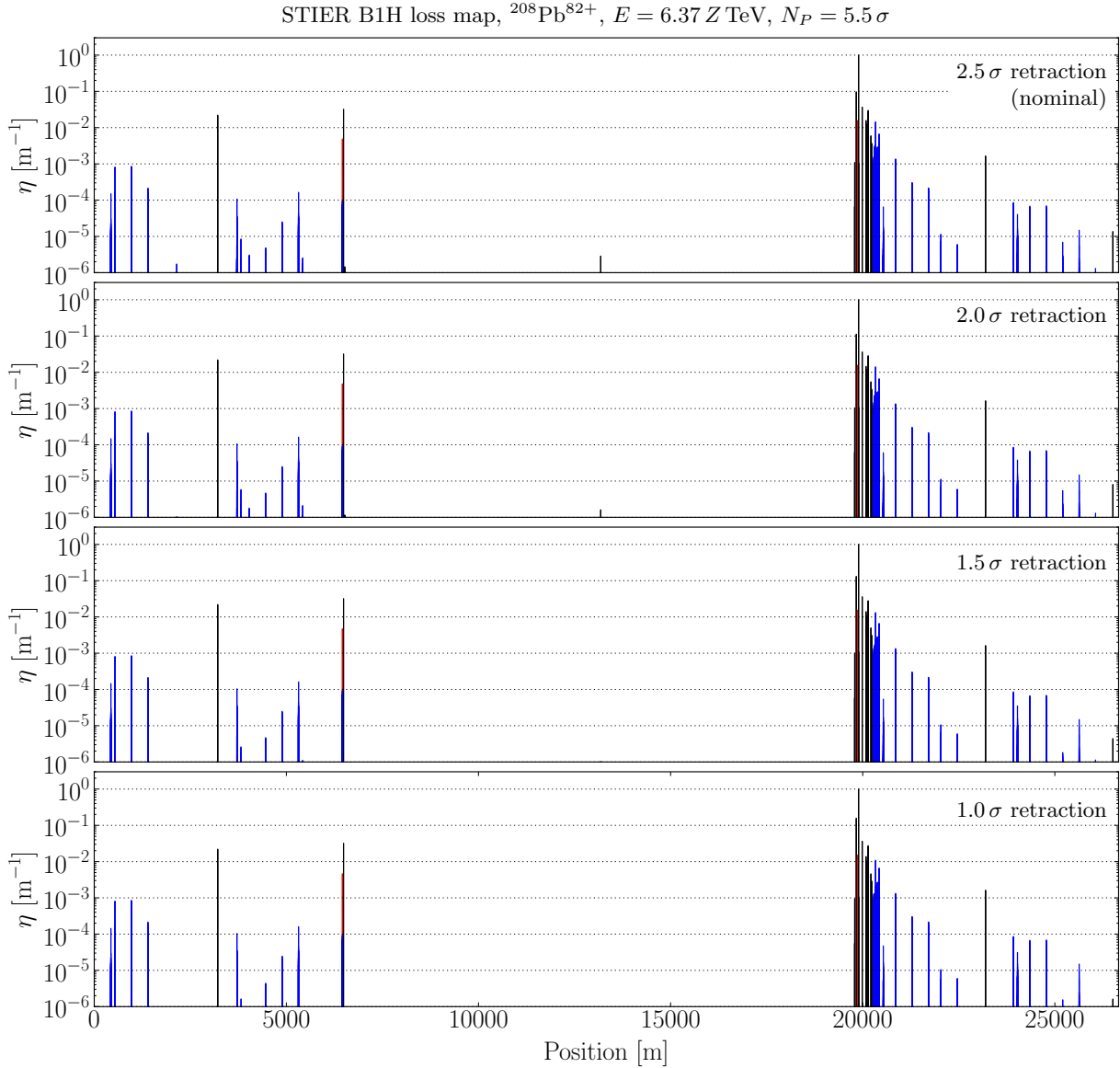


Figure A.3: STIER simulated loss maps in the 2015 configuration for different retractions of the TCSG collimators.

A.4 Accelerator Hamiltonian in a Curved Coordinate System

In dipole magnets, the trajectory of the reference particle is curved. The motion of the particles in a dipole magnet is then most elegantly described in a curved coordinate system. For the case of a purely horizontal and uniform bending magnet, the reference trajectory can be described by a bending radius ρ , as illustrated in Fig. A.4. Based on the geometry, the coordinates in the straight (x, y, s) and in the curved coordinate system (X, Y, S) can be related to each other. With a third order generating function, the momentum coordinates in the curved coordinate system and the new magnetic potentials can be calculated. The derivation presented in the following is based on [Wol14]. From the geometry shown in Fig. A.4, the new and old coordinates are connected by the simple relations:

$$\begin{aligned} x &= (\rho + X) \cos\left(\frac{S}{\rho}\right) - \rho, \\ y &= Y, \\ s &= (\rho + X) \sin\left(\frac{S}{\rho}\right). \end{aligned} \tag{A.7}$$

One can then construct a generating function of third order to calculate the particle momenta in the new coordinate system []

$$F_3(X, p_x, Y, p_y, S, p_z) = - \left[(\rho + X) \cos\left(\frac{S}{\rho}\right) - \rho \right] p_x - Y p_y - \left[(\rho + X) \sin\left(\frac{S}{\rho}\right) \right] p_z. \tag{A.8}$$

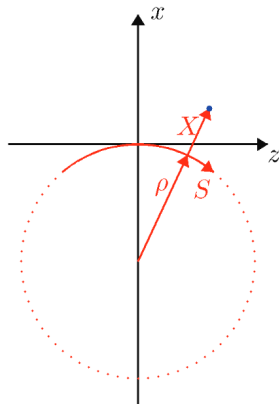


Figure A.4

The old and the new coordinates are then related by

$$x_i = -\frac{\partial F_3}{\partial p_i} \quad P_i = -\frac{\partial F_3}{\partial X_i}. \quad (\text{A.9})$$

The new momentum coordinates are given by

$$\begin{aligned} P_X &= p_x \cos\left(\frac{S}{\rho}\right) + p_z \sin\left(\frac{S}{\rho}\right), \\ P_Y &= p_y, \\ P_Z &= p_z \left(1 + \frac{X}{\rho}\right) \cos\left(\frac{S}{\rho}\right) - p_x \left(1 + \frac{X}{\rho}\right) \sin\left(\frac{S}{\rho}\right). \end{aligned} \quad (\text{A.10})$$

The vector potential is given by

$$\begin{aligned} A_X &= A_x \cos\left(\frac{S}{\rho}\right) - A_z \sin\left(\frac{S}{\rho}\right), \\ A_Y &= A_y, \\ A_S &= A_z \cos\left(\frac{S}{\rho}\right) + A_x \sin\left(\frac{S}{\rho}\right), \end{aligned} \quad (\text{A.11})$$

When the Hamiltonian is now transformed into the curved coordinate system in the accelerator frame, the transformation follows the same steps as shown in Chap. ??.

A.5 Implementation of hiSixTrack

The SixTrack source is saved altogether in the three files `sixtrack.s`, `lielib.s` and `dabnew.s`. To build the SixTrack executable, a compilation file `make_six` is executed with dedicated flags that activate given functionalities. Examples for such flags are the `collimat` flag to compile the collimation version of SixTrack. An excellent overview of the compilation of SixTrack is given in [F⁺13]. Specific functions of the SixTrack-FLUKA coupling are stored in an external module saved as `mod_fluka.f90`.

A.5.1 Variables in hiSixTrack

SixTrack tracks a variety of different arrays, to store information of the tracked particle bunch. Besides the obvious arrays `xv(i,j),yv(i,j),sigmv(j),dpsv(j)` containing information about the six-dimensional particle coordinates, other arrays store information about the particle energy

Table A.1: Variables in SixTrack [DM⁺16].

Variable	Description	Symbol	Unit	Definition
<code>j</code>	particle index			
<code>npx</code>	number of tracked particles			
<code>npart</code>	maximum number of tracked particles			
Reference particle properties				
<code>e0</code>	Energy of the reference particle	E_0	MeV	
<code>e0f</code>	Momentum of the reference particle	P_0	MeV/c^2	
<code>pma</code>	Proton rest mass	m_p	MeV/c^2	
Particle arrays				
<code>xv(1,j)</code>	Horizontal coordinate	x	mm	Eq. (2.1)
<code>xv(2,j)</code>	Vertical coordinate	x	mm	Eq. (2.1)
<code>yv(1,j)</code>	Horizontal slope	x'	mrad	
<code>yv(2,j)</code>	Vertical slope	y'	mrad	
<code>sigmv(j)</code>	Path length difference	σ	mm	Eq. (7.27)
<code>dpsv(j)</code>	Relative momentum offset	δ	-	
<code>oidpsv(j)</code>	Relative momentum offset	$\frac{1}{1+\delta}$	-	
<code>ejfv(j)</code>	Particle momentum	P	MeV/c	
<code>ejv(j)</code>	Particle energy	E	MeV	

and momentum as well as auxiliary quantities derived from them. In the process of tracking, the latter are re-initialized every time the particle momentum (and in hiSixTrack the particle species) may have changed, which is true for the collimators and accelerating elements. An overview of the most relevant particle arrays is given in Table A.1.

Some of these variables are re-defined in hiSixTrack in order to be compatible with the generic multi-isotopic definitions introduced in Chap. 2.1.2. This includes the relative offset of the momentum per mass unit δ which is implemented in the SixTrack as the relative momentum offset. The implementation in both SixTrack and hiSixTrack is shown in List. A.1. The quantity $\frac{\delta}{1+\delta}$ follows the re-definition of δ .

```

1 !      dpsv(j) = (ejfv(j)-e0f)/e0f          ! SixTrack
2      dpsv(j) = (ejfv(j)*(nucm0/nucm(j))-e0f)/e0f    ! hiSixTrack
3      oidpsv(j) = one/(one+dpsv(j))

```

Listing A.1: Definition of δ in SixTrack and hiSixTrack.

In addition, new variables are introduced to keep track of the particle species and to facilitate the implementation of the heavy-ion tracking maps. These variables are summarized in Table A.2. For the identification of the tracked particles, the mass number A and charge multiplicity Z and rest mass m are stored in arrays. The latter is not important for the identification of the particle, but is used to calculate χ . The information about the reference species A_0, Z_0, m_0 is read from `fort.3` with a newly introduced block `HION`, described in the next subsection.

Table A.2: Variables introduced or modified in hiSixTrack.

Variable	Description	Symbol	Unit	Definition
Reference particle properties				
<code>zz0</code>	Charge multiplicity of the reference ion species	Z_0	-	
<code>aa0</code>	Nucleon number of the reference ion species	A_0	-	
<code>nucm0</code>	Rest mass of the reference ion species	m_0	GeV/c^2	
Particle arrays				
<code>nzz(j)</code>	Charge multiplicity of the tracked ion	Z	-	
<code>naa(j)</code>	Nucleon number of the tracked ion	A	-	
<code>nucm(j)</code>	Rest mass of the tracked ion	m	GeV/c^2	
<code>mtc(j)</code>	Relative mass to charge ratio	χ	-	Eq. (2.14)
<code>dpsv(j)</code>	Relative momentum per mass offset	δ	-	Eq. (2.13)
<code>moidpsv(j)</code>	Relative rigidity offset	$\frac{\chi}{1+\delta}$	-	Eq. (2.15)

The quantity `mtc(j)` represents the relative mass to charge ratio χ . Its definition in the SixTrack source is shown in List. A.5. Note that instead of using the particle charge Q , hiSixTrack uses the nuclear charge multiplicity Z , assuming that the all electrons are removed from the tracked particle and the reference particle. If non-fully stripped ions should be tracked with hiSixTrack, the source has to be extended for an additional array storing the effective ion charge. The variable `moipdsv(j)` describes the auxiliary quantity $\frac{\chi}{1+\delta}$ representing the relative difference in magnetic rigidity.

While in SixTrack the particle mass is hard-coded as a constant parameter `pma` that is applied for all particles, hiSixTrack requires a new implementation of mass-dependent equations in which the particle mass is a variable. Depending on the context, `pma` refers to the mass of the reference particle or of the tracked particle and is replaced in hiSixTrack by `nucm0` or `nucm(j)` accordingly. In List. A.2, the Einstein energy-momentum relation is shown as it is implemented in SixTrack and hiSixTrack for both the reference particle and for a tracked particle.

```

1 !      MOMENTUM OF THE REFERENCE PARTICLE
2   e0f=sqrt(e0**2-pma**2)                      ! SixTrack
3   e0f=sqrt(e0**2-nucm0**2)                      ! hiSixTrack
4 !
5 !      ENERGY OF THE TRACKED ION j
6   ejv(j)=sqrt(ejfv(j)**2+pma**2)                ! SixTrack
7   ejv(j)=sqrt(ejfv(j)**2+nucm(j)**2)            ! hiSixTrack

```

Listing A.2: Definition of the reference momentum in SixTrack and hiSixTrack.

A.5.2 Initialization of hiSixTrack

hiSixTrack is activated by calling the new `HION` block in the `fort.3` file. This block acquires information on the reference particle species (A_0, Z_0, m_0). The code defining the `HION` block in the hiSixTrack source code is shown in List. A.3. An example input block to call hiSixTrack for different heavy-ion reference species is given in List. A.4.

```

1 ! P. HERMES 01-07-2015
2 ! HEAVY ION BLOCK
3 2400 read(3,10020, end=1530, iostat=ierro) ch
4   if(ierro.gt.0) call perror(58)
5   if(ch(1:1).eq.'/') goto 2400
6   if(ch(:4).eq.next) goto 110
7   ch1(:nchars+3)=ch(:nchars)//' / '
8   read(ch1,*) aa0, zz0, nucm0
9   nucm0 = nucm0 * 1.0D+03 ! [GeV/c^2] -> [MeV/c^2] ! hiSixTrack
10  write(*,*) 'Heavy-ion reference species:', aa0, zz0, nucm0
11  goto 110

```

Listing A.3: Definition of the information acquisition from the `fort.3` in the hiSixTrack source file.

```

1 HION
2 /1      1      0.93827231          /PROTONS
3 /40     18     37.2155493          /ARGON IONS
4 208     82     193.68769          /LEAD IONS
5 NEXT

```

Listing A.4: New heavy-ion block in the `fort.3` file to activate hiSixTrack. In the given example, the chosen reference ion species is $^{208}\text{Pb}^{82+}$. Lines starting with '/' are commented out.

A.5.3 Initial Particle Distribution

In the framework of the SixTrack-FLUKA coupling, SixTrack provides subroutine `dist_readdis` to load an initial distribution from an external file. The subroutine is called by the `DIST` block in the `fort.3` file. For hiSixTrack, the routine is adapted to read also A , Z and the particle mass m . Already the implementation in SixTrack foresaw different isotopes, so only minor changes are required to access the heavy-ion specific properties from the input file.

When the initial distribution is read from the file, the acquired quantities are processed to fill the required arrays for the tracking. The modification includes the new definition of δ , the correct nuclear rest mass (as shown in the previous sub-section), the initialization of χ and auxiliary quantities derived from it. The relevant code is shown in List. A.5.

```

1      call dist_readdis( napx, npart, enom, pnom, clight,
2      &                                x, y, xp, yp, s, pc, aa, zz, m )
3 !     [...]
4 !     LOOP OVER ALL PARTICLES
5     do j=1, napx
6 !       VALUES RELATED TO LOSSES
7         nlostp(j) = j
8         pstop (j) = .false.
9 !       VALUES RELATED TO MOMENTUM (MODIFIED IN HISIXTRACK)
10        ejv   (j) = sqrt(ejfv(j)**2+nucm(j)**2)
11        dpsv  (j) = (ejfv(j)*(nucm0/nucm(j))-e0f)/e0f
12        oidpsv(j) = one/(one+dpsv(j))
13 !       NEW IN HISIXTRACK
14        mtc   (j) = (nzz(j)*nucm0)/(zz0*nucm(j))
15        moidpsv (j) = mtc(j)*oidpsv(j)
16        omoidpsv(j) = c1e3*((one-mtc(j))*oidpsv(j))
17 !     [...]

```

Listing A.5: Definition of the subroutine `dist_readdis` in hiSixTrack.

A.5.4 Implemented Heavy-Ion Tracking Maps

Some of the re-defined tracking maps in hiSixTrack are shown in List. A.6 to List. A.9.

```

1 +cd kickv01h
2 +if .not.tilt
3 !           yv(1,j)=yv(1,j)+(strack(i)*oidpsv(j))          ! SixTrack
4           yv(1,j)=yv(1,j)+(strack(i)*oidpsv(j))*mtc(j)    ! hiSix
5 +ei
6 +if tilt
7           yv(1,j)=yv(1,j)+(strackc(i)*oidpsv(j))*mtc(j)
8           yv(2,j)=yv(2,j)+(stracks(i)*oidpsv(j))*mtc(j)
9 +ei

```

Listing A.6: Definition of the transfer map of an horizontal kicker.

```

1 +cd kickvxxh
2 +if .not.tilt
3     yv(1,j)=yv(1,j)+((strack(i)*oidpsv(j))*crkve)*mtc(j) ! P. HERMES
4     yv(2,j)=yv(2,j)-((strack(i)*oidpsv(j))*cikve)*mtc(j) ! P. HERMES
5 +ei
6 +if tilt
7     yv(1,j)=yv(1,j)+(oidpsv(j)*(strackc(i)*crkve+ &
8     &stracks(i)*cikve))*mtc(j)
9     yv(2,j)=yv(2,j)+(oidpsv(j)*(stracks(i)*crkve- &!hr02
10    &strackc(i)*cikve))*mtc(j) !hr02
11 +ei

```

Listing A.7: Definition of the transfer map of an horizontal kicker.

```

1 +cd kickv01v
2 +if .not.tilt
3     yv(2,j)=yv(2,j)+(strack(i)*oidpsv(j))*mtc(j) ! modified for
hiSixTrack
4 +ei
5 +if tilt
6     yv(1,j)=yv(1,j)-(stracks(i)*oidpsv(j))*mtc(j) ! modified for
hiSixTrack
7     yv(2,j)=yv(2,j)+(strackc(i)*oidpsv(j))*mtc(j) ! modified for
hiSixTrack
8 +ei

```

Listing A.8: Definition of the transfer map of a vertical dipole kick.

```

1 +cd kickvxxxv
2           !write(*,*), 'PH: kickvxxxv'
3 +if .not.tilt
4 !hr02      yv(1,j)=yv(1,j)+strack(i)*oidpsv(j)*cikve
5          yv(1,j)=yv(1,j)+((strack(i)*oidpsv(j))*cikve)*mtc(j) ! P. HERMES
6           !hr02
7 !hr02      yv(2,j)=yv(2,j)+strack(i)*oidpsv(j)*crkve
8          yv(2,j)=yv(2,j)+((strack(i)*oidpsv(j))*crkve)*mtc(j) ! P. HERMES
9           !hr02
10 +ei
11 +if tilt
12          yv(1,j)=yv(1,j)+(oidpsv(j)*(strackc(i)*cikve-
13 &           &stracks(i)*crkve))*mtc(j)
14          yv(2,j)=yv(2,j)+(oidpsv(j)*(strackc(i)*crkve+
15 &           &stracks(i)*cikve))*mtc(j)
16 +ei

```

Listing A.9: Definition of the transfer map of a vertical dipole kick.

A.6 Implementation of the hiSixTrack-FLUKA Coupling

A.6.1 Code Structure

The SixTrack-FLUKA coupling requires various changes with respect to the standalone tools to provide particle exchange between the different codes. First an active server must provide the particle exchange, which is provided by a network port, the FlukaIO protocol, developed for this purpose [tea12]. Before the set up of hiSixTrack, this protocol was already equipped with a function to send information about A, Z, m back and forth. Only minor modifications (implemented by V. Vlachoudis) were necessary to adapt the FlukaIO for the hiSixTrack-FLUKA coupling.

The coupled codes hiSixTrack (tracker) and FLUKA (server) need modifications to communicate over network port. In FLUKA, this

A.6.2 Changes in FLUKA Input and Subroutines

This subsection gives a brief overview of the modifications at the FLUKA user routines, input file and compilation to allow for the accurate heavy-ion exchange appropriate fragmentation simulation.

Initialization and Particle Reception

The communication between FLUKA and the FlukaIO is established via the user routine `source.f` [] and the corresponding `SOURCE` card in the FLUKA input file. Among other applications which are not used for the heavy-ion simulations, it is used to receive the particle distribution from SixTrack and write the `toucMap` file. The function to write the latter is extended for the heavy-ion application by additional information on A, Z . Furthermore, the initialization of FLUKA variables is implemented (author: A. Mereghetti), depending on the particle type.

Sending Particles back to the Tracker

The particle bunch is sent back to the tracker via the `fluscw.f` user routine, which is activated over the `USRBDX` card with the special `SDUM` keyword `BACK2ICO` (see [?]). In this user routine the particles are selected and the `fort.66` file containing the correction data for the collimator losses is populated as shown in List. A.10. The user routine is activated when the boundary crossing condition is fulfilled (in this framework a transition from the vacuum surrounding the collimators to black absorber). The type of boundary crossing is defined in the `USRBDX` card, as shown in List. A.11, for the nominal SixTrack-FLUKA coupling on top and for the heavy-ion version on the bottom. In the latter, the particle type is changed to the scoring of all particles instead of only protons.

```

1      DOUBLE PRECISION FUNCTION FLUSCW ( IJ      , PLA      , TXX      ,
2      &                                TZZ      , WEE      , XX       , YY      ,
3      &                                ZZ       , NREG    , IOLREG   , LLO      ,
4      &                                NSURF  )
5      [...]
6 *  | boundary crossing when ISCRNG=1
7     IF ( ISCRNG .EQ.1 ) THEN
8 *  | | ...the SDUM of which is the special one:
9     IF ( TITUSX(JSCRNG) .EQ. SPCSDM ) THEN
10 *         (PLA is kinetic energy [GeV] (PLA<0), ESCO is total energy)
11         ESCO = -PLA + AM(IJ)
12 *         hiST: write all particles not sent back to fort.66
13         IF ( IJ .GT. 0 .OR. IJ .LT. -6 ) THEN
14             WRITE(66,*)
15         &           IJ, IBARCH(IJ), ICHRGE(IJ),ICPPNT,ESCO
16         RETURN
17     END IF
18     [...]

```

Listing A.10: Send particles to FLUKA as implemented in hiSixTrack.

1	*USRBDX	99.0	PROTON	-42.0	VAROUND	BLKROUND	BACK2ICO
2	*USRBDX	8000.0	1.0E-04	210.0			&
3	USRBDX	99.0	ALL-PART	-42.0	VAROUND	BLKROUND	BACK2ICO
4	USRBDX	576000.0	1.0E-04	210.0			

Listing A.11: USRBDX card in the FLUKA input for the nominal SixTrack-FLUKA coupling (commented out) and the heavy-ion version on bottom.

Compilation

The computation high-energy hadronic interactions in FLUKA requires the activation of the DPMJET-III [?]. For this purpose, the linking of the user routines is done with a different linker, which is incorporated in the FLUKA `Makefile` in the framework of the hiSixTrack-FLUKA coupling where the usage of the default `lfluka` linker is replaced by `1dpm3qmd`.

Input File

Besides the changes on the USRBDX card mentioned above, minor changes at the FLUKA input make the framework compatible for heavy-ion applications. The SDUM of the BEAM card is changed from PROTON to HEAVYION with the subsequent definition of the main beam isotope. Furthermore,

heavy-ion specific EMD and nuclear evaporation are activated by means of their dedicated cards, as shown in List. A.12.

```

1 * activate EMD and Evaporation for heavy-ions
2 PHYSICS          2.0                                EM-DISSO
3 PHYSICS          3.0                                EVAPORAT
4 * maximum momentum per nucleon (3000 for 3.5Z TeV, 6000 for 6.37Z TeV)
5 BEAM            6000.                             HEAVYION
6 HI-PROPE        82.      208.
7 *

```

Listing A.12: Changes in the FLUKA input for heavy-ion applications

A.6.3 Changes in hiSixTrack

Heavy-ion SixTrack requires multiple changes to make adapt the software for the exchange of different ion species. The subroutines related to particle exchange are summarized in the `mod_fluka` module but are still called from `sixtrack.s`.

```

1      subroutine kernel_fluka_entrance( nturn, i, ix )
2      use mod_fluka
3      [...]
4 +ca hions
5      [...]                                     ! nucleons sent to FLUKA
6      nnuc0 = 0                                ! ion energy sent to FLUKA
7      ien0 = 0.0
8
9      do j=1,npart                           ! initialize array of particle ids
10         pids(j) = 0
11     end do
12
13     do j=1,napx
14         nnuc0 = nnuc0 + naa(j)           ! count nucleons
15         ien0 = ien0 + ejv(j)            ! count energy [GeV]
16         pids(j) = fluka_uid(j)        ! array of particle ids sent to FLUKA
17     end do
18
19     ret = fluka_send( nturn, fluka_geo_index(ix), eltot, napx,          &
20     & xv(1,:), yv(1,:), xv(2,:), yv(2,:), sigmv, ejv, naa(:), nzz(:), &
21     &nucm(:) )
22
23     [...]
24     return
25   end subroutine

```

Listing A.13: Send particles to FLUKA as implemented in hiSixTrack.

kernel_fluka_exit

The subroutine `kernel_fluka_exit` is called when the particle bunch is sent back from FLUKA to hiSixTrack. It makes use of the `fluka_receive` subroutine defined in the `mod_fluka` module.

```

1
2     subroutine kernel_fluka_exit( nturn, i, ix )
3     use mod_fluka
4     [...]
5 +ca hions
6     [...]
7     ret = fluka_receive( nturn, fluka_geo_index(ix), eltot, napx,      &
8     & xv(1,:), yv(1,:), xv(2,:), yv(2,:), sigmv, ejv, naa(:),nzz(:)      &
9     & ,nucm(:) )
10
11    nnuc1 = 0                      ! init. number of nucleons leaving collimator
12    ien1 = 0.0                      ! init. total energy leaving collimator
13    do j=1,napx
14        [...]
15 !       Update hiST arrays (naa, nzz, nucl are initialized by fluka_receive)
16     ejfv(j) = sqrt((ejv(j)-nucl(j))*(ejv(j)+nucl(j))) ! ion momentum
17     rvv(j) = (ejv(j)*e0f)/(e0*ejfv(j))                  ! beta0/beta
18     dpsv(j) = (ejfv(j)*(nucl0/nucl(j))-e0f)/e0f        ! delta
19     oidpsv(j) = 1.0D+00/(1.0D+00+dpsv(j))              ! 1/(1+delta)
20     dpsv1(j) = (dpsv(j)*1.0D+03)*oidpsv(j)            !
21     mtc(j) = (nzz(j)*nucl0)/(zz0*nucl(j))              ! chi
22     moidpsv(j) = mtc(j)*oidpsv(j)                      ! chi/(1+delta)
23     omoidpsv(j) = 1.0D+03*((1.0D+00-mtc(j))*oidpsv(j)) !
24     nnuc1 = nnuc1 + naa(j)                                ! increase
25
26 !       nucleon counter
27     ien1 = ien1 + ejv(j)                                ! increase energy
28
29 !       counter
30     end do
31
32 !       hiSixTrack: if energy is lost at the collimator, write to fort.208
33     if ((ien0-ien1).gt.one) then
34         write(208,*), fluka_geo_index(ix), nnuc0-nnuc1,           &
35 & (ien0-ien1)*1d-3
36     end if
37
38 !       hisix: check which particle ids have not been sent back
39 !             write their ids to fort.209
40 !             pids(j) was defined in the subroutine kernel_fluka_entrance
41 !             napx: number of particles received
42
43     do j=1,npart                                         ! loop over all pids
44
45 !       possible
46     pid_q = zero
47     do k=1,napx                                         ! loop over pids received
48         if (pids(j).eq.fluka_uid(k)) then
49             pid_q = one
50         end if
51     end do
52     if (pid_q.eq.zero.and.pids(j).ne.zero) then
53         write(209,*), fluka_geo_index(ix), pids(j)
54     end if
55     end do

```

Listing A.14: Receive particles from FLUKA as implemented in hiSixTrack.

Bibliography

- [A⁺06] R. W. Assmann *et al.* *The final collimation system for the LHC. Proceedings of EPAC 2006, Edinburgh, Scotland*, (TUODFI01):986–988, 2006.
- [A⁺11] R. W. Assmann *et al.* *Summary of MD on nominal collimator settings*. CERN-ATS-Note-2011-036 MD, 2011.
- [A⁺15] B. Auchmann *et al.* *Testing beam-induced quench levels of LHC superconducting magnets in Run I*. *Phys. Rev. ST Accel. Beams*, 18:061002, 2015.
- [AGV⁺02] R. Assmann, B. Goddard, E. Vossenberg, and E. Weisse. *The Consequences of Abnormal Beam Dump Actions on the LHC Collimation System*. (LHC Project Note 293), 2002.
- [AmBB⁺02] R. Aßmann, M. Brugger, L. Bruno, H. Burkhardt, G. Burtin, B. Dehning, C. Fischer, B. Goddard, E. Gschwendtner, M. Hayes, J. B. Jeanneret, I. Baishev, and D. Kaltchev. *Requirements for the LHC Collimation System. Proceedings of EPAC 2002, Paris, France*, (TUAGB001):197–199, 2002.
- [Ass05] R. W. Assmann. *Collimators and Beam Absorbers for Cleaning and Machine Protection*. LHC Project Workshop XIV, Chamonix, France, 2005.
- [ASS14] A. N. Artemyev, V. G. Serbo, and A. Surzhykov. *Double lepton pair production with electron capture in relativistic heavy-ion collisions*. *Eur. Phys. J. C*, 74:2829, 2014.
- [Ast08] A. Aste. *Bound-free pair production cross-section in heavy-ion colliders from the equivalent photon approach*. *EPL*, 81(6), 2008.
- [B⁺04a] H. H. Braun *et al.* *Collimation of heavy ion beams in LHC. Proceedings of EPAC 2004, Lucerne, Switzerland*, (MOPLT010):551, 2004.
- [B⁺04b] O. Brüning *et al.* *LHC Design Report (Volume I, The LHC Main Ring)*. CERN, 2004.

- [B⁺¹³] R. Bruce *et al.* *Sources of machine-induced background in the ATLAS and CMS detectors at the CERN Large Hadron Collider.* *Nucl. Instrum. Methods Phys. Res., Sect. A*, 729(0):825 – 840, 2013.
- [B^{+14a}] V. Boccone *et al.* *Beam-machine Interaction at the CERN LHC.* *Nuclear Data Sheets*, 120:215–218, 2014.
- [B^{+14b}] T. T. Böhlen *et al.* *The FLUKA code: developments and challenges for high energy and medical applications.* *Nuclear Data Sheets*, 120:211–214, 2014.
- [B^{+14c}] R. Bruce *et al.* *Simulations and measurements of beam loss patterns at the CERN Large Hadron Collider.* *Phys. Rev. ST Accel. Beams*, 17(081004), 2014.
- [B⁺¹⁵] R. Bruce *et al.* *Collimator Layouts for HL-LHC in the Experimental Insertions.* *Proceedings of IPAC 2015, Richmond, VA, USA*, (TUPTY028):2064–2067, 2015.
- [BAB⁺⁰⁹] T. Böhlne, R. Assmann, C. Bracco, B. Dehning, S. Redaelli, T. Weiler, and C. Zamanzas. *Energy Deposition Simulations and Measurements in an LHC Collimator and Beam Loss Monitors.* *Proceedings of PAC 2009, Vancouver, Canada*, (TH5RFP035):3525–3527, 2009.
- [BAF⁺⁰⁶] C. Bracco, R. W. Assmann, A. Ferrari, S. Redaelli, G. Robert-Demolaize, M. Santana-Leitner, V. Vlachoudis, and T. Weiler. *The final collimation system for the LHC.* *Proceedings of EPAC 2006, Edinburgh, Scotland*, (TUPLS018):1529–1531, 2006.
- [Bar09] J. Bartke. *Relativistic Heavy Ion Physics.* World Scientific Publishing, 2009.
- [BAR15] R. Bruce, R. W. Assmann, and S. Redaelli. *Calculations of safe collimator settings and β^* at the CERN Large Hadron Collider.* *Phys. Rev. ST Accel. Beams*, 18(061001), 2015.
- [BBC⁺¹¹] A. Bertarelli, V. Boccone, F. Carra, F. Cerutti, A. Dallocchio, N. Mariani, L. Peroni, and M. Scapin. *Limits for Beam Induced Damage: Reckless or too Cautious?* *Chamonix 2011 Workshop on LHC Performance*, 2011.
- [BBF⁺¹³] F. Bordry, S. Baird, K. Foraz, A. L. Perro, R. Saban, and J. P. Tock. *The first Long Shutdown (LS1) for the LHC.* *Proceedings of IPAC 2013, Shanghai, China*, (MOZB202):44–48, 2013.
- [BBG⁺⁰⁹] R. Bruce, D. Bocian, S. Gilardoni, and J. M. Jowett. *Beam losses from ultra-peripheral nuclear collisions between $^{208}\text{Pb}^{82+}$ ions in the Large Hadron Collider and their alleviation.* *Phys. Rev. ST Accel. Beams*, 12(071002), 2009.

- [BBM12] O. Brüning, H. Burkhardt, and S. Myers. *The Large Hadron Collider. Prog. Part. Nucl. Phys.*, 67(3):705 – 734, 2012.
- [BC07] O. Brüning and P. Collier. *Building a behemoth*. *Nature*, 448:285–289, 2007.
- [BDS09] D. Bocian, B. Dehning, and A. Siemko. *Quench limit model and measurements for steady state heat deposits in LHC magnets*. *IEEE Trans. Appl. Supercond.*, 19(3):2446–2449, 2009.
- [BFF⁺14] H. H. Braun, A. Fassò, A. Ferrari, J. M. Jowett, P. R. Sala, and G. I. Smirnov. *Hadronic and electromagnetic fragmentation of ultrarelativistic heavy ions at LHC*. *Phys. Rev. ST Accel. Beams*, 17:021006, 2014.
- [BLM16] LHC Beam Loss Monitoring System Homepage. <https://ab-div-bdi-bl-blm.web.cern.ch/ab-div-bdi-bl-blm/>, April 2016.
- [BMR14] R. Bruce, A. Marsili, and S. Redaelli. *Cleaning performance with 11T dipoles and local dispersion suppressor collimation at the LHC*. *Proceedings of IPAC 2014, Dresden, Germany*, (MOPRO042):170–173, 2014.
- [BMW15] M. Berz, K. Makino, and W. Weishi. *An Introduction to Beam Physics*. Taylor & Francis Group, 2015.
- [BR16] O. Brüning and L. Rossi. *The High Luminosity Large Hadron Collider*. Advanced Series on Directions in High Energy Physics: Volume 24, 2016.
- [BRS87] D. P. Barber, G. Ripken, and F. Schmidt. *A non-linear canonical formalism for the coupled synchro-betatron motion of protons with arbitrary energy*. DESY-87-036, 1987.
- [Bru14] R. Bruce. New pencil beam in SixTrack and impact parameter study, 2014. Presentation at the 166th CWG Meeting.
- [CDS⁺12] B. V. Carlson, R. Donangelo, S. R. Souza, W. G. Lynch, A. W. Steiner, and M. B. Tsang. *Fermi breakup and the statistical multifragmentation model*. *Nuclear Physics A*, 876:77 – 92, 2012.
- [Col95] ALICE Collaboration. *Technical Proposal for A Large Ion Collider Experiment*. (CERN-LHCC-95-71), 1995.
- [Col12a] ATLAS Collaboration. *Observation of a new particle in the search for the Standard Model Higgs boson with the ATLAS detector at the LHC*. *Physics Letters B*, 716(1):1–29, 2012.

- [Col12b] CMS Collaboration. *Observation of a new boson at a mass of 125 GeV with the CMS experiment at the LHC*. *Physics Letters B*, 716(1):30–61, 2012.
- [Dep16] CERN IT Department. Batch System (Website). <http://information-technology.web.cern.ch/services/batch>, 2016.
- [Dir58] P. Dirac. *The Principles of Quantum Mechanics*. Oxford at the Clarendon Press, 4. edition, 1958.
- [DM⁺16] R. De Maria *et al.* SixTrack Developer’s Wiki, 2016.
- [DMFH15] R. De Maria, M. Fjellstrom, and P.D. Hermes. *SixTrackLib Manual*. 2015. Unpublished Note.
- [Duv01] V. Duvivier. Cross section of LHC dipole.. Dipole LHC: Coupe transversale. AC Collection. Legacy of AC., 2001.
- [F⁺13] M. Fjellstrom *et al.* *Particle Tracking in Circular Accelerators Using the Exact Hamiltonian in SixTrack*. Master’s thesis, 2013.
- [FJ14] W. Fischer and J. M. Jowett. *Ion Colliders. Reviews of Accelerator Science and Technology*, 07:49–76, 2014.
- [FLS65] R. P. Feynman, R. B. Leighton, and M. Sands. *The Feynman Lectures on Physics*. Vol. II. Addison-Wesley, 1965.
- [FSB⁺03] A. Fassò, P. R. Sala, F. Ballarini, A. Ottolenghi, G. Battistoni, F. Cerutti, E. Gadioli, M. V. Garzelli, A. Empl, and J. Ranft. *The physics models of FLUKA: status and recent developments*. *Proceedings of CHEP 2003, La Jolla, California, USA*, (MOMT005), 2003.
- [FSF⁺05] A. Ferrari, P. R. Sala, A. Fasso, and J. Ranft. *FLUKA: A multi-particle transport code (Program version 2005)*. *CERN-2005-10 (2005), INFN/TC_05/11, SLAC-R-773*, 2005.
- [GGG⁺11] R. Garoby, S. Gilardoni, B. Goddard, K. Hanke, M. Meddahi, and M. Vretenar. *Plans for the Upgrade of the LHC Injectors*. *Proceedings of IPAC 2011, San Sebastián, Spain*, (WEPS017):2517–2519, 2011.
- [Gri13] D.J. Griffiths. *Introduction to electrodynamics*, volume 4. Pearson, 2013.
- [Gua05] G. Guaglio. *Reliability of the beam loss monitors system for the Large Hadron Collider at CERN*. PhD thesis, 2005.

- [GvW14] P. Granieri and R. van Weelderen. *Deduction of Steady-State Cable Quench Limits for Various Electrical Insulation Schemes with Application to LHC and HL-LHC Magnets.* *IEEE Trans. Appl. Supercond.*, 24, 2014.
- [H⁺05] E.B. Holzer *et al.* *Beam loss monitoring system for the LHC.* volume 2, pages 1052–1056, 2005.
- [H⁺08] E.B. Holzer *et al.* *Development, Production and Testing of 4500 Beam Loss Monitors.* *Proceedings of EPAC 2008, Genoa, Italy,* (TUPC037):1134, 2008.
- [H⁺14] P. D. Hermes *et al.* *Studies on Heavy Ion Losses from Collimation Cleaning at the LHC.* *Proceedings of HB 2014, East-Lansing, MI, USA,* (MOPAB43):138–142, 2014.
- [HAB⁺16] P. D. Hermes, B. Auchmann, R. Bruce, W. Hofle, E. B. Holzer, M. Kalliokoski, G. Kotzian, A. Mereghetti, D. Mirarchi, E. Quaranta, S. Redaelli, B. Salvachua, G. Valentino, D. Valuch, D. Wollmann, and M. Zerlauth. *LHC Heavy-Ion Collimation Quench Test at 6.37Z GeV.* CERN-ACC-NOTE-2016-0031 MD, 2016.
- [HB⁺J⁺15] P. D. Hermes, R. Bruce, J. M. Jowett, and S. Redaelli. *Betatron Cleaning for Heavy Ion Beams with IR7 Dispersion Suppressor Collimators.* *Proceedings of IPAC 2015, Richmond, VA, USA,* (TUPTY025):2057–2059, 2015.
- [HB⁺J⁺16] P. D. Hermes, R. Bruce, J. M. Jowett, S. Redaelli, B. Salvachua Ferrando, *et al.* *Measured and Simulated Heavy-Ion Beam Loss Patterns at the CERN Large Hadron Collider.* *Nucl. Instr. Meth. Phys. Res. A*, 819:73–83, 2016.
- [Her03] W. Herr. *Concept of luminosity.* *Proceedings of CERN Accelerator School: 5th Intermediate Accelerator Physics Course,* 2003. CERN-2006-002.
- [HIT] Heidelberger Ionenstrahl Therapiezentrum - Website. <https://www.klinikum.uni-heidelberg.de/Beschleuniger-Anlage.117968.0.html>. Last accessed: 07.08.2015.
- [Hol08] N. Holden. Development of the ICOSIM Program and Application to Magnetised Collimators in the LHC. Technical Report CERN-AB-Note-2008-054, 2008.
- [HRS95] K. Heinemann, G. Ripken, and F. Schmidt. *Construction of Nonlinear Symplectic Six-Dimensional Thin-Lens Maps by Exponentiation.* DESY-95-189, 1995.
- [Iwa09] Y. Iwasa. *Case studies in superconducting magnets: design and operational issues.* Springer Science & Business Media, 2 edition, 2009.

- [J⁺11] J. M. Jowett *et al.* *First Run of the LHC as a Heavy-Ion Collider. Proceedings of IPAC 2011, San Sebastián, Spain,* (TUPZ016):1837, 2011.
- [J⁺12a] Beringer J. *et al.* *Review of Particle Physics.* *Phys.Rev.*, D86:010001, 2012.
- [J⁺12b] J. M. Jowett *et al.* *Heavy Ions in 2012 and the Programme up to 2022. Chamonix 2012 Workshop on LHC Performance,* 2012.
- [J⁺13] J. M. Jowett *et al.* *Proton-Nucleus Collisions in the LHC. Proceedings of IPAC 2013, Shanghai, China,* (MOODB201):49, 2013.
- [JLO⁺96] J. B. Jeanneret, D. Leroy, L. Oberli, and T. Trnkler. *Quench Levels and Transient Beam Losses in LHC Magnets.* (LHC Project Report 44), 1996.
- [JSA⁺16] J. M. Jowett, M. Schaumann, R. Alemany, R. Bruce, M. Giovannozzi, P. D. Hermes, W. Hofle, M. Lamond, T. Mertens, S. Redaelli, J. Uythoven, and J. Wenninger. *The 2015 Heavy-Ion Run of the LHC. Proceedings of IPAC 2016, Busan, Korea,* (TUPMW027):1493–1496, 2016.
- [JSV13] J. M. Jowett, M. Schaumann, and R. Versteegen. *Future heavy-ion performance of the LHC. Review of LHC and Injector Upgrade Plans Workshop,* 2013.
- [Kal15] M. Kalliokoski. *BLM Thresholds for 2015 Ion Quench Tests. CERN Engineering Change Request,* (LHC-BLM-ECR-0043), 2015.
- [Lam05] M. Lamont. *Estimates of Annual Proton Doses in the LHC.* (LHC Project Note 375), 2005.
- [Lam13] M. Lamont. *The First Years of LHC Operation for Luminosity Production. Proceedings of IPAC 2013, Shanghai, China,* (MOYAB101):6–10, 2013.
- [Lec14] A. Lechner. BLM thresholds for post-LS1 LHC operation: UFOs and orbit bumps in the arcs and straight sections, 2014. Presentation at Workshop on Beam-Induced Quenches, 16.09.2014.
- [Lee12] S.Y. Lee. *Accelerator physics.* World scientific Singapore, 2012.
- [Lef08] Christiane Lefèvre. The CERN accelerator complex. Dec 2008.
- [M⁺13a] A. Mereghetti *et al.* *SixTrack-FLUKA active coupling for the upgrade of the SPS Scraper.* *Proceedings of IPAC 2013, Shanghai, China,* (WEPEA064):2657–2659, 2013.

- [M⁺13b] V. Moens *et al.* Comparison of LHC Beam Loss Maps Using the Transverse Damper Blow Up and Tune Resonance Crossing Methods. Technical Report CERN-ACC-2013-0074, 2013.
- [M⁺16] D. Mirarchi *et al.* Cleaning Performance of the Collimation System of the High Luminosity Large Hadron Collider. *Proceedings of IPAC 2016, Busan, Korea*, (WEPMW030):2494–2497, 2016.
- [MAD] MAD - Methodical Accelerator Design. <http://cern.ch/madx/>. Last accessed: 05.05.2016.
- [Man14] D. Manglunki. *Performance of the Injectors with Ions after LS1. Proceedings of RLIUP: Review of LHC and Injector Upgrade Plans, Archamps, France*, pages 157–162, 2014.
- [MB83] S. K. Mtingwa and J. D. Bjorken. *Intrabeam scattering. Part. Acc.*, 13:115–143, 1983.
- [MBC⁺12] A. Mereghetti, V. Boccone, F. Cerutti, R. Versaci, and V. Vlachoudis. *The FLUKA Linebuilder and Element Database: Tools for building complex Models of Accelerator Beam Lines. Proceedings of IPAC 2012, New Orleans, Louisiana, USA*, (WEPPD071):2687–2689, 2012.
- [MCD⁺15] M. Meddahi, J. Coupard, H. Damerau, A. Funken, S. Gilardoni, B. Goddard, K. Hanke, L. Kobzeva, A. Lombardi, D. Manglunki, S. Mataguez, B. Mikulec, G. Rumolo, E. Shaposhnikova, and M. Vretenar. *LHC Injectors Upgrade (LIU) Project at CERN. Proceedings of IPAC 2015, Richmond, VA, USA*, (THPF093):3915–3918, 2015.
- [MHH⁺01] H. Meier, Z. Halabuka, K. Hencken, and D. Trautmann. *Bound-free electron-positron pair production in relativistic heavy-ion collisions. Phys.Rev.*, 63:032713–1 – 032713–7, 2001.
- [MRS⁺15] D. Mirarchi, S. Redaelli, W. Scandale, and G. Hall. *Crystal Collimation for LHC*. PhD thesis, Imperial College, London, 2015.
- [P⁺16] G. Papotti *et al.* Operation of the LHC with Protons at High Luminosity and High Energy. *Proceedings of IPAC 2016, Busan, Korea*, (WEPCA01):2066–2068, 2016.
- [PAA⁺16] G. Papotti, M. Albert, B. Auchmann, E. B. Holzer, M. Kalliokoski, and A. Lechner. *Macroparticle-induced Losses during 6.5 TeV LHC Operation. Proceedings of IPAC 2016, Busan, Korea*, (TUPMW023):1481–1484, 2016.

- [Piw74] A. Piwinski. *Intra-Beam Scattering*. *Proceedings of the IXth International Conference on High Energy Accelerators, Stanford, CA, USA*, (SLAC-R-839):405–409, 1974.
- [Pro94] CERN Accelerator School: 5th General Accelerator Physics Course, 1994. CERN-94-01-V-1.
- [Pro95] *Proceedings of CERN Accelerator School: 5th Advanced Accelerator Physics Course*, 1995. CERN-1995-006.
- [Psh16] I. A. Pshenichnov. *Private Communication*. 2016.
- [QBM⁺15] E. Quaranta, R. Bruce, A. Mereghetti, S. Redaelli, and A. Rossi. *Collimation cleaning at the LHC with advanced secondary collimator materials*. *Proceedings of IPAC 2015, Richmond, VA, USA*, (TUPTY029):2068–2071, 2015.
- [R⁺00] S. Rösler *et al.* *The Monte Carlo Event Generator DPMJET-III*. *Proceedings of the Monte Carlo 2000 Conference, Lisbon, Portugal*, pages 1033–1038, 2000.
- [R⁺12] S. Redaelli *et al.* *Aperture Measurements in the LHC Interaction Regions*. *Proceedings of IPAC 2012, New Orleans, Louisiana, USA*, (MOPPD062):508–510, 2012.
- [RARD05] S. Redaelli, R. Assmann, and G. Robert-Demolaize. *LHC Aperture and Commissioning of the Collimation System*. *Proceedings of LHC Project Workshop - Chamonix XIV*, 2005.
- [RBB⁺14] S. Redaelli, A. Bertarelli, R. Bruce, F. Carra, A. Mereghetti, and B. Salvachua. Collimator BLM threshold strategy, 2014. Proceedings of the Workshop on Beam-Induced Quenches, CERN, Geneva, Switzerland.
- [RD⁺05a] G. Robert-Demolaize *et al.* *A new Version of SixTrack with Collimation and Aperture Interface*. *Proceedings of PAC 2005, Knoxville, Tennessee, USA*, (FPAT081):4084, 2005.
- [RD⁺05b] G. Robert-Demolaize *et al.* *A New Version of Sixtrack with Collimation and Aperture Interface*. *Proceedings of PAC 2005, Knoxville, TN, USA*, (FPAT081):4084–4086, 2005.
- [Red13] S. Redaelli. The collimation system: defence against beam loss, 2013.
- [Ree03] J. R. Rees. *Symplecticity in Beam Dynamics: An Introduction*. SLAC-PUB-9939, Stanford Linear Accelerator Center, Stanford, CA, USA, 2003.

- [Rip85] G. Ripken. *Non-linear canonical equations of coupled synchro-betatron motion and their solution within the framework of a non-linear 6-dimensional (symplectic) tracking program for ultra-relativistic protons.* DESY-85-084, 1985.
- [RS95] G. Ripken and F. Schmidt. *A symplectic Six-Dimensional Thin-Lens Formalism for Tracking.* CERN-SL-95-12 (AP), 1995.
- [S⁺07] R. Schmidt *et al.* *LHC Machine Protection.* (LHC Project Report 1053), 2007.
- [S⁺14a] B. Salvachua *et al.* *Handling 1 MW Losses with the LHC Collimation System. Proceedings of IPAC 2014, Dresden, Germany,* (MOPRO043):174–177, 2014.
- [S⁺14b] M. Serluca *et al.* *HI-Lumi LHC Collimation Studies with Merlin Code. Proceedings of IPAC 2014, Dresden, Germany,* (MOPRI077):784–787, 2014.
- [SAFBC⁺15] M. Schaumann, R. Alemany Fernandez, C. Bahamonde Castro, B. Auchmann, V. Chetvertkova, R. Giachino, J. Jowett, M. Kallikoski, A. Lechner, T. Mertens, and L. Ponce. *LHC BFPP Quench Test with Ions (2015).* CERN-ACC-NOTE-2015-0024, 2015.
- [SBC⁺15] E. Skordis, R. Bruce, F. Cerutti, A. Ferrari, P. G. Ortega, P. D. Hermes, A. Lechner, A. Mereghetti, S. Redaelli, and V. Vlachoudis. *Impact of Beam Losses in the LHC Collimation Regions. Proceedings of IPAC 2015, Richmond, VA, USA,* (TUPTY046):2116–2119, 2015.
- [Sch94] F. Schmidt. *SixTrack Version 4.2.16 Single Particle Tracking Code Treating Transverse Motion with Synchrotron Oscillations in a Symplectic Manner - User's Reference Manual.* 1994. CERN/SL/94-56 (AP).
- [Sch06] F. Schmidt. *MAD-X a worthy successor for MAD8?* *Proceedings of ICAP04, St. Petersburg, Russia,* 558(1):47 – 49, 2006.
- [Sch15] M. Schaumann. *Heavy-Ion Performance of the LHC and Future Colliders.* PhD thesis, RWTH Aachen, Germany, 2015.
- [SCL⁺13] E. Skordis, F. Cerutti, A. Lechner, and A. Mereghetti. FLUKA Energy deposition simulations for quench tests, 2013. Talk at the LHC Collimation Review 30/5/2013.
- [Scr15] R. Scrivens. *Beam parameter from Linac3 to the PSB stopper.* *CERN EDMS: 1570447,* 2015.

- [Sie13] A. Siemko. Safeguarding the superconducting magnets, 2013.
- [SOL] Synchrotron SOLEIL - Sources et accélérateur. <http://www.synchrotron-soleil.fr/portal/page/portal/SourceAccelerateur>. Last accessed: 07.08.2015.
- [SRS⁺13] M. Sapinski, S. Redaelli, R. Schmidt, M. Bednarek, A. Priebe, D. Valuch, B. Salvachua, A. Verweij, T. Baer, A. Lechner, *et al.* *Beam induced quenches of LHC magnets*. *Proceedings of IPAC 2013, Shanghai, China*, (THPEA045):3243–3245, 2013.
- [Tam14] C. Tambasco. *An improved scattering routine for collimation tracking studies at LHC*. Master’s thesis, 2014. CERN-THESIS-2014-014.
- [tea12] The CERN FLUKA team. FlukaIO twiki, 2012.
- [Tin04] M. Tinkham. *Introduction to superconductivity*. Courier Corporation, 2 edition, 2004.
- [TJ94] T. Trenkler and J.B. Jeanneret. *K2: A Software Package evaluating Collimation Systems in Circular Colliders (Manual)*. CERN SL Note, 1994. SL/Note 94-105 (AP).
- [V⁺11] G. Valentino *et al.* *Semi-Automatic Beam-Based Alignment Algorithm for the LHC Collimation System*. *Proceedings of IPAC 2011, San Sebastián, Spain*, (THPZ034):3768–3770, 2011.
- [V⁺15] G. Valentino *et al.* *Characterization of Embedded BPM Collimators*. CERN-ACC-Note-2015-0028, 2015.
- [W⁺08] T. Weiler *et al.* *Beam Cleaning and Beam Loss Control*. *Proceedings of HB 2008, Nashville, Tennessee, USA*, (WGD08):359–362, 2008.
- [Web12] LHC Collimation Group Website. Tracking Code for Collimation Studies, 2012.
- [Wie99] H. Wiedemann. *Particle accelerator physics I: basic principles and linear beam dynamics*, volume 1. Springer Verlag, 1999.
- [Wol12] A. Wolski. *Linear Dynamics in Particle Accelerators. Lecture at the University of Liverpool*, 2012.
- [Wol14] A. Wolski. *Beam Dynamics in High Energy Particle Accelerators*. World Scientific, 2014.

List of Symbols and Acronyms

Symbols

ϵ_N Normalized transverse r.m.s. emittance.

γ Relativistic Lorentz factor.

S reference area.

Acronyms

ADT	Transverse damper.
B1	LHC Beam 1, rotating in clockwise direction.
B2	LHC Beam 2, rotating in counter-clockwise direction.
BLM	Beam loss monitor.
LHC	Large Hadron Collider.
TCLD	Target collimator long dispersion suppressor.
TCP	Target collimator primary (primary collimator).
TCSG	Target collimator secondary (secondary collimator).
TCT	Target collimator tertiary (tertiary collimator).

Selbstständigkeitserklärung

Hiermit erkläre ich, diese Arbeit selbstständig verfasst und keine anderen als die angegebenen Hilfsmittel benutzt zu haben.

Pascal Dominik Hermes